UNIVERSITÉ DE SHERBROOKE
Faculté de génie
Département de génie civil

FLEXURAL STRENGTH AND SERVICEABILITY OF CIRCULAR CONCRETE MEMBERS REINFORCED WITH FRP BARS AND SPIRALS

Étude de la résistance en flexion et du comportement en service d'éléments circulaires en béton armé de barres et de spirales de PRF

Thèse de doctorat
Spécialité: génie civil

Salaheldin Abdallah Ali Abdelhamed MOUSA

A dissertation submitted in partial fulfillment
of the requirements for the degree of
Doctor of Philosophy
(Civil Engineering)

Sherbrooke (Québec) Canada
July 2018

JURY MEMBRES

Prof. Brahim BENMOKRANE
Supervisor

Prof. Ehab EL-SALAKAWY
Examiner

Prof. Adel ELSAFTY
Examiner

Prof. Sébastien LANGLOIS
Examiner

DEDICATION

To the memory of my father

To my mother

To my wife and my daughters

To my sister and my brother

To those who appreciate the value of science and knowledge

ABSTRACT

Circular reinforced concrete (RC) members are widely used in infrastructure systems, such as bridge piers and piles, contiguous pile walls, and fender piles in marine structures. This is due to the simplicity of construction and because their strength characteristics under lateral loads are similar in all directions. Such members are usually exposed to aggressive environments that corrode the steel reinforcement. The result is structure deterioration, leading to costly repairs and rehabilitation. The use of fiber-reinforced polymer (FRP) as alternative reinforcing bars in RC structures has emerged as an alternative solution to overcoming the corrosion problem. In this research study, an experimental program was designed to investigate the flexural behavior and serviceability of concrete members with circular section and reinforced with FRP bars and spirals. A total of nine large-scale specimens with a total length of 6,000 mm and 500 mm in diameter were constructed and tested under four-point bending. The test parameters included the longitudinal-reinforcement ratio and the longitudinal-reinforcement type, including glass FRP (GFRP), carbon FRP (CFRP), basalt FRP (BFRP), and steel bars. The experimental results are reported in terms of moment–deflection behavior, flexural capacity, mode of failure, crack patterns, crack spacing, and crack widths. An analytical strain-compatibility model capable of predicting the flexural strength of circular FRP-RC members, including the sequential progressive failure, was developed and verified with the experimental results. Moreover, a simplified method, including design equations and design chart is presented using non-iterative analysis. This method accurately and simply predicted the flexural capacity and can be considered a simple and more straightforward for practicing engineers. In addition, the developed finite element model predicted the response of tested specimens with a reasonable degree of accuracy and was used to extend the range of investigated parameters. Crack-control models in the current FRP codes and design guidelines are reexamined, extended, and applied to circular FRP-RC members. The comparison with the experimental results indicates that the crack-control formulae developed from rectangular FRP-RC members are intended to allow for the cracking control of circular FRP-RC members by using the redefined parameters developed and proposed in this study. Finally, the measured deflections and experimental values of the effective moment of inertia (I_e) were analyzed and compared with those predicted using available models. The ACI 440.1R-15 model is found to overestimate the effective moment of inertia at service load level, and an appropriate modification is presented based on the results of the tested circular specimens. Moreover, an analytical model has been developed by using a layer-by-layer approach to predict the load-deflection relationship of circular FRP-RC members. The model predictions were in a good agreement with the experimental results.

Keywords: concrete; FRP bars; circular members; piles; flexural strength; serviceability; sectional analysis; finite element analysis.

RÉSUMÉ

Les éléments circulaires en béton armé (BA) sont largement utilisés dans les structures comme les piliers et pieux de ponts, les parois berlinoises et les colonnes de soutien pour les structures marines. L'utilisation bien répandue de ce type d'éléments est principalement due à leur simplicité de mise en place, leur résistance caractéristique et la résistance similaire en flexion dans toutes les directions. Ces éléments sont souvent exposés à des environnements agressifs, ce qui accélère la corrosion des barres en acier. Il en résulte des structures qui se détériorent plus rapidement menant à des coûts importants de réparation et de réhabilitation. L'utilisation des polymères renforcés de fibres (PRF) est une alternative intéressante de renforcement des structures en BA afin de contrer les problèmes liés à la corrosion de l'armature. Dans cette étude, un programme expérimental a été conçu pour étudier le comportement en flexion, à l'ultime et en service, des éléments en béton ayant une section circulaire et renforcés avec des barres et des spirales en PRF. Pour ce faire, neuf spécimens de grande taille, soit d'une longueur totale de 6 000 mm et d'un diamètre de 500 mm, ont été construits et testés en flexion en quatre points. Les paramètres d'essai comprenaient le ratio et le type de renforcement longitudinal, y compris le PRF de verre (PRFV), le PRF de carbone (PRFC), le PRF de basalte (PRFB) et les barres d'acier. Les résultats expérimentaux comprennent le comportement moment-déformation, la résistance en flexion, le mode de rupture, le patron de fissuration, l'espacement des fissures et la largeur des fissures. Un modèle analytique basé sur la compatibilité des déformations, capable de prédire la résistance en flexion des éléments circulaires en BA-PRF et incluant le mode de rupture progressif, a été développé et validé avec les résultats expérimentaux. De plus, une méthode simplifiée, non itérative, comprenant des équations et un graphique pour la conception est présentée. Cette méthode prédit précisément et simplement la capacité en flexion et est considérée comme une méthode suffisamment simple pour être utilisée par les ingénieurs de la pratique. En outre, le modèle développé par éléments finis a prédit la réponse des échantillons testés avec un degré de précision raisonnable et a été utilisé pour étendre la gamme des paramètres étudiés. Les modèles de contrôle de fissure dans les codes sur PRF et les directives actuelles de conception sont réexaminés, étendus et appliqués aux éléments circulaires de BA-PRF. La comparaison avec les résultats expérimentaux indique que les équations permettant de limiter la fissuration, développées à partir des éléments rectangulaires en BA-PRF, peuvent être utilisées pour contrôler la fissuration des éléments circulaires en BA-PRF en utilisant les paramètres redéfinis proposés dans cette étude. Finalement, les déplacements mesurés et les valeurs expérimentales du moment d'inertie effectif (I_e) ont été analysés et comparés aux valeurs prédites en utilisant les modèles disponibles dans les normes. Le modèle de l'ACI 440.1R-15 surestime le moment d'inertie effectif au niveau de la charge de service. Afin de pallier cet écart, une modification est présentée sur la base des résultats des essais sur les éléments circulaires. De plus, un modèle analytique a été développé en utilisant une approche couche par couche pour

prédire la relation charge-déformation des éléments circulaires en BA-PRF. Finalement, les prédictions effectuées par ce modèle sont en accord avec les résultats expérimentaux.

Mots-clés: béton; barres en PRF; éléments circulaires; piles; résistance en flexion; service; analyse sectionnelle; analyse par éléments finis.

ACKNOWLEDGEMENT

First of all, ***thanks to God*** for his grace and mercy, and for giving me the effort to complete this work.

I am fortunate enough to carry out this work under the supervision of ***Prof. Brahim Benmokrane***. It was a great honor to work with a great professor like him. He sincerely supported me throughout this work and offered any possible help to overcome every difficulty I faced.

Words will never be able to express my deepest gratitude and appreciation to ***Dr. Hamdy Mohamed***, for his kindness, great patience, continuous support and unlimited help throughout the work.

Many thanks to Profs. Ehab El-salakawy, Adel Elsafty, and Sébastien Langlois for accepting to be jury members of this dissertation and giving time to read and review.

The author would like to express his special thanks and gratitude to the Natural Science and Engineering Research Council of Canada (NSERC), Canada Research Chair Program, the Fonds de la recherche du Quebec–Nature et Technologie – (FRQ-NT) for their financial support, and Pultrall Inc. (Thetford Mines, QC, Canada) for the donation of the FRP materials.

The author thanks the technical staff of the CFI structural laboratory in the Department of Civil Engineering at the University of Sherbrooke. The author is grateful to Marc Demers and Jérôme Lacroix for their valuable contributions to testing.

Many thanks also go to my colleagues and friends at the University of Sherbrooke for their invaluable help during the experimental program.

Last but not least, I would like to convey my love to ***my mother, my wife, my daughters, my sister, and my brother*** for their invocation and encouragement to finish this dissertation.

TABLE OF CONTENTS

LIST OF FIGURES

Page

LIST OF TABLES

Page

CHAPTER 1. INTRODUCTION

1.1. General

Reinforced concrete (RC) members with circular cross sections are frequently used in practice, such as laterally loaded piers and piles in bridge foundations and in jetty substructures for marine and port infrastructure systems. In addition, they are used as secant piling systems for building combined earth-retention and groundwater cutoff walls in deep foundations for buildings and tunnel excavation applications. This is due to the simplicity of construction and because their strength characteristics under lateral loads are similar in all directions. Such members are usually exposed to aggressive environments that corrode the steel reinforcement. The result is structure deterioration, leading to costly repairs and rehabilitation. Estimates indicate that the United States spends billions of dollars annually to repair and replace bridge substructures such as pier columns ($2 billion) and marine piling systems ($1 billion) (Mohamed et al. 2014). The use of fiber-reinforced polymer (FRP) as alternative reinforcing bars in RC structures has emerged as an alternative solution to overcoming the corrosion problem. Since they are noncorroding material, FRP reinforcing bars constitute a better alternative to steel reinforcement. FRP bars have many advantages compared to steel: a density from one-quarter to one-fifth that of steel, neutrality to electrical and magnetic disturbances, and high tensile strength (ACI 440.1R-15).

Extensive research programs have been carried out over the last two decades to investigate the flexural response of FRP-RC members with rectangular sections (ACI 440.1R-15). These studies are greatly improving our knowledge of how rectangular concrete members reinforced with FRP bars should be analyzed and designed. Based on this knowledge, design provisions, equations, and limitations have been developed and included in design guidelines and codes (ACI 440.1R-15; CSA S806-12; CSA S6-14). In contrast, no research seems to have investigated RC members of circular cross section reinforced with FRP bars under flexural loads. Moreover, there are practically no code provisions or guidelines for the flexural design of circular concrete members with FRP reinforcement. ACI 440.1R-15, however, points out that there is no evidence that the flexural theory—developed for rectangular sections—applies

equally well to nonrectangular sections; the behavior of such members has yet to be confirmed experimentally.

In general, the flexural capacity of rectangular members can be easily determined (ACI 440.1R-15; CSA S806-12; CSA S6-14). In contrast to rectangular RC members, the bars in circular RC members are usually distributed in a circle at discrete points, giving rise to some difficulties in calculating the equilibrium of forces and strain compatibility. In addition, the stresses, which are variable over the section depth, are also distributed over an area of variable width. This fact leads to a very small part of the circular section exhibiting a maximum compression strain. On the other hand, the extreme tension reinforcement might reach the ultimate strain and stress, while the other layers of reinforcement have lower stresses, possibly equal to zero in proximity to the neutral axis. This produces a larger concrete compression zone and a smaller internal lever arm when compared to rectangular sections with equivalent dimensions. As a result of this behavior, smaller flexural capacities might be obtained in members with circular sections when compared to those with rectangular sections.

Crack control is an important serviceability criterion in the design of concrete members reinforced with FRP bars. Crack-width limits under service loads can govern the design of FRP-RC members. On the other hand, FRP bars are corrosion-resistant, so larger crack widths can be tolerated in FRP-RC members than in steel-RC members when reinforcement corrosion is the primary reason for crack control. Other considerations with regards to acceptable crack-width limits include aesthetics, creep rupture, and shear effects (ACI 440.1R-15). Crack spacing and crack width in FRP-RC members are dependent on many design parameters, including FRP-bar bond characteristics, the ratio of reinforcement area to surrounding concrete area, tensile strain in FRP bars, bar spacing, and concrete tensile strength. The bond capacity between FRP bars and concrete depends on concrete cover, bar size, surface treatments, concrete strength, and modulus of elasticity of FRP bars. Significant research has been carried out over the last two decades to determine relationships between concrete crack width and the aforementioned design parameters in FRP-RC members. The experimental work has focused mainly on beams with rectangular cross sections (Faza and GangaRao 1993; Masmoudi et al. 1996; Theriault and Benmokrane (1998); Toutanji and saafi 2000; Toutanji and Deng 2003; El-Salakawy and Benmokrane 2004; Ospina and Bakis 2007; El-Nemr et al. 2013 and 2016; Noel and Soudki

2014; Elgabbas et al. 2016 and 2017; Barris et al. 2017). In these studies, crack widths were predicted with the empirically proposed Gergely-Lutz 1968 equation and Frosch's 1999 physical model. Since crack width is a function of reinforcement stiffness and bond properties, the effect of the reinforcement type is significant. Hence, various modifications to the steel-based models have been proposed to account for the mechanical properties of FRP reinforcing bars (Faza and GangaRao 1993; Masmoudi et al. 1998; Toutanji and saafi 2000; Ospina and Bakis 2007; Noel and Soudki 2014). In addition, several design codes and guidelines have been published to control the cracks in rectangular FRP-RC members: AASHTO (2009), CSA S6 (2014), ACI 440-1R (2015), CSA S806 (2012), CNR-DT 203 (2006) and JSCE (1997). In contrast, studies on the cracking behavior of circular concrete members that can be reinforced with FRP bars have not yet been introduced.

Deflection control is an important performance criterion that needs to be satisfied to ensure the serviceability of fiber reinforced polymer (FRP) reinforced concrete (RC) structures. Under similar circumstances, in terms of concrete strength, applied loads, identical size, and reinforcement layout, FRP-RC members are expected to develop larger deformations than steel RC members due to the variable stiffness, linear elastic behavior, and particular bond features of FRP reinforcement (ACI 440.1R-15). Deflections of flexural members are commonly computed using an elastic deflection equation in conjunction with an effective moment of inertia I_e, a concept that empirically provides a transition between the upper and lower bounds of gross moment of inertia, I_g, and cracked moment of inertia, I_{cr}, as a function of the ratio of cracking to applied moment, M_{cr}/M_a. Several authors have proposed coefficients to modify Branson's equation to simulate the real behavior of rectangular FRP-RC members (Benmokrane et al. (1996); Theriault and Benmokrane (1998); Alsayed et al. (2000); Toutanji and Saafi (2000); Yost et al. (2003); Mousavi and Esfahani (2012); Adam et al. (2015)). Others have proposed deflection calculation models that derived from integration of curvatures (Razaqpur et al. (2000); Bischoff (2005, 2007); Bishcoff and Gross (2011a, b)). Based on these different approaches, equations for calculating deflections of FRP-RC members have been included in design guidelines and codes (ACI 440.1R-15; CSA S806-12; CNR-DT 203/2006). These models and code provisions were developed mainly based on experimental work on FRP-RC members with rectangular sections. Despite the valuable applications of circular RC members,

no research seems to have investigated RC members of circular cross-section reinforced with FRP bars.

This research intended to originally examine the flexural performance and serviceability of concrete members with circular sections and reinforced with FRP bars and spirals.

1.2. Research significance

Over the last two decades, substantial number of experimental research studies and discussions have been published related to the flexural behavior and serviceability of FRP-RC members with rectangular sections (ACI 440.1R-15). So far, this research is the first testing program aimed at investigating the flexural strength and serviceability of full-scale circular concrete members reinforced with GFRP bars and spirals. The results will contribute to implementing the use of FRP bars in circular concrete piles, which can be an innovative solution to the corrosion problem in infrastructure applications. This study also provides new insights into the analysis and design of circular concrete members reinforced with FRP reinforcements with an extensive theoretical study. The experimental data and design analysis provide the evidence required to include design provisions in the forthcoming ACI 440 code and updated CSA S6 code for the use of FRP bars and spirals as internal reinforcement in circular members under flexure.

1.3. Research objectives

This paper describes the results from nine full-scale circular RC members tested under four-point bending, including three specimens reinforced internally with GFRP, which is the most common type of FRP due to its cost effectiveness; three specimens reinforced with CFRP bars; two specimens reinforced with BFRP bars; and one reinforced with steel for comparison purposes. The main objective of this investigation is to examine the feasibility and efficiency of using FRP bars and spirals in circular RC members under flexural load. A number of specific research objectives were identified and are listed below.

1- To investigate the effect of the FRP reinforcement ratio on flexural strength and serviceability of circular FRP-RC members.

2- To discover the failure mechanisms of such members under flexural loads.

3- To assess the ductility and deformability of such members.

4- Assess the accuracy of the current FRP design provisions that were developed on rectangular sections for estimating the flexural strength, crack control, and deflection of the tested circular specimens, including ACI 440-1R-15, AASHTO-09, CSA S6-14, JSCE (1997), and Italian National Research Council CNR-DT 203/2006.

5- To propose simple and accurate design procedures for predicting the flexural strength, crack control, and deflection of circular FRP-RC members.

6- To develop a reliable analytical 3-D model using non-linear finite element analysis program (ANSYS) to predict the behavior and flexural capacity of circular FRP-RC members.

1.4. Research methodology

To achieve the objectives of this research, extensive experimental and analytical programs were designed. The experimental program was conducted to investigate the flexural behavior and serviceability of concrete members with circular section and reinforced with FRP bars and spirals. A total of nine large-scale specimens with a total length of 6,000 mm and 500 mm in diameter were constructed and tested under four-point bending. Testing was intended to assess the flexural strength of circular FRP-RC members, so all of the specimens were designed such that their shear strength exceeded their flexural strength. This was achieved by reducing the shear influence and choosing a shear span-to-depth ratio greater than five (Kani 1964). The current study addressed the worst (critical) case when the flexural demand prevails over the axial load in columns, piles and piers. In addition, there are some applications for using a circular section, such as soft-eyes in tunnels and fender piles in marine structures that are usually subjected to pure bending moment without axial load. The test parameters included the longitudinal-reinforcement ratio and the longitudinal-reinforcement type, including three specimens reinforced internally with GFRP, which is the most common type of FRP due to its cost effectiveness; three specimens reinforced with CFRP bars; two specimens reinforced with BFRP bars; and one reinforced with steel. It should be noted that only two specimens were reinforced with newly produced BFRP bars for comparison purposes with specimens reinforced

with GFRP and CFRP bars. The experimental results were reported in terms of moment–deflection behavior, flexural capacity, mode of failure, crack patterns, crack spacing, and crack widths. The ductility and deformability of the test specimens were estimated using different approaches. An analytical strain-compatibility model capable of predicting the flexural strength of circular FRP-RC members, including the sequential progressive failure, was developed and verified with the experimental results. Moreover, a simplified method including design equations, design chart, and step-by-step design procedures were presented using non-iterative analysis. In addition, the finite element model developed predicted the response of tested specimens with a reasonable degree of accuracy and was used to extend the range of investigated parameters. On the other hand, crack-control models in the current FRP codes and design guidelines were reexamined, extended, and applied to circular FRP-RC members. Finally, the measured deflections and experimental values of the effective moment of inertia (I_e) were analyzed and compared with those predicted using available models.

1.5. Dissertation Layout

The dissertation consists of eight chapters. The contents of each chapter can be summarized as follows:

Chapter 1 presents the introduction, research significance, objectives, and methodology of this study.

Chapter 2 provides a brief summary of the main characteristics and properties of the FRP materials used as internal reinforcement. The main studies that investigated the flexural behavior and serviceability of concrete members reinforced with FRP bars. The code provision that related to flexural behavior and serviceability of FRP reinforced concrete members are also presented.

Chapter 3 (1st article) investigates the flexural strength and behavior of concrete members with circular section and reinforced with GFRP bars and spirals both experimentally and theoretically. The test parameters included reinforcement flexural stiffness (GFRP versus steel) and GFRP longitudinal-reinforcement ratio. Ductility and deformability of the tested specimens were calculated and evaluated. An analytical strain-compatibility model capable of predicting the flexural strength of circular GFRP-RC members, including the sequential progressive

failure, was developed and verified with the experimental results. Moreover, a simplified method, including design equations and design chart, was presented using non-iterative analysis [**Reference**: Mousa, S., Mohamed, H. M., and Benmokrane, B. (2018) "Flexural Strength and Design Analysis of Circular RC Members with GFRP Bars and Spirals." *ACI Structural Journal*, accepted].

Chapter 4 (2nd article) reports on a study in which the flexural strength and deformability of circular concrete members with hybrid reinforcement—CFRP bars and GFRP spirals—were assessed experimentally and analytically. Detailed design procedures using a computer program were proposed for estimating the flexural capacity of circular CFRP-RC members using A Microsoft Excel Spreadsheet. The experimental and analytical results were discussed and compared [**Reference**: Mousa, S., Mohamed, H. M., and Benmokrane, B. (2018) "Strength and Deformability Aspects of Circular Concrete Members Reinforced with Hybrid Carbon-/Glass-FRP Reinforcement under Flexure." submitted to *Journal of Composites for Construction*, ASCE, under review].

Chapter 5 (3rd article) reports on the experimental results of flexural tests on full-scale circular RC members with BFRP reinforcement, followed by an intensive analytical study and finite-element analysis. The main investigated parameters were the ratio and type of longitudinal reinforcement. An analytical model was developed using a layer-by-layer approach to estimate the flexural strength of the tested specimens. In addition, the finite-element model developed predicted the response of the tested specimens with a reasonable degree of accuracy and was used to extend the range of the investigated parameters [**Reference**: Mousa, S., Mohamed, H. M., Benmokrane, B., and Ferrier, E. (2018) "Flexural Behavior of Full-Scale Circular Concrete Members Reinforced with Basalt FRP Bars and Spirals: Tests and Theoretical Studies." *Composite structures*, 203, 217-232].

Chapter 6 (4th article) investigates the cracking and crack control of circular FRP-RC members experimentally and theoretically. The experimental results are reported in terms of crack patterns, crack spacing, and crack width versus flexural tension-bar strain and the applied moment. Crack-control models in the current FRP codes and design guidelines were reexamined, extended, and applied to circular FRP-RC members [**Reference**: Mousa, S., Mohamed, H. M., and Benmokrane,

B. (2018) "Cracking and Crack Control in Circular Concrete Bridge Members Reinforced with Fiber-Reinforced-Polymer (FRP) Bars." *Journal of Bridge Engineering*, ASCE, accepted].

Chapter 7 (5th article) investigates serviceability performance in terms of deflection predictions of circular FRP-RC members experimentally and theoretically. The measured deflections and experimental values of the effective moment of inertia (I_e) were analyzed and compared with those predicted using available models in the literature, as well the models included in the design guidelines and codes. Based on the analysis of the test results, a new equation was developed to accurately predict the deflection of the tested circular specimens. Moreover, an analytical model has been developed by using a layer-by-layer curvature analysis approach based on cross-sectional analysis satisfying strain compatibility and equilibrium conditions [**Reference**: Mousa, S., Mohamed, H. M., and Benmokrane, B. (2018) "Deflection Prediction Methodology for Circular RC Members Reinforced with FRP Bars." submitted to *ACI Structural Journal*, accepted].

Chapter 8 presents summary, conclusions, and the recommendations for future study.

CHAPTER 2. LITERATURE REVIEW

2.1. General

This chapter provides a brief summary of the main characteristics and properties of the Fiber-reinforced polymer (FRP) materials used as internal reinforcement. This is followed by a demonstration of the main studies that investigated the flexural behavior and serviceability of concrete members reinforced with FRP bars. The code provision that related to flexural behavior and serviceability of FRP reinforced concrete members are also presented.

2.2. FRP Materials

2.2.1. FRP Constituent materials

FRP is a specific type of two-component composite material consisting of high strength fibers embedded in a polymer matrix. As the FRP materials are composed of two distinct materials, overall FRP material properties depend primarily on those of the individual constituents. The fibers are significantly stronger than the resin material and control the elastic modulus and final strength of the composite. The mechanical properties of the final FRP product depend on a number of parameters. This includes fiber type, quality, volumetric ratio, adhesion resin and most importantly the manufacturing process (ACI 440.1R-15).

2.2.1.1. Fibers

The fibers provide the strength and stiffness of FRP. Because the fibers used in most structural FRP applications are continuous and are oriented in specified directions, FRP materials are orthotropic, and they are much stronger and stiffer in the fiber direction(s). Fibers are generally selected to have high stiffness, high ultimate strength, low variation of strength between individual fibers, stability during handling, and uniform diameter. In civil engineering applications, the most commonly used fiber types are glass, carbon, aramid, and recently basalt fibers. The suitability of the various fibers for specific applications depends on a number of factors including the required strength, stiffness, durability considerations, cost constraints, and the availability of component materials.

2.2.1.2. Resins

The resin (matrix) is the binder of the FRP and plays many important roles. Some of the more critical functions played by the matrix are to bind the fibers together, protect the fibers from abrasion and environmental degradation, separate and disperse fibers within the composite, and transfer the forces between the individual fibers. Matrix materials for FRPs can be grouped into two broad categories: thermoplastics and thermosetting resins. Thermoplastics include such polymer compounds as polyethylene, nylon, and polyamides, while thermosetting materials include Polyesters, epoxies, and vinylesters.

2.2.2. Manufacturing process

There are three main manufacturing processes for FRP composites; pultrusion, braiding, and filament winding (ISIS Canada 2007). Pultrusion is a common technique for manufacturing continuous lengths of FRP bars that are of the constant or nearly constant profile. A schematic drawing of this technique is shown in Fig. 2.1. Continuous strands of reinforcing material are drawn from creels, through a resin tank, where they are saturated with resin, and then through a number of wiper rings into the mouth of a heated die. The speed of pulling through the die is predetermined by the curing time needed. To ensure a good bond with concrete, the surface of the bars is usually braided or sand-coated.

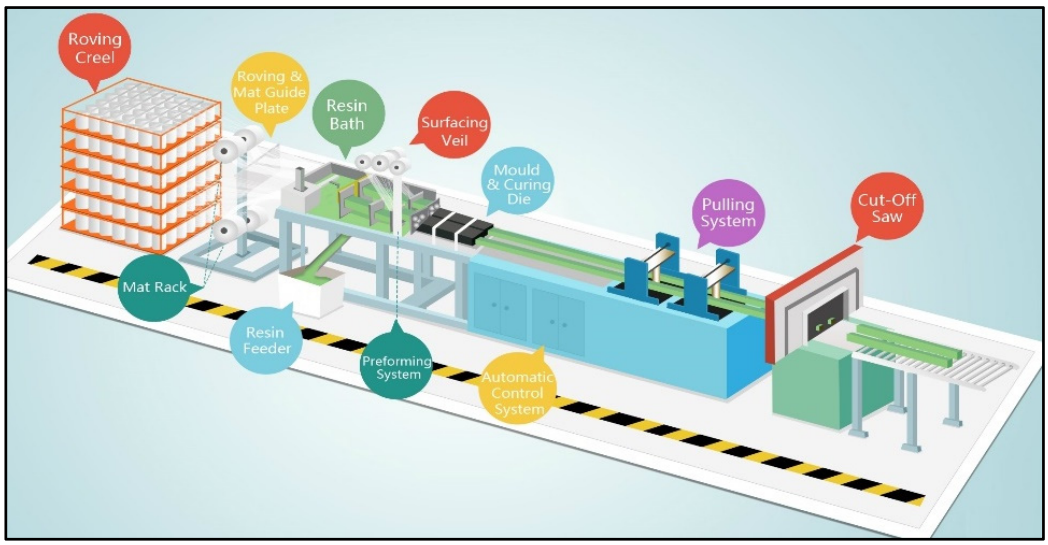

Figure 2.1 A schematic drawing of Pultrusion process.

2.2.3. FRP products as internal reinforcement

FRP reinforcing bars are manufactured from continuous fibers (such as carbon, glass, aramid, and basalt) embedded in matrices (thermosetting or thermoplastic). Similar to steel reinforcement, FRP bars are produced in different diameters, depending on the manufacturing process. FRP materials are anisotropic and are characterized by high tensile strength with no yielding only in the direction of the reinforcing fibers (ACI 440.1R-15). The tensile behavior of FRP bars consisting of one type of fiber material is characterized by a linearly elastic stress-strain relationship until failure. Compared to ductile steel, FRPs generally have higher tensile capacity and relatively lower modulus of elasticity. Table 2.1 summarizes the typical mechanical tensile properties of FRP bars compared to those of steel reinforcement. More details about various properties of FRP reinforcement can be found in other publications (ACI 440.1R-15; AASHTO-09).

Table 2.1 Typical tensile properties of reinforcing bars (ACI 440.1R-15)

Properties	Steel	GFRP	CFRP	AFRP
Nominal yield stress, MPa	276 to 517	N/A	N/A	N/A
Tensile strength, MPa	483 to 1600	483 to 690	600 to 3960	1720 to 2540
Elastic modulus, GPa	200	35 to 51	120 to 580	41 to 125
Yield strain, percent	0.14 to 0.25	N/A	N/A	N/A
Rupture strain, percent	6.0 to 12.0	1.2 to 3.1	0.5 to 1.7	1.9 to 4.4

2.3. Flexural behavior and strength of rectangular FRP-RC members

2.3.1. Flexural capacity of rectangular FRP-RC members

The theoretical flexural capacity of rectangular FRP-RC members can be calculated based on the principles of force equilibrium and strain compatibility between the concrete and FRP bars. The design philosophy is based on the following assumptions:

1. Strain in the concrete and the FRP reinforcement is proportional to the distance from the neutral axis (a plane section remains plane after deformation up to failure).
2. The maximum usable compressive strain in the concrete is assumed to be 0.003 as per ACI 440.1R-15 or 0.0035 as per CSA S806-12.
3. The tensile strength of concrete is ignored.

4. The tensile behavior of the FRP reinforcement is linearly elastic until failure.
5. The strain in the FRP reinforcement, whether in tension or compression, is the same as that in the surrounding concrete (i.e. perfect bond exists between the FRP reinforcement and concrete).
6. The distribution of concrete compressive stress can be described by the equivalent rectangular stress block shown in Fig. 2.2 with parameters α_1 and β_1, calculated from Eqns. (2.1.a and b) for ACI 440.1R-15 and Eqns. (2.2.a and b) for CSA S806-12:

$$\alpha_1 = 0.85 \tag{2.1.a}$$

$$\beta_1 = 0.85 - \frac{0.05\left(f_c' - 28\right)}{7} \geq 0.65 \tag{2.1.b}$$

$$\alpha_1 = 0.85 - 0.0015 f_c' \geq 0.67 \tag{2.2.a}$$

$$\beta_1 = 0.97 - 0.0025 f_c' \geq 0.67 \tag{2.2.b}$$

Flexural design of concrete members reinforced with FRP bars is based on strain compatibility and depends on whether the failure is governed by rupture of the tensile reinforcement or concrete crushing. There are three possible modes of flexural failure are available for concrete member reinforced with FRP bars:

- Balanced failure: simultaneous rupture of FRP and crushing of concrete;
- Compression failure: concrete crushing while FRP remains in the elastic range with a strain level smaller than the ultimate strain; and,
- Tension failure: rupture of FRP in which FRP reaches its ultimate strain level before concrete crushing.

The mode of failure can be determined theoretically by comparing the reinforcement ratio $\left(\rho_f\right)$ with the balanced reinforcement ratio $\left(\rho_{fb}\right)$. The FRP reinforcement ratio can be computed from Eq. 2.3, and the balanced FRP reinforcement ratio can be computed from Eq. 2.4. If the

reinforcement ratio is less than the balanced ratio ($\rho_f < \rho_{fb}$), the FRP rupture limit state controls. Otherwise, ($\rho_f > \rho_{fb}$) the concrete crushing limit state controls.

$$\rho_f = \frac{A_f}{bd} \tag{2.3}$$

$$\rho_{fb} = \alpha_1 \beta_1 \frac{f_c'}{f_{fu}} \frac{E_f \varepsilon_{cu}}{E_f \varepsilon_{cu} + f_{fu}} \tag{2.4}$$

where f_c' is the specified compressive strength of concrete; f_{fu} and E_f are the ultimate tensile strength and modulus of elasticity of FRP bars, respectively; and ε_{cu} is the maximum usable compressive strain in the concrete.

Most of the current codes and design guidelines recommended the compression failure for the design of flexural members reinforced with FRP bars (CSA-S806-12; ACI 440.1R-15). ACI 440.1R-15, however, accepts both failure modes (compression failure or tension failure) if strength and serviceability criteria are satisfied. On the other hand, CSA S806-12 accepts the tension failure mode if the factored resistance of a section is greater than 1.6 times the effect of the factored loads.

When $\rho_f > \rho_{fb}$, the controlling limit state is crushing of the concrete, and the stress distribution in the concrete can be approximated with a rectangular stress block. Based on the equilibrium of forces and strain compatibility (shown in Fig. 2.2).

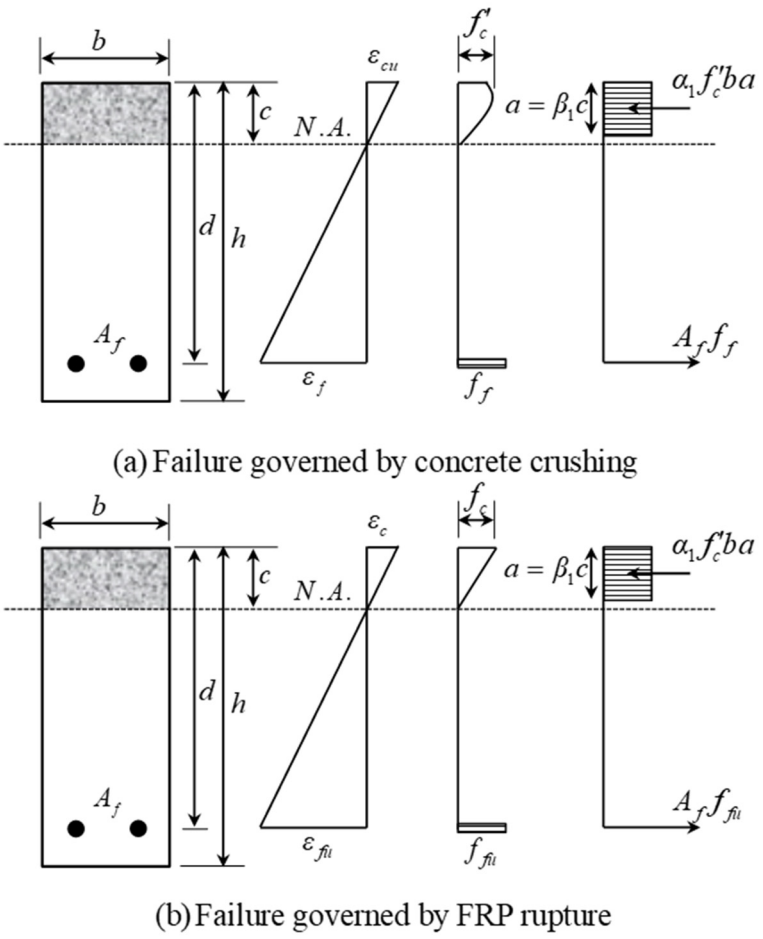

Figure 2.2 Strain and stress distribution at the ultimate condition.

The nominal flexural strength of a section can be expressed in terms of the FRP reinforcement ratio, as given in Eq. 2.5 (ACI 440.1R-15).

$$M_n = \rho_f f_f \left(1 - 0.59 \frac{\rho_f f_f}{f_f}\right) bd^2 \tag{2.5}$$

When $\rho_f < \rho_{fb}$, the controlling limit state is rupture of the FRP reinforcement, and the nominal flexural strength of a section can be computed as shown in Eq. 2.6 (ACI 440.1R-15).

$$M_n = A_f f_{fu} \left(d - \frac{\beta_1 c}{2}\right) \tag{2.6}$$

With regards to the available experimental results on FRP-RC members, Benmokrane et al. (1996); Masmoudi et al. (1998); and Theriault and Benmokrane (1998) reported that the ultimate

moment was 15% underestimated by ACI 440.1R formula when the section failed by compression failure, but it was 5% overestimated in the case that the section failed by tension failure. This difference was attributed to the variability of the compressive strength of concrete and tensile strength of the FRP reinforcing bars.

Rafi et al. (2008) found that ACI 440.1R formulations underestimated the moment capacity of their four tested FRP beams to about 33%, probably because the actual strain in concrete exceeded the maximum concrete strain of 0.003 as a result of the confinement provided especially by the stirrups.

Barris et al. (2009) reported that for their tested beams the experimental ultimate load was 51% higher than expected according to ACI 440.1R predictions. This difference probably occurred because the ultimate concrete compressive strain observed in the experiments was higher than the value indicated by the theoretical approaches.

2.3.2. Parameters affecting moment capacity of FRP-RC members

2.3.2.1. Effect of reinforcement ratio

Masmoudi et al. (1998) and Theriault and Benmokrane (1998) stated that as the reinforcement ratio increases, the ultimate moment capacity increases, but this increase is limited by the concrete compressive failure strain of over-reinforced concrete beams.

Kassem et al. (2011) reported concrete crushing in FRP-RC beams, whereas the increased ρ_f did not significantly increase the flexural capacity. The increases were 4 and 16% when ρ_f was increased by 50 and 100%, respectively.

El-Nemr et al. (2013) found that in the case of the normal strength concrete (NSC) beams, increasing ρ_f from 0.36 to 1.47% increased the load-carrying capacity by 143%. Increasing ρ_f from 0.55 to 1.78% increase the capacity by 224%. Increasing ρ_f by three to four times resulted in an average increase of 83.5% in the load-carrying capacity. Similarly, for the HSC beams, increasing ρ_f from 0.36 to 1.47% and from 0.55 to 1.78% increased the ultimate load-carrying capacity by 28% and 116%, respectively.

2.3.2.2. Effect of concrete strength

Theriault and Benmokrane (1998) stated that as the concrete strength increases, the ultimate moment capacity increases, but this increase is limited by the concrete compressive failure strain of over-reinforced concrete beams. Similar remarks have been made by Nanni (l993), who reported that the maximum moment capacity is highly variable because it depends on the concrete maximum strain.

Yost and Gross (2002) reported that using higher concrete strength resulted in the more efficient use of the FRP. For some of their tested beams, increasing the concrete strength increased the ultimate load-carrying capacity. The increased ratio was not consistent because of the lower measured concrete strains at failure.

2.3.2.3. Effect of FRP reinforcement surface

Nanni (1993) studied the flexural behavior of concrete beams reinforced with different GFRP bars (smooth or sand-coated) and steel deformed bars. It was noted that the sand-coated FRP increased the ultimate flexural capacity by approximately 25% compared with the equivalent uncoated rebars. The authors state that the ultimate strength could be predicted on the basis of the material properties of the concrete and reinforcement. On the other hand, Kassem et al. (2011) indicated that the surface texture played no role in beam flexural capacity when sand-coated bars and ribbed-surface bars were used.

2.4. Ductility and deformability

Ductility is a structural-design requirement in most design codes. The traditional definition of ductility for steel-reinforced concrete members, which considers the yielding of steel bars as a reference point, cannot be directly applied to members reinforced with FRP reinforcement due to the linear-elastic behavior of the FRP bars up to failure. Several methods have been proposed to calculate the ductility of FRP-RC structures. These methods can be divided into three categories depending on the approach used:

- Energy-based ductility index

- Deformability factor
- Curvature-based deformability index

2.4.1. Energy-Based Ductility Index

Naaman and Jeong (1995) defined ductility as the ratio of the total energy to the elastic energy and proposed the following equation to compute the ductility index, μ_e, which can be applied to steel- and FRP-RC members:

$$\mu_e = \frac{1}{2}\left(\frac{E_{tot}}{E_{el}} + 1\right) \tag{2.7}$$

where E_{tot} = the total energy computed as the area under the load-deflection curve, and E_{el} = the elastic energy released upon failure computed as the area of the triangle formed at failure load by the line having the weighted average slope of the two initial straight lines of the load-deflection curve, as shown in Fig. 2.3.

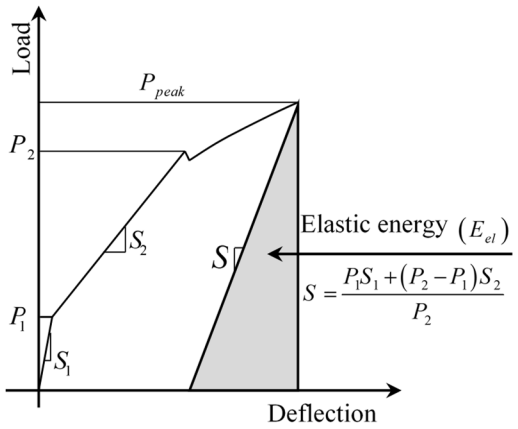

Figure 2.3 Ductility index definition.

2.4.2. Deformability Factor

The *Canadian Highway Bridge Design Code* (CAN/CSA S6-14) adopted the Jaeger et al. 1997 (*J*-factor) approach to evaluate the deformability index of FRP-RC members. In this approach, the absorbed energy is measured based on deformability rather than ductility to ensure adequate deformation of FRP-reinforced structures before failure. The deformability *J*-factor takes into

account the strength effect as well as the curvature effect at service and ultimate conditions. The deformability *J*-factor can be calculated as follows:

$$J = \frac{M_{ultimate}}{M_c} \times \frac{\psi_{ultimate}}{\psi_c} \tag{2.8}$$

where ψ_c = curvature at a concrete strain equal to 0.001 (service condition); $\psi_{ultimate}$ = curvature at ultimate; M_c = moment at concrete strain equal to 0.001; $M_{ultimate}$ = ultimate moment. CSA S6-14 requires a *J*-factor exceeding 4 and 6 for rectangular sections and T-sections, respectively, with no recommendation for circular sections.

2.4.3. Curvature-Based Deformability Index

Vijay and GangaRao (2001) defined the deformability factor as the ratio of energy absorption (area under moment–curvature curve or area under the load-deflection curve) at ultimate, E_{tot}, to energy absorption at a limiting curvature value of 0.005/d, $E_{\psi=0.005/d}$, which satisfies the serviceability criteria of both deflection and crack width.

$$J_{VG} = \frac{E_{tot}}{E_{\psi=0.005/d}} \tag{2.9}$$

2.5. Serviceability performance of rectangular FRP-RC members

Serviceability can be defined as satisfactory performance under service load conditions. FRP-RC members have a relatively small stiffness after cracking when compared to steel-RC members with the same reinforcement ratio. Consequently, permissible deflections under service loads can control the design. In general, designing FRP-reinforced cross sections for flexural strength may not satisfy serviceability criteria for crack control and deflection.

2.5.1. Crack control of FRP-RC members

Crack control is an important serviceability criterion in the design of concrete members reinforced with FRP bars. Crack-width limits under service loads can govern the design of FRP-RC members. On the other hand, FRP bars are corrosion-resistant, so larger crack widths can be tolerated in FRP-RC members than in steel-RC members when reinforcement corrosion is

the primary reason for crack control. Other considerations with regards to acceptable crack-width limits include aesthetics, creep rupture, and shear effects (ACI 440.1R-15).

Cracking control of RC flexural members is mainly developed for steel RC members with rectangular sections, based on empirical models of analyzing experimental data (Gergely and Lutz 1968) or on a physical model by multiplying the crack spacing by the mean strain of flexural reinforcement (Frosch 1999). For the cracking control of FRP-RC members, design equations and prediction models are generally based on similar formulation to that of steel rectangular reinforced concrete members, with coefficients that depend on the different characteristics of the FRP bars and their interaction with concrete

In 1993, Faza and GangaRao replaced steel strain with FRP strain in Gergley-Lutz equation to predict the crack width of FRP-RC members**.** Masmoudi et al. (1996) carried out an experimental investigation on the cracking behavior of concrete beams reinforced with fiber reinforced plastic rebars. The effects of reinforcement ratio on the cracking pattern, crack spacing, cracking moment, and crack width were investigated. The authors showed that as the reinforcement ratio increases, the number of cracks increases and the crack spacing decreases. However, they found that the effect of the reinforcement ratio on cracking moment was negligible. In addition, the authors introduced a coefficient in the Gergely-Lutz equation to account for the bond characteristics of FRP bars. The predictions of the modified model compared well to the test results achieved by Theriault and Benmokrane (1998).

Theriault and Benmokrane (1998) tested 12 concrete beams reinforced with FRP bars. The main parameters investigated in this study were the reinforcement ratio and the concrete strength. The authors concluded from their work that the effect of the concrete strength and the reinforcement ratio on the crack spacing is negligible, and the crack spacing slightly decreases as the load increases. The higher the concrete strength is, the wider the crack for the same applied moment. Moreover, Theriault and Benmokrane (1998) explained that those wider cracks are due to the release of greater stress at crack initiation, followed by a sudden crack formation. However, the reinforcement ratio shows a strong influence on the crack width: A smaller crack width is obtained by means of a higher reinforcement ratio.

Toutanji and Saafi (2000) tested six GFRP reinforced concrete beams under flexure; two balanced-condition beams and four over-reinforced beams. The authors investigated the crack widths and compared the experimental results with results from existing models. The authors proposed an equation to predict crack widths, developed using a regression analysis on experimental results which is a modified Gergely-Lutz equation, with k_g being modified from a constant to a factor which depends on reinforcement ratio and reinforcement modulus of elasticity.

El-Salakawy et al. (2002) presented an experimental study that included 14 full-scale reinforced concrete beams. The test parameters were the type of reinforcing bars and reinforcement ratio. The authors found that, at service load levels, increasing the CFRP reinforcement ratio by 50% and 100% decreased the maximum crack width by approximately 37% and 55%, respectively. They concluded that for beams reinforced with approximately the same reinforcement ratio of CFRP bars and steel, the crack width at service load level of beam increased by 44% compared to the control beam.

In 2001, ACI 440.1R stated that crack width is proportional to the reinforcement strain rather than stress, and adopted a modified form of the Gergley-Lutz equation by introducing a factor k_b to account for the bond between FRP and concrete (Gao et al. 1998). It states that, if the bond is similar to steel, then k_b is equal to 1. If the bond is lower than that of steel, then k_b is greater than 1, and vice versa. If k_b is unknown, a value of 1.2 should be assigned. Toutanji and Deng (2003) concluded that ACI 440.1R-01 provided satisfactorily crack-width predictions if FRP bars were placed in one layer.

In 2002, the Canadian building code (CSA-S806) introduced a z factor based on the Gergely and Lutz (1968) equation for crack control. This z factor should not exceed 45 kN/mm for interior exposure and 38 kN/mm for exterior exposure. Furthermore, it stated that the value of k_b shall be determined experimentally, but, in the absence of test data, it may be taken as 1.2 for deformed rods. El-Salakawy and Benmokrane (2004) reported that the ACI 440.1R-01 approach with a k_b coefficient of 1.0 provided correlated well but conservatively with their test results on FRP-RC slabs and that all specimens yielded a z factor lower than 38 kN/mm.

ACI 440.1R-06 and CSA S6-06 included the physical model proposed by Frosch (1999) with some modifications to control cracking of FRP-RC members. In the absence of test data, ACI 440.1R-06 recommended 1.4 for the bond coefficient k_b, while CSA S6-06 recommended 0.8 and 1.0 for sand-coated and deformed FRP bars, respectively. ISIS Canada (2007) provided a k_b coefficient with a recommended value equal to 1.2. ACI 440.1R-15 has replaced the traditional crack-width formula for crack control with an indirect procedure that controls flexural-crack widths with a maximum reinforcing-bar spacing. This formula is based on the equation proposed by Ospina and Bakis (2007), which is based on the Frosch (1999) approach. The recommended value for the bond coefficient k_b was taken as 1.4, if not determined experimentally.

The bond factor k_b of different types of FRP bars (carbon, glass, and aramid) was estimated based on experimental crack-width results and using the ACI 440.1R-06 design equation (Kassem et al. 2011). The estimated values ranged from 0.86 to 1.32. El-Nemr et al. (2013 and 2016) found that the ACI 440.1R-06 bond coefficient k_b value of 1.4 was very conservative for both sand-coated and helically grooved GFRP bars. In contrast, the k_b of 0.8 recommended by CSA S6-06 yielded unconservative predictions. Reasonable crack-width predictions were obtained from the ACI 440.1R-06 and CAN/CSA S6-06 equations using a k_b factor of 1.2 for helically grooved GFRP bars and 1.0 for sand-coated GFRP bars (El-Nemr et al. 2013 and 2016). Noel and Soudki (2014) proposed a simple modification to the Frosch model to account for the variation in reinforcement stress between cracks. The proposed modification accounts for the contribution of the concrete between cracks and gives consistently accurate predictions for all reinforcement stress levels in the service range. The bond coefficient of 1.3 for sand-coated GFRP bars was recommended to be used in the modified equation. Recently, Elgabbas et al. (2016b and 2017) conducted experimental investigations on sand-coated and ribbed basalt-FRP (BFRP) bars. The k_b factor was found to be 0.76 and 0.83 for the sand-coated and ribbed bars, respectively.

2.5.2. Deflection of FRP-RC members

Deflection is an important performance criterion that needs to be satisfied to ensure the serviceability of FRP-RC structures. Under similar circumstances, in terms of concrete strength, applied loading, identical size, and reinforcement layout, FRP-RC members are expected to develop larger deformations than steel RC members due to the variable stiffness, linear elastic behavior, and particular bond features of FRP reinforcement (ACI 440.1R-15). Deflections of flexural members are commonly computed using an elastic deflection equation in conjunction with an effective moment of inertia I_e, a concept that empirically provides a transition between the upper and lower bounds of gross moment of inertia, I_g, and cracked moment of inertia, I_{cr}, as a function of the ratio of cracking to applied moment, M_{cr}/M_a.

At the pre-cracking stage $(M_a \le M_{cr})$, the applied moment M_a is less than the cracking moment M_{cr}. Accordingly, the uncracked section has a moment of inertia equal to the gross moment of inertia, I_g. While at post-cracking stage $(M_a \ge M_{cr})$, the contribution of concrete to the tensile stiffness between the cracks of a reinforced concrete member is influenced by the tension stiffening phenomenon. This phenomenon affects the stiffness and deflection of flexural members. The building code ACI 318-14 and the Canadian concrete design standard CSA A23.3-14 design codes provide an expression introduced by Branson (1965) for establishing the effective moment of inertia used in the deflection analysis of steel-reinforced concrete members as follows:

$$I_e = \left(\frac{M_{cr}}{M_a}\right)^3 I_g + \left[1 - \left(\frac{M_{cr}}{M_a}\right)^3\right] I_{cr} \le I_g \qquad (2.10)$$

In which $M_{cr} = f_r I_g / y_t$, where f_r= the modulus of rupture and can be calculated as $0.62\sqrt{f_c'}$ (Mpa) (ACI 318-14) or $0.6\sqrt{f_c'}$ (Mpa) (CSA A23.3-14); y_t= the distance from the centroidal axis of the cross-section to the extreme fiber in tension; f_c' = unconfined concrete strength, obtained from the cylinder tests.

Several authors have proposed effective moment of inertia expressions for FRP-RC rectangular members. Benmokrane et al. (1996) performed experimental studies on eight beams, four of

them were reinforced with GFRP bars and the others reinforced with steel. One of the major goals of this test program was to investigate the deflection behavior for beams which fail by both compression and tension failures. Both failure modes were observed in the GFRP-reinforced beams. The authors recorded beam deflections which were significantly higher than those predicted by Branson's equation. Based on this study, the authors proposed the following deflection model based on a modified Branson's equation:

$$I_e = \left(\frac{M_{cr}}{M_a}\right)^3 \frac{I_g}{\beta} + \left[1 - \left(\frac{M_{cr}}{M_a}\right)^3\right] \alpha I_{cr} \le I_g \tag{2.11}$$

Where α and β are reduction factors. For their experimental data, α and β are equal to 0.84 and 7, respectively. These factors were attributed to the nature of the FRP reinforcement that exhibited larger deformation than the steel reinforcement, resulting in greater reduction of the compressed concrete section when the applied moment reached the cracking moment.

Thériault and Benmokrane (1998) continued to investigate experimentally the deflection behavior of GFRP-RC beams, and then the authors introduced a new modification to Branson's equation, as follows:

$$I_e = \left(\frac{M_{cr}}{M_a}\right)^3 \beta_d I_g + \left[1 - \left(\frac{M_{cr}}{M_a}\right)^3\right] I_{cr} \le I_g \tag{2.12}$$

where β_d = reduction coefficient equal to 0.6. This factor was later modified by Gao et al. (1998) [Eq. (2.13)] and adopted by ACI 440.1R-03.

$$\beta_d = \alpha_b \left(\frac{E_f}{E_s} + 1\right) \tag{2.13}$$

in which α_b = bond-dependent coefficient, assumed to be 0.5 until more data became available; E_f and E_s = modulus of elasticity of the FRP and steel reinforcements, respectively.

Yost et al. (2003) proposed an equation for α_b to account for the effect of the reinforcement ratio ρ_f with reference to balanced reinforcement ratio ρ_{fb}, as follows:

$$\alpha_b = 0.064\frac{\rho_f}{\rho_{fb}} + 0.13 \tag{2.14}$$

Based on an evaluation of experimental results from several studies, the ACI 440.1R-06 has proposed the following simple relationship for β_d :

$$\beta_d = \frac{1}{5}\left(\frac{\rho_f}{\rho_{fb}}\right) \le 1.0 \tag{2.15}$$

Alsayed et al. (2000) proposed two models to determine I_e for beams reinforced with GFRP bars based on experimental results. In the first model (model A), the equation suggested replacing the power of 3 by 5.5 in the Branson equation, as shown in Eq. (2.16).

$$I_e = \left(\frac{M_{cr}}{M_a}\right)^{5.5} I_g + \left[1 - \left(\frac{M_{cr}}{M_a}\right)^{5.5}\right] I_{cr} \le I_g \tag{2.16}$$

The second model (model B) was suggested by regression analysis of the experimental results for beams reinforced with GFRP bars, as shown in Eq. (2.17):

$$I_e = \left[1.4 - \frac{2}{15}\left(\frac{M_a}{M_{cr}}\right)\right] I_{cr} \text{ for } 1 < \frac{M_a}{M_{cr}} < 3,\ I_e = I_{cr} \text{ for } \frac{M_a}{M_{cr}} > 3 \tag{2.17}$$

Toutanji and saafi (2000) tested six GFRP reinforced concrete beams under flexure; two balanced-condition beams and four over-reinforced beams. The authors investigated load-deflection behavior and compared the experimental results with results from existing models. They concluded that Branson's equation over-estimates flexural stiffness for GFRP reinforced concrete beams and that this effect is more pronounced as longitudinal reinforcement ratio decreases. A model was proposed to modify Branson's equation to account for longitudinal reinforcement ratio and elastic modulus of GFRP [Eq. (2.18)].

$$I_e = \left(\frac{M_{cr}}{M_a}\right)^m I_g + \left[1 - \left(\frac{M_{cr}}{M_a}\right)^m\right] I_{cr} \le I_g \tag{2.18}$$

Where $m = 6 - \frac{E_f}{E_s}\rho_f$ for $\frac{E_f}{E_s}\rho_f < 0.3$, $m = 3$ for $\frac{E_f}{E_s}\rho_f \ge 0.3$

Razaqpur et al. (2000) proposed a deflection model derived independently of Branson's equation. The authors stated that applying empirically derived modification factors to Branson's equation may not be suitable for GFRP-RC members, as these factors depend upon numerous variables, such as loading arrangement, GFRP properties, and support conditions. The model proposed by the authors is based on first principles and is independent of support or loading conditions. In developing this model, the authors make the following assumptions: the depth of the neutral axis after cracking is constant, regardless of the applied load; tension stiffening of concrete is negligible; shear deflections are negligible; and the moment-curvature curve of the beam is trilinear, as shown in Fig. 2.4. The authors applied the direct integration methods of virtual work to common arrangements of load and support conditions for beams and derived Maximum deflection formulas for typical FRP reinforced concrete. For example, deflection of a beam under four-point loading:

$$\delta_{\max} = \frac{PL^3}{48E_cI_{cr}}\left[3\left(\frac{a}{L}\right) - 4\left(\frac{a}{L}\right)^3 - 8\left(1-\frac{I_{cr}}{I_g}\right)\left(\frac{L_g}{L}\right)^3\right] \tag{2.19}$$

Where L_g is distance from support to point where $M_a = M_{cr}$.

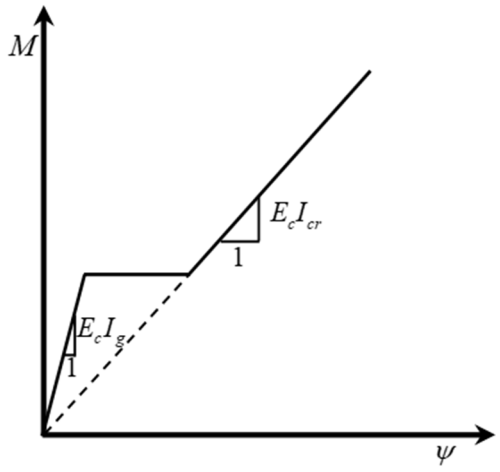

Figure 2.4 Idealized trilinear moment-curvature relation for FRP reinforced section (Razaqpur et al. (2000)).

El-Salakawy et al. (2002) investigated the deflection of concrete beams reinforced with different types and ratios of CFRP bars. They observed that increasing the reinforcement ratio decreases the deflection at service load due to higher stiffness and lower FRP bar stresses. Moreover, at

the service load level, the measured deflection reduced by approximately 31% and 43% due to the increase of reinforcement ratio by 50% and 100%, respectively. In addition, very similar behavior of beams reinforced with both sand-coated and ribbed deformed carbon FRP bars was obtained.

On the basis of a study conducted by Mota et al. (2006), ISIS Canada No.3 (2007) proposed an equation to calculate the effective moment of inertia I_e as follows:

$$I_e = \frac{I_t I_{cr}}{I_{cr} + \left(1 - 0.5\left(\frac{M_{cr}}{M_a}\right)^2\right)\left(I_t - I_{cr}\right)} \tag{2.20}$$

In which I_t and I_{cr} are the moment of inertia of a non-cracked section transformed to concrete and cracked moment of inertia, respectively.

Bischoff (2005, 2007) proposed a new expression for the effective moment of inertia, I_e, based on the fundamental concepts of tension stiffening, as follows:

$$I_e = \frac{I_{cr}}{1 - \left(1 - \frac{I_{cr}}{I_g}\right)\left(\frac{M_{cr}}{M_a}\right)^2} \tag{2.21}$$

Bischoff and Gross (2011a, b) proposed an equation for the calculation of I_e [Eq. (2.22)] which includes an additional factor, γ, to account for the change of stiffness along the length of beams and dependent on the boundary conditions and type of loading.

$$I_e = \frac{I_{cr}}{1 - \gamma\left(1 - \frac{I_{cr}}{I_g}\right)\left(\frac{M_{cr}}{M_a}\right)^2} \tag{2.22}$$

For a four-point bending load, which is the load arrangement used in this testing, Bischoff and Gross (2011a) suggested the following expression based on the integration of curvature along the span for the calculation of the factor γ.

$$\gamma = \frac{3\left(\frac{a}{L}\right) - 4\left[4\left(\frac{M_{cr}}{M_a}\right) - 3\right]\left(\frac{a}{L}\right)^3}{3\left(\frac{a}{L}\right) - 4\left(\frac{a}{L}\right)^3} \quad (2.23)$$

ACI 440.1R-15 recommended the calculation of I_e based on the equation proposed by Bischoff and Gross (2011a) [Eq. (2.22)].

Finally, the deflection was influenced by many factors. **Tension stiffening**, **Bond quality**, **reinforcement type and ratio**, and **concrete strength** are the most considered parameters in investigating the deflection of the FRP- reinforced concrete elements.

2.6. Cracking and Deflection code provisions for FRP-RC members

2.6.1. Canadian Standards Association CAN/CSA S806-12

2.6.1.1. Cracking

CAN/CSA-S806-12 requires that if the maximum strain of FRP bars in the tension zone under full-service loads exceeds 0.0015, cross-sections of maximum positive and negative moment shall directly proportional to the quantity, z , given by

$$z = k_b \frac{E_s}{E_f} f_f \sqrt[3]{d_c A} \quad (2.24)$$

The quantity (z) must not exceed 45,000 N/mm for interior exposure and 38,000 N/mm for exterior exposure. The stresses in the reinforcement at the specified load, f_f , is calculated as the internal moment divided by the product of the reinforcement area and the internal moment arm. CSA S806-12 indicates the value of k_b shall be determined experimentally, but in the absence of data, k_b will be equal to 1.2 for deformed rods. Finally, the CAN/CSA-S806 (2012) recommended that the effective clear cover should not be greater than 50 mm in the calculation of d_c and A .

2.6.1.2. Deflection

CSA-S806 (2012), based on Razaqpur et al. (2000), has recommended the integration of curvature along the span to determine deflections. The CSA S806-12 (2012) approach is based on an assumption that the moment-curvature relationship of a cracked FRP-RC member remains linear under increasing load, which ignores the tension stiffening effect. A simple equation, derived by Razaqpur et al. (2000), for calculating the deflection of simply supported four-point bending FRP-RC members was provided as follows:

$$\delta_{\max} = \frac{PL^3}{48E_cI_{cr}}\left[3\left(\frac{a}{L}\right) - 4\left(\frac{a}{L}\right)^3 - 8\left(1-\frac{I_{cr}}{I_g}\right)\left(\frac{L_g}{L}\right)^3\right] \tag{2.25}$$

Where L_g is distance from support to point where $M_a = M_{cr}$.

2.6.2. Canadian Standards Association CAN/CSA S6-14

2.6.2.1. Cracking

The *Canadian Highway Bridge Design Code* (CAN/CSA-S6-14) states that, if the maximum strain of FRP bars in the tension zone under full-service loads exceeds 0.0015, cross sections of the maximum positive and negative moment regions shall be proportioned in such a way that the crack width does not exceed 0.5 mm for members subjected to aggressive environments and 0.7 mm for other members, with the crack width calculated based on the physical model proposed by Frosch (1999) as follows:

$$w = 2\frac{f_f}{E_f}\frac{h_2}{h_1}k_b\sqrt{{d_c}^2 + \left(\frac{s}{2}\right)^2} \tag{2.26}$$

The value of k_b shall be determined experimentally, but, in the absence of data, values of 0.8 for sand-coated and 1.0 for deformed FRP bars shall be used. In addition, the clear cover shall not be greater than 50 mm in calculating d_c.

2.6.3. American Concrete Institute ACI440.1R-15

2.6.3.1. Cracking

ACI 440.1R-15 recommends an indirect procedure that controls flexural-crack widths with a maximum reinforcing-bar spacing based on the approach proposed by Ospina and Bakis (2007) as follows:

$$s_{\max} = 1.15\frac{E_f w}{f_{fs} k_b} - 2.5c_c \le 0.92\frac{E_f w}{f_{fs} k_b} \tag{2.27}$$

where $s_{\max}$ = maximum permissible center-to-center bar spacing for flexural-crack control (mm); w = maximum allowable crack width (mm); f_{fs} = stress level induced in FRP at service loads (MPa); E_f = design or guaranteed modulus of elasticity of FRP reinforcement defined as the mean modulus of a sample of test specimens (MPa); c_c = clear cover (mm); and k_b is the bond-dependent coefficient. When k_b is not known from experimental data, a conservative value of 1.4 should be assumed (smooth bars and grids are specifically excluded from this recommendation).

A similar equation is currently being considered for ACI 440-H for a future design code by controlling and replacing the crack width w in Equation (2.27) with 0.7 mm as follows:

$$\begin{aligned} s_{\max} &= 1.15\frac{0.7\times E_f}{f_{fs} k_b} - 2.5c_c \le 0.92\frac{0.7\times E_f}{f_{fs} k_b} \\ &= \frac{0.805\times E_f}{f_{fs} k_b} - 2.5c_c \le \frac{0.644\times E_f}{f_{fs} k_b} \end{aligned} \tag{2.28}$$

A lower k_b value of 1.2 is intended to be considered by the ACI 440-H committee for GFRP bars.

2.6.3.2. Deflection

ACI 440.1R-15 (ACI Committee 440 2015), based on Bischoff (2005) and Bischoff and Scanlon (2007), proposed an alternative expression for the effective moment of inertia I_e that works

equally well for both steel and FRP-reinforced concrete members without the need for empirical correction factors. The expression is presented by Eq. (2.29).

$$I_e = \frac{I_{cr}}{1-\gamma\left(1-\frac{I_{cr}}{I_g}\right)\left(\frac{M_{cr}}{M_a}\right)^2} \le I_g \tag{2.29}$$

In which $\gamma = 1.72 - 0.72\left(\frac{M_{cr}}{M_a}\right)$ for a simply-supported beam with a uniformly distributed load.

2.6.4. Japan Society of Civil Engineers JSCE-97

2.6.4.1. Cracking

The maximum crack width can be calculated according to JSCE-97 using the following equation:

$$w_{\max.} = k_b\left(4c_c + 0.7\left(s - d_b\right)\right)\left(\frac{f_{fe}}{E_f} + \varepsilon'_{csd}\right) \tag{2.30}$$

in which c_c is the concrete cover (mm); s and d_b are the center-to-center distance and diameter of the FRP reinforcement (mm), respectively; k_b is a constant expressing the effects of bond characteristics and multiple placement of reinforcing materials (generally between1.0 and 1.3); f_{fe} is the stress increase in reinforcement; and ε'_{csd} is the compressive strain for assessing the increment of crack width due to concrete shrinkage and creep. According to JSCE-97, the allowable crack widths for esthetic considerations may generally be set to not more than 0.5 mm, depending on the ambient environment of the structure.

2.6.5. Italian National Research Council CNR-DT 203/2006

2.6.5.1. Cracking

In CNR-DT 203/2006, the maximum crack-width value for FRPRC members is calculated as follows:

$$w_{\max} = \beta s_{rm} \varepsilon_{fm} \tag{2.31}$$

where β = 1.7 when cracking is caused by load; when cracking is caused by superimposed deformations, β shall be taken as 1.7 for cross sections with a minimum dimension exceeding 800 mm and 1.3 for cross sections with a minimum dimension of 300 mm or less (linear interpolation may be used to calculate β for cross sections with a minimum dimension between these limits); s_{rm} = average crack spacing; and ε_{fm} = average strain in FRP reinforcement.

The average crack spacing, s_{rm}, can be calculated as follows (mm):

$$s_{rm} = 50 + 0.25 k_b k_l \frac{d_b}{\rho_{f,eff}} \tag{2.32}$$

where k_b = 1.6 is a coefficient accounting for the bond properties of the FRP bars; k_l = 0.5 for flexure and 1.0 for pure tension; d_b is the equivalent diameter of the FRP bars in mm; and $\rho_{f,eff}$ is the effective reinforcement ratio, equal to $A_f / A_{c,eff}$, where $A_{c,eff}$ is the effective area in tension defined as the concrete area surrounding the tensile FRP reinforcement, having a depth equal to 2.5 times the distance between tension fiber and bar centroid.

The average strain in the FRP reinforcement ε_{fm} shall be calculated as follows:

$$\varepsilon_{fm} = \frac{f_f}{E_f}\left[1 - \beta_1 \beta_2 \left(\frac{f_{fr}}{f_f}\right)^2\right] \tag{2.33}$$

where f_f is the stress in tension reinforcement at the serviceability limit state and f_{fr} is the stress in FRP reinforcement under conditions causing initial cracking; both are calculated on the basis

of a cracked section; β_1 = 0.5 and is a nondimensional coefficient accounting for the bond properties of FRP bars; and β_2 is a nondimensional coefficient accounting for the duration of loading (1.0 for short loads and 0.5 for long or cyclic loads).

2.6.5.2. Deflection

CNR-DT 203/2006 calculated the deflection, δ_{max}, for FRP concrete members using Eq. (2.34) based on Eurocode (EC2-2004). After cracking occurs, the deflection δ_{max} is obtained by deflection δ_1, considering the inertia of the uncracked section, and deflection δ_2, considering the inertia of the cracked section, by the following expression:

$$\delta_{max} = \beta_1\beta_2\left(\frac{M_{cr}}{M_a}\right)^2\delta_1 + \left[1-\beta_1\beta_2\left(\frac{M_{cr}}{M_a}\right)^2\right]\delta_2 \qquad (2.34)$$

Where β_1 = 0.5 is a non-dimensional coefficient accounting for bond properties of FRP bars; and β_2 = is a non-dimensional coefficient accounting for the duration of loading (1.0 for short time loads, 0.5 for long time or cyclic loads).

CHAPTER 3. FLEXURAL STRENGTH AND DESIGN ANALYSIS OF CIRCULAR RC MEMBERS WITH GFRP BARS AND SPIRALS

Foreword

Authors and Affiliation:

- Salaheldin Mousa: Ph.D. candidate, Department of Civil Engineering, Université de Sherbrooke, Sherbrooke, Quebec, Canada, J1K 2R1.
- Hamdy M. Mohamed: Research Associate/Lecturer, Department of Civil Engineering, Université de Sherbrooke, Sherbrooke, Quebec, Canada, J1K 2R1.
- Brahim Benmokrane: Professor, Department of Civil Engineering, Université de Sherbrooke, Sherbrooke, Quebec, Canada, J1K 2R1.

Journal Title: *ACI Structural Journal*

Paper Status: Accepted on March 07, 2018.

Contribution in thesis:

In this chapter, the flexural strength and behavior of concrete members with circular section and reinforced with GFRP bars and spirals are investigated both experimentally and theoretically. The test parameters included reinforcement flexural stiffness (GFRP versus steel) and GFRP longitudinal-reinforcement ratio. Ductility and deformability of the tested specimens were calculated and evaluated. An analytical strain-compatibility model capable of predicting the flexural strength of circular GFRP-RC members, including the sequential progressive failure, was developed and verified with the experimental results. Moreover, a simplified method, including design equations and design chart, was presented using non-iterative analysis.

Abstract

ACI440.1R design provisions provide conservative estimates for the flexural design strength of glass-fiber-reinforced-polymer (GFRP) reinforced-concrete (RC) members with rectangular sections. That being said, these provisions do not apply equally well to non-rectangular sections, which motivated our study. Our study investigated the flexural strength and behavior of concrete members with circular section and reinforced with GFRP bars and spirals both experimentally and theoretically. Large-scale specimens with a total length of 6,000 mm (236.22 in) and 500 mm (20 in) in diameter were constructed and tested under four-point bending. The test parameters included reinforcement flexural stiffness (GFRP versus steel) and GFRP longitudinal-reinforcement ratio. In this paper, ductility and deformability of the tested specimens were defined, calculated, and evaluated. Test results show that the deformability of the tested GFRP-RC circular members ranged between 19 and 40, which significantly exceeds the requirements of North American codes. Moreover, the nominal flexural strengths of the GFRP-RC specimens were 1.5 and 3.0 times that of the steel counterpart specimen, when considering a similar reinforcement ratio and equivalent longitudinal axial stiffness, respectively. An analytical strain-compatibility model capable of predicting the flexural strength of circular GFRP-RC members, including the sequential progressive failure, was developed and verified with the experimental results. Moreover, a simplified method, including design equations and design chart, is presented using non-iterative analysis. This method accurately and simply predicted the flexural capacity and can be considered a simple and more straightforward method for practicing engineers.

Keywords: concrete; circular members; piles; flexural strength; FRP bars; spirals.

3.1. Introduction

Circular reinforced-concrete (RC) members are widely used in infrastructure systems, such as bridge piers and piles, contiguous pile walls, and fender piles in marine structures. This is due to the simplicity of construction and because their strength characteristics under lateral loads are similar in all directions. Such members are usually exposed to aggressive environments that corrode the steel reinforcement. The result is structure deterioration, leading to costly repairs and rehabilitation. Estimates indicate that the United States spends billions of dollars annually to repair and replace bridge substructures such as pier columns ($2 billion) and marine piling systems ($1 billion) (Mohamed et al. 2014). The use of fiber-reinforced polymer (FRP) as alternative reinforcing bars in RC structures has emerged as an alternative solution to overcoming the corrosion problem. Since they are noncorrosive material, FRP reinforcing bars constitute a better alternative to steel reinforcement. FRP bars have many advantages compared to steel: a density from one-quarter to one-fifth that of steel, neutrality to electrical and magnetic disturbances, and high tensile strength (ACI 440.1R-15; Mohamed and Benmokrane 2014).

Extensive research programs have been carried out over the last two decades to investigate the flexural response of FRP-RC members with rectangular sections (ACI 440.1R-15). These studies are greatly improving our knowledge of how rectangular concrete members reinforced with FRP bars should be analyzed and designed. Based on this knowledge, design provisions, equations, and limitations have been developed and included in design guidelines and codes (ACI 440.1R-15; CSA S806-12; CSA S6-14). The flexural design of concrete members reinforced with FRP bars is based on strain compatibility and depends on whether the failure is governed by rupture of the tensile reinforcement or concrete crushing. Three possible modes of flexural failure can occur in concrete sections reinforced with FRP bars (ACI 440.1R-15; CSA S806-12; CSA S6-14): balanced failure, compression failure, and tension failure. In tension failure, the FRP reaches its ultimate strain level before concrete crushing. The three modes of failure are accepted, although concrete-crushing failure is more desirable, since it is more progressive and has a higher degree of deformability (Nanni 1993).

Steel and FRP codes and standards do not usually propose specific formulations or instructions for flexural design and analysis of circular RC members in contrast to its widespread use. The uniform distribution of longitudinal reinforcing bars, defining the geometry of compression

concrete block, and calculating the effective depth and width of such members make their analysis and design more challenging than in the case of RC members with rectangular sections. Nonetheless, the flexural behavior of circular concrete members reinforced with glass-FRP (GFRP) bars has not yet been investigated. ACI 440.1R-15, however, points out that there is no evidence that the flexural theory—developed for rectangular sections—applies equally well to nonrectangular sections. Accordingly, the behavior of nonrectangular sections has yet to be confirmed by experimental results.

This experimental study is part of an ongoing comprehensive research program carried out under the Tier-1 Canada Research Chair on Advanced Composite Materials for Civil Structures in the Department of Civil Engineering at the University of Sherbrooke, in which full-scale FRP-RC members with circular sections are tested under different loading conditions—concentric (Afifi et al. 2014a, 2015; Mohamed et al. 2014), combined axial and flexural loading (Hadhood et al. 2017 a and b); shear (Ali et al. 2017 a and b); and flexural (current study)—to investigate different variables and design parameters.

3.2. Research Significance

Over the last two decades, substantial number of experimental research studies and discussions have been published related to the flexural behavior of GFRP-RC members with rectangular sections (ACI 440.1R-15). So far, ours is the first testing program aimed at investigating the flexural strength and behavior of full-scale circular concrete members reinforced with GFRP rebars and spirals. The results will contribute to implementing the use of GFRP bars in circular concrete piles, which can be an innovative solution to the corrosion problem in infrastructure applications. This study also provides new insights into the analysis and design of circular concrete members reinforced with GFRP with an extensive theoretical study. The experimental data and design analysis provide the evidence required to include design provisions in the forthcoming ACI 440 code and updated CSA S6 code for the use of GFRP bars and spirals as internal reinforcement in circular members under flexure.

3.3. Experimental Program

3.3.1. Materials

The GFRP reinforcement employed in this study was manufactured from glass fibers impregnated with vinyl-ester resin with the pultrusion process. The longitudinal and transversal reinforcement used was #6 GFRP bars and #4 GFRP spirals, respectively. The GFRP bars and spirals had a sand-coated surface to enhance bond and force transfer between the bars and concrete. The fiber content in percentage by weight was 82% for the GFRP bars. The ultimate tensile strength, f_{fu}, and modulus of elasticity, E_f, of the longitudinal GFRP bars (#6) and the straight portion of the bent GFRP bars (#4) were determined according to ASTM D7205 (ASTM 2011), as reported by the manufacturer (Table 3.1). Two diameters of steel bar were used to reinforce the control specimen. No. 20M deformed steel bars were used as longitudinal reinforcement and No. 10M deformed steel bars were used as spirals. Table 3.1 gives the mechanical proprieties of the steel bars used in this study. All of the circular specimens were cast using normal-weight, ready-mixed concrete with a target compressive strength of 40 MPa (5.8 ksi). The actual compressive strength was 41.43 MPa (6.0 ksi), as determined based on the average test results of 10 concrete cylinders measuring 100 x 200 mm (4 x 8 in), tested on the same day as the start of testing of the specimens.

Table 3.1 Mechanical properties of the GFRP and steel reinforcement

RFT Type	d_b (mm)	A_f [a] (mm²)	A_{im} [d] (mm²)	E_f (GPa)	f_{fu} (MPa)	ε_{fu} (%)
GFRP bars & spirals	13	129	148.3±1.1	52.1±1.19	1126 [b] ±20	2.20±0.0
	20	285	339±0.5	63.9±0.39	1591±13	2.50±0.2
Steel	10M	100	---	200.0	f_y [c] = 480±10	ε_y [c] = 0.24
	20M	300	---	200.0	f_y = 460±15	ε_y = 0.23

[a] Nominal cross-sectional area.
[b] Tensile strength of straight bars.
[c] f_y and ε_y are the yield strength and strain of the steel bars, respectively.
[d] Immersed cross-sectional area (measured).
Note: Properties calculated based on the nominal cross-sectional area, (1 mm = 0.0394 in; 1 mm² = 0.00155 inch²; 1 MPa = 0.145 ksi).

3.3.2. Test Specimens

A total of four large-scale circular RC specimens, including three reinforced totally with GFRP bars and spirals, and one with steel reinforcement, were prepared and tested. The specimens were 500 mm (20 in) in diameter and 6000 mm (236.22 in) in length. The clear concrete cover was kept constant at 38 mm (1.5 in). The specimens were tested under four-point bending. The

shear-span-to-depth ratio was chosen to be greater than five to achieve the full flexural capacity of the specimens (Kani 1964) and avoid shear failure. Figure 3.1 shows the dimensions and reinforcement details of the test specimens. The test parameters were flexural stiffness of the longitudinal reinforcement (GFRP versus steel reinforcement) and the longitudinal-reinforcement ratio.

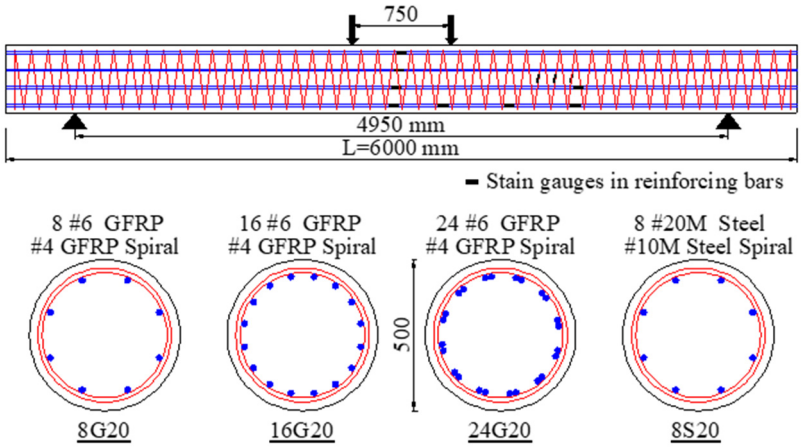

Figure 3.1 Dimensions and reinforcement details of the test specimens. (Note: all dimensions in mm; 1 mm = 0.0394 in)

Table 3.2 provides the test matrix and reinforcement details of the test specimens. Each specimen code consists of a letter and numbers. The first number indicates the number of longitudinal bars. The letters G and S identify specimens as being reinforced totally with GFRP or steel reinforcement, respectively. The second number indicates the nominal diameter of the longitudinal bars. The GFRP-RC specimens were reinforced longitudinally with 8, 16, or 24 No. 20 mm (#6) bars. The specimen reinforced with 24 bars was arranged as 12-by-2 bundled bars to ensure easy placement of the fresh concrete between and around the bars during casting. The longitudinal-reinforcement ratios of 1.2%, 2.3%, and 3.5% were chosen to represent the minimum ratio and the practical reinforcement ratios in pile applications. The reinforcement ratio (ρ) was estimated considering the total nominal area of longitudinal bars divided by the total cross-sectional area of the member (A_g). The steel-reinforced control specimen (8S20) had almost the same reinforcement ratio (1.22%) as the GFRP-RC specimen (8G20) but with 8 M20 deformed steel bars. The axial stiffness of the steel reinforcing bars in this specimen was similar to that of the GFRP bars in the GFRP-RC specimen (24G20). Figure 3.2 shows an overview of

GFRP and steel cages, and the circular specimens. The circular specimens were prepared for casting in very stiff Sonotubes. The Sonotubes were placed in an inclined position at 25°. A concrete pump was used to cast the specimens using a rubber concrete pumping hose that was inserted into the Sonotubes (at least 5000 mm (196.8 in)) to discharge the concrete and prevent segregation.

Table 3.2 Test matrix, test results, curvature, ductility, and deformability of the test specimens

Specimen ID	Long. Reinf. (ρ_{ft} %)	Spiral Reinf.	M_{peak1} † (kN.m)	M_{peak2} † (kN.m)	Curvature ψ, $1/d$ § at M_{peak1}	Ductility and deformability‡			$M_{exp.}/M_{pred.}$			
									M_{peak1}			M_{peak2}
						μ_e	J	J_{VG}	Ignore comp. bars	Consider comp. bars	Proposed method	
8G20	8 GFRP #6 (1.2)	# 4 @125	264	359	0.0156	1.5	19	21	1.16	1.10	1.15	1.09
16G20	16 GFRP #6 (2.3)	# 4 @125	441	584	0.0152	1.5	40	18	1.34	1.26	1.41	1.06
24G20	24 GFRP #6 (3.5)	# 4 @125	444	704	0.0113	1.4	24	15	1.19	1.05	1.20	1.09
8S20*	8 Steel #20 M (1.22)	10 M @125	134	237	0.0022	1.9	-	-	1.03	1.01	-	-
Average‡									**1.23**	**1.14**	**1.26**	**1.08**
C.O.V. (%)‡									**7.7**	**9.5**	**10.9**	**1.9**

* Values calculated at $M_{peak1} = M_y$, and M_{peak2} = maximum moment at concrete crushing.

§ The effective depth, d, calculated using Eq. 20.

‡ The ductility and deformability values were calculated based on the experimental results.

† The moment values of M_{peak1} and M_{peak2} were calculated at mid-span ((the measured actuator load/2) $\times$ shear span).

‡ Specimen 8S20 was excluded from the calculation of the average and COV.

Note: 1 kN.m = 0.7376 kip.ft, 1 mm = 0.0394 in.

Figure 3.2 Fabrication of test specimens (Overview of cages and circular specimens).

3.3.3. Instrumentation and Test Setup

Strains in the longitudinal reinforcing bars and spirals were measured using electrical resistance strain gauges with a gauge length of 10 mm. In addition, nine strain gauges with a gauge length of 60 mm were mounted on the concrete surface at three different levels (0D, D/8, and D/4) at mid-span and at quarter-span to measure compressive strains. Specimen deflection was measured with three linear potentiometers (LPOTs) placed at the mid-span and at the quarter-span. The test setup was designed and fabricated at the University of Sherbrooke's CFI structural laboratory. Steel saddles were designed to accommodate the circular geometry at loading and support points. The specimens were loaded with four-point bending, as shown in Figure 3.3, using a servo-controlled, 1000 kN MTS hydraulic actuator attached to a spreader beam. The load was applied at a displacement-controlled rate of 0.5 mm/min. An automatic data-

acquisition system monitored by a computer was used to record the readings of the LPOTs, load cells, and strain gauges.

Figure 3.3 Test setup.

3.4. Test Results and Discussion

This section summarizes the experimental results, including the moment–deflection behavior, flexural capacity, crack pattern and mode of failure, strains in reinforcement and concrete, neutral-axis depth, ductility, and deformability.

3.4.1. Moment–Deflection Behavior

This section presents the moment–deflection curves of the test specimens in two groups to show the effect of test parameters on flexural behavior, as shown in Figure 3.4. All the specimens exhibited similar linear moment–deflection behavior from initial loading up to the occurrence of the first flexural crack. The uncracked response for all the specimens showed insignificant deflection, reflecting gross section stiffness and the fact that flexural stresses were mainly resisted by the concrete. As the load increased, flexural cracking eventually occurred within the test region, and the post-cracking flexural stiffness was considerably reduced. This change in

stiffness represents the transition from gross- to effective-section properties. After cracking, the specimens reinforced with GFRP bars and spirals behaved nearly linearly with reduced stiffness up to failure. This is attributed to the linear–elastic characteristics of the GFRP reinforcement. After cracking occurred, however, the moment–deflection curve of the steel-RC specimen was initially linear and then became nonlinear, showing a typical yielding plateau after yielding.

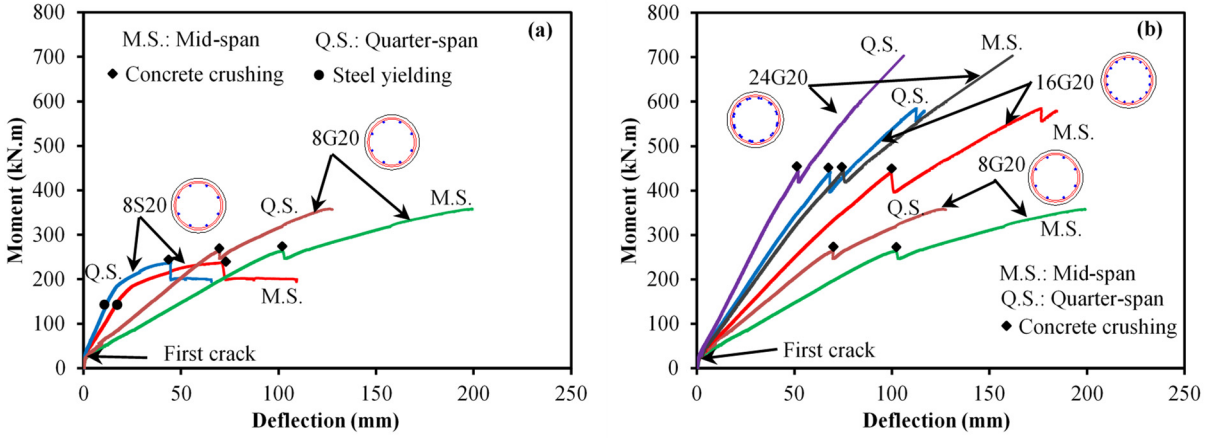

Figure 3.4 Moment–deflection relationship: (a) effect of reinforcement type; (b) effect of GFRP reinforcement ratio. (Note: 1 mm = 0.0394 in; 1 kN.m = 0.7376 kip.ft)

3.4.2. Effect of Modulus of Elasticity and Axial Stiffness of Flexural Reinforcement

The GFRP- and steel-RC specimens (8G20 and 8S20) were designed to have the same flexural-reinforcement ratio, (1.2%). In contrast, 24G20 was designed with longitudinal GFRP reinforcing bars equivalent to the axial stiffness of the flexural steel reinforcing bars in the counterpart steel-RC specimen (8S20). Figure 3.4(a) presents the moment–deflection curves for 8G20 and its counterpart reinforced with steel (8S20). The post-cracking flexural stiffness was calculated as the average slope of the curve. Specimen stiffness at this stage was highly dependent on the axial stiffness of the reinforcing bars, which is a function of the area A and modulus of elasticity E of the tensile reinforcement. Figure 3.4(a) indicates that the post-cracking flexural stiffness of the steel-RC specimen (8S20) was almost 3.22 times of that of its GFRP counterpart (8G20). This value is approximately similar to the ratio of the modulus of elasticity of the steel (200 GPa (29,000 ksi)) to that of the GFRP bars (63.9 GPa (6,498 ksi)). Figure 3.4(b) shows that 24G20, with equivalent axial stiffness, had similar post-cracking

flexural stiffness to that of the steel-RC specimen. The GFRP-RC specimens, however, evidenced longer post-peak ascending branches than the steel-RC specimen. This is mainly due to the fact that, after yielding, the steel bars had a very low tangent modulus and did not contribute to the flexural strength, compared to the GFRP bars, which maintained their modulus of elasticity throughout the entire duration of loading. It should be noted that the linear-elastic behavior of the GFRP bars resulted in insignificant residual deflection of the GFRP-RC specimens when the load was removed in comparison to the specimen reinforced with steel. Basically, Table 3.2 indicates that the nominal flexural strength of 8G20, at the first and second peak points, respectively, was almost 2.0 and 2.6 times greater than that of the yield-moment strength of 8S20. The corresponding values were 3.25 and 5.15, when considering 24G20, which had axial stiffness similar to 8S20.

3.4.3. Effect of GFRP Reinforcement Ratio

The influence of the amount of longitudinal reinforcement on flexural strength of the specimens reinforced with GFRP was assessed. The minimum reinforcement ratio of 1% was considered, as recommended in most codes and standards, to avoid brittle tension failure by GFRP-bar rupture (CSA S806-12, CSA S6-14, ACI 440.1R-15). Eight No. 6 GFRP bars were used to reinforce 8G20 at a reinforcement ratio 1.2%. The reinforcement ratio was increased to 2.3% in 16G20 with 16 GFRP No. 6 bars. The maximum reinforcement ratio was limited to 3.5% to avoid reinforcement congestion by using 2 x 12 bundles of No. 6 bars. Figure 3.4(b) provides a comparison of the moment–deflection curves of the three GFRP-reinforced specimens. The figure indicates that increasing the reinforcement ratio enhanced the flexural strength and stiffness of the test specimens. Specimens 16G20 and 24G20 experienced lower deflection and higher flexural strength than 8G20. The flexural strength of specimens 16G20 and 24G20 increased by 63% and 96%, respectively, when the reinforcement ratio was increased by 100% and 200%. In addition, the post-cracking flexural stiffness of 16G20 and 24G20 increased by 100% and 168%, respectively, when the reinforcement ratio was increased by 100% and 200%. Indeed, the flexural strength and behavior of the test specimens depended significantly on the GFRP reinforcement ratio.

3.4.4. Flexural Capacity, Crack Pattern, and Mode of Failure

Table 3.2 provides the flexural capacity of the test steel and GFRP-RC specimens. In all of the specimens, two or three flexural cracks first appeared between the two concentrated loads, where the flexural stress was highest and shear stress zero. The specimens developed these cracks when the maximum applied tensile stress reached the concrete's tensile strength. The cracking moment, M_{cr}, ranged between 24 kN.m (17.8 kip.ft) and 27 kN.m (19.85 kip.ft). As the applied load increased, the initial cracks widened; additional parallel cracks propagated along the specimen shear span, opening towards the neutral axis. With further loading, the cracks formed along the shear span curving towards the loading points. The main difference in the final crack patterns was the number and spacing of the flexural and diagonal cracks that developed along the span. Generally, it was observed that the specimens with lower reinforcement ratios (8G20 and 8S20)—regardless of the type of reinforcement—experienced fewer flexural cracks. Specimen 8G20, however, experienced wider crack widths at service load than the counterpart steel specimen 8S20 with the same reinforcement ratio. Increasing the reinforcement ratio in the GFRP-RC specimens, however, increased the total number of cracks and reduced the average crack width at the same load level. The GFRP-RC specimens continued to sustain more load until reaching the first peak moment due to the gradual spalling of the concrete cover. The cover spalling was marked by the separation of small pieces of concrete on the compression side between the loading points. The first peak moment, M_{peak1}, was 264 kN.m (195 kip.ft), 441 kN.m (325 kip.ft), and 444 kN.m (327 kip.ft) for 8G20, 16G20, and 24G20, respectively. After full cover spalling, the confining restraint provided by the spirals was activated, and the specimens were again able to sustain load. Then, loading continued and post-compressive and tensile strains in the GFRP bars in the compression and tension sides, respectively, maintained strain compatibility and internal-force equilibrium, leaving the section strength intact. The post-spalling behavior provided a pseudo-ductile failure and warning with the soft and gradual crushing of the compression block, formation of visible wide cracks, and excessive deformation, which led to the test being stopped at the second peak moment (M_{peak2}). The second peak moment, M_{peak2}, was 359 kN.m (265 kip.ft), 584 kN.m (431 kip.ft), and 704 kN.m (519 kip.ft) for 8G20, 16G20, and 24G20, respectively. The corresponding ratio between M_{peak2} and M_{peak1} for these specimens was 136%, 133%, and 159%. Specimen 8S20, however, failed after flexural yielding occurred first, followed by concrete crushing at mid-span. Two

significant flexural cracks formed and widened in this specimen. The test was then terminated as the specimen experienced excessive concrete crushing and severe deformation at mid-span. The first (yielding of the extreme tension bars) and second peak (concrete crushing) moments for 8S20 were 134 kN.m (98 kip.ft), and 237 kN.m (175 kip.ft), respectively. When the applied load was released, all the GFRP-RC specimens recovered most of their deflection during the unloading process, because the GFRP bars on the tension and compression sides did not reach rupture strain. In contrast, 8S20 retained deflection after unloading. Figure 3.5 provides the crack patterns at failure of all the test specimens.

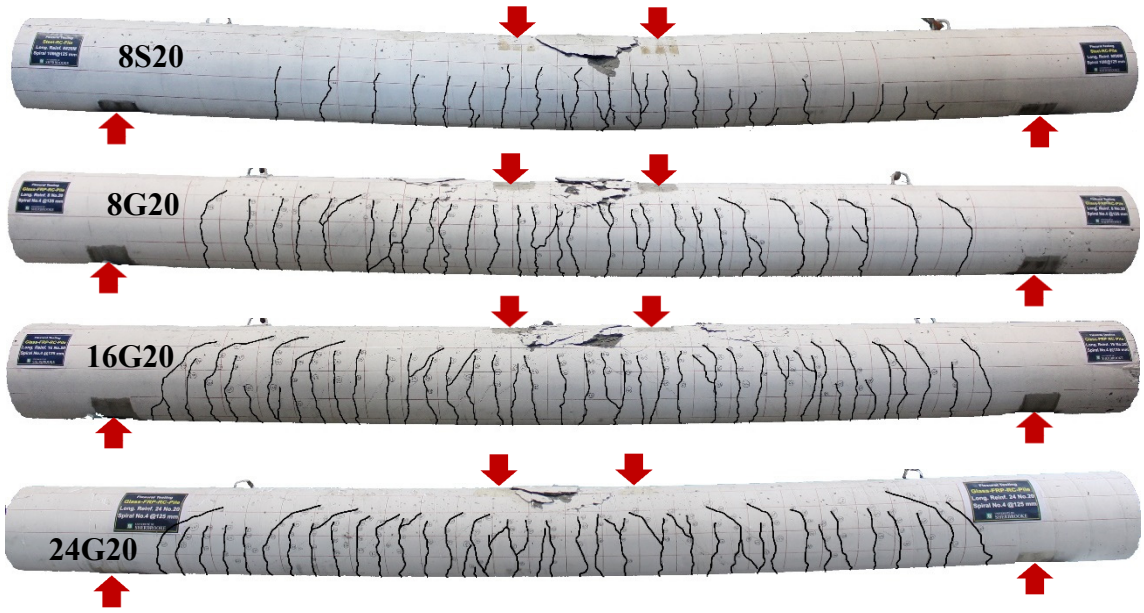

Figure 3.5 Cracking pattern of test specimens at failure.

3.4.5. GFRP Flexural-Strain Behavior

Figures 3.6(a) and (b) plot the moment versus flexural-tension strain relationships at two locations in the specimens. The figure shows that the bars were stressed only after initial cracking. After cracking occurred, a significant jump in the strain values took place, with no increase in the corresponding moment. This indicates the transfer of major internal forces from the concrete to the bars. Then, loading continued and the bar strain began to gradually increase. Test results indicate that the 8S20 exhibited less bar strain than its GFRP counterpart (8G20) at the same load level. This is due to the low modulus of elasticity of the GFRP bars compared to that of the steel bars. Furthermore, increasing the reinforcement ratio from 1.2% to 2.3% and

3.5% reduced the measured strain at all load levels. Prior to yielding, the steel-RC specimen (8S20) had strain behavior similar to that of its GFRP counterpart (24G20). This can be attributed to the fact that the axial stiffness of the GFRP reinforcing bars (24 No. 20) was comparable to the axial stiffness of the steel bars (8 No. 20M).

The steel-RC specimen yielded at an applied moment of 134 kN.m (98 kip.ft) (approximately 56% of the specimen's maximum moment capacity). Then, the steel reinforcement exhibited a yielding plateau, followed by a rapid increase in strain up to failure. In contrast, the GFRP-RC specimens showed a gradual strain increasing up to cover spalling (first peak moment) reaching 12,800, 11,900, and 8,400 με (50%, 46%, and 33% of the ultimate tensile GFRP bar strain) in 8G20, 16G20, and 24G20, respectively. The maximum recorded strains in the GFRP bars before terminating the test were 15,300, 16,000, and 13,300 με representing 57%, 64%, and 52% of the ultimate tensile GFRP bar strain, for 8G20, 16G20, and 24G20, respectively. In general, these strain levels show that flexural failure was not triggered by the GFRP bars rupturing. In addition, the test results show that the strain values measured by the two strain gauges attached to the two bundled bars were almost identical, indicating that no slippage occurred during the whole test. Moreover, no signs of anchorage problems were observed in any of the specimens.

Figure 3.6(c) plots the moment versus flexural-compression strain relationships at mid-span in the specimens. The recorded compressive strains at first peak were 2,350, 3,400, 2,850, and 500 με for 8G20, 16G20, 24G20, and 8S20, respectively. After the first peak load, the specimens experienced slight strength decays due to cover spalling or steel yielding. In this context, cover spalling or steel yielding does not represent the termination of flexural capacity. Rather, compressive strain in the GFRP bars at the post-peak stage and the post-yield strain compatibility and internal-force equilibrium were maintained in the GFRP-RC and steel-RC specimens, leaving the section strength intact. The maximum recorded compressive strains in the bars were 11,200 and 9,100 for 8G20 and 24G20, respectively, representing a percentage of 44% and 35% of the maximum tensile strain of the GFRP bar.

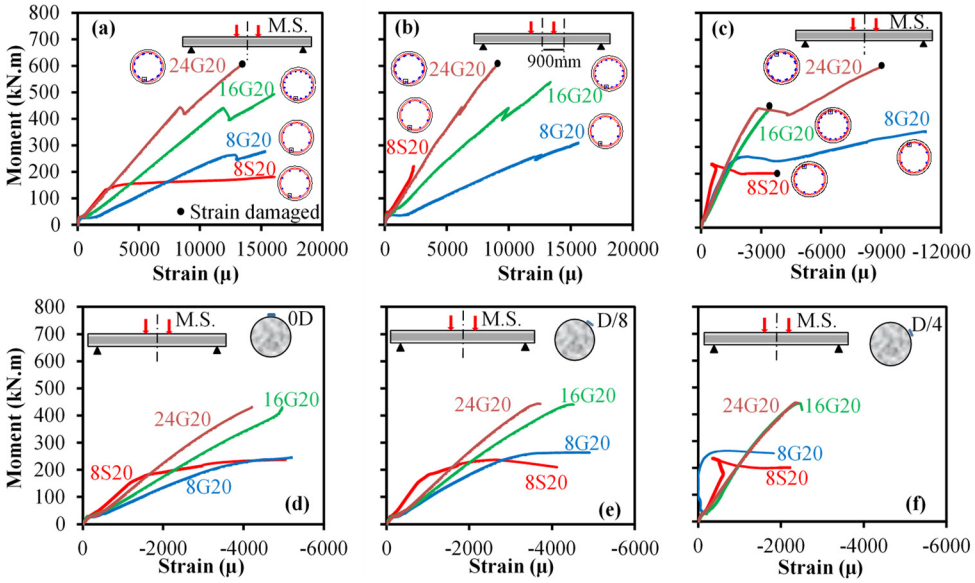

Figure 3.6 Moment–flexural-strain relationship at mid-span: (a and b) tension bar strain; (c) compression bar strain; (d, e, and f) concrete-strain. (Note: 1 kN.m = 0.7376 kip.ft).

3.4.6. Concrete Strain

Figures 3.6 (d), (e), and (f) provide the measured compressive concrete strains at the mid-span at three different levels from the top (D, D/8, and D/4). Figure 3.6(d) indicates that, before cracking, the concrete strains were insignificant in all of the specimens and ranged from 100 to 160 με. After cracking, the strains in the GFRP-RC specimens increased almost linearly up to initiation of concrete crushing and gradual cover spalling (first peak moment). The steel-RC specimen showed a yielding plateau after the steel reinforcing bars had yielded. The maximum recorded compressive strains were 5,100, 4,900, 4,200, and 5,000 με for 8G20, 16G20, 24G20, and 8S20, respectively. The recorded compressive concrete strains were higher than the specified design limit in ACI440.1R-15 (3000 με) and CSA S806-12 (3500 με). Figures 3.6(e) and (f) show the recorded concrete strains at D/8 and D/4 for the GFRP- and steel-RC specimens. Figure 3.6(e) demonstrates that, at all moment levels, the strain at D/8 was less than that at D, reaching 4,900, 4,500, 3,700, and 4,100 με for 8G20, 16G20, 24G20, and 8S20, respectively.

3.4.7. Neutral-Axis Depth

The experimental position of the neutral axis was estimated considering the recorded strain test results of the GFRP and steel bars and concrete strains. Figure 3.7 indicates that the neutral-axis depth before cracking was located at approximately the geometrical centroid of the circular cross section and shifted towards the compression side just after cracking. Subsequently, its value remained constant and increased slightly at high load level just before concrete crushing occurred. Furthermore, Fig. 3.7 shows that the neutral-axis depth of 8G20 is less than that of 8S20 with a similar reinforcement ratio. This could be attributed to the fact that the steel bars had a higher modulus of elasticity than that of the GFRP bars. Moreover, the neutral-axis depth of the GFRP specimens increased as did the reinforcement ratio. The equilibrium of forces requires a larger circular concrete compression segment for the greater forces arising from larger areas of tensile reinforcement. Figure 3.7 reveals that the position of the neutral axis in 16G20 and 24G20 is almost the same after approximately 50% of M_{peak1} was reached. A possible explanation for this might be that 24G20 achieved the full flexural capacity of the circular cross section. Failure and the neutral-axis depth were governed by the concrete contribution and strength in all GFRP cases.

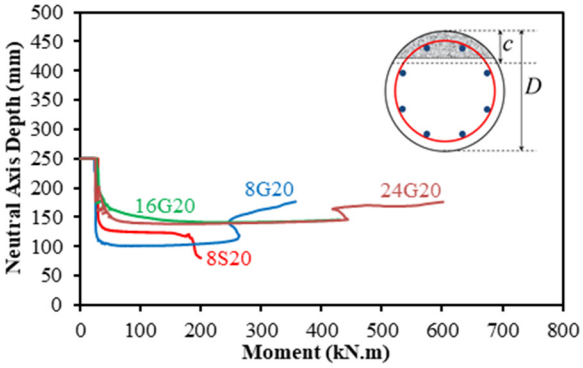

Figure 3.7 Neutral-axis depth. (Note: 1 kN.m = 0.7376 kip.ft).

3.5. Ductility and Deformability

Since GFRP reinforcement responds linearly up to failure, the traditional definition of ductility for steel-RC members, which considers the yielding of steel bars as a reference point, cannot be directly applied. Two approaches have been introduced in the literature to define the ductility of FRP-RC members. The first approach is based on the absorbed energy (Naaman and Jeong

1995), and the second on the deformation concept (CSA S6-14; Jaeger et al. 1997; Vijay and GangaRao 2001).

3.5.1. Absorbed-Energy Approach

Naaman and Jeong (1995) defined ductility as the ratio of the total energy to the elastic energy and proposed the following equation to compute the ductility index, μ_e, which can be applied to steel- and FRP-RC members:

$$\mu_e = \frac{1}{2}\left(\frac{E_{tot}}{E_{el}} + 1\right) \tag{3.1}$$

where E_{tot} = the total energy computed as the area under the load-deflection curve, and E_{el} = the elastic energy released upon failure, computed as the area of the triangle formed at the failure load by the line having the weighted average slope of the two initial straight lines of the load-deflection curve. Table 3.2 provides the computed ductility indices for the GFRP- and steel-RC specimens. Increasing the reinforcement ratio from 1.2% to 2.3% did not affect ductility, while increasing the reinforcement ratio to 3.5% slightly reduced the ductility (6.6%). The ductility index of 8G20 was slightly less (21%) than that of its steel counterpart (8S20).

3.5.2. Deformability Approach

The Canadian Highway Bridge Design Code (CAN/CSA S6-14) adopted Jaeger et al. 1997 (J-factor) approach to evaluate the deformability index of FRP-RC members. In this approach, the absorbed energy is measured based on deformability rather than ductility to ensure adequate deformation of FRP-reinforced structures before failure. The deformability J-factor takes into account the strength effect as well as the curvature effect at service and ultimate conditions. The deformability J-factor can be calculated as follows:

$$J = \frac{M_{ultimate}}{M_c} \times \frac{\psi_{ultimate}}{\psi_c} \tag{3.2}$$

where ψ_c = curvature at a concrete strain equal to 0.001 (service condition); $\psi_{ultimate}$ = curvature at ultimate (M_{peak1} was considered in the calculation); M_c = moment at concrete strain equal to 0.001; $M_{ultimate}$ = ultimate moment (M_{peak1} was considered in the calculation). For this study, the curvature at ultimate limit states was calculated using the maximum actual experimental concrete strain, rather than a theoretical value. In the same way, ultimate moment is given as the first peak moment recorded during the test. CSA S6-14 requires a J-factor exceeding 4 and 6 for rectangular sections and T-sections, respectively, with no recommendation for circular sections. A J-factor exceeding 6 might be recommended and used for the circular sections similar to that for T-sections, considering both as irregular non-rectangular sections. Table 3.2 reveals that all the test specimens demonstrated adequate deformability when compared with the CSA-S6-14 (2014) Code limit of 6 (for non-rectangular sections). The higher the J-factor values the more ample warning the FRP-RC specimen gives before failure. In other words, the J-factor indicates the amount of cracks and deflections of the FRP-reinforced concrete member will exhibit through load history from service to ultimate conditions. Table 3.2 indicated that increasing the reinforcement ratio in specimens 8G20 and 16G20 from 1.2% to 2.3% increased the J-factor from 19 to 40, respectively. Specimen 16G20 had the highest deformability J-factor (40) of all the GFRP specimens. This result might be explained by the fact that 16G20 reached a higher level of compressive concrete strain, resulting in a higher flexural strength factor in comparison to the other GFRP-RC specimens.

Vijay and GangaRao (2001) defined the deformability factor as the ratio of energy absorption (area under moment–curvature curve or area under the load-deflection curve) at ultimate to energy absorption at a limiting curvature value of 0.005/d, which satisfies the serviceability criteria of both deflection and crack width. Table 3.2 provides the calculated values based on the deformability factor proposed by Vijay and GangaRao (2001), J_{VG}. The estimated values indicate that increasing the GFRP reinforcement ratio tended to decrease this factor.

3.6. Theoretical Study

This section presents a theoretical study to calculate the flexural capacity of circular concrete members reinforced with GFRP bars. In fact, circular member need more design procedures to analyze than rectangular ones. The bars are usually disturbed in a circle at discrete points. In

addition, the stresses, which are variable over the section depth, are also distributed over an area of variable width. Based on the observations from moment–deflection and moment–strain curves for circular GFRP-RC specimens, two peak moments appeared (M_{peak1} and M_{peak2}). The following sections present two stages of analysis based on first and second peak moments.

3.6.1. Stage 1: Analysis of the First Peak Moment

The theoretical flexural capacity of the circular GFRP-RC specimens was calculated based on the principles of force equilibrium and strain compatibility in the concrete cross sections between the GFRP bars and concrete. The theoretical first peak moment, M_{peak1}, was drawn based on the assumptions applicable to rectangular GFRP-RC members. The assumptions are:

1. Strain in the concrete and the GFRP reinforcement is proportional to the distance from the neutral axis (a plane section remains plane after deformation up to failure).
2. The maximum usable compressive strain in the concrete is assumed to be 0.003.
3. The tensile strength of concrete is ignored.
4. The tensile behavior of the GFRP reinforcement is linearly elastic until failure.
5. The strain in the GFRP reinforcement, whether in tension or compression, is the same as that in the surrounding concrete (i.e. perfect bond exists between the GFRP reinforcement and concrete).
6. The distribution of concrete compressive stress can be described by the equivalent rectangular stress block shown in Fig. 3.8(a) with parameters α_1 and β_1 as presented in the following equations satisfying the requirements of ACI440.1R-15.

$$\alpha_1 = 0.85 \tag{3.3}$$

$$\beta_1 = 0.85 - \frac{0.05(f_c' - 28)}{7} \geq 0.65 \tag{3.4}$$

To obtain the theoretical first peak moment of the GFRP-RC test specimens, the procedure can be summarized in the following steps, in relation to Fig. 3.8(a):

1. Specify the circular section diameter, materials properties, locations and areas of GFRP bars.

2. Assume a value for neutral-axis depth, c.
3. Calculate the compression force in concrete, F_c, using Eq. 3.5.

$$F_c = \alpha_1 f_c' A_c \tag{3.5}$$

$$A_c = r^2 \left(\theta - \sin\theta \cos\theta\right) \tag{3.6}$$

$$\bar{y} = \frac{2r}{3}\left(\frac{\sin^3\theta}{\theta - \sin\theta\cos\theta}\right) \tag{3.7}$$

$$\cos\theta = 1 - \frac{\beta_1 c}{r} \tag{3.8}$$

where f_c'=concrete cylinder strength; A_c= the area of the circular concrete segment; and r= the radius of the circular cross section.

4. For each layer of reinforcement, compute the strain in the tension and compression reinforcement, ε_{fi}, according to the meaning of strain compatibility with reference to ultimate concrete strain in the case of compression failure, and with reference of ultimate GFRP strain in the case of tension failure.
5. Calculate the tensile and compressive forces in GFRP bars using Eqns. 3.9 and 3.10.

$$F_{tb} = \sum_{i=1}^{n_t} \varepsilon_{fi} E_f A_{fi} \tag{3.9}$$

$$F_{cb} = \sum_{i=1}^{n_c} \varepsilon_{fi} E_f A_{fi} \tag{3.10}$$

where F_{tb} = the tensile force in GFRP bars; F_{cb} = the compressive force in GFRP bars; E_f and A_{fi} = modulus of elasticity and area for the row of the FRP bars at level i, respectively.

6. Check for equilibrium considering or ignoring the contribution of GFRP bars in compression by satisfying the condition that the absolute value of the sum of the total tensile and compressive forces is less than a certain allowable tolerance.

7. If equilibrium is not satisfied, revise estimate of c and repeat from step 2 until equilibrium is achieved.
8. Once equilibrium is satisfied, the first peak moment, M_{peak1}, can be calculated with Eq. 3.11 or Eq. 3.12 by taking the moment of the forces around the centroid of the circular cross section.

Case 1: Ignoring the contribution of FRP bars in compression

$$M_{peak\,1} = F_c \bar{y} + \sum_{i=1}^{n_t} \varepsilon_{fi} E_f A_{fi} y_{ti} \tag{3.11}$$

Case 2: Considering the contribution of FRP bars in compression

$$M_{peak\,1} = F_c \bar{y} + \sum_{i=1}^{n_c} \varepsilon_{fi} E_f A_{fi} y_{ci} + \sum_{i=1}^{n_t} \varepsilon_{fi} E_f A_{fi} y_{ti} \tag{3.12}$$

where y_{ti} = the distance between the center of i^{th} GFRP bars on the tension side of the centroid of the concrete cross section; and y_{ci} = the distance between the center of i^{th} GFRP bars on the compression side and the centroid of the concrete cross section.

3.6.2. Stage 2: Analysis of the Second Peak Moment

After the GFRP-RC specimens failed in compression by cover spalling on the compression side of the circular cross section, the section started to sustain more stresses and forces due to the confinement of the concrete core produced by the GFRP spirals and longitudinal bars. Consequently, the confined stress-strain model proposed by Afifi et al. (2015) was adopted to define the confining stress and strain for the confined concrete core. The concrete confined stress, f'_{cc}, and the confined concrete strain, ε_{cc}, can be calculated from Eq. 3.13 and Eq. 3.14, respectively.

$$f'_{cc} = f'_{co}\left(0.85 + \sqrt{0.17 + 6.43\frac{f'_l}{f'_{co}}} - 2\frac{f'_l}{f'_{co}}\right) \tag{3.13}$$

$$\varepsilon_{cc} = \varepsilon_{co}\left(0.97 + 18.08\frac{f_l'}{f_{co}'}\right) \tag{3.14}$$

$$f_l' = k_e \frac{2f_{fb}A_{tf}}{Sd_s} \tag{3.15}$$

$$k_e = \frac{1-(S'/2d_s)}{1-\rho_{cc}} \tag{3.16}$$

where f_{co}' = the strength of the unconfined concrete calculated as 0.85 of the concrete cylinder strength (f_c') in MPa; ε_{co} = unconfined concrete strain corresponding to f_{co}' (0.003 mm/mm for the current study); A_{tf} = the cross-sectional area of FRP spirals (mm^2); S = the spacing between spirals (mm); S' = the clear spacing between spirals (mm); d_s = the concrete core diameter until the spiral centerline (mm); ρ_{cc} = the ratio of area of longitudinal reinforcement to area of core of section; and f_{fb} = the bend strength of spirals in MPa and can be calculated using Eq. (3.17), as recommended in ACI 440.1R-15.

$$f_{fb} = \left(0.05\frac{r_b}{d_b} + 0.3\right) f_{fu} \le f_{fu} \tag{3.17}$$

where r_b = inner radius of the spirals; d_b = diameter of the spiral bars; and f_{fu} = ultimate tensile strength of the straight FRP bars.

The theoretical second peak moment, M_{peak2}, for the GFRP-RC specimens was drawn based on the assumptions used in Stage 1, excluding assumption no. 2 for the maximum usable compressive strain in the concrete, which was replaced by ultimate confined strain in concrete, ε_{cc}. In relation to Fig. 3.8(b) and by following the same iterative procedure used in stage 1, the second peak moment, M_{peak2}, can be calculated with Eq. 3.18 by taking the moment of the forces around the centroid of the circular cross section.

$$M_{peak\,2} = F_c\bar{y} + \sum_{i=1}^{n_c}\varepsilon_{fi}E_f A_{fi}y_{ci} + \sum_{i=1}^{n_t}\varepsilon_{fi}E_f A_{fi}y_{ti} \tag{3.18}$$

where the compression force in concrete, F_c, can be calculated with Eq. 3.19.

$$F_c = \alpha_1 f'_{cc} A_c \tag{3.19}$$

3.6.3. Comparison between the Theoretical and Experimental Results

The nominal flexural-moment capacity of the GFRP-RC circular specimens was compared to the predictions using the aforementioned flexural-design equations and considering ACI 440.1R-15 requirements, when available. Moreover, the experimental values were compared to the predicted values at first and second peak moments. In one scenario, neglecting the contribution of the GFRP longitudinal bars in the compressive block to the moment-carrying capacity at the first peak was assumed to be equivalent to the concrete and, in the second, the GFRP longitudinal bars in the compressive block was considered assuming that the GFRP tensile and the compressive Young's modulus were equal. In all the analyses, the concrete density factor, material resistance factor, and member safety factor were taken as equal to unity. Table 3.2 presents the experimental-to-predicted ratios for the flexural capacities of the test specimens. The table indicates accurate predictions since any combination of the experimental over the theoretical predictions is greater than 1.0. The level of conservatism and degree of accuracy depend on the assumptions of considering and ignoring the contribution of the GFRP bars in the compressive block. The table reveals that with the ACI 440.1R design considerations provided accurate predictions when considering the bar contribution in compression. The average $M_{exp.}/M_{pred.}$ at the first peak was 1.14 with a coefficient of variation of 9.5%. Neglecting the bar contribution in compression increased the level of conservatism of the predicted results. The average $M_{exp.}/M_{pred.}$ was 1.23 with a coefficient of variation of 7.7%. Kara and Ashour (2012) compared the predictions of ACI 440.1R against the experimental moment capacities of 107 FRP-reinforced concrete beams collected from the literature. The average $M_{exp.}/M_{pred.}$ was 1.13 with a coefficient of variation of 16.8%. These predictions agree well with the predictions of M_{peak1} for the tested GFRP circular specimens. On the other hand, Table 3.2 presents the experimental-to-predicted ratios for the second peak flexural moments. At this load level, the test observations based on the compression-bar strains indicate that the bars in the compression block were able to resist the compression forces. Therefore, the contribution of the longitudinal

GFRP bars in the compressive block was considered at this stage. Table 3.2 indicates that the developed design procedures provided accurate predictions since the average value of the experimental results over the predicted results was greater than 1.08, with a coefficient of variation of 1.9%.

3.6.4. Proposed Simplified Method for Designing Circular GFRP-RC Members

This section provides simplified procedures to estimate the nominal flexural capacity of circular GFRP-RC members corresponding to the first peak moment. The assumptions stated above in Stage 1 for the calculation of first peak moment should be considered with these additional assumptions:

1. The area of tension reinforcement, A_f, is the area of the GFRP bars below the mid-depth of the section.

2. The effective depth, d, is taken as the distance from the extreme compression fiber to the centroid of the tension reinforcement (see Fig. 3.8(c)) and can be calculated using Eq. 3.20 given in AASHTO *LRFD Bridge Design Specifications (2012).*

$$d = \frac{D}{2} + \frac{D_r}{\pi} \tag{3.20}$$

where D_r = the diameter of the circle passing through the centers of the longitudinal reinforcement.

3. The compressive strength of GFRP reinforcement shall be disregarded in calculating flexural strength.

4. The reinforcement ratio and balanced reinforcement ratio can be computed from Eq. 3.21 and Eq. 3.22, respectively.

$$\rho_f = \frac{A_f}{Dd} \tag{3.21}$$

$$\rho_{fb} = 0.85\frac{f_c'}{f_{fb}}\frac{r^2\left(\theta_b - sin\theta_b cos\theta_b\right)}{Dd} \tag{3.22}$$

$$\theta_b = cos^{-1}\left(1-\frac{\beta_1 c_b}{r}\right) \tag{3.23}$$

$$c_b = \left(\frac{\varepsilon_{cu}}{\varepsilon_{cu}+\varepsilon_{fb}}\right)d \tag{3.24}$$

where f_{fb} and ε_{fb} are the average stress and strain in the GFRP tension reinforcement at the balanced condition, respectively.

When $\rho_f > \rho_{fb}$, the controlling limit state is the crushing of the concrete. Based on the equilibrium of forces and strain compatibility, shown in Fig. 3.8 (c), the following can be derived

$$M_{peak1} = A_f f_f\left(\bar{y}+\frac{D_r}{\pi}\right) \tag{3.25}$$

$$f_f = 0.85\frac{f_c'}{A_f}r^2\left(\theta - sin\theta cos\theta\right) \tag{3.26}$$

where f_f = the average stress in tension reinforcement; $\bar{y}$ = distance between the centroid of the circular concrete segment on the compression side to the centroid of the concrete cross section and can be calculated using Eq. (3.7).

The value of the angle (θ) defining the compressive block of the cross section can be determined with regression analysis based on the factors affecting the equilibrium of forces. Equation (3.27) is proposed using regression analysis to determine the value of θ or can be determined using the chart in Fig. 3.9.

$$\theta = 2.14\rho_{ft}^{0.18}\left(1.03-0.69\left(\frac{f_c'}{E_f}\right)^{0.17}\right) \tag{3.27}$$

$$\rho_{ft} = \frac{A_{ft}}{A_g} \tag{3.28}$$

where the angle θ is expressed in radians; f_c' = concrete cylinder strength in MPa; E_f = modulus of elasticity of the GFRP reinforcing bars in GPa; and ρ_{ft} = the ratio between the total reinforcement area and the gross area of the circular cross section expressed as a percentage (%).

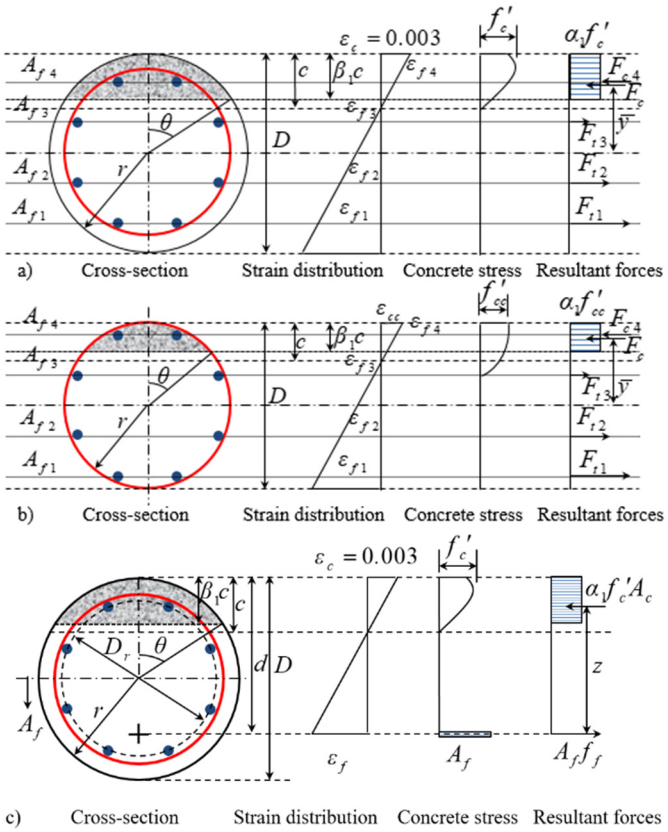

Figure 3.8 Idealized cross section and stress and strain distributions in the theoretical study: (a) first peak moment; (b) second peak moment; (c) proposed simplified method.

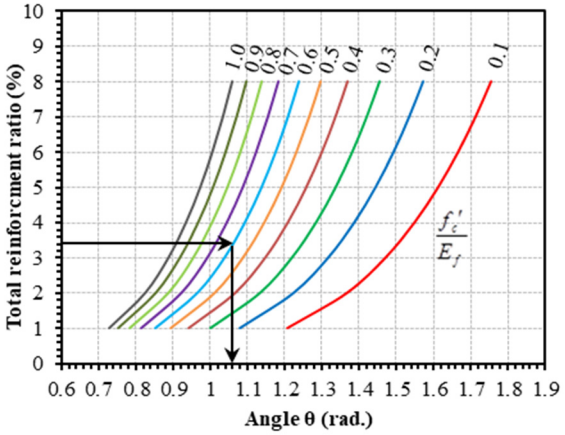

Figure 3.9 Chart for angle θ on the basis of reinforcement ratio, concrete compressive strength, and GFRP modulus of elasticity.

Table 3.2 presents the experimental to predicted ratios of the flexural capacities of test specimens using the proposed design procedures in the simplified method. Only one scenario—neglecting the contribution of the longitudinal GFRP bars in the compressive block—was assumed to be equivalent to the concrete in estimating the first peak moment.

The proposed simplified method yields a more reasonable estimate of the flexural capacity and yet was conservative for the test specimens, since the average experimental flexural strength over the predicted value was 1.26 with a coefficient of variation of 10.9%. A sample calculation with the proposed simplified method is given in the appendix. For the reader's convenience, the chosen calculation example of a circular GFRP-RC member is similar to Example 3M in the ACI440.1R-15 section on rectangular-sections.

3.7. Conclusions

In this paper, the flexural strength and behavior of full-scale circular concrete members reinforced with GFRP bars and spirals were investigated experimentally and theoretically. The experimental data provided the evidence required to include design provisions in the forthcoming ACI 440 code and updated CSA S6 for the use of GFRP bars and spirals as internal reinforcement in circular members. Based on the experimental results and the theoretical study presented herein, the following conclusions can be drawn.

1. The failure of circular GFRP-RC specimens occurred by gradual concrete crushing, while the steel-RC specimen failed due to steel yielding followed by concrete crushing. Interestingly, the GFRP-RC specimens did not lose their load-carrying capacity after concrete crushing. Instead, they continued to sustain additional loads. This behavior can be attributed to the confinement effect provided by the GFRP bars and spirals that enhanced specimen deformability and strength.
2. Based on the test results, the failure of circular GFRP-RC specimens is not triggered by GFRP bar rupture, provided that the minimum reinforcement ratio is not less than 1%. The maximum average tensile strain attained by the test specimens at initiation of cover spalling still represented less than 50% of the ultimate tensile strain of the GFRP bars.
3. The compression strain of the GFRP reinforcing bars in the test specimens did not show compression failure up to the first and second peak moments. In addition, the GFRP bars

developed up to 11,000 με of compressive strain, confirming that the GFRP bars were effective in resisting compression until after crushing of the concrete.

4. The experimental evidence of this study indicates that using GFRP spirals as transverse reinforcement effectively prevented the buckling of the GFRP bars and confined the concrete core in the post-peak stages up to a high strain level. The flexural strength at concrete crushing of GFRP-RC specimens was almost two times greater than that of the counterpart steel-RC specimen with a similar reinforcement ratio.
5. Increasing the longitudinal-reinforcement ratio from 1.2% to 3.5% significantly increased the strength and post-cracking flexural stiffness of the test specimens. Although all the circular GFRP-RC specimens failed due to compression failure, a high degree of deformability was attained before failure. In all cases, the calculated deformability factor was higher than that required in CSA S6.
6. A deformability J-Factor exceeding 6 is proposed and recommended to be used for GFRP-RC members with circular sections similar to that required in CSA S6 for nonrectangular section (T-section).
7. A strain compatibility model was developed to predict the flexural capacity of circular GFRP-RC members using the ACI 440.1R-15 guideline assumptions, strain compatibility, and force equilibrium (setting the strength factors to unity). This model was capable of conservatively predicting the flexural capacity of the test specimens. Considering the compression contribution of the GFRP bars in the strain-compatibility and force-equilibrium analyses provided accurate predictions of the flexural-moment capacities, while neglecting this contribution added to the level of conservativeness.
8. A simplified method, including design equations and design chart, was presented using non-iterative analysis. This method can be considered simple and more straightforward for practicing engineers.

CHAPTER 4. STRENGTH AND DEFORMABILITY ASPECTS OF CIRCULAR CONCRETE MEMBERS REINFORCED WITH HYBRID CARBON-/GLASS-FRP REINFORCEMENT UNDER FLEXURE

Foreword

Authors and Affiliation:

- Salaheldin Mousa: Ph.D. candidate, Department of Civil Engineering, Université de Sherbrooke, Sherbrooke, Quebec, Canada, J1K 2R1.
- Hamdy M. Mohamed: Research Associate/Lecturer, Department of Civil Engineering, Université de Sherbrooke, Sherbrooke, Quebec, Canada, J1K 2R1.
- Brahim Benmokrane: Professor, Department of Civil Engineering, Université de Sherbrooke, Sherbrooke, Quebec, Canada, J1K 2R1.

Journal Title: *Journal of Composites for Construction, ASCE.*

Paper Status: Submitted on October 11, 2017.

Contribution in thesis

This chapter reports on a study in which the flexural strength and deformability of circular concrete members with hybrid reinforcement—CFRP bars and GFRP spirals—were assessed experimentally and analytically. Detailed design procedures using a computer program were proposed for estimating the flexural capacity of circular CFRP-RC members using A Microsoft Excel Spreadsheet. The experimental and analytical results were discussed and compared.

Abstract

While the flexural behavior of fiber-reinforced-polymer (FRP) reinforced-concrete (RC) members has been the focus of many studies in recent years, no research work has examined such behavior in FRP-RC members with circular cross sections. This paper reports on a study in which the flexural strength and deformability of circular concrete members with hybrid reinforcement—carbon-FRP (CFRP) bars and glass-FRP (GFRP) spirals—were assessed experimentally and analytically. Three large-scale RC specimens with a total length of 6,000 mm and 500 mm in diameter were constructed and tested under four-point bending. Three CFRP longitudinal-reinforcement ratios (0.8%, 1.2%, and 1.8%) were considered. A steel-reinforced concrete specimen with a reinforcement ratio of 1.2% and steel spirals was fabricated as a reference. Test results indicate that the CFRP-RC specimens failed gradually at a high degree of deformability before concrete crushing. Moreover, the flexural strength of the CFRP-RC specimen with a reinforcement ratio of 1.2% was almost 3.3 times greater than the counterpart steel specimen (with a similar reinforcement ratio) at steel yielding. GFRP spirals were used to eliminate shear cracks and achieve the full flexural capacity. The ductility and deformability of the test specimens were estimated using different approaches. The estimated deformability factor was significantly higher than that required by North American FRP-design standards. Detailed design procedures using a computer program are proposed for estimating the flexural capacity of circular CFRP-RC members. The experimental and analytical results are discussed and compared.

Keywords: concrete; circular members; piles; flexural strength; FRP bars; spirals.

4.1. Introduction

Recent years have seen valuable research work on and widespread applications of fiber-reinforced-polymer (FRP) bars as flexural reinforcement for concrete structures. These efforts have led to noticeable advances in incorporating flexural-design provisions for FRP into guidelines and standards (ACI440.1R (2015); CSA S806 (2012); CSA S6 (2014)). These provisions were developed based on experimental work on rectangular concrete members reinforced with FRP bars. Limited experimental results on the flexural behavior of circular concrete members reinforced with glass FRP (GFRP) can be found in the literature (Hadi et al. 2016; Karim et al. 2017). In contrast, no research seems to have investigated RC members of circular cross section reinforced longitudinally with carbon-FRP (CFRP) bars under flexural loads. Moreover, there are practically no code provisions or guidelines for the flexural design of circular concrete members with FRP reinforcement. ACI 440.1R-15, however, points out that there is no evidence that the flexural theory—developed for rectangular sections—applies equally well to nonrectangular sections; the behavior of such members has yet to be confirmed experimentally.

RC members with circular cross sections are frequently used in practice, such as laterally loaded piers and piles in bridge foundations and in jetty substructures for marine and port infrastructure systems. In addition, they are used as secant piling systems for building combined earth-retention and groundwater cutoff walls in deep foundations for buildings and tunnel excavation applications. Despite these valuable applications, only limited research on the behavior of such structural members has been published. The life span of these circular members is often threatened by deterioration of their steel bars and spirals as the result of exposure to deicing salts and/or aggressive environments (Mohamed and Benmokrane 2014). Noncorroding FRP bars and spirals can be used to overcome this problem. CFRP is one of the most common types of FRP bars used as primary reinforcement in flexural members. CFRP bars offer exceptionally high tensile strength-to-weight ratios and tensile modulus-to-weight ratios. GFRP spirals are also efficient in providing shear strength (Ali et al. 2017a; Mohamed et al. 2017), laterally supporting compression and tension bars, and confining the compressive concrete core (Afifi et al. 2014b; Hadi et al. 2016; Hadhood et al. 2017a). In the tested specimens, we used CFRP bars

as longitudinal reinforcement, while GFRP spirals were used for transverse reinforcement. GFRP costs less than other types of FRP materials.

4.2. Research on Circular Concrete Members reinforced with CFRP

A comprehensive research program on the performance of circular concrete members reinforced with FRP bars and spirals under different loading conditions is being conducted under the Tier-1 Canada Research Chair on Advanced Composite Materials for Civil Structures in the Department of Civil Engineering at the University of Sherbrooke. CFRP bars have been included in this research program, given their high strength and high tensile modulus. Afifi et al. (2014b) investigated the applicability of using CFRP bars as longitudinal reinforcement in circular concrete columns. Their test results indicated that the CFRP- and steel-reinforced columns tested behaved similarly up to their peak loads. The CFRP bars were effective in resisting compression until after concrete crushing and contributed to column capacity. Ali et al. (2017b) designed and conducted experimental tests on full-scale circular RC members reinforced with CFRP bars but without web reinforcement under shear. They concluded that the concrete contribution to the shear strength of circular CFRP-RC members is proportional to the axial stiffness of the longitudinal reinforcing bars. Mohamed et al. (2017) demonstrated the shear strength of circular concrete members reinforced with CFRP bars and spirals. Their investigation revealed that the test specimens reinforced with CFRP bars and spirals exhibited high shear-carrying capacity and performance comparable to that of the control specimen reinforced with steel. Hadhood et al. (2017a) evaluated the structural performance of full-scale circular RC columns reinforced with CFRP bars subjected to combined axial compression loads and bending moments. Their test results showed that the CFRP- and steel-reinforced concrete columns behaved similarly. The failure of the test specimens under different levels of eccentricity was not triggered by rupture of the CFRP bars in the tension side, but rather by gradual concrete crushing. It was concluded that CFRP reinforcement could be used as internal reinforcement in eccentric columns. On the other hand, other research programs were conducted on the behavior of circular concrete members reinforced with CFRP bars. Khan et al. (2018) conducted experimental and theoretical studies for concrete-filled carbon-fiber-reinforced-polymer tube columns reinforced internally with CFRP bars under eccentric and flexural loads. The effectiveness of CFRP reinforcement (tubes and reinforcing bars) was lower as the applied

axial-load eccentricity increased. The parametric study presented by Khan et al. (2018) showed that the actual confinement ratio, fiber orientation, and CFRP-bar reinforcement ratio significantly influenced the axial–flexural interactions of the tested specimens. Shalaby et al. (2011) studied the flexural behavior of concrete poles reinforced with CFRP bars. The study showed that the performance of the poles reinforced with CFRP bars was satisfactory under bending loads. These studies motivated a new study to assess the flexural behavior of circular concrete members reinforced with CFRP bars.

4.3. Objectives

This study aimed at providing basic technical information and yielding better understanding of the flexural strength and deformability of circular CFRP-RC members. A number of research objectives were identified and are listed below.

- To experimentally examine the feasibility and efficiency of using hybrid CFRP bars/GFRP spirals in circular RC members under flexural load.
- To investigate the effect of the CFRP reinforcement ratio on flexural strength and behavior.
- To discover the failure mechanisms of such members under flexural loads.
- To assess the ductility and deformability of such members.
- To propose simple and accurate design procedures for predicting the flexural strength.

4.4. Experimental Program

4.4.1. Material Properties

4.4.1.1. CFRP Bars and GFRP Spirals

Number 5 (15.9 mm) sand-coated CFRP bars and #4 (12.7 mm) GFRP spirals were used to reinforce the circular specimens in the longitudinal and transverse directions, respectively, as shown in Fig. 4.1. The CFRP longitudinal bars and GFRP spirals were manufactured by

pultruding continuous high-strength carbon fibers and free-boron glass fibers, respectively, impregnated with a thermosetting vinyl-ester resin (Pultrall, 2015). The ultimate tensile strength, f_{fu}, and modulus of elasticity, E_f, of the longitudinal CFRP bars (#5) and the straight portion of the bent GFRP spirals (#4) were determined according to ASTM D7205 (ASTM 2011), as reported by the manufacturer (Table 4.1).

Table 4.1 Mechanical properties of the CFRP, GFRP and steel reinforcements

RFT Type	d_b (mm)	A_f [a] (mm²)	A_{im} [d] (mm²)	E_f (GPa)	f_{fu} (MPa)	ε_{fu} (%)
GFRP spirals	12.7	127	148.3±1.1	52.1±1.19	1126 [b] ±20	2.20±0.0
CFRP bars	15.9	198	222.3±1.2	141±2.5	1680 ±22	1.19±0.1
Steel	10M	100	---	E_s = 200.0	f_y [c] = 480±10	ε_y [c] = 0.24
	20M	300	---	E_s = 200.0	f_y = 460±15	ε_y = 0.23

[a] Nominal cross-sectional area.
[b] Tensile strength of straight bars.
[c] f_y and ε_y are the yield strength and strain of the steel bars, respectively.
[d] Immersed cross-sectional area (measured).
Note: Properties calculated based on the nominal cross-sectional area.

4.4.1.2. Steel Reinforcement

Table 4.1 provides the mechanical properties of the steel bars used to reinforce the control specimen in this study. Deformed 20M (20 mm) steel bars were used as longitudinal reinforcement and deformed 10M (11.5 mm) steel bars were used as spiral reinforcement.

4.4.1.3. Concrete

All of the circular specimens were cast using normal-weight, ready-mixed concrete with a target compressive strength of 40 MPa. The actual compressive strength was 45.8 MPa for the hybrid CFRP/GFRP specimens and 41.4 MPa for the steel specimen and determined based on the average test results of ten 100 x 200 mm concrete cylinders tested on the first day as the start of testing of the specimens.

Figure 4.1 (a) GFRP spirals, (b) CFRP bars, (c) Hybrid CFRP/GFRP cages, and (d) RC specimens.

4.4.2. Specimen Details and Test Matrix

The experimental program was designed to provide data on the flexural strength and behavior of circular concrete members reinforced with CFRP bars. A total of four large-scale circular RC specimens, including three reinforced with CFRP bars and one with steel reinforcement, were tested under bending. The test specimens were 500 mm in diameter and 6,000 mm in length. The specimens were tested under four-point bending with 4,950 mm of clear span and 2,100 mm of shear span. Figure 4.2 shows the dimensions, various configurations, and reinforcement details of the test specimens. The test matrix was arranged to assess the influence of the flexural-reinforcement type (CFRP versus steel) and CFRP flexural-reinforcement ratio. Table 4.2 provides the test matrix and reinforcement details of the test specimens. The test beams are identified as follows. The first number indicates the number of longitudinal bars. The letters C and S indicate specimens reinforced longitudinally with CFRP or steel reinforcement, respectively. The second number indicates the nominal diameter of the longitudinal bars. Three

CFRP-RC specimens were reinforced longitudinally with 8, 12, and 18 #5 CFRP bars (15 mm). The longitudinal-reinforcement ratios were 0.8%, 1.2%, and 1.8%. The control steel specimen was reinforced longitudinally with 8 M20 deformed steel bars with a reinforcement ratio of 1.2%. The clear concrete cover was kept constant at 38 mm for all specimens.

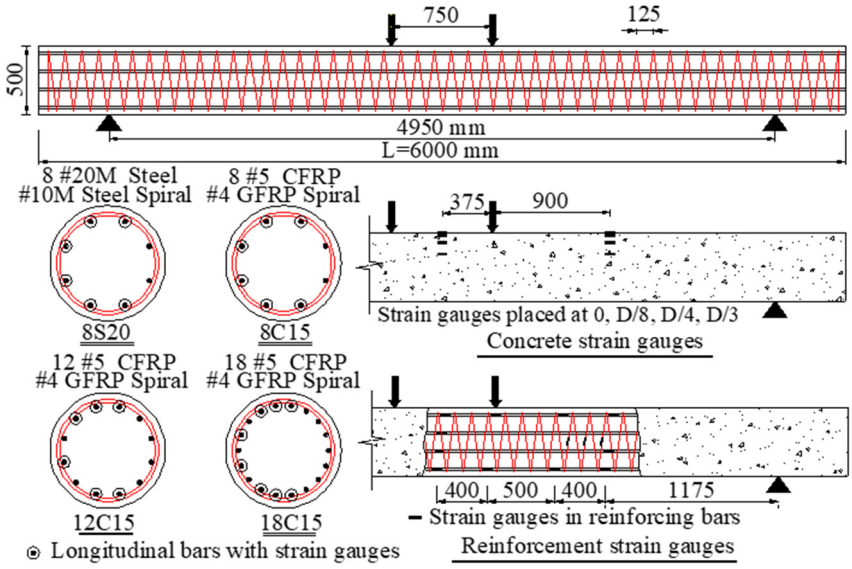

Figure 4.2 Dimensions, reinforcement details, and strain-gauge locations of the test specimens (dimensions in mm).

Table 4.2 Test matrix and details of test specimens

Specimen ID	Reinforcement Type	Longitudinal Reinforcement		ρ_f/ρ_{fb}		Transverse Reinforcement
		ρ_{ft} (%)	Number of bars	ACI 440.1R-15	CSA S806-12	
8C15	Hybrid carbon/glass FRP	0.80	CFRP bars (8 No. 15 mm)	1.37	1.14	GFRP spirals # 4 @125
12C15	Hybrid carbon/glass FRP	1.20	CFRP bars (12 No. 15 mm)	2.05	1.70	GFRP spirals # 4 @125
18C15	Hybrid carbon/glass FRP	1.80	CFRP bars (18 No. 15 mm)	3.07	2.55	GFRP spirals # 4 @125
8S20	Steel	1.20	Steel bars (8 #20M)	------	------	Steel spirals 10M @125

4.4.3. Specimen Design

The specimen design was carried out in accordance with CSA S806-12 recommendations (clause 8.4.3.10) for longitudinal-bar size (minimum 15 mm), the number of bars (minimum of 6 bars), and total longitudinal-reinforcement ratio (minimum of 1.0%). Specimen 8C15 with a reinforcement ratio of 0.8%, however, was prepared out-of-code requirements for comparison purposes and to assess the code's lower limit for the minimum reinforcement ratio. Testing was intended to assess the flexural strength of circular CFRP-RC members, so all of the specimens were designed such that their shear strength exceeded their flexural strength. This was achieved by reducing the shear influence and choosing a shear span-to-depth ratio greater than five (Kani 1964). The test specimens were designed to fail by concrete crushing in the constant-moment zone. This was accomplished by using a reinforcement ratio (ρ_f) greater than the balanced reinforcement ratio (ρ_{fb}), as shown in Table 4.2. The nominal flexural capacity was calculated based on strain compatibility and force equilibrium. The balanced reinforcement ratio (ρ_{fb}) is calculated from Eq. (4.1). An equivalent rectangular section, as shown in Fig. 4.3, was considered with an equivalent width equal to the diameter of the circular section, D, and an equivalent effective depth, d, estimated based on clause 5.8.2.9 in the 2012 edition of the *AASHTO LRFD Bridge Design Specifications*. The area of the tension reinforcement, A_f, was taken as the area of the bars below the mid-depth of the section.

$$\rho_{fb} = \alpha_1 \beta_1 \frac{f_c'}{f_{fu}} \frac{E_f \varepsilon_{cu}}{E_f \varepsilon_{cu} + f_{fu}} \tag{4.1}$$

where f_c' is the specified compressive strength of concrete; f_{fu} and E_f are the ultimate tensile strength and modulus of elasticity of FRP bars, respectively; and ε_{cu} is the maximum usable compressive strain in the concrete. The terms α_1 and β_1 are calculated from Eqns. (4.2 and 4.3) for ACI 440.1R-15 and Eqns. (4.4 and 4.5) for CSA S806-12:

$$\alpha_1 = 0.85 \tag{4.2}$$

$$\beta_1 = 0.85 - \frac{0.05(f_c' - 28)}{7} \geq 0.65 \tag{4.3}$$

$$\alpha_1 = 0.85 - 0.0015 f_c' \geq 0.67 \tag{4.4}$$

$$\beta_1 = 0.97 - 0.0025 f_c' \geq 0.67 \tag{4.5}$$

Table 4.2 provides the ratio between ρ_f and ρ_{fb} for the test specimens as per ACI 440.1R-15 and CSA S806-12. On the other hand, the concrete contribution, V_{cf}, to the nominal shear capacity was estimated based on the equation proposed by Ali et al. (2017b) for circular concrete members reinforced with FRP reinforcement as follows:

Table 4.2 provides the ratio between ρ_f and ρ_{fb} for the test specimens as per ACI 440.1R-15 and CSA S806-12. The concrete contribution, V_{cf}, to the nominal shear capacity was estimated based on the equation proposed by Ali et al. (2017b) for circular concrete members reinforced with FRP reinforcement as follows:

$$V_{cf} = 0.35\left(\frac{100A_{ft}}{b_w d}\frac{E_f}{E_s}\right)^{1/3}\left(\frac{500}{d}\right)^{1/4}\left(1.25f_c'\right)^{1/3} b_w d \,/\, \gamma_m \tag{4.6}$$

where A_{ft} is the total area of longitudinal reinforcement; b_w is equal to the diameter of the circular cross section; E_f and E_s are the moduli of elasticity of the FRP and steel bars, respectively; γ_m is the partial safety factor of materials. The concrete contribution to the nominal shear capacity, (neglecting the contribution of spirals), was found to be 33%, 19%, and 5% greater than the required applied load to achieve the flexural failure for 8C15, 12C15, and 18C15, respectively. Hence, to optimize the cost of the designed specimens, No. 4 GFRP spirals were used, because they cost less than other types of FRP materials. Moreover, based on the test results of Ali et al. (2017a) for similar circular concrete members (500 mm in diameter) and reinforced with No. 4 GFRP spirals, the authors concluded that the use of GFRP spirals as shear

reinforcement adequately meets shear-design requirements. The developed GFRP spirals can be used as shear reinforcement for circular concrete members for pile and pier applications.

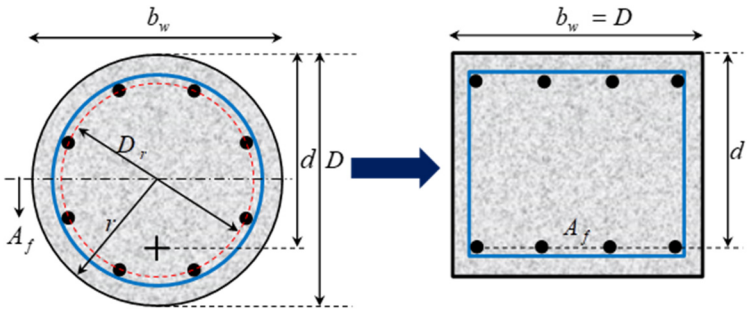

Figure 4.3 Equivalent rectangular section for calculating the balanced reinforcement ratio, ρ_{fb}.

4.4.4. Instrumentation and Test Setup

Strains in the longitudinal reinforcing bars and spirals were measured using electrical resistance strain gauges with a gauge length of 10 mm (see Fig. 4.2). In addition, nine strain gauges with a gauge length of 60 mm were mounted on the concrete outside surface at four different levels from the extreme compression surface (0, D/8, D/4, and D/3) at mid-span and at quarter-span to measure compressive strains. Specimen deflection was measured with three linear potentiometers (LPOTs) placed at the mid-span and at the quarter-span. The test setup was designed and fabricated at the University of Sherbrooke's CFI structural laboratory. Steel saddles were designed to accommodate the circular geometry at loading and support points. The specimens were loaded under four-point bending load, as shown in Fig. 4.4, using an MTS 1,000 kN servo-controlled, hydraulic actuator attached to a spreader beam. The load was applied at a displacement-controlled rate of 0.5 mm/min. An automatic data-acquisition system monitored by a computer was used to record the readings of the LPOTs, load cells, and strain gauges.

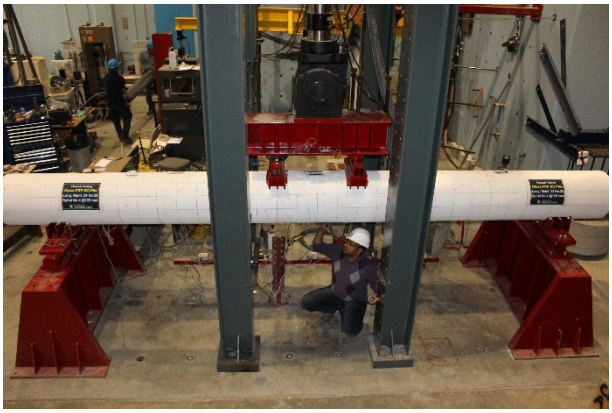

Figure 4.4 Test setup.

4.5. Test Results and Discussion

This section summarizes the experimental results, including the general behavior of the test specimens in terms of flexural capacity, crack patterns and failure modes, strains in reinforcement and concrete, neutral-axis depth, and ductility and deformability.

4.5.1. General Behavior and Failure Modes

Table 4.3 provides the flexural capacity and failure modes of the test specimens. The failure of 8C15 occurred by concrete crushing in the compression zone at mid-span, followed by rupture of CFRP tension bars. 12C15 and 18C15 failed by concrete crushing, followed by compression failure of CFRP bars in the compression side. 8S20, which was reinforced with steel, failed due to steel yielding, followed by concrete crushing (see Fig. 4.5). Figure 4.6 provides the cracking patterns at failure for all of the specimens. The first vertical flexural crack initiated at the constant-moment zone between the two loading points. The corresponding cracking load was recorded during testing and also verified from the moment–strain and moment–deflection relationships. The cracking moment, M_{cr}, ranged between 23.5 kN.m and 34.5 kN.m. At this stage, there were no significant strain-gauge readings for the CFRP and steel reinforcing bars before initiation of the first flexural crack. In addition, the concrete strains were insignificant in all specimens and ranged from –90 to –120 microstrains ($\mu\varepsilon$) at the top location of the mid-span (see Fig. 4.7). Beyond the first cracking load, additional flexural cracks developed within the constant-moment zone of the hybrid CFRP/GFRP specimens. With further loading, the flexural cracks became wider and propagated upward around the perimeter of the circular section, while some new cracks started to develop in the shear span. Before failure occurred, the

cracks along the shear span started to incline towards the loading points. The failure moment, M_n, was 332, 442, and 444 kN.m for 8C15, 12C15, and 18C15, respectively. In contrast, the early yielding of the steel bars in 8S20 resulted in wider, concentrated cracks at the constant-moment zone. 8S20 yielded (at a corresponding strain of approximately 2,300 $\mu\varepsilon$) at an applied moment of 134 kN.m (approximately at 56% of the specimen's peak moment). Figure 4.8 shows the recorded strain readings (the tension and compression strains) up to failure as measured by the electrical resistance strain gauges bonded on the reinforcing bars. It is worth mentioning, however, that some of these strain gauges did not work properly or damaged before failure because several cracks occurred in the instrumented region. The CFRP bars in the tension side showed a gradually increasing strain up to failure with strain values of 10,300, and 7,100 $\mu\varepsilon$ (87.5% and 60% of the ultimate tensile strain for the CFRP bars) for 12C15 and 18C15, respectively. Specimen 8C15 reached to a maximum applied moment of 354 kN.m, while the strain gauge in the tension reinforcement stopped to record strain readings at an applied moment of 260 kN.m. In addition, specimen 8S20 reached to a maximum applied moment of 237 kN.m, while the strain gauge in the tension reinforcement stopped to record strain readings at an applied moment of 180 kN.m. In contrast, the strain gauges in the compression reinforcement continued to record strain readings up to terminating the test in both specimens 8C15 and 8S20. The recorded compressive strains in the compression reinforcement (CFRP or steel bars) at concrete crushing in 8C12, 12C15, and 18C15, or at steel yielding in 8S20, were –5,130, –3,100, –2,100, and –500 $\mu\varepsilon$, respectively. The maximum recorded concrete compressive strains in the top fibers at mid-span were –4,300, –4,100, –3,600, and –5,000 $\mu\varepsilon$ for 8C15, 12C15, 18C15, and 8S20, respectively, (see Figure 4.7). The recorded concrete strains for the test specimens were higher than the specified limit for design by ACI440.1R-15 (–3,000 $\mu\varepsilon$) and CSA S806-12 (–3500 $\mu\varepsilon$). As expected, the recorded strains at D/8 and D/4 at mid-span were less than at the top fiber (see Fig. 4.7). The test results indicate that the recorded strains at the quarter-span were less than that at mid-span, reaching no more than –1,600 $\mu\varepsilon$. After the applied load was released, 12C15 and 18C15 recovered most of their deflection during the unloading process. Permanent deflection was observed during the unloading process of 8C15 and 8S20, due to CFRP tension bars rupturing and steel tension bars yielding, respectively. Table 4.3 provides the curvature of the test specimens at the failure moment as a function of

1/*d*. For the circular hybrid CFRP/GFRP-RC specimens, the curvature ranged from 0.0089/*d* to 0.0185/*d*.

Table 4.3 Experimental moments, mode of failure, curvature, and ductility and deformability of test specimens.

Specimen ID	M_{cr} (kN.m)	M_n (kN.m)	M_{peak} (kN.m)	Failure mode[a]	Effective depth d [c] (mm)	Curvature $\psi, 1/d$ [c] at M_n	Ductility and deformability			$M_{exp.}/M_{pred.}$ M_n		
							μ_e	J	J_{VG}	Ignore comp. bars	Consider comp. bars	Simple method
8C15	24	332	354	C.C.	372	0.0185	1.30	38	11	1.06	1.00	1.09
12C15	29	442	452	C.C.	372	0.0139	1.90	22	6	1.19	1.06	1.22
18C15	34	444	471	C.C.	372	0.0089	1.80	11	3	1.01	0.96	1.04
8S20[b]	30	134	237	S.Y.	371	0.0022	1.95	-	-	-	-	-
Average										1.10	1.01	1.12
COV (%)										11.60	5.00	8.30

[a] C.C. = concrete crushing, S.Y. = steel yielding.

[b] Values calculated at $M_n = M_y$, and M_{peak} = maximum moment at concrete crushing.

[c] The effective depth, d, calculated using Eq. 4.17.

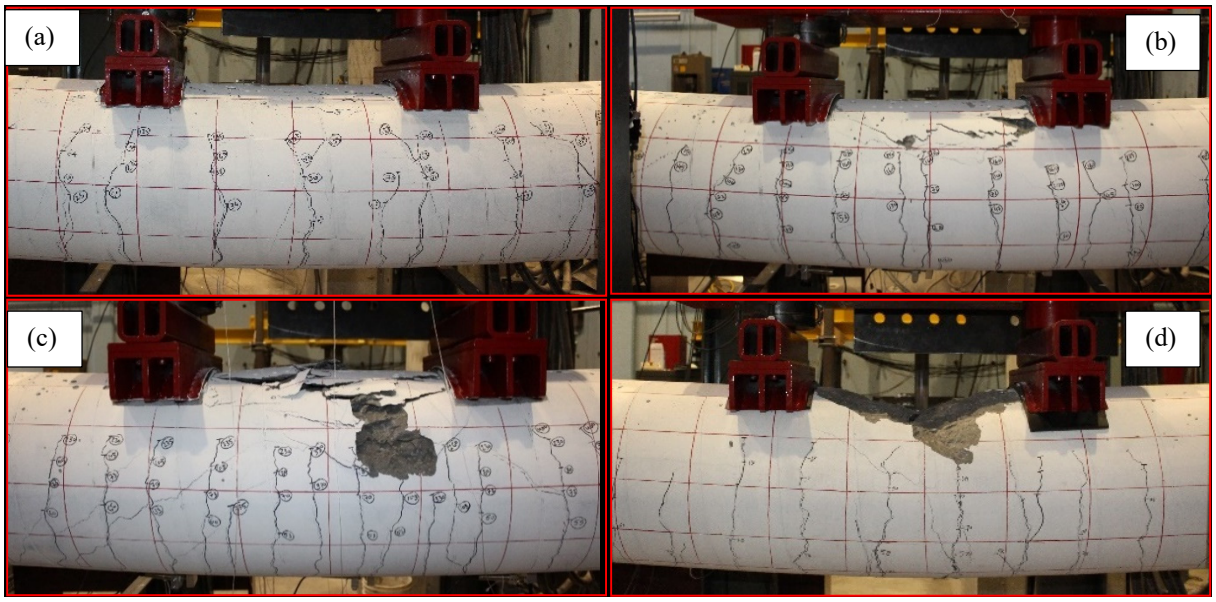

Figure 4.5 Failure modes of the circular hybrid CFRP/GFRP-RC and circular steel-RC specimen: (a) 8C15, (b) 12C15; (c) 18C15, and (d) 8S20.

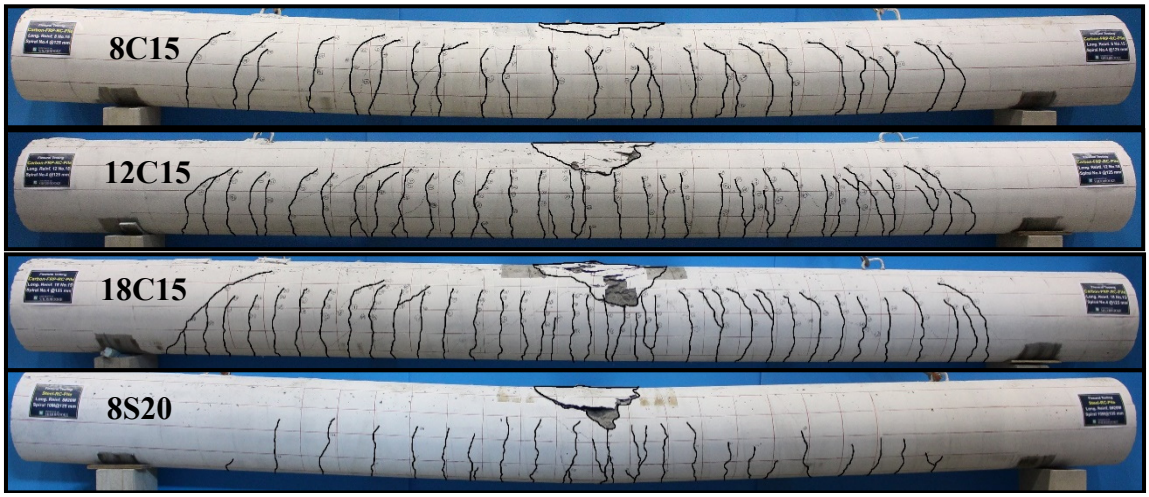

Figure 4.6 Cracking pattern of the test specimens.

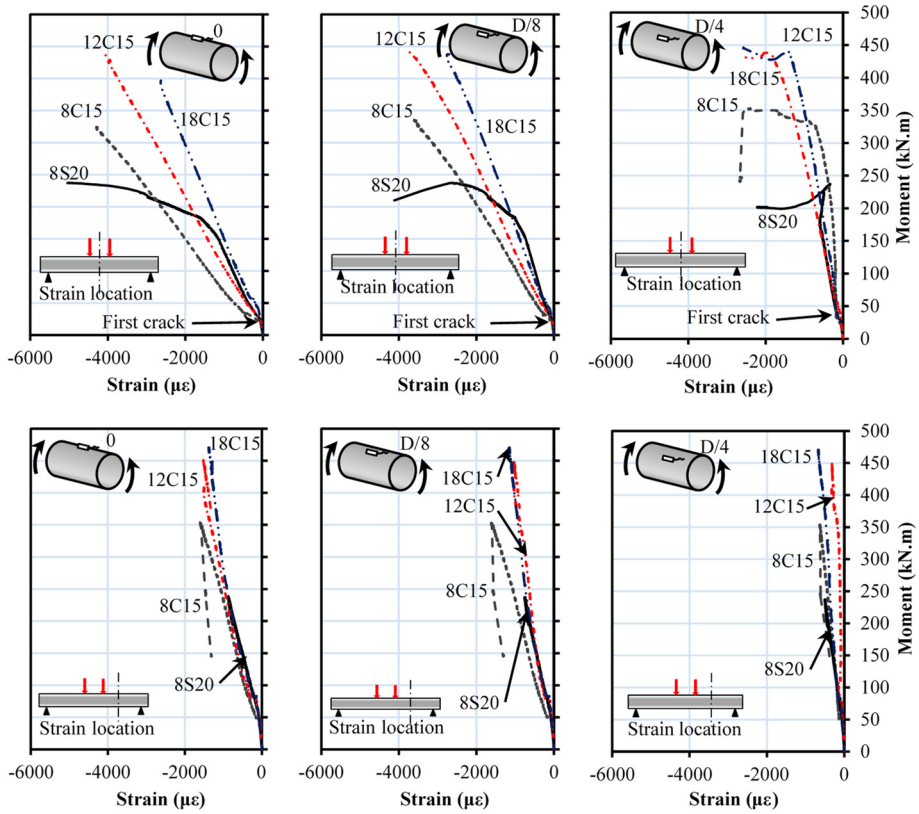

Figure 4.7 Moment–concrete strain relationship at mid-span and at quarter-span.

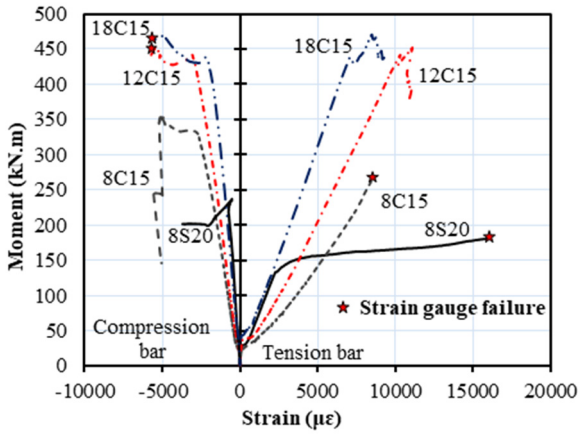

Figure 4.8 Moment–bar tension and compression–strain relationship at mid-span.

4.5.2. Effect of Test Parameters

This section presents the moment–deflection curves at mid-span of the four specimens in two groups to show the effect of test parameters on flexural behavior, as depicted in Figs. 4.9 and 4.10. Before cracking, an identical linear moment–deflection behavior was observed in all the test specimens, regardless of their reinforcement ratio and type, representing the uncracked condition governed by the properties of the circular concrete section. After cracking, the response of the hybrid CFRP/GFRP specimens was almost linear up to failure. Specimen 8C15 lost its entire strength due to rupture of CFRP tension bars, while 12C15 and 18C15 continued to sustain additional load, even after concrete crushing. The moment–deflection curve of the steel-reinforced specimen shows a typical yielding plateau, followed by concrete crushing in the compression zone. Afterward, a sudden load drop occurred, followed by total loss of flexural stiffness.

4.5.2.1. Effect of the Axial Stiffness of Longitudinal Reinforcement

12C15 and 8S20 were designed to have the same flexural longitudinal-reinforcement ratio. Before 12C15 cracked, its stiffness was similar to that of 8S20, as shown in Fig. 4.9. The post-cracking flexural stiffness, calculated as the average slope of the curve, was slightly lower for 12C15 than for its steel-reinforced counterpart, 8S20. The ratio between the post-cracking flexural stiffness of 8S20 to 12C15 was approximately 1.41. This ratio was approximately the same as the 1.44 ratio of the axial stiffness EA of steel to that of the CFRP bars. This is in good

agreement with the results of Ali et al. (2017b) and El-Sayed et al. (2006). The stiffness gap could simply be decreased by using a slightly larger amount of the CFRP reinforcement to compensate for its lower stiffness. It can be seen, however, that the CFRP-RC specimen had a longer ascending branch with higher stiffness compared to the post-yielding flexural stiffness of the steel-reinforced specimen. This is mainly due to the fact that, after yielding, the tangent modulus of the steel bars was much lower than that of the CFRP bars, which maintained their modulus of elasticity throughout the entire duration of loading. In contrast, the test results indicate that 12C15 had flexural strength 3.3 times that of 8S20 at yielding. The higher strength gain of the CFRP specimen provided sufficient ductility so that warning of failure in the form of excessive deflection and cracking would be expected before the rupture tensile strain of the CFRP bars was reached.

4.5.2.2. Effect of the Longitudinal-Reinforcement Ratio

The three hybrid CFRP/GFRP specimens (8C15, 12C15, and 18C15) were designed to have reinforcement ratios of 0.80%, 1.20%, and 1.80%, respectively. Figure 4.10 provides a comparison of the moment–deflection curves for the three specimens, indicating that 12C15 and 18C15 had smaller deflections and higher flexural strength than 8C15 by 33.1% and 33.6%, respectively. 18C15 did not gain as much strength as 12C15 when the reinforcement ratio increased from 1.20% to 1.80%. This could be attributed to the fact that 18C15 reached the flexural capacity, as it was governed by concrete and CFRP-bar crushing. In contrast, test results indicate that increasing the CFRP-reinforcement ratio significantly affected the post-cracking flexural stiffness of the test specimens. The post-cracking flexural stiffness of 12C15 (reinforcement ratio of 1.2%) was 46% higher than that of 8C15 (reinforcement ratio of 0.8%). Similarly, the post-cracking flexural stiffness of 18C15 (reinforcement ratio of 1.8%) was 120% higher than that of 8C15 (reinforcement ratio of 0.8%) and 51% higher than that of 12C15 (reinforcement ratio of 1.2%). These percentages were approximately similar to the percentage increase in the reinforcement ratio (50% from 0.8% to 1.2%, 50% from 1.2% to 1.8%, and 125% from 0.8% to 1.8%).

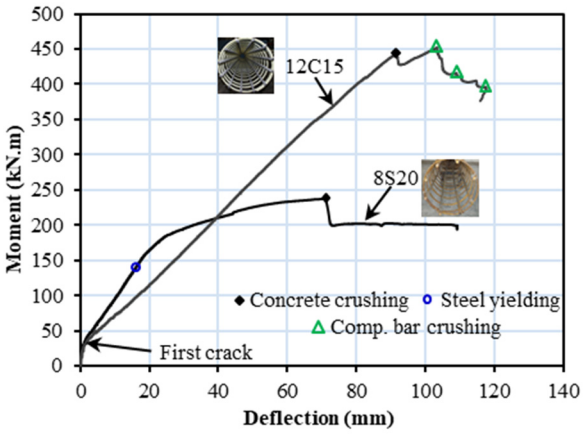

Figure 4.9 Effect of axial stiffness of flexural reinforcement on the moment–deflection relationship.

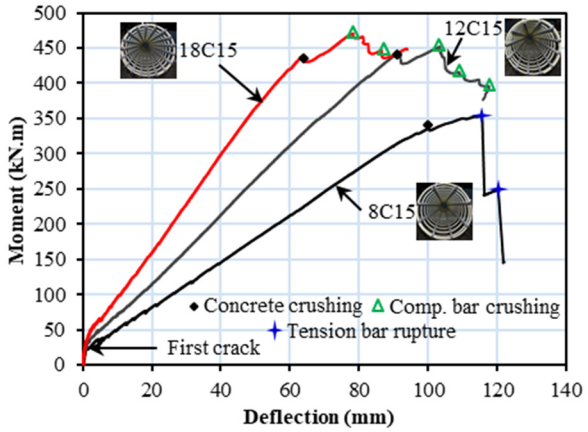

Figure 4.10 Effect of reinforcement ratio on the moment–deflection relationship.

4.5.3. Bar-Strain Distribution along the Span

Figure 4.11 shows the experimental strain profile of the longitudinal tension and compression bars along the span of the test specimens at different load levels. In Figure 4.11, the strains were typically high in the middle of the span underneath the applied load. Generally, Figure 4.11 confirms that increasing the reinforcement ratio reduced both tensile and compression strains in the bottom and top reinforcement. The strain values decreased with distance from the mid-span until reaching zero at the supports. This implies that no bond failure or slip occurred during the tests. It can be observed that, at initial stages of loading, the distribution of strains in the CFRP reinforcing bar along the span was similar to that in the steel reinforcing bar. As the applied load

increased, the strain gradually increased proportionally to the bending distribution along the span, up to failure. At the onset of the steel yielding in the steel-reinforced specimen, however, strain distribution in the longitudinal steel reinforcement tended to localize at the loaded middle zone; small strain values were recorded on the other side of the specimen. In the CFRP-RC specimens, however, the strains along the CFRP bars on the compression and tension sides maintained the same distribution and progress up to failure. This observation implies that the CFRP bars efficiently transferred load with the strains extending along both sides of the loading zone and without any signs of bond-strength degradation.

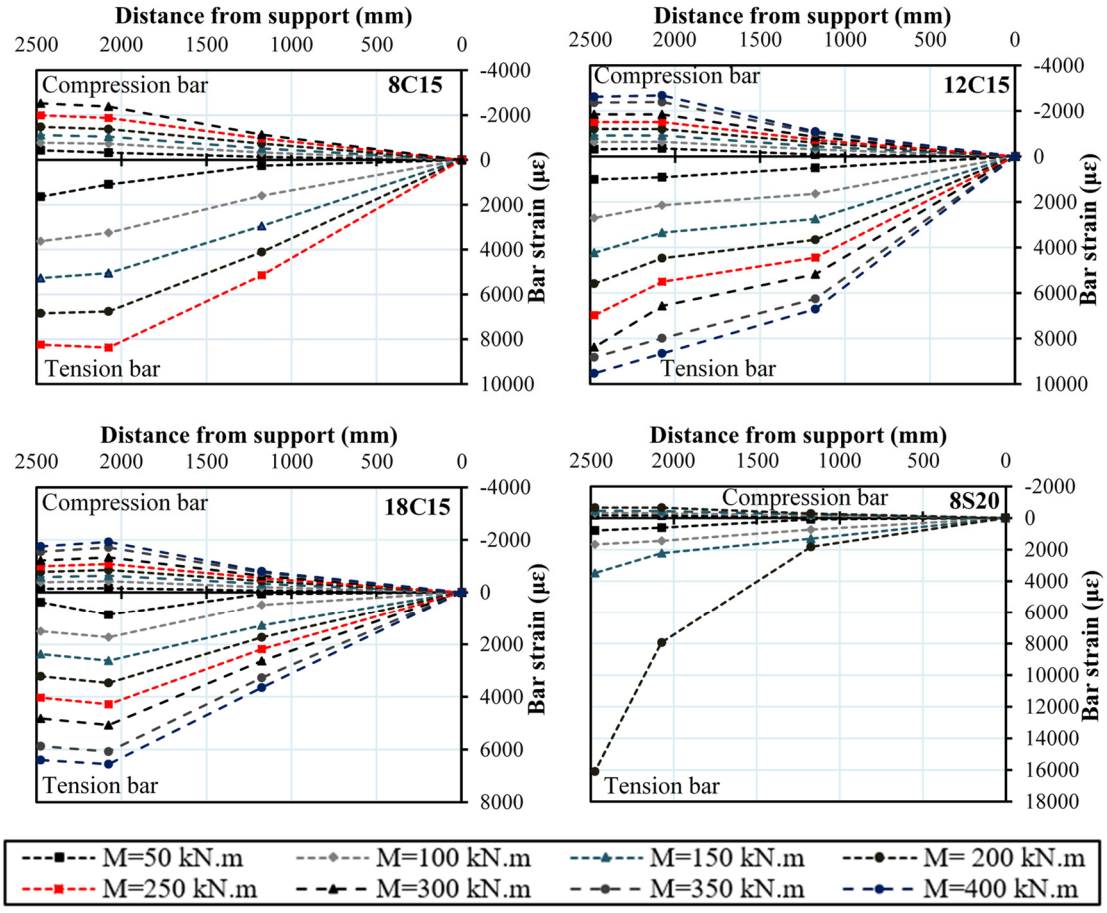

Figure 4.11 Moment–bar tension and compression strain along specimen length.

4.5.4. Strain Distribution over the Cross Section

An analysis of strains along the cross section was carried out using the results from the concrete and bar strain gauges at the mid-span of specimens, as shown in Fig. 4.2, and the experimental neutral-axis depth was deduced. Figure 4.12 presents the strain profile along the depth of the section at different moment levels. The figure shows that the strain profile is linear with some deviation. The Bernoulli hypothesis (a plane section remains plane after deformation up to failure), however, may be considered as an acceptable simplification for this behavior.

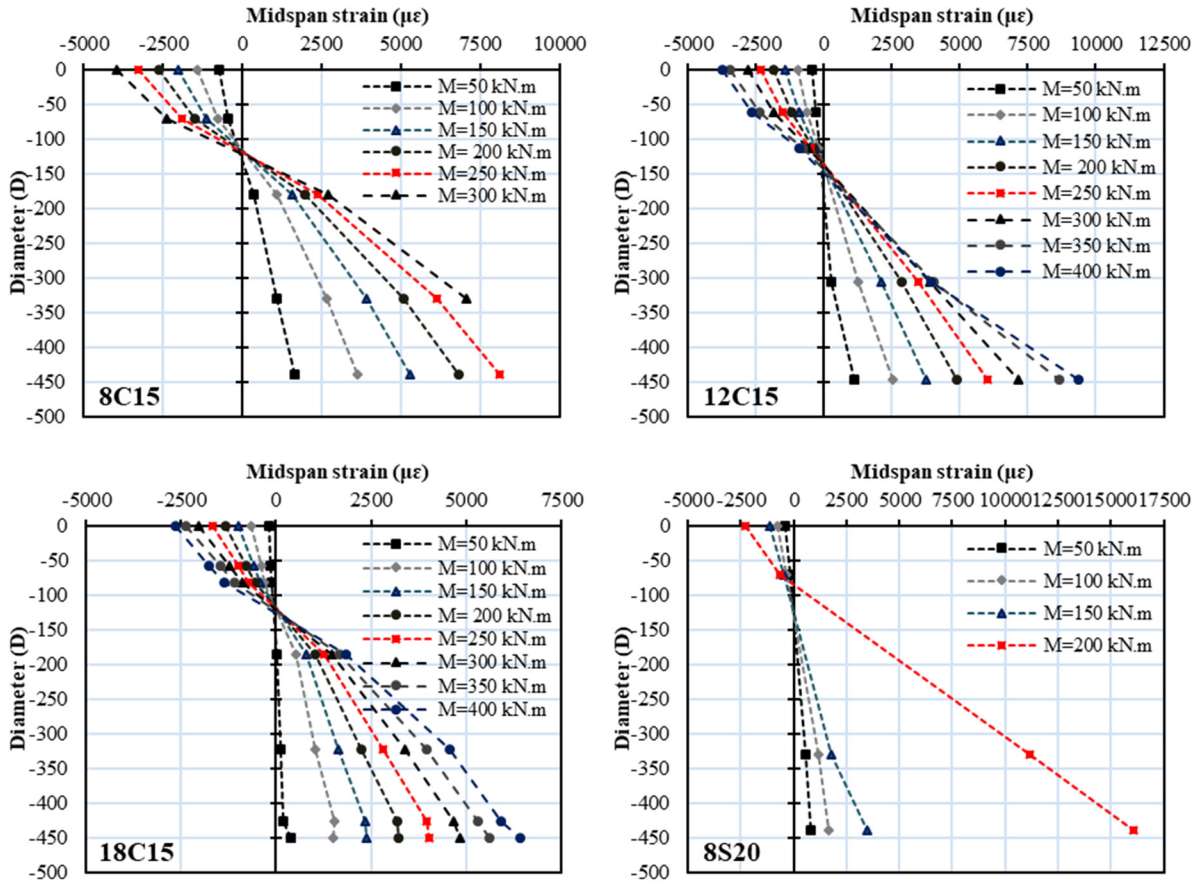

Figure 4.12 Strain along the mid-span cross-section diameter.

Figure 4.13 illustrates the relation between neutral-axis depth at mid-span with the applied moment for the test specimens. The position of the neutral axis at a section prior to cracking remained unchanged, located at the geometrical centroid of the circular cross section. After cracking, the neutral-axis depth decreased rapidly at first and then tended to stabilize. In the

specimens with CFRP reinforcement, the stabilizing behavior continued up to concrete crushing. In contrast, the yielding of tensile steel in the reinforced-steel specimen resulted in a quick decrease in the neutral-axis depth. Figure 4.13 also shows that the neutral-axis depth for 12C15 was smaller than that of 8S20 with a similar reinforcement ratio. This could be attributed to the difference in the modulus of elasticity of the CFRP and steel bars. Moreover, the neutral-axis depth in the hybrid CFRP/GFRP specimens increased with a higher reinforcement ratio. The neutral-axis depth increased by approximately 25% and 88% in 12C15 and 18C15, respectively, compared to 8C15.

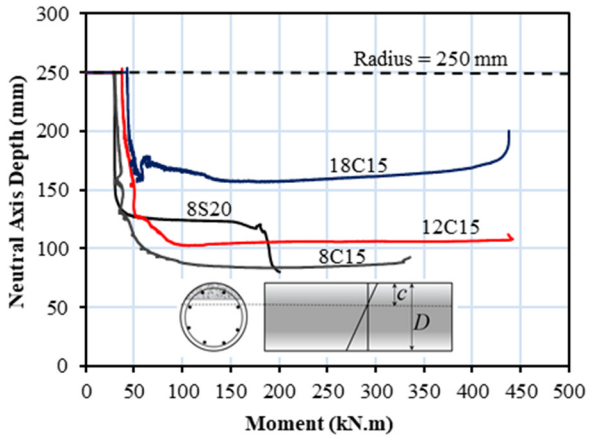

Figure 4.13 Neutral-axis depth.

4.5.5. Efficiency of GFRP Spirals

Figure 4.14 shows the moment–spiral strain relationships for hybrid CFRP/GFRP specimens. The strains were measured in three spirals located within a distance equal to 1,200 mm from the support. As the applied load increased, the measured strains in the GFRP spirals gradually increased in all the specimens with no sign of shear cracks developing along the shear span up to failure. The maximum strain in the GFRP spirals measured at failure was 2,200, 3,200, and 3,100 με in 8C15, 12C15, and 18C15 (see Fig. 4.14), respectively, which is 10%, 15%, and 14% of the ultimate strain of the GFRP spirals. It can be concluded that the GFRP spirals were sufficient to resist and eliminate the formation of shear cracks up to the flexural capacity of the test specimens. On the other hand, the maximum measured spiral strain at the shear span for 8S20 at failure was 1,400 με (see Fig. 4.14), which is 60% of the steel yield strain.

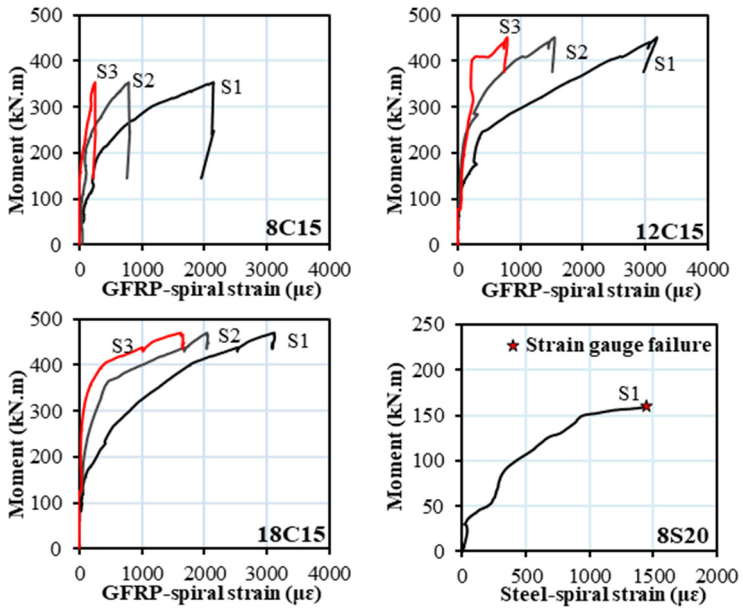

Figure 4.14 Moment–GFRP-spiral strain relationship at the shear span.

4.6. Ductility and Deformability

Ductility is a structural-design requirement in most design codes. The traditional definition of ductility for steel-reinforced concrete members, which considers the yielding of steel bars as a reference point, cannot be directly applied to members reinforced with FRP reinforcement due to the linear-elastic behavior of the FRP bars up to failure. Several methods have been proposed to calculate the ductility of FRP-RC structures. These methods can be divided into three categories depending on the approach used:

- Energy-based ductility index
- Deformability factor
- Curvature-based deformability index

4.6.1. Energy-Based Ductility Index

Naaman and Jeong (1995) defined ductility as the ratio of the total energy to the elastic energy and proposed the following equation to compute the ductility index, μ_e, which can be applied to steel- and FRP-RC members:

$$\mu_e = \frac{1}{2}\left(\frac{E_{tot}}{E_{el}} + 1\right) \tag{4.7}$$

where E_{tot} = the total energy computed as the area under the load–deflection curve, and E_{el} = the elastic energy released upon failure computed as the area of the triangle formed at failure load by the line having the weighted average slope of the two initial straight lines of the load–deflection curve, as shown in Fig. 4.15. Table 4.3 lists the computed μ_e for the hybrid CFRP/GFRP and steel specimens. The computed μ_e increased by 46.2% and 38.5% when the reinforcement ratio was increased by 50% and 125%, respectively. Considering the type of reinforcement, 12C15 showed a ductility index comparable (2.56% less) to 8S20, its steel-reinforced counterpart.

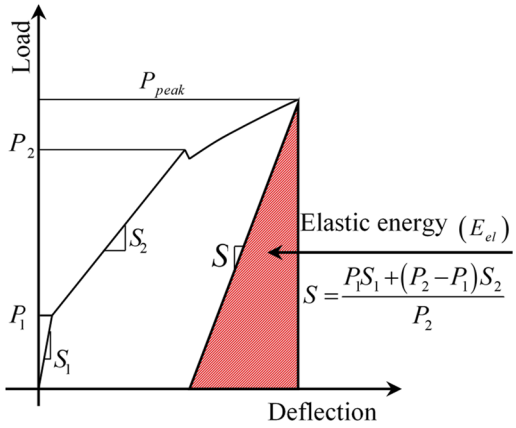

Figure 4.15 Ductility index definition.

4.6.2. Deformability Factor

The *Canadian Highway Bridge Design Code* (CAN/CSA S6-14) adopted the Jaeger et al. 1997 (J-factor) approach to evaluate the deformability index of FRP-RC members. In this approach, the absorbed energy is measured based on deformability rather than ductility to ensure adequate deformation of FRP-reinforced structures before failure. The deformability J-factor takes into account the strength effect as well as the curvature effect at service and ultimate conditions. The deformability J-factor can be calculated as follows:

$$J = \frac{M_{ultimate}}{M_c} \times \frac{\psi_{ultimate}}{\psi_c} \tag{4.8}$$

where ψ_c = curvature at a concrete strain equal to 0.001 (service condition); $\psi_{ultimate}$ = curvature at ultimate; M_c = moment at concrete strain equal to 0.001; $M_{ultimate}$ = ultimate moment. CSA S6-14 requires a J-factor exceeding 4 and 6 for rectangular sections and T-sections, respectively, with no recommendation for circular sections. A *J*-factor exceeding 6 might be recommended and used for circular sections—similar to that for T-sections—considering both as irregular nonrectangular sections. Table 4.3 reveals that all the test specimens demonstrated adequate deformability when compared with the CSA-S6-14 (2014) code limit of 6 (for nonrectangular sections). The higher the *J*-factor values, the more ample warning given by the FRP-RC specimen before failure. In other words, the *J*-factor indicates the amount of cracking and deflection that the FRP-reinforced concrete member will exhibit throughout the load history from service to ultimate conditions. Table 4.3 indicates that the *J*-factor of the test specimens ranged between 11 and 38. The higher value was for the specimen with a low reinforcement ratio (8C15) and the lower values were for specimens with higher reinforcement ratios (12C15 and 18C15).

4.6.3. Curvature-Based Deformability Index

Vijay and GangaRao (2001) defined the deformability factor as the ratio of energy absorption (area under the moment–curvature curve or area under the load–deflection curve) at ultimate, E_{tot}, to energy absorption at a limiting curvature value of $0.005/d$, $E_{\psi=0.005/d}$, which satisfies the serviceability criteria of both deflection and crack width as follows:

$$J_{VG} = \frac{E_{tot}}{E_{\psi=0.005/d}} \tag{4.9}$$

Table 4.3 gives the results of the curvature-based deformability factor, J_{VG}. The estimated J_{VG} values were 11, 6, and 3 for 8C15, 12C15, and 18C15, respectively. The tendency of these results agree well with the computed *J*-factor considering the effect of reinforcement ratio.

4.7. Analytical Model

This section presents an analytical model using a computer program to predict the flexural capacity of circular concrete members reinforced with CFRP bars. Applying the principles of

force equilibrium and strain compatibility provides the most direct approach for analyzing reinforced-concrete members subjected to bending moment. Circular members, however, are more complex to analyze than rectangular sections. The bars are usually disturbed in a circle at discrete points, making it difficult to calculate flexural capacity. In addition, the stresses, which are variable over the section depth, are also distributed over an area of variable width. The computer program is summarized in the following sections.

4.7.1. Proposed Computer Program

The computer program presented in this study was developed based on the principles of force equilibrium and strain compatibility in the circular cross section. The program is based on the following assumptions:

1. Strain in the concrete and the FRP reinforcement is proportional to the distance from the neutral axis (a plane section remains plane after deformation up to failure).
2. The maximum usable compressive strain in the concrete is assumed to be 0.0035.
3. The tensile strength of concrete is ignored.
4. The tensile behavior of the FRP reinforcement is linearly elastic until failure.
5. The strain in the FRP reinforcement, whether in tension or compression, is the same as that in the surrounding concrete (i.e., a perfect bond exists between the FRP reinforcement and concrete).
6. The distribution of concrete compressive stress can be described by the equivalent rectangular stress block shown in Fig. 4.16 with the parameters α_1 and β_1, as presented in Eqns. (4.4) and (4.5) satisfying the requirements of CSA S806-12.

4.7.1.1. Solution Procedure

Running the computer program begins with entering the circular-section diameter, material properties, and locations and areas of FRP bars. Then, a reasonable value of the neutral-axis depth, c, is assumed and entered in the program. The program starts by assuming that the failure is compression controlled as this mode of failure is more desirable in the case of the concrete members reinforced with CFRP bars. In relation to Fig. 4.16, for each layer of reinforcement,

the program computes the strain in tension and compression reinforcement, ε_{fi}, according to the meaning of strain compatibility with reference to ultimate concrete strain.

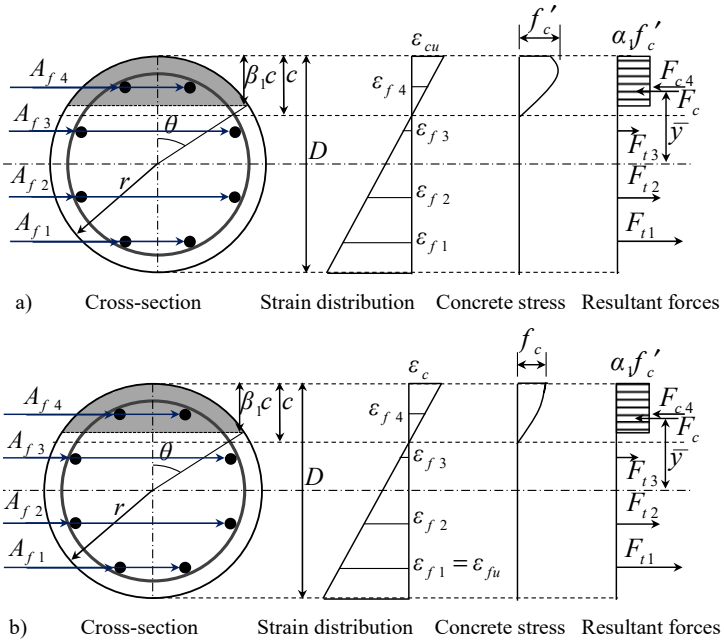

Figure 4.16 Idealized cross section and stress and strain distributions in the analytical model: a) Failure governed by concrete crushing, b) Failure governed by FRP rupture.

The program uses Eqns. 4.10 to 4.12 to calculate the compression force in concrete, F_c.

$$F_c = \alpha_1 f_c' r^2 \left(\theta - \sin\theta \cos\theta\right) \tag{4.10}$$

$$\bar{y} = \frac{2r}{3}\left(\frac{\sin^3\theta}{\theta - \sin\theta\cos\theta}\right) \tag{4.2}$$

$$\cos\theta = 1 - \frac{\beta_1 c}{r} \tag{4.3}$$

where f_c' = concrete cylinder strength and r = the radius of the circular cross section.

The tensile and compressive forces in CFRP bars are computed using Eqns. 4.13 and 4.14.

$$F_{tb} = \sum_{i=1}^{n_t} \varepsilon_{fi} E_f A_{fi} \tag{4.4}$$

$$F_{cb} = \sum_{i=1}^{n_c} \varepsilon_{fi} E_f A_{fi} \tag{4.5}$$

where F_{tb} = the tensile force in FRP bars; F_{cb} = the compressive force in FRP bars; E_f and A_{fi} = the modulus of elasticity and area for the row of FRP bars at the level i, respectively.

Lastly, the program checks for equilibrium considering or ignoring the contribution of FRP bars in compression by satisfying the condition that the absolute value of the sum of the total tensile and compressive forces is less than a certain allowable tolerance. If equilibrium is not satisfied, the program assumes another value for c and repeats the process until equilibrium is satisfied.

Once equilibrium has been satisfied, the computer checks for the strain in the extreme tension bars with reference to the ultimate bar strain. If the strains exceed the ultimate bar strain, then the failure is tension failure and the preceding procedure is repeated. In this case, the program computes the strain in tension and compression reinforcement, ε_{fi}, according to the meaning of strain compatibility with reference to ultimate tension-bar strain.

The failure moment, M_n is then calculated with Eq. 4.15 or Eq. 4.16 by taking the moment of the forces around the centroid of the circular cross section.

Case 1: Ignoring the contribution of FRP bars in compression

$$M_n = F_c \bar{y} + \sum_{i=1}^{n_t} \varepsilon_{fi} E_f A_{fi} y_{ti} \tag{4.6}$$

Case 2: Considering the contribution of FRP bars in compression

$$M_n = F_c \bar{y} + \sum_{i=1}^{n_c} \varepsilon_{fi} E_f A_{fi} y_{ci} + \sum_{i=1}^{n_t} \varepsilon_{fi} E_f A_{fi} y_{ti} \tag{4.7}$$

where y_{ti} = the distance between the center of i^{th} FRP bars on the tension side to the centroid of the concrete cross section; and y_{ci} = the distance between the center of i^{th} FRP bars on the compression side and the centroid of the concrete cross section. Figure 4.17 provides the program's flow chart.

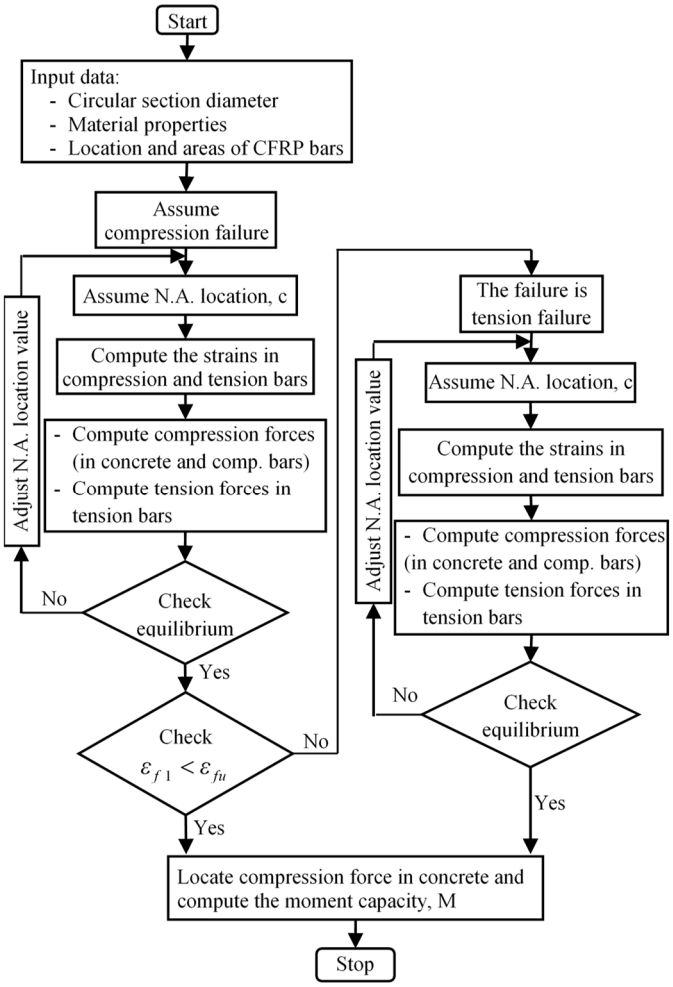

Figure 4.17 Flow chart of the computer program.

4.7.1.2. Comparison between the Theoretical and Experimental Results

The nominal flexural-moment capacity of the hybrid CFRP/GFRP specimens was compared to the computer program's predictions. In one scenario, the contribution of the CFRP longitudinal bars in the compressive block to the moment-carrying capacity was neglected by assuming an equivalent area of concrete and, in the second, the CFRP longitudinal bars in the compressive block were considered by assuming that the CFRP tensile and the compressive Young's moduli were equal. In all the analyses, the concrete density factor, material resistance factor, and member safety factor were taken as equal to unity. Table 4.3 presents the experimental-to-predicted ratios for the flexural capacities of the test specimens. The table indicates good predictions since the experimental-to-predicted ratios ranged from 0.96 to 1.19. The level of

conservatism and degree of accuracy depend on the assumptions of considering and ignoring the contribution of the CFRP bars in the compressive block. The table reveals that the CSA S806-12 design considerations provided accurate predictions when considering the bar contribution in compression. The average $M_{\text{exp.}} / M_{pred.}$ was 1.01 with a coefficient of variation of 5%. Neglecting the bar contribution in compression increased the level of conservatism of the predicted results. The average $M_{\text{exp.}} / M_{pred.}$ was 1.10 with a coefficient of variation of 11.6%.

4.7.2. Simple Model for Flexural Strength

The calculations of the flexural strength of circular concrete members reinforced with FRP bars can be simplified by the following assumptions:

1. The area of tension reinforcement, A_f, is the area of the FRP bars below the mid-depth of the section.

2. The effective depth, d, is taken as the distance from the extreme compression fiber to the centroid of the tension reinforcement (see Fig. 4.18) and can be calculated using Eq. 4.17 given in AASHTO LRFD Bridge Design Specifications (2012),

$$d = \frac{D}{2} + \frac{D_r}{\pi} \tag{4.17}$$

   where D_r = the diameter of the circle passing through the centers of the longitudinal reinforcement.

3. The compressive strength of FRP reinforcement shall be disregarded in the calculation of the flexural strength.

4. The reinforcement ratio and balanced reinforcement ratio can be computed from Eqns. 4.18 and 4.19, respectively.

$$\rho_f = \frac{A_f}{Dd} \tag{4.8}$$

$$\rho_{fb} = \alpha_1 \frac{f_c'}{f_{fb}} \frac{r^2 \left(\theta_b - sin\theta_b cos\theta_b\right)}{Dd} \tag{4.9}$$

$$\theta_b = cos^{-1}\left(1 - \frac{\beta_1 c_b}{r}\right) \tag{4.20}$$

$$c_b = \left(\frac{\varepsilon_{cu}}{\varepsilon_{cu} + \varepsilon_{fb}}\right) d \tag{4.21}$$

where f_{fb} , ε_{fb} = the average stress and strain in FRP tension reinforcement at the balanced condition, respectively.

When $\rho_f > \rho_{fb}$, the controlling limit state is the crushing of the concrete. Based on the equilibrium of forces and strain compatibility, shown in Fig. 4.18, the following can be derived:

$$M_n = A_f f_f \left(\bar{y} + \frac{D_r}{\pi}\right) \tag{4.10}$$

$$f_f = \alpha_1 \frac{f_c'}{A_f} r^2 \left(\theta - sin\theta cos\theta\right) \tag{4.11}$$

where f_f = the average stress in tension reinforcement; $\bar{y}$ = the distance between the centroid of the circular concrete segment on the compression side to the centroid of the concrete cross section and can be calculated using Eq. (4.11).

The value of the angle θ defining the compressive side of the cross section can be determined with regression analysis based on the factors affecting the equilibrium of forces. The value of θ can be determined using Eq. (4.24).

$$\theta = 1.67 \rho_{ft}^{0.18} \left(1.02 - 0.81\left(\frac{f_c'}{E_f \varepsilon_{cu}}\right)^{0.26}\right) \tag{4.24}$$

$$\rho_{ft} = \frac{A_{ft}}{A_g} \tag{4.25}$$

where the angle θ is expressed in radians; f_c' = the concrete cylinder strength in MPa; E_f = the modulus of elasticity of the FRP reinforcing bars in MPa; and ρ_{ft} = the ratio between the total reinforcement area and the gross area of the circular cross-section expressed in percentage (%).

When $\rho_f < \rho_{fb}$, the controlling limit state is rupture of the FRP reinforcement. A simplified, conservative calculation of the nominal flexural strength of the member can be based on Eq. 4.26, as suggested in ACI 440.1R-15.

$$M_n = A_f f_{fu}\left(\bar{y}_b + \frac{D_r}{\pi}\right) \tag{4.26}$$

where f_{fu} = the average stress in tension reinforcement when the strain in extreme tension bars reaches its maximum value; $\bar{y}_b$ = the distance between the centroid of the circular concrete segment on the compression side to the centroid of the concrete cross section at the balanced condition. Table 4.3 presents the experimental to predicted ratios of the flexural capacities of test specimens using the design procedures in the simple model. Only one scenario—neglecting the contribution of the longitudinal CFRP bars in the compressive block—was assumed to be equivalent to the concrete in estimating the failure moment. The proposed simplified model yields a reasonable conservative estimate of the flexural capacity as the average experimental flexural strength over the predicted value was 1.12 with a coefficient of variation of 8.3%.

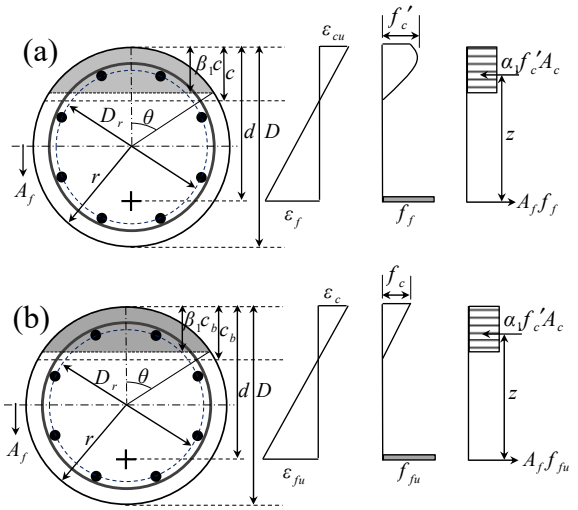

Figure 4.18 Simplified cross-section method and stress and strain distributions: a) Failure governed by concrete crushing, b) Failure governed by FRP rupture.

4.8. Conclusions

This paper reports on an experimental and analytical investigation of the flexural strength and behavior of circular concrete members reinforced with CFRP bars and GFRP spirals. Based on the experimental results and the analytical study presented in this paper, the following conclusions can be drawn:

1. The failure of the circular hybrid CFRP/GFRP-RC specimens occurred by concrete crushing, followed by rupture of tension bars in 8C15 and compressive failure of compression bars in 12C15 and 18C15. 8S20 failed as the result of steel yielding, followed by concrete crushing.

2. All the circular hybrid CFRP/GFRP-RC specimens behaved linearly until cracking and almost linearly between cracking and concrete crushing, with reduced slope.

3. The flexural strength at concrete crushing of CFRP-RC specimen was almost 3.3 times greater than that of its steel-reinforced counterpart with a similar reinforcement ratio.

4. The reinforcement ratio significantly affected the behavior of the circular hybrid CFRP/GFRP-RC specimens. As the reinforcement ratio increased, both the flexural stiffness and capacity increased. The flexural capacity at concrete crushing, however, was limited by concrete compressive strength and strain.

5. Based on the test results, the failure of the specimens reinforced with CFRP bars under flexural load is not triggered by bar rupture on the tension side and a minimum reinforcement ratio of 0.8 % might be reasonable for normal-strength concrete ($30 \leq f_c' \leq$ 60 MPa).

6. The maximum recorded compressive and tensile strains in the CFRP bars were –5,130 and 10,300 $\mu\varepsilon$, respectively, which means that the CFRP bars were effective in resisting compressive and tensile stresses.

7. The maximum recorded strains of GFRP spirals at the shear span were less than 15% of the ultimate strain of the GFRP, indicating the efficiency of using GFRP spirals as shear reinforcement in circular flexural CFRP-RC members.

8. The recorded concrete strains for all specimens were higher than the specified design limit in ACI440.1R-15 (–3,000 με) and CSA S806-12 (–3,500 με).

9. The neutral-axis depth before cracking was located at approximately the mid-height of the circular cross section and shifted towards the compression side just after cracking. Subsequently, its value remained constant and increased slightly at high load levels just before concrete crushing occurred.

10. Although all the circular hybrid CFRP/GFRP-RC specimens failed due to compressive failure, a high degree of deformability was attained before failure. In all cases, the calculated deformability factor was higher than 6, as recommended by CSA S6-14.

11. A deformability *J*-factor exceeding 6 is proposed and recommended to be used for CFRP-RC members with circular sections similar to that required in CSA S6 for nonrectangular sections (T-section).

12. The computer program proposed in this study is capable of predicting the flexural capacity of circular hybrid CFRP/GFRP-RC members. The accuracy of the computer program's results were in good agreement with the measured values. Moreover, the simplified method presented using noniterative procedures may be considered as simpler and more straightforward for design purposes.

CHAPTER 5. FLEXURAL BEHAVIOR OF FULL-SCALE CIRCULAR CONCRETE MEMBERS REINFORCED WITH BASALT FRP BARS AND SPIRALS: TESTS AND THEORETICAL STUDIES

Foreword

Authors and Affiliation:

- Salaheldin Mousa: Ph.D. candidate, Department of Civil Engineering, Université de Sherbrooke, Sherbrooke, Quebec, Canada, J1K 2R1.
- Hamdy M. Mohamed: Research Associate/Lecturer, Department of Civil Engineering, Université de Sherbrooke, Sherbrooke, Quebec, Canada, J1K 2R1.
- Brahim Benmokrane: Professor, Department of Civil Engineering, Université de Sherbrooke, Sherbrooke, Quebec, Canada, J1K 2R1.
- Emmanuel Ferrier: Professor, Director of the Laboratory of Composite Materials for Construction, University Lyon 1, IUT LYON 1, Villeurbanne Cedex, France.

Journal Title: *Composite Structures, Elsevier.*

Paper Status: Final version Published online.

Reference: Mousa, S., Mohamed, H. M., Benmokrane, B., and Ferrier, E. (2018) "Flexural Behavior of Full-Scale Circular Concrete Members Reinforced with Basalt FRP Bars and Spirals: Tests and Theoretical Studies." *Composite structures*, 203, 217-232.

Contribution in thesis

This chapter reports on the experimental results of flexural tests on full-scale circular RC members with BFRP bars and spirals, followed by an intensive analytical study and finite-element analysis. The main investigated parameters were the ratio and type of longitudinal reinforcement. An analytical model was developed using a layer-by-layer approach to estimate the flexural strength of the tested specimens. In addition, the finite-element model developed predicted the response of the tested specimens with a reasonable degree of accuracy and was used to extend the range of the investigated parameters

Abstract

This paper reports on the experimental results of flexural tests on full-scale circular reinforced concrete (RC) members with a total length of 6,000 mm and diameter of 500 mm reinforced with Basalt Fiber-Reinforced-Polymer (BFRP) reinforcement, followed by an intensive analytical study and finite-element analysis. The main investigated parameters were the ratio and type of longitudinal reinforcement. A steel-reinforced concrete specimen was fabricated as a reference. Test results show that the deformability of the tested circular BFRP-RC members significantly exceeded the limitations in North American codes. Moreover, the nominal flexural strength of one BFRP-RC specimen was almost two times that of its steel-reinforced counterpart with the same reinforcement ratio. The analytical model presented herein using a layer-by-layer analysis was capable of predicting the flexural strength of the circular BFRP-RC members. In addition, a non-iterative analysis method including simple design equations are presented. This method accurately and simply predicts the flexural capacity and can be considered a simple and more straightforward method for practicing engineers. Furthermore, the finite-element model developed predicted the response of the tested specimens with a reasonable degree of accuracy and was used to extend the range of the investigated parameters.

Keywords: Concrete; circular RC members; piles; BFRP bar; flexural strength; stress; strain; design equations; finite element analysis.

5.1. Introduction

The past two decades have yielded a great development of and innovation in fiber-reinforced-polymer (FRP) technology (Barris et al. 2009; Miàs et al. 2010; Sharbatdar et al. 2011; Kara and Ashour 2012; Matos et al. 2012; Miàs et al. 2013; Kara et al. 2015). Basalt FRP (BFRP) has been recently developed and received wide attention, in addition to the commonly used composites based on glass (GFRP) and carbon (CFRP) fibers. Basalt fibers are produced from basaltic rocks through melting processes. The basaltic rocks can be finely divided into small particles that can be made into continuous filaments of basalt fibers. Studies on the mechanical and durability characteristics of BFRP have shown an acceptable performance overall due to its cost effectiveness, freeze-thaw performance, high-temperature resistance, and ease of fabrication (Benmokrane et al. 2015; Elgabbas et al. 2015). Basalt fibers have higher tensile strength than the E-glass fibers, greater failure strain than the carbon fibers, and good resistance to chemical attack and impact load (Zhang et al. 2015).

BFRP does not appear in FRP material specifications (ACI 440.3R-12, CSA S807-10) or design guidelines and codes (ACI 440.1R-15, CSA S806-12, CSA S6-14, CNR DT 203/2006, and fib Bulletin 40 2007) as an alternative to other FRP materials due to the lack of experimental data. Recently, few studies have been carried out to investigate the structural response of BFRP-reinforced concrete (RC) members (Urbański et al. 2013; Tomlinson and Fam 2015; Gribniak et al. 2015; Ovitigala et al. 2016; Elgabbas et al. 2016a and b, 2017; Kara et al. 2017; Mahroug et al. 2014) as a step to including BFRP in design guidelines and codes. All the research studies for using FRP bars as flexural reinforcement in the literature is based on experimental work on rectangular concrete members (Barris et al. 2009; Miàs et al. 2010; Sharbatdar et al. 2011; Kara and Ashour 2012; Matos et al. 2012; Miàs et al. 2013; Kara et al. 2015; Kassem et al. 2011; El-Nemr et al. 2013; Jua et al. 2017; Maranan et al. 2018). Limited research has been carried out during the last decade on the flexural and shear behavior of circular GFRP-RC members (Hadi et al. 2016; Mohamed and Masmoudi 2010; Ali et al. 2016, 2017 a and b). In contrast, no research seems to have investigated RC members of circular cross section reinforced with BFRP bars under flexural loads. Moreover, there are practically no code provisions or guidelines for the flexural design of circular concrete members with FRP reinforcement. ACI 440.1R-15, however, points out that there is no evidence that the flexural theory—developed for rectangular

sections—applies equally well to nonrectangular sections; the behavior of such members has yet to be confirmed experimentally.

This study addressed the worst (critical) case when the flexural demand prevails over the axial load in columns, piles and piers. In addition, there are some applications for using a circular section, such as soft-eyes in tunnels and fender piles in marine structures that are usually subjected to pure bending moment without axial load. In general, the flexural capacity of rectangular members can be easily determined. In contrast to rectangular RC members, the bars in circular RC members are usually distributed in a circle at discrete points, giving rise to some difficulties in calculating the equilibrium of forces and strain compatibility. In addition, the stresses, which are variable over the section depth, are also distributed over an area of variable width. This fact leads to a very small part of the circular section exhibiting a maximum compression strain. On the other hand, the extreme tension reinforcement might reach the ultimate strain and stress, while the other layers of reinforcement have lower stresses, possibly equal to zero in proximity to the neutral axis. This produces a larger concrete compression zone and a smaller internal lever arm when compared to rectangular sections with equivalent dimensions. As a result of this behavior, smaller flexural capacities might be obtained in members with circular sections when compared to those with rectangular sections.

Developing analytical procedures for predicting the structural response of RC members has many benefits, as the experimental work is considered expensive and time-consuming (De Domenico et al. 2014; Bencardino et al. 2016). There are many nonlinear techniques to fully simulate the behavior of RC members up to failure, including numerical models and finite-element models. The finite-element model that can successfully handle reinforced-concrete members should be capable of including the nonlinear variation in the material properties of concrete as well as detecting both its cracking and crushing failure modes and the failure of FRP reinforcement. For this study, the commercially available finite-element package ANSYS was used because it has these capabilities.

5.2. Research on Concrete Members Reinforced with BFRP Bars

Few studies have been conducted to investigate the full structural behavior of concrete elements reinforced with BFRP. Urbański et al. (2013) investigated the flexural performance of concrete

beams reinforced with BFRP bars. The results showed that the BFRP-RC beams did not fail suddenly due to the transformation of the beams into a tie system because the flexural reinforcement did not rupture. The deflections of the BFRP-RC beams were higher than those of the counterpart steel-RC beam due to the lower modulus of elasticity of BFRP bars compared to that of steel bars. Tomlinson and Fam (2015) evaluated the flexural and shear performances of concrete beams reinforced with BFRP bars and stirrups. Their work showed that the ultimate capacities of the beams were directly related to the flexural-reinforcement ratio regardless of whether the failure mode was flexural or shear. On the other hand, load-deflection responses within the service-load range were not noticeably affected by the shear reinforcement type. In addition, ACI 440.1R-06 and CSA S806-12 were adequate for predicting the flexural strength of beams with BFRP flexural reinforcement. Gribniak et al. (2015) experimentally investigated the deformation and cracking behavior of four concrete beams reinforced with BFRP bars and strengthened with BFRP sheets. The tested beams were preloaded until failure, then strengthened with the polymer sheets and tested again. The structural stiffness as well as the load-bearing capacity before and after strengthening were assessed. The author concluded that, due to the high elasticity and high strength of the BFRP materials, the polymer reinforcement did not experience bond failure. This allows for assessing beam deformation behavior without considering the bond–slip effects. Ovitigala et al. (2016) tested up to failure eight over-reinforced concrete beams reinforced with BFRP. The beams failed by concrete crushing; it was concluded that the desired deflection at service can be achieved by increasing the BFRP reinforcement. The strain-compatibility equation per ACI 440.1R-06 was conservative in predicting the ultimate flexural strain in the BFRP bars and the ultimate-moment capacity. Elgabbas et al. (2016a) investigated the performance of six full-scale edge-restrained concrete bridge-deck slabs reinforced with BFRP bars. The deck slabs measured 3,000 mm long × 2,500 mm wide × 200 mm thick. The slabs were tested up to failure under a single concentrated load acting on the center of each slab. The authors compared their findings to two slabs with the same dimensions reinforced with GFRP and CFRP bars and tested according to the same loading procedure by El-Gamal et al. (2005). The three slabs reinforced with GFRP, CFRP, and BFRP, which had the same axial-reinforcement stiffness, evidenced almost the same punching shear capacities and also displayed the same load–strain relationships up to failure. In addition, the authors concluded that the current punching shear provisions in CSA S806-12 provided

reasonable yet conservative predictions for the punching shear capacity of their BFRP-RC deck slabs. On the other hand, ACI 440.1R-06 underestimated the punching shear strength of the tested slabs. Elgabbas et al. (2016b, 2017) conducted experimental investigations on concrete beams reinforced with sand-coated and ribbed BFRP bars. The authors observed that their tested beams reinforced with sand-coated and ribbed BFRP bars behaved in a manner similar to those reinforced with GFRP and CFRP bars tested by Kassem et al. (2011) and El-Nemr at al. (2013). The results show comparable flexural behavior in terms of failure modes, strain values, cracking patterns, and curvatures. On the other hand, the authors found that ACI 440.1R-06 and ACI 440.1R-15 underestimated the deflection of the beams reinforced with BFRP bars, while CSA S806-12 provided reasonable yet conservative deflection values. Kara et al. (2017) conducted experimental tests on simply and continuously supported concrete slabs reinforced with BFRP bars. All the continuous BFRP reinforced-concrete slabs exhibited a combined shear-flexure failure mode. The authors concluded that the ACI 440.1R-15 equations yielded reasonable predictions for the deflection of continuous slabs (after first cracking) but stiffer behavior for the simply supported slabs.

In light of the preceding discussion, research is needed into the behavior of circular concrete members reinforced with BFRP bars. The extrapolation of test results and design equations proposed for designing rectangular BFRP-reinforced concrete sections should be verified for circular members. The experimental study reported here is part of an ongoing comprehensive research program at the University of Sherbrooke in which full-scale circular concrete members are tested to investigate different variables and design parameters. The variables include loading type (pure compression (Afifi et al. 2014a), axial combined bending (Hadhood et al. 2017 a and b), shear (Ali et al. 2016, 2017 a and b), and flexure (current study)); reinforcement type (glass-, carbon-, and basalt-FRP bars); and amount of FRP longitudinal reinforcement.

5.2.1. Research Objectives

This study aimed at providing basic technical information and yielding better understanding of the flexural behavior of circular BFRPRC members. A number of research objectives were identified and are listed below.

- To experimentally examine the feasibility and efficiency of using BFRP reinforcement in circular RC members under flexural load.
- To investigate the effect of the BFRP reinforcement ratio on flexural strength and behavior.
- To discover the failure mechanisms of such members under flexural loads.
- To propose simple and accurate design procedures for predicting flexural strength.
- To develop a reliable analytical 3-D model using nonlinear finite-element analysis to predict the behavior and load-carrying capacity of circular BFRPRC members.

5.3. Experimental Program

5.3.1. Test Matrix and Parameters

A total of three full-scale circular RC specimens—including two reinforced totally with BFRP bars and spirals, and one with steel reinforcement as a reference—were prepared and tested. The tested specimens were 500 mm in diameter and 6,000 mm in length. Figure 5.1 shows the dimensions, various configurations, and reinforcement details of the tested specimens. The clear span was equal to 4,950 mm and the specimens were loaded by two equal forces 2,100 mm from support. Therefore, bending was constant in the central zone of 750 mm. All the specimens had a 525 mm overhang beyond the supports on each side as anchorage length. The specimens were designed to have a dominant flexural behavior, reducing the shear influence by choosing a shear span-to-depth ratio of more than five (Kani 1964). The test matrix was arranged to assess the influence of reinforcement type (BFRP versus steel) and longitudinal-reinforcement ratio. Table 5.1 provides the test matrix, dimensions, and reinforcement details of the specimens. Each specimen is identified with a tripartite code. The first number refers to the number of longitudinal bars. The letters S and B identify specimens as being reinforced totally with steel or BFRP reinforcement, respectively. The second number indicates the nominal diameter of the longitudinal bars. Two different amounts of longitudinal reinforcement were used to reinforce the BFRP specimens (8 and 16 No. 20 mm (#6) BFRP bars for specimens 8B20 and 16B20,

respectively, with a reinforcement ratio of 1.2% and 2.3%) and were reinforced transversally with 12.7 mm (#4) BFRP spirals at a spacing of 125 mm. The control steel specimen was reinforced longitudinally with 8 M20 steel bars with a reinforcement ratio of 1.2% and transversely with M10 steel spirals spaced at 125 mm.

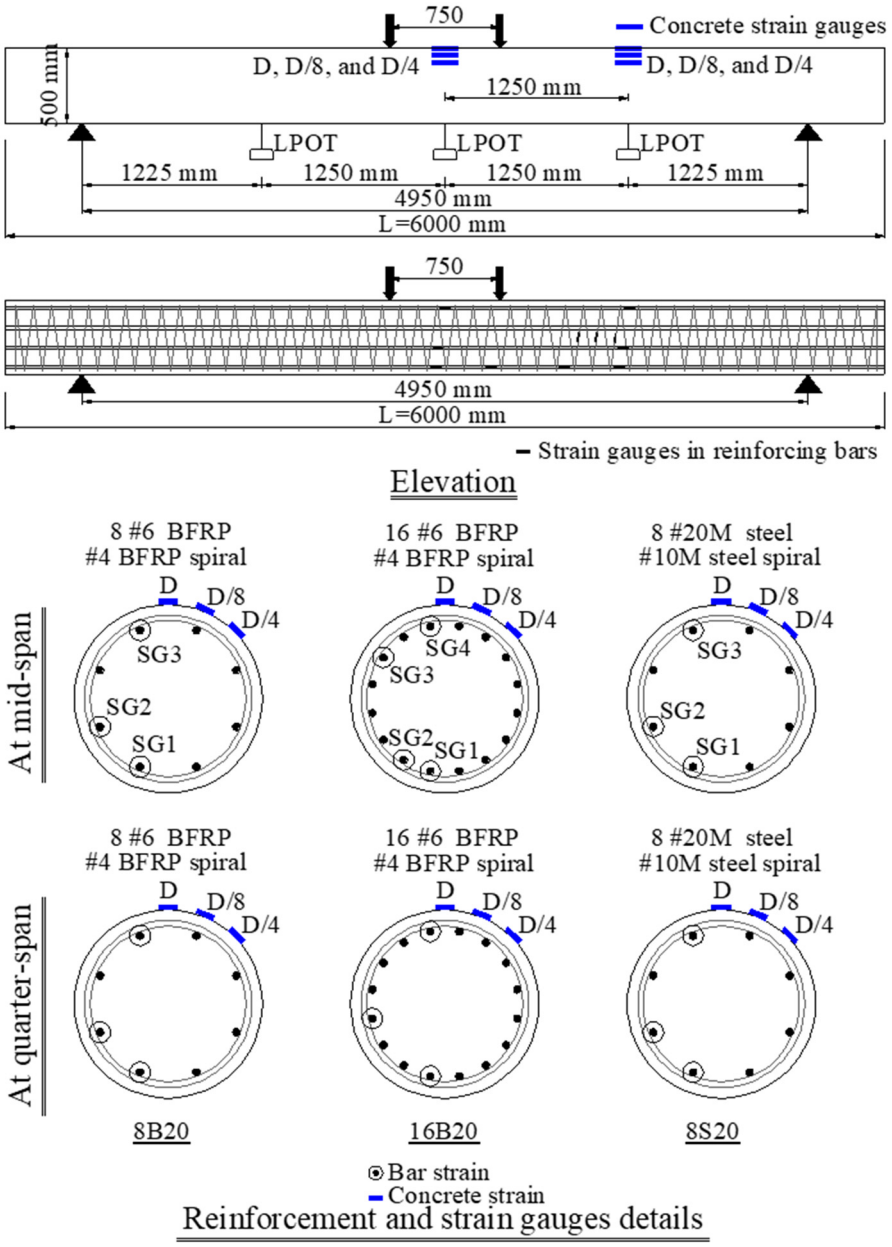

Figure 5.1 Dimensions and reinforcement details of the specimens (dimensions in mm).

Table 5.1 Test matrix and details of the specimens.

Specimen ID	Reinforcement type	Longitudinal reinforcement		Transversal reinforcement
		ρ_{ft} (%)	Number of bars	
8B20	Basalt FRP	1.2	BFRP bars (8 #20 mm)	BFRP spiral # 4 @125
16B20	Basalt FRP	2.3	BFRP bars (16 #20 mm)	BFRP spiral # 4 @125
8S20	Steel	1.2	Steel bars (8 #20 M)	Steel spiral 10 M @125

5.3.2. Material Properties

The specimens were made with normal-weight ready-mix concrete with a specified 28-day concrete strength of 40 MPa. The development of concrete strength was monitored by testing groups of cylinders at 7 and 28 days from casting. The actual concrete compressive strength at the time of testing was 41.43±1.5 MPa and was based on test results of six 100 x 200 mm concrete cylinders. An average concrete tensile strength of 3.5±0.3 MPa was obtained by performing split-cylinder tests. Sand-coated #6 BFRP bars and #4 BFRP spirals were used to reinforce the BFRP specimens in the longitudinal and transversal directions, respectively, as shown in Fig. 5.2(a). The BFRP bars and spirals were manufactured by the pultrusion process with a fiber content of 81% (by weight) in a vinyl-ester resin. The ultimate tensile strength, f_{fu}, and modulus of elasticity, E_f, of the longitudinal BFRP bars (#6) and the straight portion of the bent BFRP bars (#4) were determined according to ASTM D7205 (2011), as reported by the manufacturer (Table 5.2). The test results yielded an average ultimate tensile strength and modulus of elasticity of 1,646±40 MPa and 63.7±0.8 GPa for the BFRP bars, and 1,414±11 MPa and 51.4±0.2 GPa for the BFRP spirals. Two steel bar diameters were used in this study to reinforce the control specimen. Deformed No. 20M steel bars were used as longitudinal reinforcement and deformed No. 10M steel bars were used as spirals. Table 5.2 provides the mechanical properties of the steel bars.

5.3.3. Test-Specimen Fabrication

BFRP and steel cages were assembled for the various configurations. The clear concrete cover was kept constant at 38 mm. The specimens were prepared for casting in very stiff Sonotubes with wooden plugs to seal the ends. The Sonotubes were inclined at 25°, as shown in Fig. 5.2(b). The concrete used to cast the specimens was batched and delivered by a local ready-mix concrete supplier. The concrete was then pumped through a rubber pumping hose inserted into the Sonotubes (at least 5.0 m) to prevent segregation.

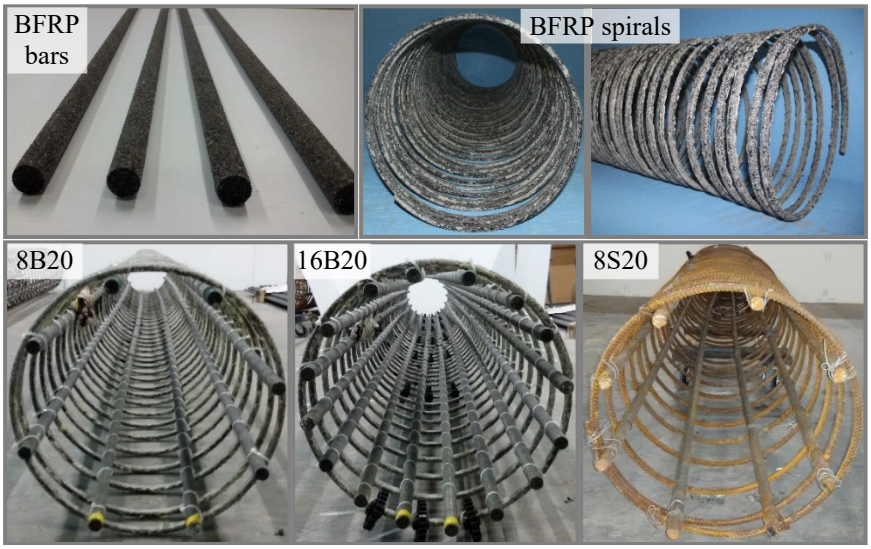

(a)

(b)

Figure 5.2 a) BFRP bars, spirals, and BFRP and steel cages; b) Specimen fabrication.

Table 5.2 Mechanical properties of the BFRP and steel reinforcement.

RFT Type	d_b (mm)	A_f [a] (mm²)	A_{im} [d] (mm²)	E_f (GPa)	f_{fu} (MPa)	ε_{fu} (%)
BFRP	13	129	139±0.80	51.4±0.20	1414 [b] ±11	2.70±0.2
	20	285	346±2.2	63.7±0.80	1646±40	2.50±0.1
Steel	10M	100	---	E_s = 200.0	f_y [c] = 480	ε_y [c] = 0.24
	20M	300	---	E_s = 200.0	f_y [c] = 460	ε_y = 0.23

[a] Nominal cross-sectional area.
[b] Tensile strength of straight bar.
[c] f_y and ε_y are the yield strength and strain of the steel bars, respectively.
[d] Immersed cross-sectional area (measured).
Note: properties calculated based on the nominal cross-sectional area.

5.3.4. Test Setup and Instrumentation

The test setup was designed and fabricated at the University of Sherbrooke's Canada Foundation for Innovation (CFI) structural laboratory. Steel saddles were designed to accommodate the circular geometry at loading and support points. The specimens were subjected to four-point bending load, as shown in Fig. 5.3, using an MTS servo-controlled, hydraulic 1,000 kN actuator attached to a spreader beam. The load was applied at a displacement-controlled rate of 0.5 mm/min. Strains in the longitudinal reinforcing bars and spirals were measured using electrical resistance strain gauges with gauge lengths of 10 mm. In addition, nine strain gauges with a gauge length of 60 mm were mounted on the concrete top surface at four different levels (D, D/8, and D/4) at mid-span and at quarter span to measure concrete compressive strains (see Fig. 5.1). Specimen deflection was measured with three linear potentiometers (LPOTs) placed at mid-span and quarter span. An automatic data-acquisition system monitored by a computer was used to record the readings of the LPOTs, load cells, and strain gauges.

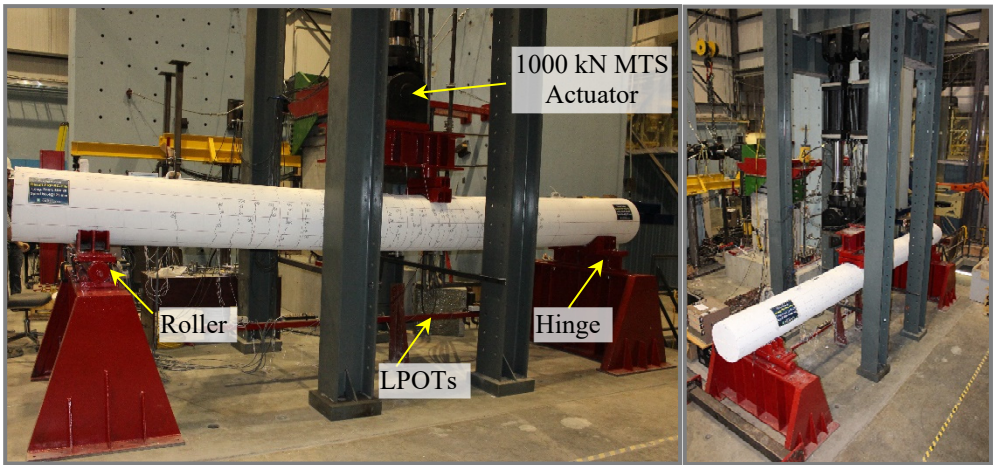

(a) Experimental photo

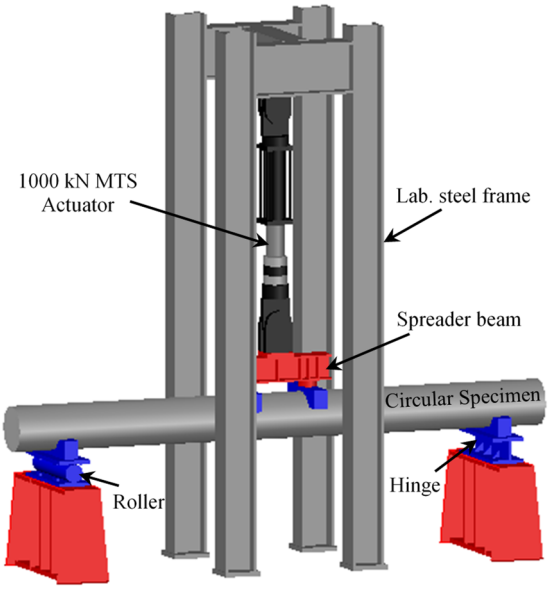

(b) 3-D sketch

Figure 5.3 Overview of the test setup.

5.4. Test Results and Observations

5.4.1. Failure Modes and Cracking Pattern

Table 5.3 summarizes the observed failure modes of the tested specimens. As presented in Fig. 5.4, 8B20 and 16B20 failed in flexure due to concrete crushing in the compression side of the mid-span. ACI 440.1R-15 and CSA S806-12 recommend this mode of failure for any concrete member reinforced with FRP bars, since it is more gradual, less brittle, and less catastrophic with higher deformability compared to the tensile rupture of FRP bars. Hadi et al. (2016)

reported a similar mode of failure for one circular specimen reinforced with GFRP bars and tested under four-point bending load. On the other hand, Fig. 5.4 shows that 8S20 also failed in flexure due to steel yielding, followed by concrete crushing. Figure 5.5 provides the cracking patterns at failure for all the specimens. During testing, the first crack in all the specimens was consistently a vertical flexural crack at the constant-moment zone between the two loading points. The corresponding cracking load was recorded and verified with the moment–strain and moment–deflection relationships. The cracking moment, M_{cr}, ranged between 24.4 kN.m and 31.7 kN.m. Beyond the first cracking load of the BFRP specimens, additional flexural cracks developed within the constant-moment zone. With further loading, new cracks continued to form at the shear span while existing ones propagated vertically toward the compression zone. Barris et al. (2009) and Kassem et al. (2011) reported similar cracking patterns on rectangular beams reinforced with GFRP and CFRP bars. Since the BFRP specimens had adequate shear reinforcement, the failure was typically initiated by flexural compression failure at mid-span. The failure moment, M_n, was 249 kN.m and 365 kN.m for 8B20 and 16B20, respectively. After concrete crushing, the BFRP specimens continued to carry additional loads until the rupture of BFRP bars in compression. The peak moment, M_{peak}, was 284 kN.m and 418 kN.m for 8B20 and 16B20, respectively. On the other hand, the early yielding of steel bars in 8S20 prior to concrete crushing resulted in wider and concentrated cracks in the constant-moment zone. The failure and peak moments for 8S20 were 134 kN.m and 237 kN.m, respectively. Both BFRP specimens recovered most of their deflection during the unloading at the end of the test, while permanent deflection was observed in 8S20 during the unloading process.

Table 5.3 Experimental moments, mode of failure, curvature, and deformability of the specimens.

Specimen ID	M_{cr} (kN.m)	M_n (kN.m)	M_{peak} (kN.m)	Failure mode[a]	Curvature ψ, $1/d$[c] at M_n	Deformability *J*-factor	Strain in reinforcement $\varepsilon_{exp.}$ at M_n ($\mu\varepsilon$)				$\varepsilon_{exp.}/\varepsilon_{pred.}$ Layered approach (Non-iterative method)				$M_{exp.}/M_{pred.}$ M_n		
							SG1	SG2	SG3	SG4	SG1	SG2	SG3	SG4	Layered approach (consider comp. bars)	Layered approach (Ignore comp. bars)	Non-iterative method
8B20	24.4	249	284	C.C.	0.0154	18	+13,200	+9,570	-1,650	-	1.09 (1.12)	1.13 (1.18)	1.18	-	1.00	1.03	1.09
16B20	31.7	365	418	C.C.	0.0131	15	+9,670	+9,480	-660	-2,900	1.19 (1.10)	1.18 (1.19)	1.15	1.18	1.02	1.08	1.18
8S20[b]	29.9	134	237	S.Y.	0.0022	-	+2,300	+1,560	-500	-	-	-	-	-	-	-	-
Average															1.01	1.05	1.13
COV (%)															1.4	3.4	5.6

[a] C.C. = concrete crushing, S.Y. = steel yielding.

[b] Values calculated at $M_n = M_y$, and M_{peak} = maximum moment at concrete crushing.

[c] The effective depth, d , calculated using Eq. 5.6.

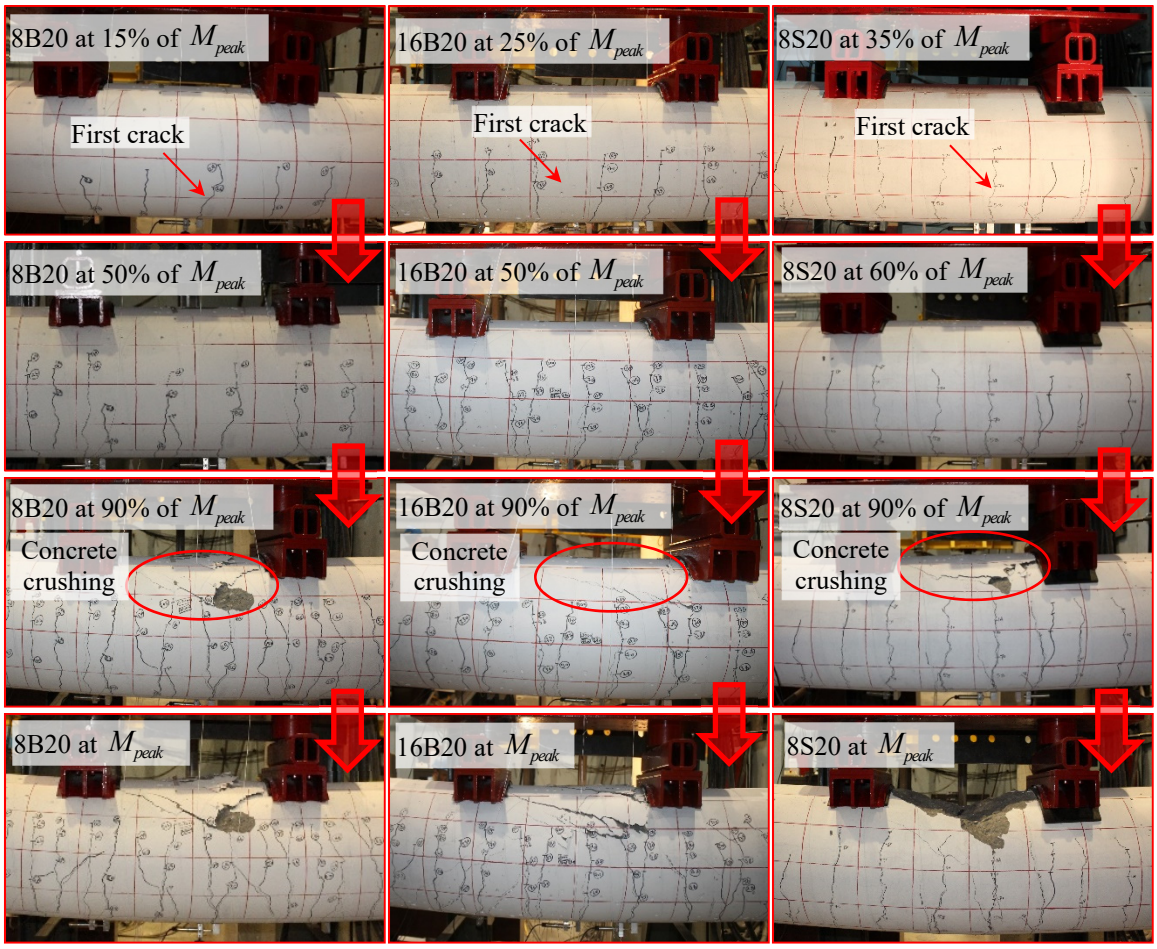

Figure 5.4 Failure sequence of the BFRP- and steel-reinforced specimens.

5.4.2. Flexural Behavior of the Specimens

The experimental moment–deflection relationships at mid-span and quarter span for the specimens are presented in two groups to show the influence of test parameters on the flexural behavior (see Figs. 5.6 and 5.7). While the moment–deflection relationship of all the specimens was bilinear (pre- and post-cracking behavior) up to failure, a post-failure behavior either after concrete softening due to crushing in 8B20 and 16B20 or yielding of steel in 8S20 was also observed. Table 3 provides the curvature of the specimens at failure as a function of 1/*d*. The curvature was 0.015/*d* and 0.013/*d* for 8B20 and 16B20, respectively. These curvature values are in agreement with the range of the test results (0.008/*d* to 0.015/*d*) obtained by Kassem et al. (2011) and El-Nemr et al. (2013) for rectangular beams reinforced with GFRP and CFRP

bars. Table 5.3 also presents the deformability of the BFRP-RC specimens. The *Canadian Highway Bridge Design Code* (CAN/CSA S6-14) approach (*J*-factor) was used to evaluate the deformability index. The *J*-factor takes into account the strength effect as well as the curvature effect at service and ultimate conditions. The *J*-factor can be calculated as follows:

$$J = \frac{M_{ultimate}}{M_c} \times \frac{\psi_{ultimate}}{\psi_c} \tag{5.1}$$

where ψ_c = curvature at a concrete strain equal to 0.001 (service condition); $\psi_{ultimate}$ = curvature at ultimate; M_c = moment at concrete strain equal to 0.001; and $M_{ultimate}$ = ultimate moment.

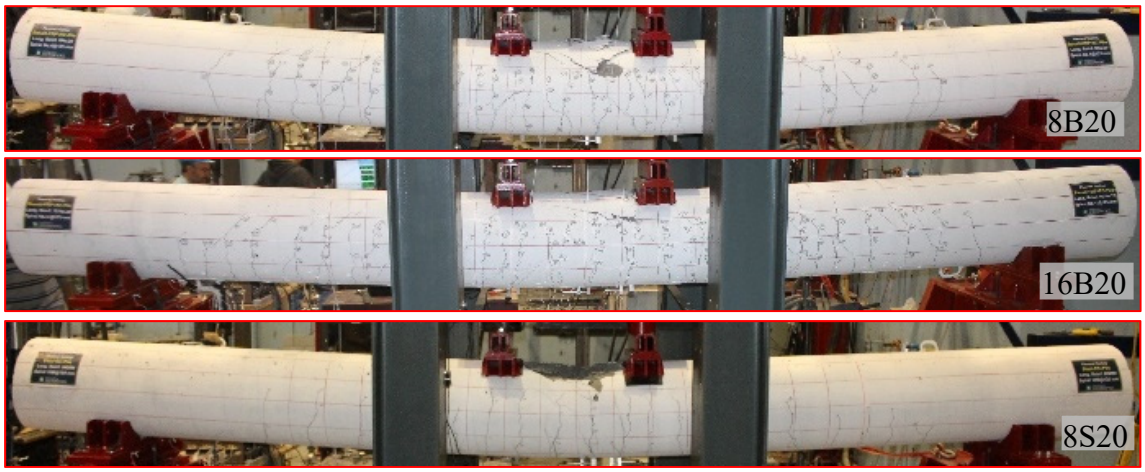

(a) Before releasing the load

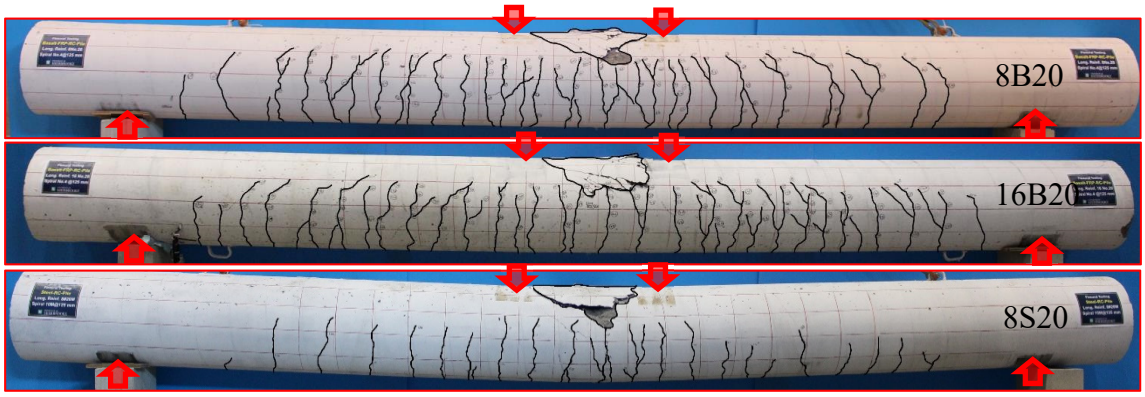

(b) After releasing the load

Figure 5.5 Cracking pattern of the specimens at failure.

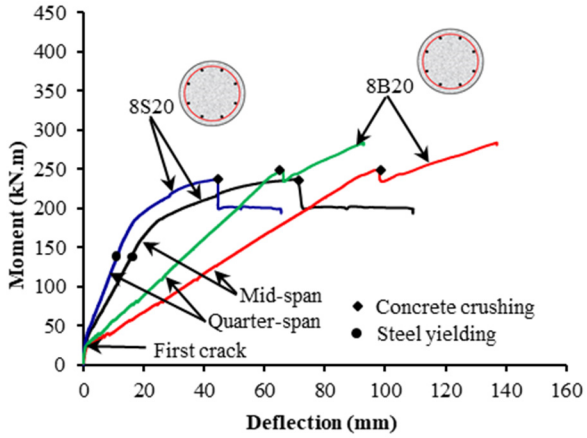

Figure 5.6 Influence of reinforcement type on the moment–deflection relationship.

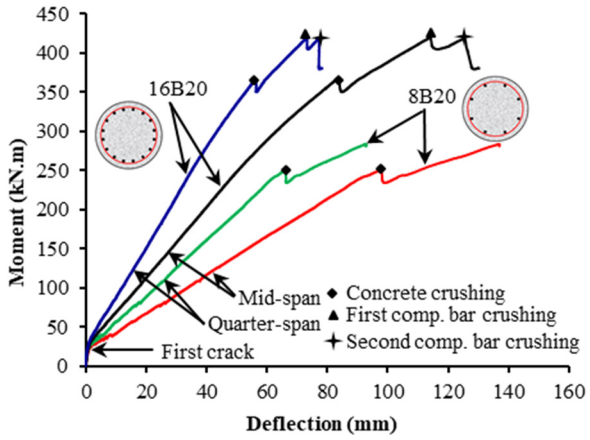

Figure 5.7 Influence of reinforcement type on the moment–deflection relationship.

Table 5.4 presents a comparison of the normalized flexural capacity $\left(M_n / f_c^{'} bd^2\right)$ of the tested circular specimens and rectangular beams reinforced with different types of FRP bars (GFRP, CFRP, and BFRP) collected from past studies (Barris et al. 2009; Elgabbas et al. 2016b; Kassem et al. 2011; El-Nemr et al. 2013). The rectangular beams were reinforced with sand-coated FRP bars; all the beams failed due to concrete crushing in the compression zone. Generally, the normalized flexural capacity of the tested circular specimens was lower than that of rectangular beams, mainly due to the bars in the tested circular specimens being distributed in a circle at discrete points, which resulted in a smaller internal lever arm compared to rectangular sections.

Consequently, smaller normalized flexural capacities were obtained in the members with circular sections in comparison to those with rectangular sections.

Table 5.4 Normalized flexural capacity of the tested BFRP-RC specimens and the FRP-RC rectangular beams obtained from past studies.

Reference	Specimen ID	Reinforcement type	ρ_f (%)	$\frac{M_n}{f_c' b d^2}$ (%)
Current study	8B20	BFRP	0.6[a]	8.8[b]
	16B20	BFRP	1.15[a]	12.9[b]
Elgabbas et al. (2016b)	B-2#16mm	BFRP	0.77	12.7
	B-4#16mm	BFRP	1.54	17.6
Kassem et al. (2011)	C1-4	CFRP	0.6	13.6
	G1-6	GFRP	1.6	18.4
El-Nemr et al. (2013)	N3#13G1	GFRP	0.56	10.3
	N5#15-G2	GFRP	1.52	21.8
Barris et al. (2009)	C-212-D1	GFRP	0.99	16.9
	C-212-D2	GFRP	0.99	21.1

[a] The BFRP bars below the mid-depth of the section were considered in the calculation of ρ_f.

[b] The section width taken as the diameter, D, and the effective depth, d, calculated using Eq. 5.6.

5.4.3. Strains in Concrete

Figures 5.8 and 5.9 provide the measured compressive concrete strains at mid-span and quarter span at three different levels from the top of the circular cross section (D, D/8, and D/4), respectively. Figure 5.8 indicates that, before cracking occurred, the concrete strains were insignificant in all the tested specimens. After cracking, the strains increased almost linearly up to concrete crushing in 8B20 and 16B20, while 8S20 showed a yielding plateau after the steel reinforcing bars had yielded. The maximum recorded compressive strains at mid-span were –3,600, –4,300, and –5,000 $\mu\varepsilon$ for 8B20, 16B20, and 8S20, respectively. The recorded strains were higher than the specified limit for design by ACI440.1R-15 (–3,000 $\mu\varepsilon$) and CSA S806-12 (–3,500 $\mu\varepsilon$). Barris et al. (2009) reported a maximum compressive strain in the range of –4000 to –5000 $\mu\varepsilon$ for rectangular concrete beams reinforced with GFRP bars, which is in agreement with the measured results. On the other hand, the recorded concrete strains at level D/8 and D/4 were less than that at level D. This indicates that the maximum strain was reached at the top surface of the circular cross section. The values of the concrete compressive strain at

quarter span were less than the values at mid-span, reaching a maximum strain of –1,600, –2,200, and –1,060 με at the top surface of the circular cross section in 8B20, 16B20, and 8S20, respectively, as shown in Fig. 5.9. In contrast, the strain values at levels D/8 and D/4 at quarter span were insignificant, reaching no more than –1,700 με.

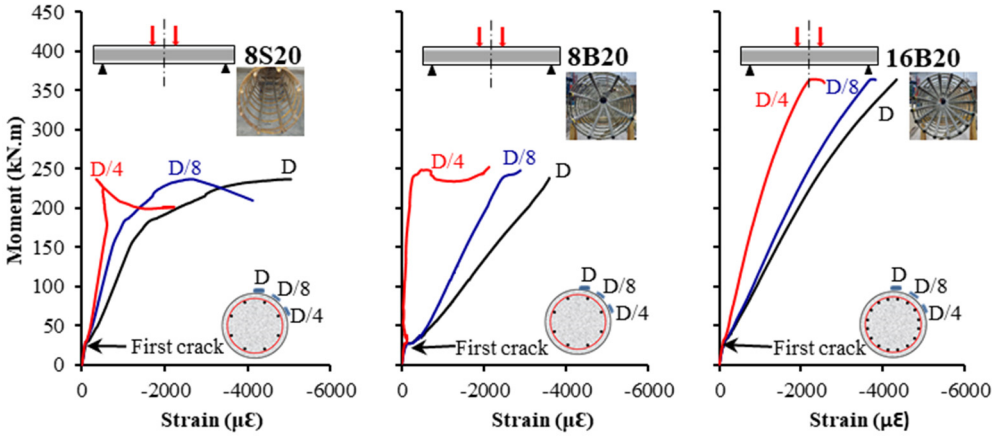

Figure 5.8 Moment–concrete-strain relationship at mid-span.

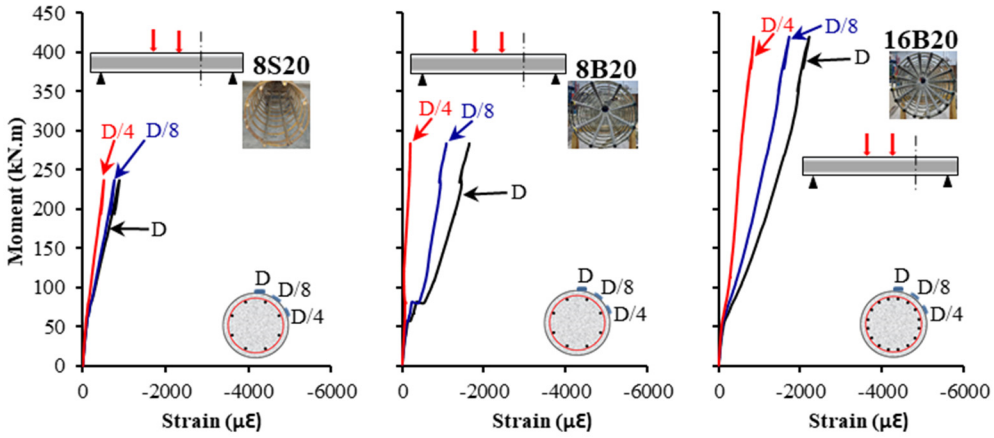

Figure 5.9 Moment–concrete-strain relationship at quarter span.

5.4.4. Strains in Longitudinal and Transverse Reinforcement

Figures 5.10 and 5.11, respectively, show the moment–strain behavior in the longitudinal bars and transverse spirals. As shown in Fig. 5.10, the tensile-strain-gauge readings for the BFRP and steel reinforcing bars were minimal before the initiation of the first flexural crack. After cracking occurred, a significant increase in tensile strains was observed in all three specimens. The BFRP specimens showed progressively increasing strain up to concrete crushing (failure

moment) with tensile strain values of 13,200 and 9,670 με (53% and 39% of the ultimate tensile strain in the BFRP bars) for 8B20 and 16B20, respectively. After concrete crushing, the moment values dropped, and the strain gauges continued to read more values up to peak moment. The maximum recorded tensile strains in the BFRP bars were 16,100 and 12,840 με (64% and 51% of the ultimate tensile strain in the BFRP bars) for 8B20 and 16B20, respectively. In contrast, 8S20 yielded (a corresponding strain of approximately 2,300 με) at an applied moment of 134 kN.m (approximately at 56% of the specimen's maximum moment). The steel reinforcement then exhibited a yielding plateau, followed by a rapid increase in the strain values up to failure, reaching a maximum strain of 16,200 με. The recorded compressive strains for the BFRP and steel reinforcing bars were low compared to the tensile strains at the same moment up to failure, as shown in Fig. 5.10. The values of compressive strains just before failure either due to concrete crushing or steel yielding were –1,650, –2,900, and –500 με for 8B20, 16B20, and 8S20, respectively. The maximum measured compressive strains before the damage to the strain gauges were –5,850, –5,700, and –3,700 με for 8B20, 16B20, and 8S20, respectively. In the case of transverse reinforcement, the maximum measured spiral strains in the shear span at failure were 1,350, 600, and 1,400 με for 8B20, 16B20, and 8S20, respectively (see Fig. 5.11). These values, respectively, are 5% and 2.1% of the ultimate strain of the BFRP spirals and 60% of the steel yield strain.

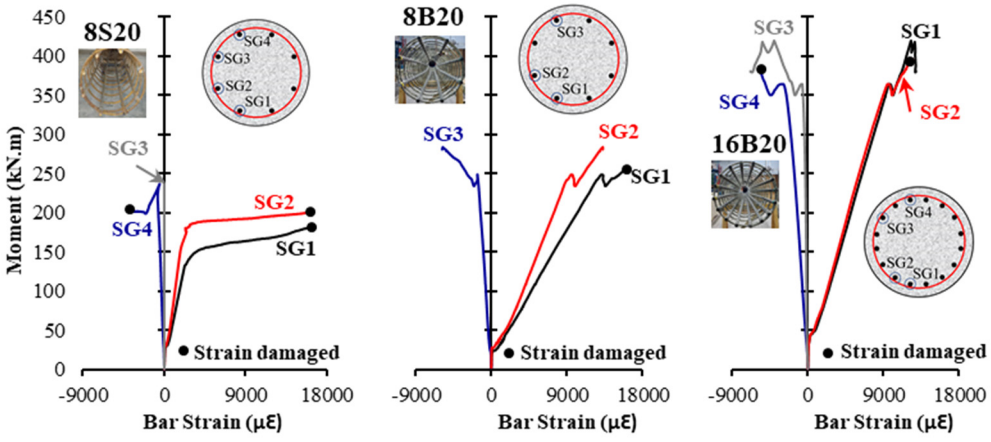

Figure 5.10 Moment–bar strain relationship at mid-span.

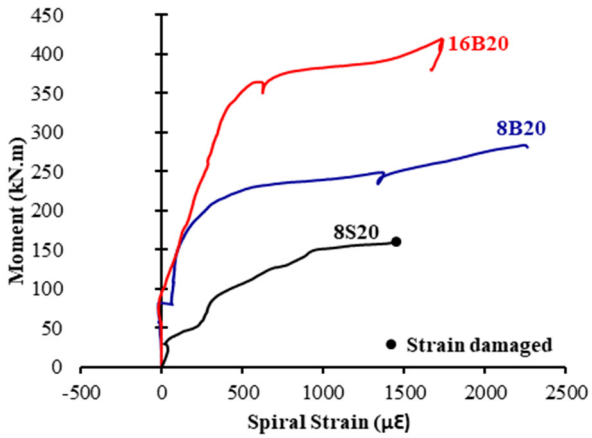

Figure 5.11 Moment–spiral strain relationship at shear span.

5.4.5. Variation in Neutral-Axis Depth

Figure 5.12 illustrates the relationship between the neutral-axis depth at the mid-span with the applied moment. The experimental position of the neutral axis was deduced from the measured strains in the concrete and longitudinal bars. The position of the neutral axis in a section prior to cracking remained unchanged at the geometrical centroid of the circular cross section. After cracking occurred, the neutral-axis depth rapidly decreased initially and then tended to stabilize. The stabilizing behavior continued up to concrete crushing in the BFRP-RC specimens. In contrast, the yielding of the tensile steel lead to a quick decrease in the neutral-axis depth in 8S20. Furthermore, Fig. 5.12 shows that the neutral-axis depth of 8B20 is less than that of 8S20 with a similar reinforcement ratio. This could be attributed to the steel bars having a higher modulus of elasticity than the BFRP bars. Moreover, the neutral-axis depth increased as did the reinforcement ratio in the BFRP-RC specimens. The neutral-axis depth was approximately 30% greater in 16B20 than in 8B20. This result may be explained by the fact that the equilibrium of forces requires a larger compression block for the greater forces arising from larger areas of reinforcement.

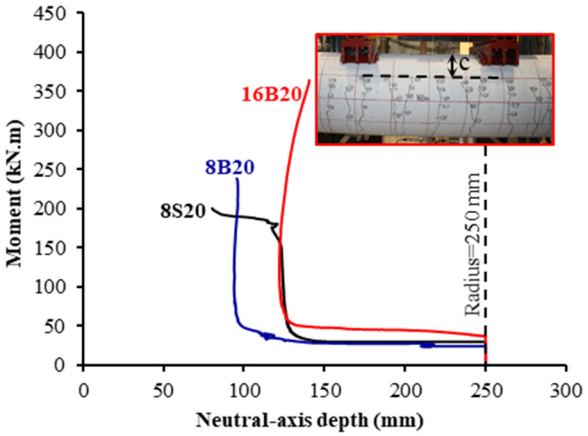

Figure 5.12 Neutral-axis depth.

5.5. Discussion

5.5.1. Influence of Longitudinal-Reinforcement Type

8B20 and 8S20 were designed to have the same longitudinal-reinforcement ratio. Before first flexural crack occurred, the two specimens behaved similarly to the uncracked section using the gross moment of inertia of the concrete cross section, as shown in Fig. 5.6. After cracking occurred, the flexural stiffness for the specimen reinforced with BFRP bars (8B20) was lower than that of the one reinforced with steel (8S20). This result reflects the effect of the reinforcing-bar modulus of elasticity on the post-cracking flexural stiffness. The average ratio between the post-cracking flexural stiffness of 8S20 to 8B20 was approximately 3.45. This ratio was similar to the ratio of the axial stiffness of the steel bars to that of the BFRP bars (3.30). This is in good agreement with the results of Ali et al. (2016) for circular members reinforced with GFRP and CFRP bars. Consequently, it can be concluded that specimen flexural stiffness was a function of the reinforcing-bar axial stiffness, which is a function of the area and modulus of elasticity of the longitudinal reinforcement. In contrast, the flexural capacity 8B20 at failure was 1.9 times that of 8S20. while the deflection levels on failure of 8B20 were larger than those of 8S20.

5.5.2. Influence of the Reinforcement Ratio

Increasing the amount of the longitudinal reinforcement enhanced the performance of the BFRP specimens. Figure 5.7 shows an increase in flexural capacity and reduction in deflection for an

increase in longitudinal reinforcement. In addition, the flexural stiffness significantly increased with a higher reinforcement ratio. Increasing the reinforcement ratio from 1.2% to 2.3% in the BFRP specimens (8B20 and 16B20) increased the flexural capacity by 46% (from 249 kN.m to 365 kN.m) with a reduction in mid-span deflection of 18% (from 97.3 mm to 82.6 mm). The flexural stiffness of 16B20 (reinforcement ratio = 2.3%) after initial cracking increased by 80% compared to 8B20 (reinforcement ratio = 1.2%). Similar behavior was reported by Kassem et al. (2011) for CFRP-RC beams reinforced with two types of CFRP bars. The ultimate capacity increased by 26% and 31% as a result of increasing the CFRP reinforcement ratio by 100% for two types of CFRP bars. Moreover, El-Nemr et al. (2013) concluded that increasing the reinforcement ratio three to four times resulted in an average increase of 83.5% in the load-carrying capacity of GFRP-RC beams.

CSA S6-14 requires a deformability factor (*J*-factor) exceeding 4 and 6 for rectangular sections and T-sections, respectively, with no recommendation for circular sections. A *J*-factor greater than 6 might be recommended and used for circular sections, similarly to that for T-sections, considering both as irregular nonrectangular sections. Table 5.3 shows that all the specimens exhibited adequate deformability with respect to the CSA S6-14 limit of 6 with *J*-factors of 18 and 15 for 8B20 and 16B20, respectively. The *J*-factor for the BFRP specimens decreased by 19.5% when the reinforcement ratio was increased from 1.2% to 2.3%.

5.6. Analytical Model

In the following sections, a layer-by-layer iterative procedure was used to obtain the flexural capacity of circular concrete members reinforced with FRP bars by idealizing the cross section as a series of layers to evaluate the sectional forces corresponding to a given strain distribution. This method was originally proposed by Newmark (1943) and has been widely adopted for the analysis of RC members (Kara and Ashour 2012; Kara et al. 2015).

5.6.1. Materials Relationships

The unconfined-concrete stress-strain model proposed by Popovics (1973) was used in this study. As shown in Fig. 5.13(a), the compressive stress f_c, corresponding to strain ε_c in the Popovics model, is given by:

$$f_c = \frac{f_c'(\varepsilon_c/\varepsilon'_c)r}{r-1+(\varepsilon_c/\varepsilon'_c)^r} \tag{5.2}$$

where f_c' = unconfined concrete strength, obtained from the cylinder tests; ε'_c = corresponding strain; and $r = E_{\tan}/(E_{\tan}-E_{\sec})$. The tangent and secant moduli, $E_{\tan}$ and $E_{\sec}$, are determined as $E_{\tan} = 4700\sqrt{f_c'}$ (MPa), as recommended in ACI 318-14, and $E_{\sec} = f_c'/\varepsilon'_c$, respectively.

For concrete in tension, the Vecchio and Collins (Collins and Mitchell 1997) model is adopted, as illustrated in Fig. 5.13 (a). The tensile stress in concrete f_c, corresponding to strain ε_c, is given as $f_c = E_{tan}\varepsilon_c$, for the strain $\varepsilon_c < \varepsilon_{cr}$. For $\varepsilon_c > \varepsilon_{cr}$, the following equation is used:

$$f_c = \frac{f_{cr}}{1+\sqrt{500(\varepsilon_c-\varepsilon_{cr})}} \tag{5.3}$$

where f_{cr} = cracking strength of concrete, taken as $f_{cr} = 0.62\sqrt{f_c'}$ (MPa) (ACI 318-14) and is related to the cracking strain ε_{cr} as $f_{cr} = E_{\tan}\varepsilon_{cr}$.

The BFRP longitudinal bars are modeled as linear elastic up to failure, as shown in Fig. 5.13(b).

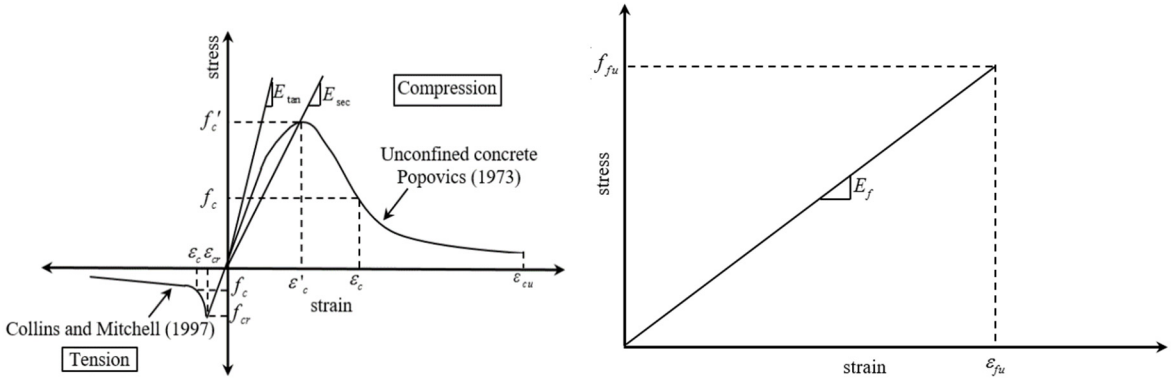

(a) Concrete (b) FRP bars

Figure 5.13 Stress–strain curves of the materials used in the analytical model.

5.6.2. Model Description

Based on the principles of force equilibrium and strain compatibility, an analytical model has been developed to predict the flexural capacity of circular BFRP-RC members by using a layer-by-layer approach to integrate the stresses over the cross-sectional areas of the concrete and longitudinal bars. Figure 5.14 shows the actual cross section and the idealized geometry of the BFRP-RC circular members. The depth of the section, D, is divided into n number of layers of equal thickness, t_i. The centroid of each layer is located at its mid-thickness, and the depth to its center from the top level is h_i. Strains are linearly distributed along the depth of the section. The stresses in the concrete and FRP bars are based on the material relationships shown in Figs. 5.13(a) and 5.13(b). The stresses at the centroid of a strip are assumed constant throughout its thickness. Figure 5.14 also shows the linear strain distribution across the depth, where the top and bottom strains are ε_{Top} and ε_{Bottom}, respectively. The depth of the compression zone from the top of the section is the neutral-axis depth, c.

To obtain the analytical moment capacity of circular BFRP-RC members, the procedure can be summarized in the following steps, in relation to Fig. 5.14:

1. Specify the circular-section diameter, materials properties, locations and areas of FRP bars, and number of layers, n.
2. Assume that the failure is compression failure and that the concrete strain at the top reaches the maximum strain of 0.0035, as recommended by CSA S806-12.
3. Assume a value for neutral-axis depth, c.
4. For each layer i, from 1 to n, calculate h_i and the area of concrete, A_{ci}.
5. For each layer i, calculate the strain ε_i by the meaning of strain compatibility and compute the corresponding compressive or tensile stresses f_{ci}.
6. Calculate the strain ε_j in the FRP bars at each level j by the meaning of strain compatibility, then calculate the corresponding stress f_{bj}.
7. Calculate the compressive and tensile forces of concrete C_{ci} and T_{ci} as the summation of all the forces for all layers.

8. Calculate the compressive and tensile forces C_{bj} and T_{bj} in the FRP bars at each level j.
9. Check for equilibrium by satisfying the condition that the absolute value of the sum of the total compressive and tensile forces is less than a certain allowable tolerance.
10. If equilibrium is not satisfied, go to step 3, assume another value of c, and repeat the process until equilibrium is satisfied.
11. Once equilibrium is satisfied, check for maximum FRP bars strain with reference to the ultimate strain of the FRP bars used.
12. If the maximum strain exceeds the ultimate FRP-bar strains, go to step 2 and repeat the process, assuming that the failure is tension failure.
13. The flexural capacity of the circular cross section can be calculated as the summation of internal moments for individual layers of concrete and FRP bars.

It should be noted that analysis accuracy was affected by the chosen number of horizontal layers and the tolerance adopted in the analysis. A convergence study showed that the appropriate number of horizontal layers needed to reliably predict the capacity of the circular BFRP-RC members was found to be over 50. A Microsoft Excel spreadsheet was prepared to facilitate the calculation procedures for the flexural capacity of circular FRPRC members.

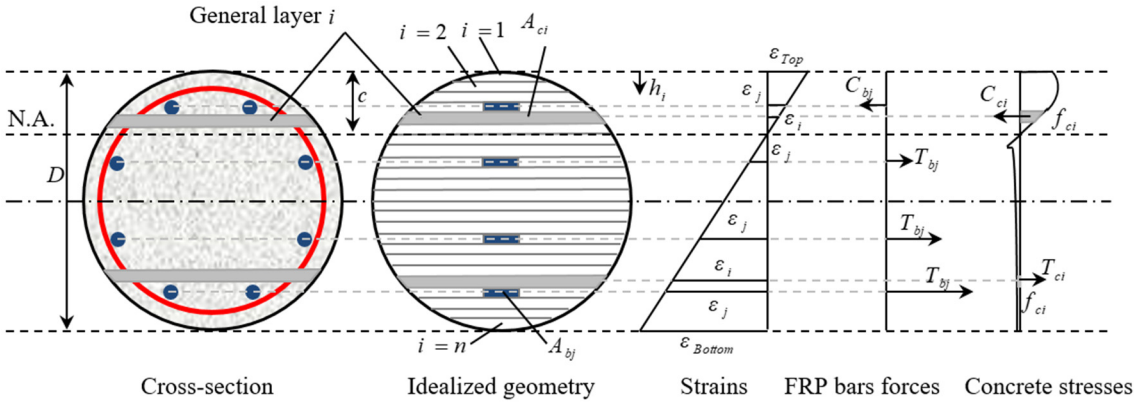

Figure 5.14 Idealized cross section and stress and strain distributions in the analytical model.

5.6.3. Comparison of the Analytical and Experimental Results

The experimental failure moment for circular BFRP-RC specimens was compared to the predictions using the aforementioned layer-by-layer approach. In one scenario, ignoring the contribution of the BFRP longitudinal bars in the compression side to the moment-carrying

capacity was assumed to be equivalent to the concrete and, in the second, the BFRP longitudinal bars in the compression side was considered assuming that the BFRP tensile and the compressive Young's moduli were equal. In all the analyses, the concrete density factor, material resistance factor, and member safety factor were taken as equal to unity. Table 5.3 presents the experimental-to-predicted ratios for the flexural capacities and BFRP bar strains of the test specimens. The level of conservatism and degree of accuracy depend on the assumptions of considering and ignoring the contribution of the BFRP bars in compression. By considering the BFRP bars in compression, the average $M_{\text{exp.}} / M_{pred.}$ at the failure moment was 1.01 with a coefficient of variation of 1.4%. Neglecting the bar contribution in compression increased the level of conservatism of the predicted results. The average $M_{\text{exp.}} / M_{pred.}$ was 1.05 with a coefficient of variation of 3.4%. On the other hand, the experimental-to-predicted strains of BFRP bars ranged between 1.09 and 1.18 considering the contribution of the BFRP bars in compression.

5.7. Non-Iterative Analysis Method for Calculating Nominal Flexural Strength

This section presents a simplified non-iterative method to calculate the flexural capacity of circular concrete members reinforced with BFRP bars. Based on the principles of force equilibrium and strain compatibility, the following calculation procedures were mathematically derived and proposed for circular concrete members reinforced with BFRP bars, in relation to Fig. 5.15.

1. Strain in the concrete and FRP reinforcement is proportional to the distance from the neutral axis (a plane section remains plane after deformation up to failure).
2. The maximum usable compressive strain in the concrete is assumed to be 0.0035, as recommended by CSA S806-12.
3. The tensile strength of concrete is ignored.
4. The tensile behavior of the FRP reinforcement is linearly elastic up to failure.
5. The strain in FRP reinforcement, whether in tension or compression, is the same as that in the surrounding concrete (i.e., a perfect bond exists between the FRP reinforcement and concrete).

6. The distribution of concrete compressive stress can be described by the equivalent rectangular stress block shown in Fig. 5.15 with parameters α_1 and β_1 as presented in the following equations satisfying the requirements of CSA S806-12:

$$\alpha_1 = 0.85 - 0.0015 f_c' \geq 0.67 \tag{5.4}$$

$$\beta_1 = 0.97 - 0.0025 f_c' \geq 0.67 \tag{5.5}$$

7. The area of tension reinforcement, A_f, is the area of the FRP bars below the mid-depth of the section.
8. The effective depth, d, is taken as the distance from the extreme compression fiber to the centroid of the tension reinforcement (see Fig. 5.15) and can be calculated with Eq. 5.6 given in AASHTO *LRFD Bridge Design Specifications* (2012):

$$d = \frac{D}{2} + \frac{D_r}{\pi} \tag{5.6}$$

where D_r = the diameter of the circle passing through the centers of the longitudinal reinforcement.

9. The compressive strength of FRP reinforcement shall be disregarded in calculating the flexural strength, as recommended by CSA S806-12.
10. The reinforcement ratio and balanced reinforcement ratio can be computed with Eqns. 5.7 and 5.8, respectively, which were mathematically derived and proposed for the circular section by assuming a section width, D, and an effective depth, d .

$$\rho_f = \frac{A_f}{Dd} \tag{5.7}$$

$$\rho_{fb} = \alpha_1 \frac{f_c'}{f_{fb}} \frac{r^2 \left(\theta_b - sin\theta_b cos\theta_b\right)}{Dd} \tag{5.8}$$

$$\theta_b = cos^{-1}\left(1 - \frac{\beta_1 c_b}{r}\right) \tag{5.9}$$

$$c_b = \left(\frac{\varepsilon_{cu}}{\varepsilon_{cu} + \varepsilon_{fb}}\right) d \tag{5.10}$$

where f_{fb} , ε_{fb} = the average stress and strain in FRP tension reinforcement at the balanced condition, respectively.

When $\rho_f > \rho_{fb}$, the controlling limit state is concrete crushing. Based on the equilibrium of forces and strain compatibility (shown in Fig. 5.15), the following can be derived for circular sections:

$$M_n = A_f f_f \left(\bar{y} + \frac{D_r}{\pi} \right) \tag{5.11}$$

$$f_f = \alpha_1 \frac{f_c'}{A_f} r^2 \left(\theta - sin\theta cos\theta \right) \tag{5.12}$$

where f_f = the average stress in tension reinforcement and $\bar{y}$ = distance between the centroid of the circular concrete segment on the compression side to the centroid of the concrete cross section and can be calculated using Eq. 5.13.

$$\bar{y} = \frac{2r}{3} \left(\frac{sin^3 \theta}{\theta - sin\,\theta\, cos\,\theta} \right) \tag{5.13}$$

The value of the angle (θ) defining the compressive block of the cross section can be determined with regression analysis based on the factors affecting the equilibrium of forces. Equation (5.14) was proposed using regression analysis to determine the value of θ, as follows:

$$\theta = 1.67 \rho_{ft}^{0.18} \left(1.02 - 0.81 \left(\frac{f_c'}{E_f \varepsilon_{cu}} \right)^{0.26} \right) \tag{5.14}$$

$$\rho_{ft} = \frac{A_{ft}}{A_g} \tag{5.15}$$

where the angle θ is expressed in radians; f_c'=concrete cylinder strength in MPa; E_f = modulus of elasticity of GFRP reinforcing bars in MPa; and ρ_{ft} = the ratio between the total reinforcement area and the gross area of the circular cross section expressed in percentage (%).

When $\rho_f < \rho_{fb}$, the controlling limit state is rupture of the FRP reinforcement. A simplified and conservative calculation of the nominal flexural strength of the member can be based on Eq. 5.16, as suggested in ACI 440.1R-15:

$$M_n = A_f f_{fu}\left(\bar{y}_b + \frac{D_r}{\pi}\right) \tag{5.16}$$

where f_{fu} = the average stress in tension reinforcement when the strain in extreme tension bars reaches its maximum value and $\bar{y}_b$ = distance between the centroid of the circular concrete segment on the compression side to the centroid of the concrete cross section at the balanced condition.

Table 5.3 compares the experimental failure moment for BFRP-RC circular specimens to the moments resulting from the calculations using the non-iterative method. The proposed non-iterative method yielded good yet conservative estimates of the flexural capacity of the test specimens, since the average experimental flexural strength over the predicted value was 1.13 with a coefficient of variation of 5.6%. On the other hand, the experimental-to-predicted strains of the BFRP bars ranged between 1.10 and 1.19.

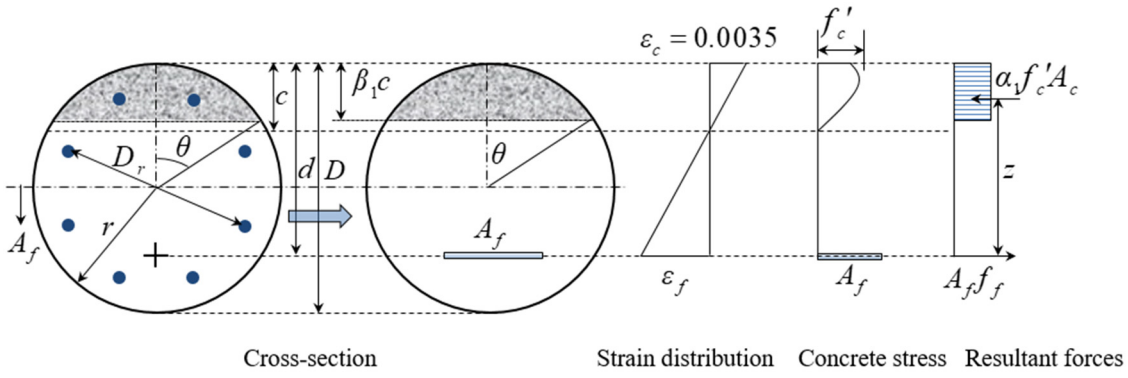

Figure 5.15 Non-iterative method cross section, stress and strain distributions.

5.8. Finite-Element Model

A nonlinear finite-element (FE) analysis using the finite-element software package ANSYS was conducted to simulate the flexural behavior of circular concrete members reinforced with BFRP bars and spirals. Several factors must be considered in finite-element modeling. These include specimen dimensions, element types, material properties, mesh generation, boundary conditions, and loading types.

5.8.1. Element-Type Descriptions

In this study, the concrete was modeled using a three-dimensional eight-node solid element, SOLID65. SOLID65 elements can account for the failure modes of concrete cracking in tension and crushing in compression. The longitudinal and transversal reinforcement was modeled as a LINK8 element, with one node at each end. This element is capable of simulating nonlinearity and plastic deformations for BFRP reinforcement. A thick steel plate, modeled using a SOLID45 element, was added at the support and load-application locations in order to avoid stress-concentration problems and to prevent localized crushing of concrete elements near the supporting points and load-application locations.

5.8.2. Material Modeling

For concrete in compression, the uniaxial multi-linear isotropic stress-strain relationship was obtained using the Popovics (1973) model, as given by Eq. (5.3) and shown in Fig. 5.13(a), up to the compressive strength f_c'. The descending part of the concrete material model in ANSYS was ignored due to convergence problems, as recommended by Wolanski (2004). The BFRP longitudinal bars are modeled as linear elastic up to failure, as shown in Fig. 5.13(b). Table 5.2 provides the material properties for the BFRP reinforcement used in the model.

5.8.3. Geometry, Loading, and Boundary Conditions

Only one-quarter of the specimen was modeled in ANSYS, taking advantage of symmetry about two axes (see Fig. 5.16). The boundary conditions at the axes of symmetry were set to represent the effect of continuity, as illustrated in Fig. 5.17(b). It should be noted that the one-quarter model was verified against full-specimen model. The support was modeled in such a way that a roller was created. A single line of nodes on the plate was given constraint in the UX and UY directions, applied as constant values of 0. Doing so allows the specimen to rotate at the support. Figure 5.17(b) shows the support condition. The force P is applied across the entire centerline of the plate, as shown in Fig. 5.17(b), to simulate the loading point in the experimental program. An important step in FE is the selection of the mesh density. A convergence of results is obtained when an adequate number of elements is used in a model. This is practically achieved when an increase in the mesh density has a negligible effect on the results. Figure 5.18 presents a mesh convergence study for 8B20. The results started to converge with a model having approximately

2,000 elements. As a result, each test specimen was typically discretized using 2,584 elements. Figures 5.17(a) and 5.17(b) provide the overall mesh of the concrete, loading, and support volumes.

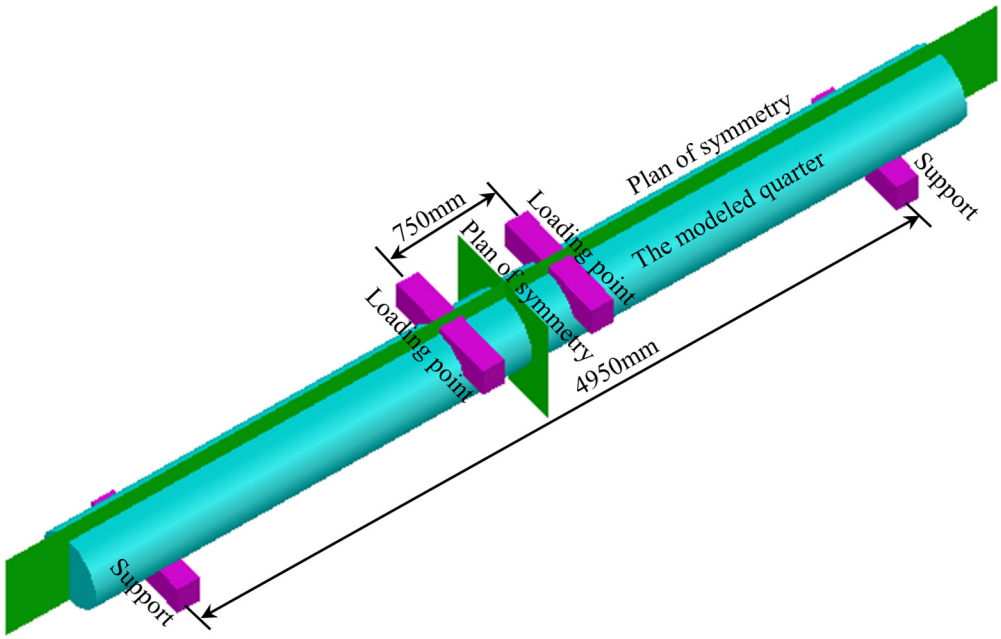

Figure 5.16 Plans of symmetry and the modeled quarter of specimen.

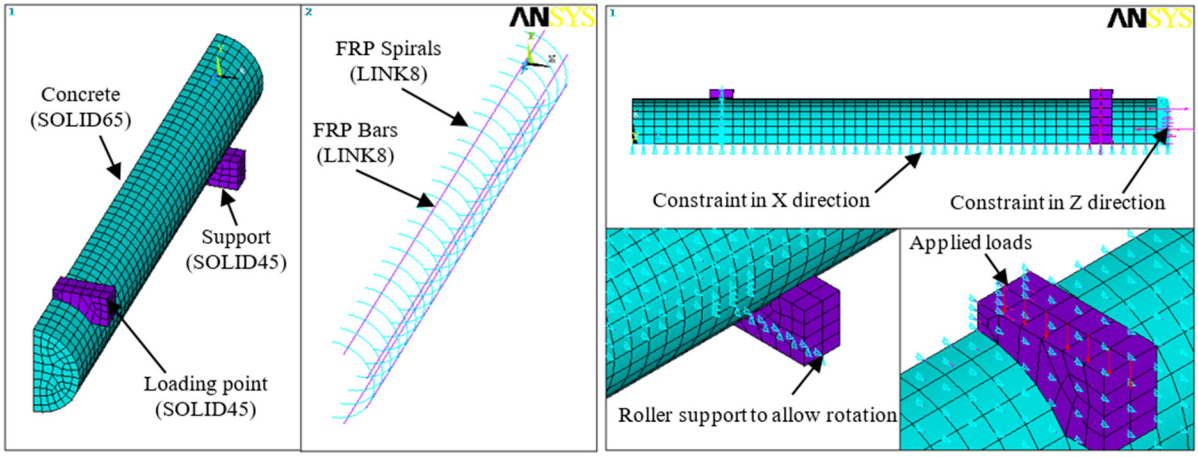

(a) (b)

Figure 5.17 ANSYS model (a) Element types, and (b) Loading and boundary conditions.

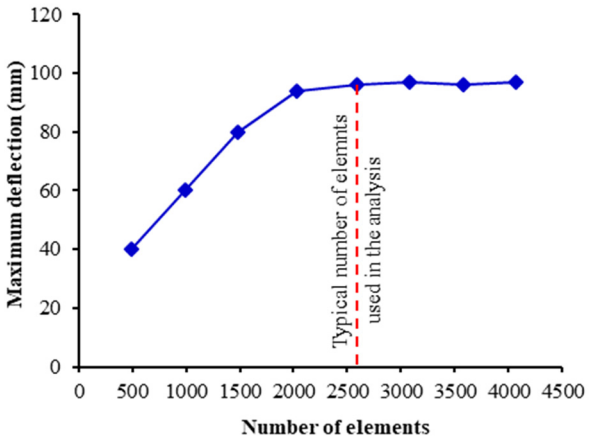

Figure 5.18 Mesh convergence study for specimen 8B20.

5.8.4. Model Verification

The results of the FE models were compared to the experimental results for the tested specimens. Figure 5.19 shows the moment–deflection relationship predicted by the FE model compared to the experimental results. It shows that the model accurately predicted the flexural response of 8B20 and 16B20 up to cracking as well as between cracking and failure. The moment–deflection curve for 8B20 shows that the model predicted the failure moment to be 231 kN.m, which is approximately 7% less than the experimental value. In the case of 16B20, the model predicted a failure moment of 360 kN.m, which is less than the experimental value by approximately 2%. Figures 5.20(a) and 5.20(b) show the deformed shape and concrete cracking of 8B20 and 16B20, respectively. The figures indicate a good prediction of the FE model used in this study.

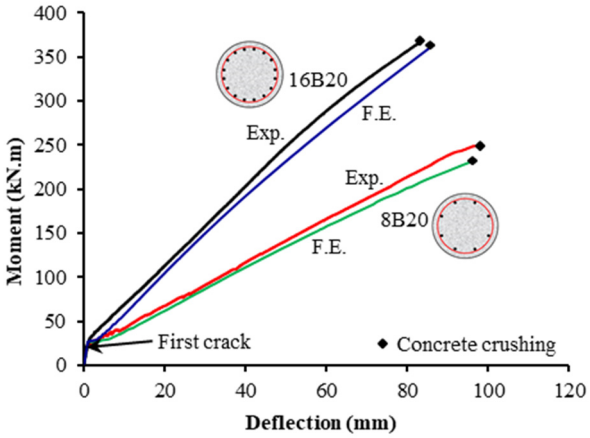

Figure 5.19 Moment–deflection relationship of the verified model against experimental results.

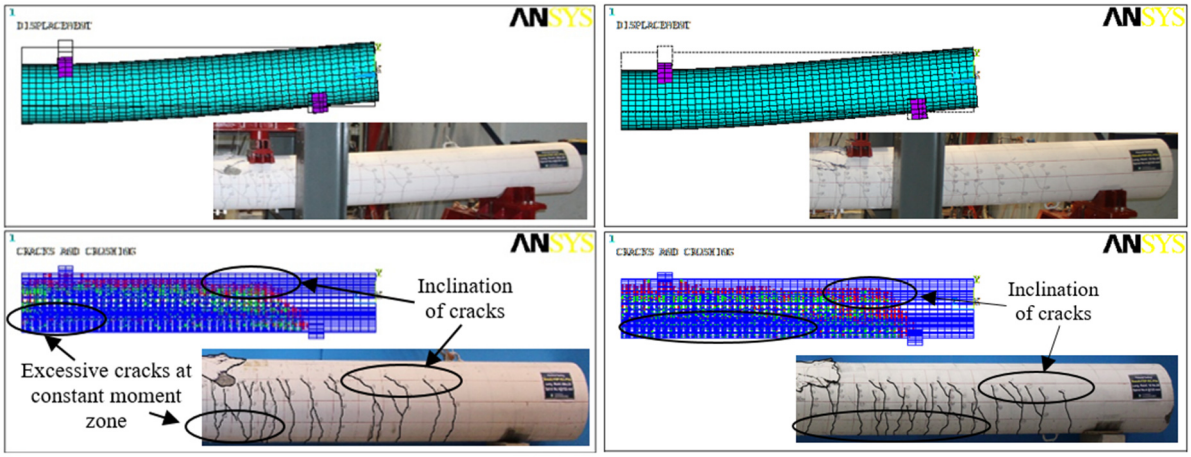

(a) (b)

Figure 5.20 Deformed shape and crack propagation of the specimens: (a) 8B20; (b) 16B20.

5.8.5. Parametric Study

The model was used in a parametric study to further examine the effects of concrete strength and longitudinal-reinforcement ratio on the flexural behavior of circular BFRP-RC members. The members were modeled in the ANSYS program by modeling one quarter only. The chosen concrete strength ranged from 25 MPa to 60 MPa, while the reinforcement ratio ranged from 1.2% to 3.5%. Based on the parametric investigation, the failure mode of all circular BFRP-RC models was initiated by concrete crushing on the compression side (compression failure).

5.8.5.1. Effect of Concrete Strength

Figure 5.21 shows the variation in a moment–deflection relationship by changing the concrete compressive strength from 25 to 60 MPa in 5 MPa increments at reinforcement ratios of 1.2% and 2.3% (equivalent to those of 8B20 and 16B20 in the experimental program, respectively). The figure clearly shows that the flexural strength and stiffness were generally enhanced as the concrete compressive strength increased while keeping the reinforcement ratio constant. As shown in Fig. 5.21, increasing the concrete compressive strength from 25 MPa to 60 MPa increased the flexural capacity by approximately 50% and 45% for the reinforcement ratios of 1.2% and 2.3%, respectively.

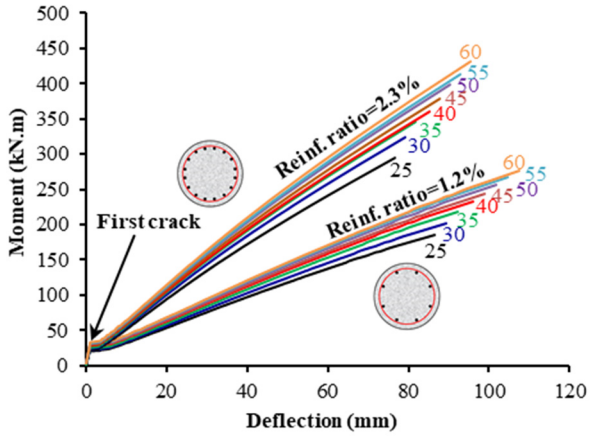

Figure 5.21 Variation in the moment–deflection relationship with concrete strength.

5.8.5.2. Effect of the Longitudinal-Reinforcement Ratio

Figure 5.22 shows the variation in a moment–deflection relationship with different reinforcement ratios. As expected, the model with a reinforcement ratio of 1.2% (equivalent to that of 8B20 in the experimental program) showed the lowest stiffness and moment capacity. As the reinforcement ratio was increased, both flexural stiffness and capacity were enhanced. Figure 5.22 shows that increasing the reinforcement ratio from 1.2% to 3.5 % reduced the deflection by approximately 20% and increased the capacity by approximately 100%.

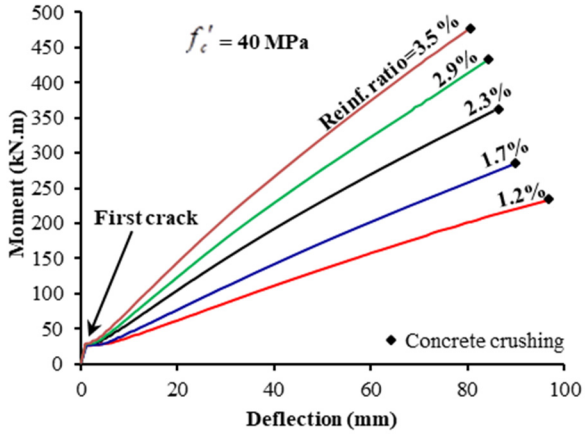

Figure 5.22 Variation in the moment–deflection relationship with reinforcement ratio.

5.9. Conclusions

This paper reports on an experimental and analytical investigation of the flexural strength and behavior of circular concrete members reinforced with BFRP bars and spirals. Based on the

experimental results and the analytical study presented in this paper, the following conclusions can be drawn:

1. The failure of the circular BFRP-RC specimens occurred by gradual concrete crushing, while the steel-RC specimen failed due to steel yielding, followed by concrete crushing. The flexural strength at concrete crushing in the BFRP-RC specimens was almost 1.9 times that of the counterpart steel-RC specimen with a similar reinforcement ratio.

2. Based on the test results, the failure of circular BFRP-RC specimens is not triggered by BFRP bar rupture, provided that the minimum reinforcement ratio is not less than 1%. The maximum average tensile strain attained at the initiation of cover spalling still represented less than 55% of the ultimate tensile strain of the BFRP bars.

3. The reinforcement ratio significantly affected the behavior of the circular BFRP-RC specimens. As the reinforcement ratio increased, both the flexural stiffness and capacity increased. The flexural capacity at concrete crushing was limited, however, by concrete compressive strength and strain.

4. A deformability *J*-factor exceeding 6 is proposed and recommended for use with BFRP-RC members with circular sections, similar to that required in CSA S6-14 for non-rectangular sections (T-sections).

5. The analytical model presented herein using a layer-by-layer analysis was capable of predicting the flexural strength of the circular BFRP-RC members. Considering the compression contribution of the BFRP bars provided accurate predictions of the flexural capacities, while neglecting this contribution added to the level of conservativeness. On the other hand, a non-iterative analysis method, including simple design equations, was proposed and presented. This method can be considered a simple and more straightforward method for practicing engineers.

6. The developed finite-element model using ANSYS was able to simulate the BFRP specimens and predict the failure moment as well as the moment–deflection relationship, providing a good prediction when compared to experimental results. The verified model was used to extend the range of investigated parameters.

7. The experimental evidence from this investigation provides some basis for including BFRP bars in the material aspects and including design provisions in the forthcoming codes and standards for the use of BFRP bars and spirals as internal reinforcement in circular concrete members.

CHAPTER 6. CRACKING AND CRACK CONTROL IN CIRCULAR CONCRETE BRIDGE MEMBERS REINFORCED WITH FIBER-REINFORCED-POLYMER (FRP) BARS

Foreword

Authors and Affiliation:

- Salaheldin Mousa: Ph.D. candidate, Department of Civil Engineering, Université de Sherbrooke, Sherbrooke, Quebec, Canada, J1K 2R1.
- Hamdy M. Mohamed: Research Associate/Lecturer, Department of Civil Engineering, Université de Sherbrooke, Sherbrooke, Quebec, Canada, J1K 2R1.
- Brahim Benmokrane: Professor, Department of Civil Engineering, Université de Sherbrooke, Sherbrooke, Quebec, Canada, J1K 2R1.

Journal Title: *Journal of Bridge Engineering, ASCE.*

Paper Status: Accepted on July 16, 2018.

Contribution in thesis

This chapter investigates the cracking and crack control of circular FRP-RC members experimentally and theoretically. The experimental results are reported in terms of crack patterns, crack spacing, and crack width versus flexural tension-bar strain and the applied moment. Crack-control models in the current FRP codes and design guidelines were reexamined, extended, and applied to circular FRP-RC members.

Abstract

Serviceability requirements are crucial in the design of fiber-reinforced-polymer (FRP) reinforced-concrete (RC) bridge members. Permissible crack width under service loads is one of the requirements that can control design. Crack-control models have been included in the Canadian Highway Bridge Design Code and AASHTO LRFD Bridge Design Specifications based on experimental work on FRP-RC members with rectangular cross-sections. In this study, the applicability of these models to RC bridge members with a circular cross-section was assessed experimentally. A total of nine full-scale, circular RC specimens measuring 0.5 m in diameter and 6 m in length were constructed and tested up to failure under four-point bending load. The test parameters included the longitudinal-reinforcement ratio and the longitudinal-reinforcement type, including glass FRP, carbon FRP, basalt FRP, and steel bars. The experimental results are reported in terms of crack patterns, crack spacing, and crack width versus flexural tension-bar strain and the applied moment. Crack-control models in the current FRP codes and design guidelines are reexamined, extended, and applied to circular FRP-RC members. Design equations for estimating the service stress in the FRP reinforcement and the cracked moment of inertia were theoretically derived and presented for the circular FRP-RC members. Crack width predictions are compared with the experimental results. The comparison indicates that the crack-control formulae developed for rectangular FRP-RC members can be used for the cracking control of circular FRP-RC members by using the redefined parameters developed and proposed in this study to take into account the geometry, bar spacing and distribution, and effective tension stiffening area.

Keywords: Circular concrete members; crack width, FRP, bond-dependent coefficient, serviceability.

6.1. Introduction

Crack control is an important serviceability criterion in the design of concrete bridge members reinforced with fiber-reinforced-polymer (FRP) bars. Crack width limits under service loads can govern the design of FRP-reinforced concrete (FRP-RC) members. On the other hand, FRP bars are corrosion-resistant, so larger crack widths can be tolerated in FRP-RC members than in steel-reinforced concrete (SRC) members when reinforcement corrosion is the primary reason for crack control. Other considerations with regards to acceptable crack width limits include aesthetics, creep rupture, and shear effects (AASHTO 2009; CSA S6 2014; ACI 440.1R 2015). Crack spacing and crack width in FRP-RC members are dependent on many design parameters, including FRP-bar bond characteristics, the ratio of reinforcement area to surrounding concrete area, tensile strain in FRP bars, bar spacing, and concrete tensile strength. Tensile stress will increase in the concrete as the reinforcing bar is loaded. A primary crack forms once the concrete's tension capacity has been exceeded. At the crack locations, the bar resists 100% of the applied load; the distribution of stress and strains is no longer uniform. Between the cracks, a portion of the load is transferred to the concrete through bond. The concrete stress is less than the concrete's tensile capacity; the concrete and reinforcing bar are composite, resulting in lower reinforcing bar strains than at the cracks. This is known as "tension stiffening." The bond stress is therefore proportional to the slope of the longitudinal reinforcing-bar stress distribution. Since the stress in the reinforcing bar is equal at each crack, the average bond stress between cracks is also equal. The initiation and development of subsequent cracks is a function of the concrete. The embedded bar—provided it is bonded to the concrete—serves to control cracking, not affect its initiation. Since the reinforcing bars alone carry stress across the cracks, crack width is inversely proportional to bar stiffness, EA. Crack spacing, however, is a function of bond behavior, that is, how efficiently the bar transfers stress to the concrete at either end and to either side of a crack. Significant research has been carried out over the last two decades to determine relationships between concrete crack width and the aforementioned design parameters in FRP-RC members. The experimental work has focused mainly on beams with rectangular cross sections (Faza and GangaRao 1993; Masmoudi et al. 1996; Theriault and Benmokrane (1998); Toutanji and saafi 2000; Toutanji and Deng 2003; El-Salakawy and Benmokrane 2004; Ospina and Bakis 2007; El-Nemr et al. 2013 and 2016; Noel and Soudki 2014; Elgabbas et al. 2016 and 2017; Barris et al. 2017). In these studies, crack widths were predicted with the empirically

proposed Gergely-Lutz 1968 equation and Frosch's 1999 physical model. Since crack width is a function of reinforcement stiffness and bond properties, the effect of the reinforcement type is significant. Hence, various modifications to the steel-based models have been proposed to account for the mechanical properties of FRP reinforcing bars (Faza and GangaRao 1993; Masmoudi et al. 1998; Toutanji and saafi 2000; Ospina and Bakis 2007; Noel and Soudki 2014). In addition, several design codes and guidelines have been published to control the cracks in rectangular FRP-RC members: AASHTO (2009), CSA S6 (2014), ACI 440.1R (2015), CSA S806 (2012), CNR-DT 203 (2006) and JSCE (1997). In contrast, studies on the cracking behavior of circular concrete members that can be reinforced with FRP bars have not yet been introduced.

Valuable research has been conducted over the last decade on concrete columns/piers reinforced with FRP bars, ties and spirals under static concentric loads (De Luca et al. 2010, Tobbi et al. 2012, Afifi et al 2014, Mohamed et al. 2014, Zadeh and Nanni 2013), eccentric loads (Hadhood et al. 2017, Guérin et al. 2018), and cyclic loading (Tavassoli et al. 2015; Ali and El- Salakawy 2016; and Elshamandy et al. 2018). To summarize, this research demonstrated that the behavior of FRP-RC columns was very similar to that of conventional steel-RC columns; no appreciable difference was observed. The experimental evidence from these investigations provide some basis for including design provisions in bridge-design specifications for the use of FRP bars, spirals, and hoops in axial compression members for bridge pier and pile applications (Mohamed et al. 2014). Nowadays, bridge and building codes and design guidelines allow the use of FRP bars in compression members and columns, neglecting their strength contribution (ACI440.1R-15: clause 3.3; CAN/CSA S806-12: clause 8.4.3.1; CAN/CSA S6-14: clause 16.11.2.3; AASHTO LRFD Bridge Design Specifications (2009): clause 1.3). In addition, based on the experimental database in the literature, new design provisions are intended to be included for FRP-RC columns/piers in the forthcoming ACI 440 code; AASHTO LRFD; CAN/CSA S6; and CAN/CSA S806.

Circular RC members are extensively used as piers and piles in bridges and as fender pilings in marine environments, because they are easy to build and provide equal strength in all directions under lateral loads (Afifi et al. 2014). These members have limited service lives and high maintenance costs when used in harsh environments due to the corrosion of steel reinforcement.

The repair and replacement of piling systems in North America has been estimated at billions of dollars annually (Ali et al. 2017; Mohamed et al. 2014). These members have been designed so that they are subjected to great moments in addition to the normal force. The risk of cracking, however, is critical in cases in which the stresses due to moments prevail and can display serious problems if cracking control is neglected. The columns of center piers and foundation piles, which belong to large-span monolithic bridges, are strained under constraint moments of significant value (Tegos et al. 2011). These moments are caused by hindered expansions and contractions, resulting in tension transverse cracks across the section of axially loaded columns in compression after a significant portion of their allowable service sustained load is removed while remaining under partial service compression axial load. The literature contains valuable research work on the cracking behavior of circular members reinforced with steel (Bergfelder and Dittfach 1992; Wiese et al. 2004; Tegos et al. 2011; Carbonell-Márquez et al. 2014). Yet no research seems to have investigated the cracking behavior and crack control of circular concrete members reinforced with FRP reinforcement. Moreover, none of the aforementioned FRP design standards have incorporated specific formulae for circular RC members. In general, FRP crack-design models can be applied to circular members, although their accuracy should, however, be assessed. The cracking control of rectangular members can be assessed easily, as the stresses in the reinforcement at service condition can be defined using the equilibrium of forces and strain compatibility. Reinforcement in the tension side, in most cases, exhibits approximately the same stress level, even when many layers of reinforcement bars are used. In contrast to rectangular RC members, the bars in circular RC members are usually distributed in a circle at discrete points, causing some difficulties in calculating the equilibrium of forces and strain compatibility. In addition, the stresses, which are variable over the section depth, are also distributed over an area of variable width. This fact leads to a very small part of the circular section exhibits maximum compression stress. On the other hand, the extreme tension reinforcement might reach the ultimate strain and stress, while the other layers of reinforcement have lower stresses, possibly equal to zero in proximity to the neutral axis. This produces a larger concrete compression zone and a smaller internal lever arm compared to rectangular sections with equivalent dimensions, resulting in a higher level of strains in the extreme layer of tension reinforcement. This may result in wider cracks in members with circular sections compared to those with rectangular sections.

6.2. Literature Review on Crack-Control Development for FRP-RC Members

Crack-control models have been developed in the literature based on valuable experimental work on FRP-RC members with rectangular cross sections (ACI 440.1R-15). Steel-based crack models have been modified to account for FRP-bar properties using the k_b factor (ACI 440.1R-15). The k_b term is a coefficient that accounts for the degree of bond between FRP bars and the surrounding concrete. For FRP bars having bond behavior similar to uncoated steel bars, the bond coefficient k_b is assumed to be equal to 1.0 (ACI 440.1R-15). In 1993, Faza and GangaRao replaced steel strain with FRP strain in the Gergley-Lutz equation to predict the crack width of FRP-RC members. Masmoudi et al. (1996) introduced a coefficient in the Gergely-Lutz equation to account for the bond characteristics of FRP bars based on an experimental investigation to predict crack width. The predictions of the modified model compared well to the test results achieved by Theriault and Benmokrane (1998). Based on a regression analysis of the experimental results, Toutanji and Saafi (2000) modified the Gergely-Lutz equation, including a k_g factor as a function of the FRP reinforcement ratio and modulus of elasticity. In 2001, ACI 440.1R stated that crack width is proportional to the reinforcement strain rather than stress, and adopted a modified form of the Gergley-Lutz equation by introducing a factor k_b to account for the bond between FRP and concrete (Gao et al. 1998). It states that, if the bond is similar to steel, then k_b is equal to 1. If the bond is lower than that of steel, then k_b is greater than 1, and vice versa. If k_b is unknown, a value of 1.2 should be assigned. ISIS Canada (2001) provided a crack width equation based on the Gergely and Lutz (1968) equation, including a k_b coefficient with a recommended value equal to 1.2. ISIS Canada (2007) limited the tensile strain in the reinforcement to 2000 $\mu\varepsilon$ to control crack width. Toutanji and Deng (2003) concluded that ACI 440.1R-01 provided satisfactorily crack width predictions if FRP bars were placed in one layer. In 2002, the Canadian building code (CAN/CSA-S806) introduced a z factor based on the Gergely and Lutz (1968) equation for crack control. This z factor should not exceed 45 kN/mm for interior exposure and 38 kN/mm for exterior exposure. Furthermore, it stated that

the value of k_b shall be determined experimentally, but, in the absence of test data, it may be taken as 1.2 for deformed rods. El-Salakawy and Benmokrane (2004) reported that the ACI 440.1R-01 approach with a k_b coefficient of 1.0 provided correlated well but conservatively with their test results on FRP-RC slabs, and that all specimens yielded a z factor lower than 38 kN/mm. ACI 440.1R (2006) and CAN/CSA S6 (2006) included the physical model proposed by Frosch (1999) with some modifications to control cracking. In the absence of test data, ACI 440.1R-06 recommended 1.4 for the bond coefficient k_b, while CAN/CSA S6 recommended 0.8 and 1.0 for sand-coated and deformed FRP bars, respectively. ISIS Canada (2007) provided a k_b coefficient with a recommended value equal to 1.2. Ospina and Bakis (2007) proposed a new crack-control formula based on FRP-bar spacing using the Frosch (1999) approach.

The bond factor k_b values were analyzed by Bakis et al. (2006) and found to range from 0.60 to 1.72, with an average of 1.10, with a recommendation for a k_b value of 1.4. The bond factor k_b of different types of FRP bars (carbon, glass, and aramid) was estimated based on experimental crack width results and using the ACI 440.1R-06 design equation (Kassem et al. (2011)). The estimated values ranged from 0.86 to 1.32. El-Nemr et al. (2013 and 2016) found that the ACI440.1R-06 bond coefficient k_b value of 1.4 was very conservative for both sand-coated and helically grooved GFRP bars. In contrast, the k_b of 0.8 recommended by in CSA S6-06 yielded unconservative predictions. Reasonable crack width predictions were obtained from the ACI 440.1R-06 and CAN/CSA S6-06 equations using a k_b factor of 1.2 for helically grooved GFRP bars and 1.0 for sand-coated GFRP bars (El-Nemr et al. (2013 and 2016)). Noel and Soudki (2014) proposed a simple modification to the Frosch model to account for the variation in reinforcement stress between cracks. The proposed modification accounts for the contribution of the concrete between cracks and gives consistently accurate predictions for all reinforcement stress levels in the service range. The bond coefficient of 1.3 for sand-coated GFRP bars was recommended to be used in the modified equation. Recently, Elgabbas et al. (2016 and 2017) conducted experimental investigations on sand-coated and ribbed basalt-FRP (BFRP) bars. The k_b factor was found to be 0.76 and 0.83 for the sand-coated and ribbed bars,

respectively. ACI 440.1R-15 has replaced the traditional crack width formula for crack control with an indirect procedure that controls flexural-crack widths with a maximum reinforcing-bar spacing. This formula is based on the equation proposed by Ospina and Bakis (2007), which is based on the Frosch (1999) approach. The recommended value for the bond coefficient k_b was taken as 1.4, if not determined experimentally, based on Bakis et al. (2006).

In light of the preceding discussion, research is needed into the behavior of circular concrete members reinforced with FRP bars. The extrapolation of test results and proposed design equations on the serviceability and design of rectangular FRP-reinforced concrete sections should be verified for circular members. The experimental study reported here is part of an ongoing comprehensive research program at the University of Sherbrooke in which circular concrete members are tested to investigate different variables and design parameters. The variables include loading type: pure compression (Afifi et al. 2014), axial combined bending (Hadhood et al. 2017), shear (Ali et al. 2017), and flexure (current study); reinforcement type (glass-, carbon-, and basalt-FRP bars); and amounts of FRP longitudinal reinforcement. Our study addressed the worst (critical) case when flexural demand prevails over axial force. As stated in AASHTO LRFD Bridge Design Specifications (2012) (clause 5.7.3.4: Crack Control), "when computing the actual stress in the reinforcement, axial tension effects shall be considered, while axial compression effects can be neglected". Clause C 5.8.2.9 also states that the axial load can be ignored in calculating the effective depth for circular members. The effect of axial compression force, however, was considered in the theoretical analysis. On the other hand, the results of our study will be used for comparison with the results from the ongoing tests under combined axial load and bending.

6.3. Research Significance

Current crack design models in AASHTO *LRFD Bridge Design Specifications* (2009) and the *Canadian Highway Bridge Design Code* (CAN/CSA S6 2014) have not been assessed for circular bridge piers or piles reinforced internally with FRP bars. This paper reports on full-scale circular concrete members reinforced with different types of FRP bars (GFRP, CFRP, and BFRP) that were tested up to failure under four-point bending load. The effect of different test parameters on the measured crack widths were investigated, including the reinforcement ratio,

the axial stiffness of the longitudinal bars, and bar spacing. In addition, the paper examines the accuracy of the available design provisions for the cracking control of circular members reinforced with FRP bars. This study also provides new insights into the effect of axial load on crack-width estimation through an intensive parametric investigation. The experimental data and theoretical analysis provide the evidence required to include design provisions in codes and standards for the cracking control of circular concrete members reinforced with FRP bars.

6.4. Experimental Investigation

6.4.1. Materials Properties

The GFRP, CFRP, and BFRP reinforcement was manufactured using the same technique of pultruding continuous glass, carbon, and basalt fibers, respectively, impregnated with a thermosetting vinyl-ester resin (Pultrall, 2015). The GFRP, CFRP, and BFRP bars and spirals had the same sand-coated surface texture to enhance bond and force transfer between the bars and concrete, as shown in Fig. 6.1. GFRP bars of 20 mm designated diameter, CFRP bars of 15 mm designated diameter, and BFRP bars of 20 mm designated diameter were used in this study as flexural longitudinal reinforcement. The fiber contents in percentage by weight were 82%, 80%, and 81% for the GFRP, CFRP, and BFRP bars, respectively. The ultimate tensile strength f_{fu} and modulus of elasticity E_f of the longitudinal GFRP, CFRP, and BFRP bars and the straight portion of the bent GFRP and BFRP spirals were determined according to ASTM D7205. Table 6.1 provides the mechanical properties of these bars. The tensile strength and elastic modulus were calculated using the nominal cross-sectional area. It is worth mentioning that the measured cross-sectional areas of the FRP bars are within the minimum and maximum limits specified in ASTM D7957 (2017). Two diameters of steel bar were used to reinforce the control specimen. No. 20M deformed steel bars were used as longitudinal reinforcement; No. 10M deformed steel bars were used as spirals. All the specimens were constructed using normal-weight ready-mixed concrete in three batches with a specified concrete strength of 40 MPa at 28 days. Table 6.2 shows the actual concrete compressive and tensile strengths.

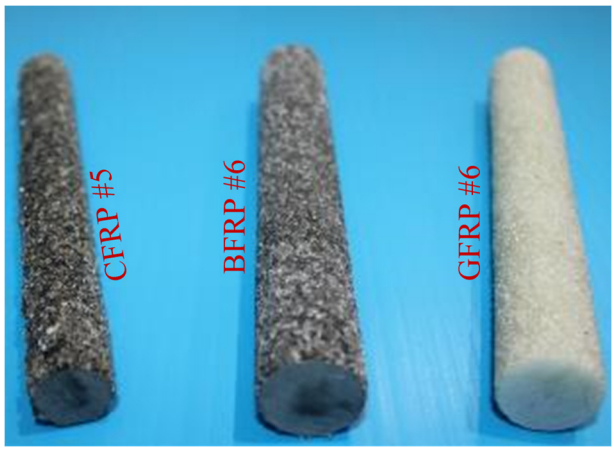

Figure 6.1 FRP bar types and surface characteristics.

Table 6.1 Mechanical properties of the GFRP, CFRP, BFRP, and steel reinforcement.

RFT Type	Material Type	d_b (mm)	A_f [a] (mm²)	A_{im} [d] (mm²)	E_f (GPa)	$E_f A_f$ [f] (kN)	f_{fu} (MPa)	ε_{fu} (%)
Longitudinal bars	GFRP [e]	20	285	339±0.5	63.9±0.4	18,212	1,591±13	2.5±0.2
	CFRP [e]	15	199	222±1.2	141±3.0	28,060	1,680 ±22	1.2±0.1
	BFRP [e]	20	285	346±2.2	63.7±0.8	18,155	1,646±40	2.5±0.1
	Steel	20M	A_s =300	---	E_s =200.0	$E_s A_s$ =60,000	f_y = 460±15	ε_y = 0.2
Spirals	GFRP [e]	13	129	148±1.1	52.1±1.2	6,720	1,126 [b] ±20	2.2±0.0
	BFRP [e]	13	129	139±0.8	51.4±0.2	6,630	1,414 [b] ±11	2.7±0.2
	Steel	10M	A_s =100	---	E_s =200.0	$E_s A_s$ =20,000	f_y [c] = 480±10	ε_y [c] = 0.2

[a] Nominal cross-sectional area.
[b] Tensile strength of straight bar.
[c] f_y and ε_y are the yield strength and strain of the steel bars, respectively.
[d] Immersed cross-sectional area (measured).
[e] The mechanical properties were determined according to ASTM D7205 (ASTM 2011).
[f] The $E_f A_f$ of #6 GFRP bars and #6 BFRP bars are almost the same.
Note: properties calculated based on the nominal cross-sectional area.

6.4.2. Specimens, Instrumentation, and Testing

A total of nine full-scale circular RC specimens, including three specimens reinforced internally with GFRP, which is the most common type of FRP due to its cost effectiveness; three specimens reinforced with CFRP bars; two specimens reinforced with BFRP bars (Groups I, II, and III, respectively); and one reinforced with steel for comparison purposes (Group IV). The test specimens were 0.5 m in diameter and 6 m in length. The specimens were tested under four-point bending with a constant bending moment zone of 0.75 m and a clear span of 4.95 m. The test parameters included the longitudinal reinforcement ratio and the longitudinal reinforcement

type (GFRP, CFRP, BFRP, and steel). The effect of reinforcement ratio on cracking behavior was investigated in Group I by testing three specimens reinforced longitudinally with 8, 16, and 24 (2 x 12 bundled) #6 GFRP bars with reinforcement ratios of 1.2%, 2.3%, and 3.5%, as shown in Fig. 2; in Group II by testing three specimens reinforced longitudinally with 8, 12, and 18 #5 CFRP bars with reinforcement ratios of 0.8%, 1.2%, and 1.8%; and in Group III by testing two specimens reinforced longitudinally with 8 and 16 #6 BFRP bars with reinforcement ratios of 1.2% and 2.3%. Table 6.2 shows the test matrix; Fig. 6.3 provides the cross-section details of the specimens. Each specimen code consists of a letter and numbers. The first number indicates the number of longitudinal bars. The letters G, C, B and S identify specimens as being reinforced totally with GFRP, CFRP, BFRP, or steel reinforcement, respectively. The second number indicates the nominal diameter of the longitudinal bars.

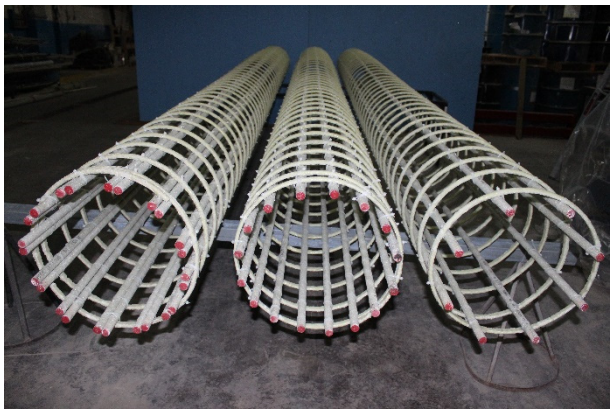

Figure 6.2 GFRP cages.

Strains in the longitudinal reinforcing bars and spirals were measured using electrical resistance strain gauges with gauge lengths of 10 mm (see Fig. 6.3). In addition, nine strain gauges with a gauge length of 60 mm were mounted on the concrete's top surface at four different levels (D, D/8, D/4, and D/3) at mid-span and at quarter-span to measure concrete compressive strains (see Fig. 6.4). Specimen deflection was measured with three linear potentiometers (LPOTs) placed at the mid-span and at the quarter-span. After the formation of flexural cracks, the width of the first three flexural cracks was monitored using high-accuracy LVDTs (±0.001 mm). The load was applied at a displacement-controlled rate of 0.5 mm/min using a servo-controlled, 1000 kN MTS hydraulic actuator attached to a spreader beam, as shown in Fig. 6.4.

Table 6.2 Test matrix and details of tested specimens.

Group	Specimen ID [a]	Reinforcement type	Longitudinal reinforcement		Transversal reinforcement	Bar spacing s (mm) [d]	f'_c (MPa) [c]	f_t (MPa) [c]	EA (kN)
			ρ_{ft} (%) [b]	Number of bars					
I	8G20	Glass FRP	1.2	GFRP bars (8 #20 mm)	GFRP spiral # 4 @125	148	41.4	3.8	145,700
	16G20		2.3	GFRP bars (16 #20 mm)	GFRP spiral # 4 @125	74			291,400
	24G20		3.5	GFRP bars (24 #20 mm)	GFRP spiral # 4 @125	99			437,100
II	8C15	Carbon FRP	0.8	CFRP bars (8 #15 mm)	GFRP spiral # 4 @125	150	45.8	4.3	224,500
	12C15		1.2	CFRP bars (12 #15 mm)	GFRP spiral # 4 @125	100			336,700
	18C15		1.8	CFRP bars (18 #15 mm)	GFRP spiral # 4 @125	66			505,100
III	8B20	Basalt FRP	1.2	BFRP bars (8 #20 mm)	BFRP spiral # 4 @125	148	41.4	3.5	145,200
	16B20		2.3	BFRP bars (16 #20 mm)	BFRP spiral # 4 @125	74			290,500
IV	8S20	Steel	1.2	Steel bars (8 #20 M)	Steel spiral 10 M @125	148	41.4	3.5	480,000

[a] Specimen code identification: number of longitudinal bars, type of reinforcement (G for GFRP, C for CFRP, B for BFRP, and S for steel), nominal diameter of the longitudinal bars.
[b] Total reinforcement ratio (longitudinal reinforcement area divided by the gross area of the circular specimen).
[c] Average of at least 3 cylinders (100 x 200 mm) at time of testing.
[d] Calculated using Eq. 6.20.

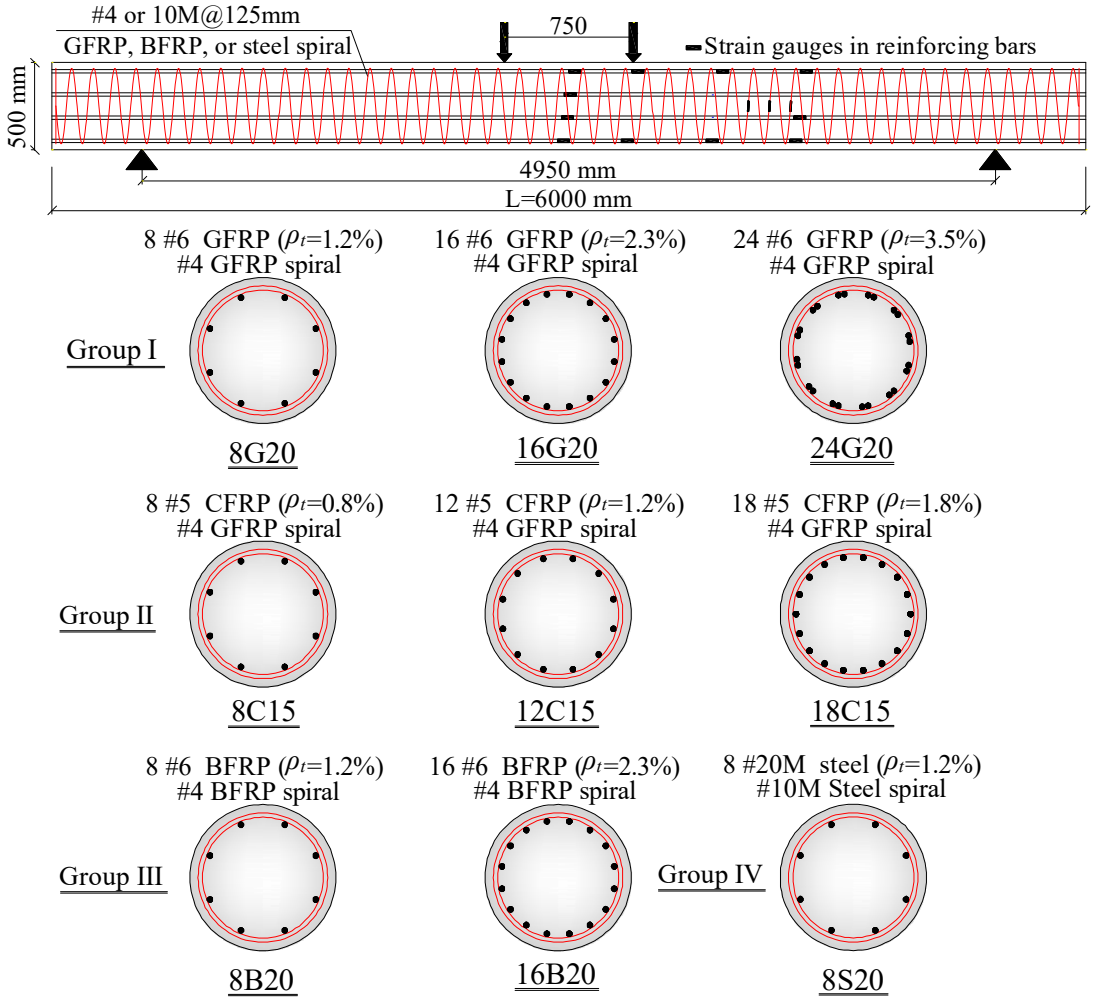

Figure 6.3 Dimensions and reinforcement details of the test specimens. (Note: all dimensions in mm)

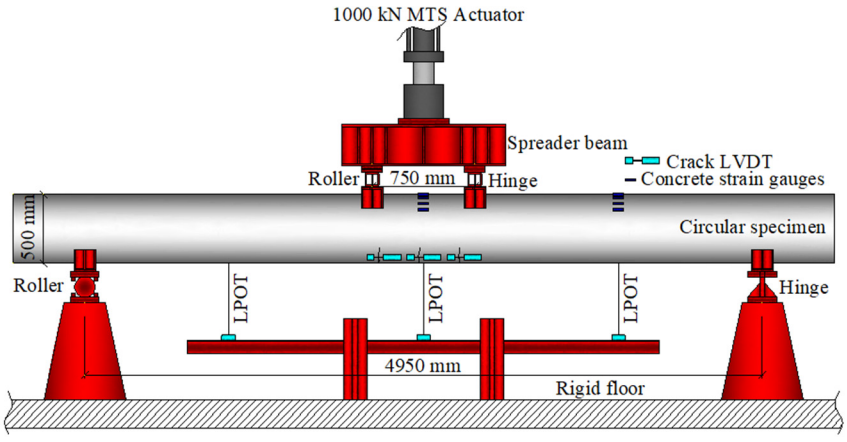

Figure 6.4 Overview of the test setup.

6.5. Test Results and Observations

This section summarizes the experimental results, including general behavior, crack appearance, crack width–tension-bar strain and moment relationships, and cracking configuration and spacing.

6.5.1. Definition of Experimental Service Load

In this study, two reference points were employed to determine experimentally the bending-moment capacity at service condition, M_s. The first defines the service moment as the moment that corresponds to a tensile strain of 2,000 με in the reinforcement, which was originally suggested by ISIS Canada in 2001 for GFRP reinforcement (ISIS Canada Research Network, 2001). This limit of 2,000 με was determined based on the consideration that the design service limit for steel was $0.6 f_y$ with a corresponding strain of 1,200 με and a corresponding crack with of 0.3 mm. Since FRP is noncorrodible, the crack width was relaxed to 0.5 mm. Consequently, the limit of 1,200 με was modified with the ratio between the crack widths of 0.5 and 0.3 (0.5/0.3 = 1.67), which yielded 1,200×1.67 = 2,000 με. The second was calculated at 30% of the nominal capacity, $0.3 M_n$, of the tested specimens, as suggested by Bischoff et al. (2009) and used by many researchers (Kassem et al. 2011; El-Nemr et al. 2013;2016; Maranan et al. 2015; Elgabbas et al. 2016 and 2017). The experimental service moments M_s were calculated (see Table 6.3).

6.5.2. Failure Mode and General Behavior

Figure 6.5 presents the typical failure modes of the test specimens. In all of the specimens, two or three flexural cracks first appeared between the two concentrated loads, where the flexural stress was highest and shear stress zero. With further loading, the cracks formed along the shear span, curving towards the loading points. The GFRP-, CFRP-, and BFRP-reinforced concrete specimens sustained increasing load until reaching the failure moment due to the gradual spalling of the concrete cover. The cover spalling was marked by the separation of small pieces of concrete on the compression side between the loading points. After full cover spalling,

loading continued with the soft and gradual crushing of the compression block, and formation of visible wide cracks that led to the test being stopped at the peak moment.

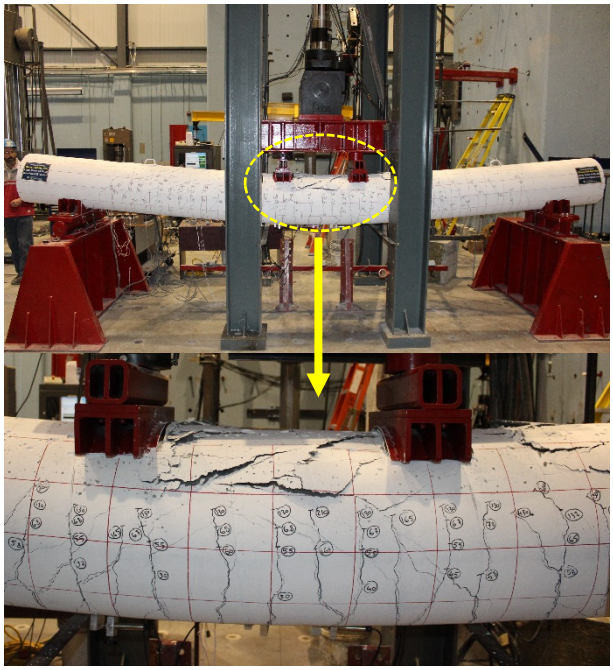

Figure 6.5 Typical failure mode of the tested specimens.

Specimen 8S20, however, failed after flexural yielding occurred, followed by concrete crushing at mid-span. Two significant flexural cracks formed and widened in this specimen. The test was then terminated as the specimen experienced excessive concrete crushing and severe deformation at mid-span.

Figure 6.6 shows the measured mid-span strains in the extreme tension bar against the applied moment until failure. This figure shows that all the specimens had similar linear pre-cracking responses regardless of reinforcement type. Following the cracking, the eight circular specimens reinforced with FRP bars showed a reduced slope linear response up to failure. This is due to the reduced post-cracking stiffness of the specimens. After concrete crushing, the moment values dropped; the strain gauges continued to read more values up to test termination due to excessive deformations in the GFRP specimens, due to tension-bar rupture or compression-bar crushing in the CFRP specimens, and due to compression-bar crushing in the BFRP specimens.

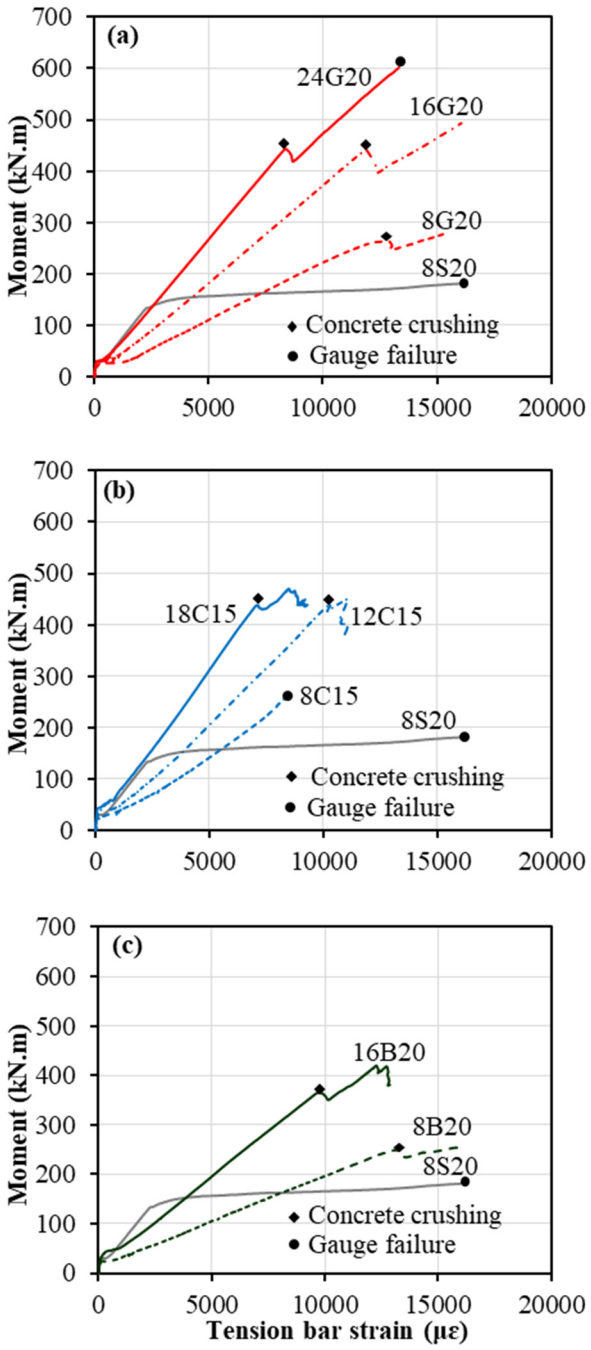

Figure 6.6 Moment–tension-bar strain relationships: (a) Group I versus Group IV, (b) Group II versus Group IV, (a) Group III versus Group IV.

Figure 6.6 shows that the strains were significantly affected by the axial stiffness of the reinforcing bars ($E_f A_f$). Specimens 8G20 ($E_f A_f$ = 145,700 kN) and 8B20 ($E_f A_f$ = 145,200 kN)—with almost the same axial stiffness—had a similar moment–strain relationship (see Figs.

6(a) and 6(c)). Similarly, 16G20 ($E_f A_f$ = 291,400 kN) had a moment–strain relationship very close to that of 16B20 ($E_f A_f$ = 290,500 kN) with almost the same axial stiffness. Specimen 12C15, with higher axial stiffness ($E_f A_f$ = 336,700 kN), exhibited stains less than specimens with similar reinforcement ratios (ρ_{fl} = 1.2%) (8G20, 8B20) at the same load level. Specimen 8C15 ($E_f A_f$ = 224,500 kN) also evidenced lower strains than 8G20 and 8B20 at the same load level. In conclusion, as the axial stiffness of the longitudinal reinforcement increased—regardless of the reinforcement type—the measured tension-bar strains decreased at the same load level. Specimens 24G20 and 18C15 had almost the same moment–strain relationship as control specimen 8S20 with an axial stiffness $E_s A_s$ of 480,000 kN until the steel yielded.

6.5.3. Crack Appearance

The cracking patterns were observed and recorded until failure, as shown in Fig. 6.7. The first crack was always a vertical flexural crack in the constant-moment zone between the two loading points. The corresponding cracking moment was recorded during the test (see Table 6.3). Subsequent to the first crack, additional flexural cracks appeared within the constant-moment zone. With further loading, new cracks started to develop at the shear span, while existing ones propagated vertically toward the compression zone. At high load levels, the cracks in the constant-moment zone widened, while the cracks along the shear span curved towards the loading points. The main difference in the final crack patterns was the number and spacing of the flexural cracks along the span. Generally, the specimens with lower reinforcement ratios—regardless of the type of FRP reinforcement—experienced fewer flexural cracks. Increasing the reinforcement ratio helped in the formation of several well-distributed flexural cracks (total number of cracks increased and average crack spacing decreased at the same load level). On the other hand, the early yielding of the steel bars in 8S20 prior to concrete crushing resulted in wider and concentrated cracks in the constant-moment zone.

6.5.4. Cracking Configuration and Spacing

The average crack spacing at service load for the tested specimens was measured between the two concentrated loads, where the bending moment is constant. The spacing between two

consecutive cracks was determined between crack-opening centers at the level of the extreme layer of reinforcement. Figure 6.7 and Table 6.3 reveal that increasing the reinforcement ratio in the circular FRP-reinforced specimens increased the total number of cracks and reduced the average crack spacing. Moreover, the crack-penetration depth also decreased when the reinforcement ratio increased. It should be noted that the three specimens with similar reinforcement ratios (8G20, 12C15, and 8B20) had almost the same number of cracks at the service-load and failure-load levels. Specimen 12C15, however, had an average crack spacing smaller than that of 8G20 and 8B20 due to the smaller bar spacing in 12C15. The same behavior was also found between 16G20 and 16B20 with the same reinforcement ratio.

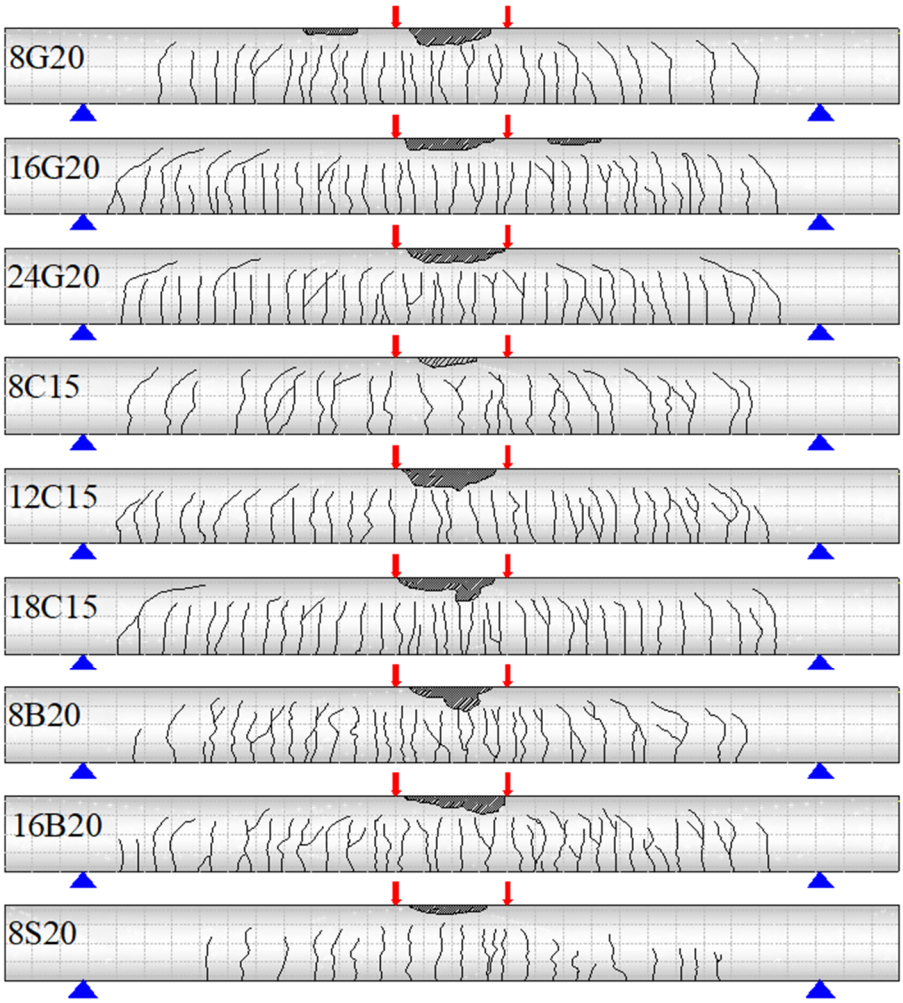

Figure 6.7 Cracking pattern of the tested specimens at failure.

Table 6.3 Experimental moments, crack width, strain in reinforcement, and crack configuration of tested specimens.

Group	Specimen ID	M_{cr} (kN.m)	M_s (kN.m)		M_n (kN.m)	Crack width w (mm)		Strain in reinforcement ($\mu\varepsilon$) at			No. of cracks		Crack spacing (mm) at service	Crack depth (mm) at failure
			at 2,000 $\mu\varepsilon$	$0.30\,M_n$		at 2,000 $\mu\varepsilon$	$0.30\,M_n$	$0.30\,M_n$	w= 0.5 mm	w= 0.7 mm	$0.3\,M_n$	M_n		
I	8G20	24.2	41	79	264	0.34	0.89	3,625	2,470	2,930	19	28	184	409
	16G20	27.9	72	132	441	0.31	0.65	3,680	2,900	3,950	23	39	155	350
	24G20	25.6	108	133	444	0.46	0.58	2,500	2,180	2,950	23	37	137	352
II	8C15	23.8	58	100	332	0.46	0.80	3,625	2,190	3,100	15	25	244	426
	12C15	28.7	79	132	442	0.41	0.69	3,740	2,360	3,750	19	33	163	375
	18C15	34.3	128	133	444	0.36	0.37	2,050	2,690	3,800	21	36	135	358
III	8B20	24.4	49	75	249	0.47	0.87	3,460	2,085	2,830	18	31	179	384
	16B20	31.7	84	110	365	0.40	0.55	2,720	2,475	3,460	22	34	151	373
IV	8S20*	29.9	73	80	134	0.28	0.32	1,325	1,260	2,150	5	21	150	395

* Values calculated at 1200 $\mu\varepsilon$, $0.6\,M_n$, $M_n = M_y$, w=0.3 mm, and w=0.5 mm.

6.5.5. Crack Width versus Tension-Bar Strain and Moment Relationships

Figure 6.8 shows the relationship between the experimental crack width and the corresponding strain in the tension reinforcement. This relationship was plotted separately for each group along with the control specimen 8S20 (Fig. 6.8(a) circular GFRP specimens; Fig. 6.8(b) circular CFRP specimens; and Fig. 6.8(c) circular BFRP specimens). These figures show that the crack width values are directly proportional to the strain in the FRP reinforcement up to failure (due to the linear-elastic behavior of FRP bars), and are affected by the axial stiffness of the reinforcement $E_f A_f$, and up to steel yielding for the specimen with steel reinforcement. In addition, Fig. 6.9 shows the variation in the measured crack width against the applied moment in the specimens. The figure shows that the crack width varied linearly with the applied moment up to failure in the specimens reinforced with FRP bars. This is attributed to the linear-elastic behavior of the FRP reinforcement. That of the control specimen (8S20), however, varied linearly until the steel reinforcement yielded.

Table 6.3 provides strains in the tension reinforcement at service condition $0.3\,M_n$, and at 0.5 and 0.7 mm crack width levels. The results indicate that the FRP-RC specimens experienced higher strain at $0.3\,M_n$ (3,200 με on average) than that at the 0.5 mm crack width (2,400 με on average). The average strain in the FRP-RC specimens was 3,350 με at a 0.7 mm crack width. On the other hand, the service moment of the GFRP-RC specimens at $0.3\,M_n$ ranged from 1.23 to 1.90 times that of the strain level of 2,000 με. The corresponding values for the CFRP-RC specimens ranged from 1.0 to 1.70 and for the BFRP-RC specimens from 1.0 to 1.5. The higher values were achieved with the specimens with lower reinforcement ratios. Table 6.3 shows the experimental results of the crack width at 2,000 με and $0.3\,M_n$. The crack width of the FRP-RC specimens ranged from 0.31 mm to 0.47 mm at 2,000 με, with an average value 0.4 mm, while the corresponding crack width ranged from 0.37 mm to 0.89 mm at $0.3\,M_n$ with an average value of 0.68 mm. Therefore, the reference point at a tensile-strain level of 2,000 με might be more reasonable in defining the experimental service moment. El-Nemr et al. (2016) made similar observations in their investigation of the cracking behavior of rectangular concrete

beams reinforced with GFRP and CFRP bars. Therefore, the cracking regime in terms of strain is similar for the circular and rectangular sections.

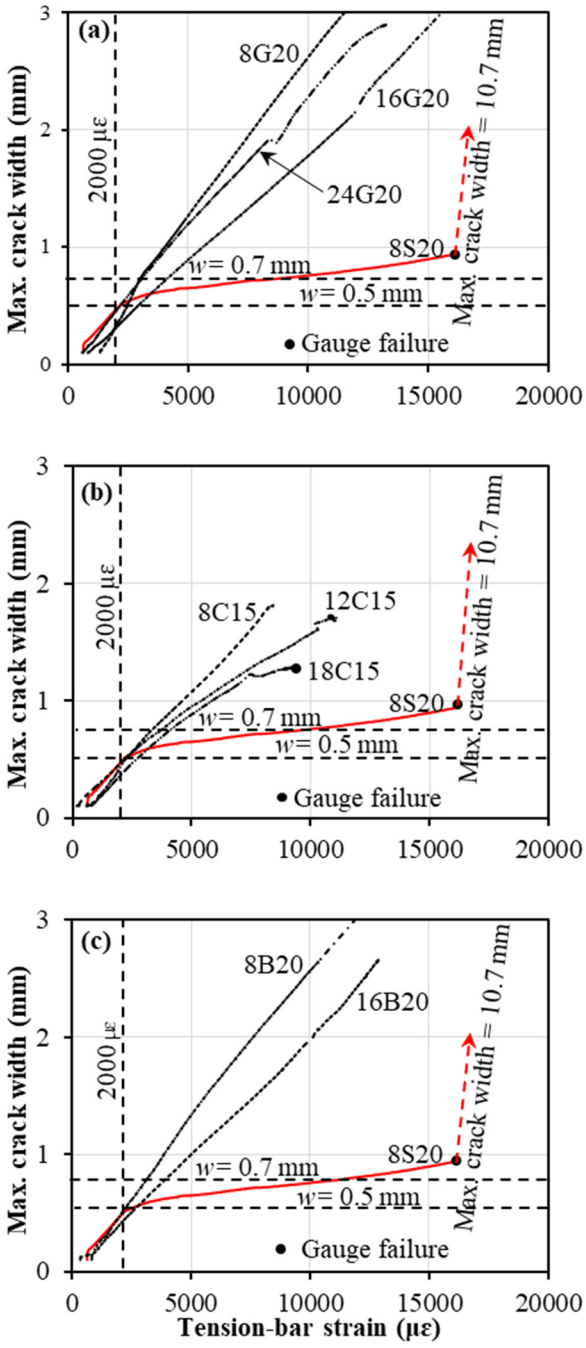

Figure 6.8 Crack width–strain in reinforcement relationships: (a) Group I versus Group IV, (b) Group II versus Group IV, (a) Group III versus Group IV.

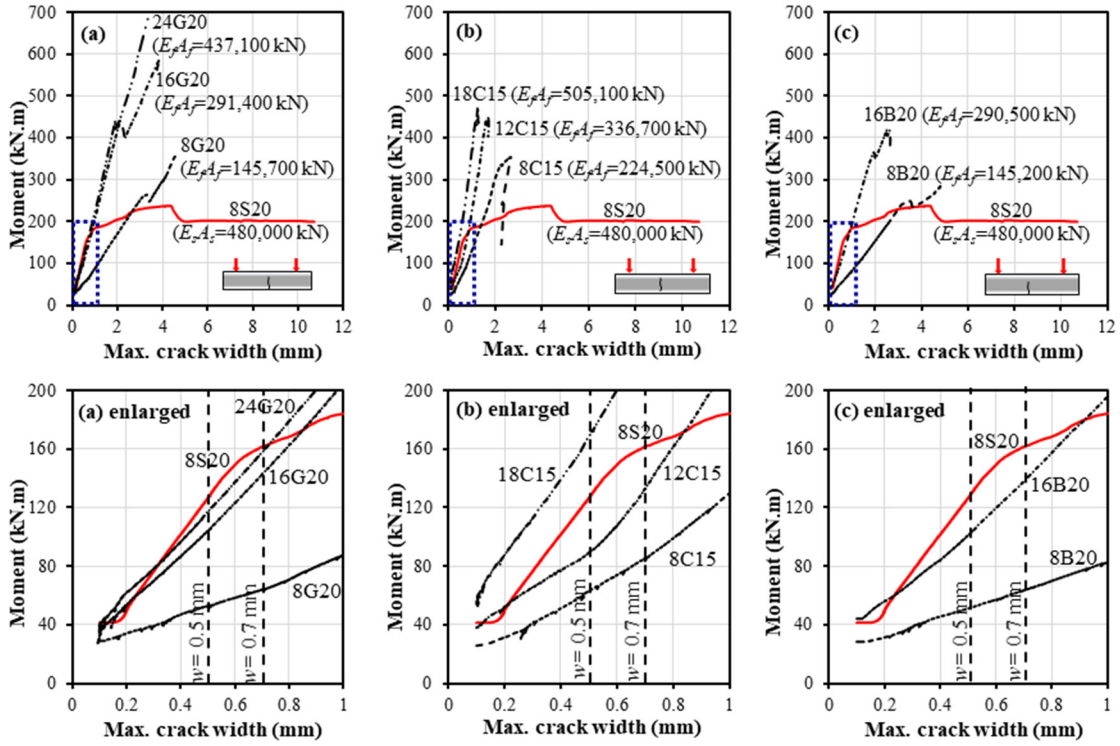

Figure 6.9 Moment–maximum crack-width relationships: (a) Group I versus Group IV, (b) Group II versus Group IV, (a) Group III versus Group IV.

6.6. Discussion of the Test Results

This section discusses the effect of the reinforcement ratio, modulus of elasticity, axial stiffness, and longitudinal-bar spacing on the measured crack widths of the specimens reinforced with FRP bars (GFRP, CFRP, and BFRP).

6.6.1. Effect of Reinforcement Ratio on the Measured Crack Width

Figure 6.9 shows that increasing the reinforcement ratio considerably reduced crack widths in the FRP specimens—regardless of reinforcement type—when compared at the same load level. Group I specimens experienced crack widths ranging between 0.31 mm (16G20) and 0.46 mm (24G20) at a service-load level of 2,000 με. Increasing the reinforcement ratio from 1.2% (8G20) to 2.3% (16G20) reduced the crack width by 9%. Increasing the reinforcement ratio from ρ_{fl} = 2.3% (16G20) to 3.5% (24G20) slightly reduced the crack width at different load levels. Specimen 8G20 (ρ_{fl} = 1.2%) experienced wider crack widths than 16G20 and 24G20

with higher reinforcement ratios (ρ_{ft} = 2.3% and 3.5%) by 27% and 35%, respectively. Increasing the CFRP reinforcement ratio (ρ_{ft}) from 0.8% to 1.8% enhanced significantly crack widths in the specimens at the same load levels. At a service moment of 0.3 M_n, the corresponding crack widths for the specimens reinforced with CFRP bars ranged between 0.37 mm (18C15) and 0.80 mm (8C15). The crack width decreased by 14% and 54% by increasing the reinforcement ratio from 0.8% (8C15) to 1.2% (12C15) and 1.8% (18C15), respectively. Finally, the measured crack widths for Group III specimens ranged between 0.40 mm (16B20) and 0.47 mm (8B20) at a service moment corresponding to 2,000 με. Increasing the reinforcement ratio from 1.2% (8B20) to 2.3% (16B20) reduced the crack width by 15%, while the measured crack widths, at a service moment of 0.3 M_n, ranged between 0.55 mm (16B20) and 0.87 mm (8B20). The crack in 8B20 (ρ_{ft} = 1.2%) was wider than that in 16B20 (ρ_{ft} = 2.3%) by 37%. At 2,000 με, all of the FRP specimens showed a crack width lower than 0.5 mm, while, at 0.3 M_n, seven specimens exceeded this limit. As mentioned previously, the strains at 0.3 M_n were high and not expected to satisfy the crack width criterion for external exposure at this load level.

6.6.2. Effect of Modulus of Elasticity and Axial Stiffness on the Measured Crack Width

The axial stiffness of the FRP specimens ($E_f A_f$) significantly affected the measured crack width. Figure 6.9 shows that 8G20 ($E_f A_f$ = 145,700 kN) and 8B20 ($E_f A_f$ = 145,200 kN)—with almost the same axial stiffness—had a similar moment–crack width relationship (see enlarged Figs. 6.9(a) and 6.9(c)). Similarly, 16G20 ($E_f A_f$ = 291,400 kN) had a moment–crack width relationship very close to that of 16B20 ($E_f A_f$ = 290,500 kN) with almost the same axial stiffness. Specimen 12C15, with higher axial stiffness ($E_f A_f$ = 336,700 kN), exhibited narrower widths at the same load level compared to specimens with similar reinforcement ratios (ρ_{ft} = 1.2%) (8G20, 8B20). Specimen 8C15 ($E_f A_f$ = 224,500 kN) also evidenced narrower crack

widths when compared to 8G20 and 8B20 at the same load level. In conclusion, as the axial stiffness of the longitudinal reinforcement increased—regardless of the reinforcement type—the measured crack width decreased at the same load level. Specimens 16G20, 24G20, 16B20, and 18C15 had almost the same moment–crack width relationship as control specimen 8S20 with an axial stiffness $E_s A_s$ of 480,000 kN until the steel yielded. On the other hand, as the surface conditions of the bars are similar, one value of k_b can be used for the GFRP, CFRP, and BFRP bars.

6.6.3. Effect of Bar Spacing on the Measured Crack Width

Bar spacing is one of the main parameters affecting the measured crack width. As can be seen from Fig. 6.9, the crack width decreased as did the bar spacing. It is worth mentioning that bar spacings were calculated with Eq. 6.20 in relation to Fig. 6.12. Specimens 8G20 and 8B20, with the same bar spacing (s = 148 mm) and almost the same axial stiffness, had similar moment–crack width relationships. The same behavior was observed in 16G20 and 16B20, with the same bar spacing (s = 74 mm) and almost the same axial stiffness. In addition, 16G20 and 24G20, with bar spacings of 74 mm and 99 mm, respectively, had quite similar moment–crack width relationships. This is attributed to the effect of distributing the bars in 24G20 as bundled bars (2x12), resulting in greater bar spacing when compared to a single-bar configuration. Similarly, the lower bar spacing in 8C15, 12C15, and 18C15, along with their increased axial stiffness, decreased the crack width when compared at the same load level. These results are in agreement with the AASHTO-09, CSA S6-14, and ACI 440.1R-15 models for cracking, as crack width is directly proportional to maximum bar spacing.

6.7. Theoretical Crack-Width Prediction

This section presents the details of estimating the crack width predictions for the FRP-RC members, including the calculation of service stresses, the redefinition of different variables in the prediction equations in design codes and guidelines in order to consider circular sections, and comparison with the experimental results.

6.7.1. Overview of Crack-Control Design Provisions

Two design methodologies exist for proportioning reinforcement to control flexural cracking: (1) a direct procedure in which crack widths are calculated, and (2) an indirect procedure in which maximum bar-spacing limits are specified. *AASHTO LRFD Bridge Design Specifications* (2012) (clause C 5.7.3.4) recommends cracking control for all reinforced-concrete members subject to cracking under any load condition, including thermal effects and deformation restraint, that produces tension in the gross section in excess of the concrete's cracking strength. The following sections provide a summary of codes and design guidelines for the flexural-cracking control of FRP-RC flexural members.

6.7.1.1. AASHTO LRFD Bridge Design Specifications AASHTO-09

AASHTO-09 recommends the calculation of crack width based on the physical model proposed by Frosch (1999), with crack width limit shall be set equal to 0.5 mm when GFRP reinforcement is used, as follows:

$$w_{\max} = 2\frac{f_{fs}}{E_f}\frac{h_2}{h_1}k_b\sqrt{d_c{}^2 + \frac{s^2}{4}} \qquad (6.1)$$

where $_w$ = maximum allowable crack width at the tension face (mm); f_{fs} = stress level induced in FRP at service loads (MPa); $_s$ = center-to-center bar spacing (mm); E_f = modulus of elasticity of GFRP reinforcement (MPa); and k_b = coefficient that accounts for the degree of bond between GFRP bars and surrounding concrete. The bond dependent coefficient, k_b, may be set equal to 1.4, unless a more detailed determination from experimental data is available.

6.7.1.2. Canadian Highway Bridge Design Code CAN/CSA S6-14

The *Canadian Highway Bridge Design Code* (CAN/CSA-S6-14) states that, if the maximum strain of FRP bars in the tension zone under full-service loads exceeds 0.0015, cross sections of the maximum positive and negative moment regions shall be proportioned in such a way that the crack width does not exceed 0.5 mm for members subjected to aggressive environments and 0.7 mm for other members, with the crack width calculated using a similar equation to that of AASHTO-09 [Eq. (6.1)]. The value of k_b shall be determined experimentally, but, in the

absence of data, values of 0.8 for sand-coated and 1.0 for deformed FRP bars shall be used. In addition, the clear cover shall not be greater than 50 mm in calculating d_c.

6.7.1.3. American Concrete Institute ACI440.1R-15

ACI 440.1R-15 recommends an indirect procedure that controls flexural-crack widths with a maximum reinforcing-bar spacing based on the approach proposed by Ospina and Bakis (2007) as follows:

$$s_{\max} = 1.15\frac{E_f w}{f_{fs} k_b} - 2.5c_c \le 0.92\frac{E_f w}{f_{fs} k_b} \tag{6.2}$$

where $s_{\max}$ = maximum permissible center-to-center bar spacing for flexural-crack control (mm); $_w$ = maximum allowable crack width (mm); f_{fs} = stress level induced in FRP at service loads (MPa); E_f = design or guaranteed modulus of elasticity of FRP reinforcement defined as the mean modulus of a sample of test specimens (MPa); c_c = clear cover (mm); and k_b is the bond-dependent coefficient. When k_b is not known from experimental data, a conservative value of 1.4 should be assumed (smooth bars and grids are specifically excluded from this recommendation).

A similar equation is currently being considered for Subcommittee ACI 440-H (ACI 440, 2017) for a future design standard by controlling and replacing the crack width w in Equation (6.2) with 0.7 mm as follows:

$$\begin{aligned} s_{\max} &= 1.15\frac{0.7\times E_f}{f_{fs} k_b} - 2.5c_c \le 0.92\frac{0.7\times E_f}{f_{fs} k_b} \\ &= \frac{0.805\times E_f}{f_{fs} k_b} - 2.5c_c \le \frac{0.644\times E_f}{f_{fs} k_b} \end{aligned} \tag{6.3}$$

A lower k_b value of 1.2 is intended to be considered by the Subcommittee ACI 440-H for GFRP bars.

6.7.1.4. Italian National Research Council CNR-DT 203/2006

In CNR-DT 203/2006, the maximum crack width value for FRP-RC members is calculated as follows:

$$w_{\max} = \beta s_{rm} \varepsilon_{fm} \tag{6.4}$$

where β = 1.7 when cracking is caused by load; when cracking is caused by superimposed deformations, β shall be taken as 1.7 for cross sections with a minimum dimension exceeding 800 mm and 1.3 for cross sections with a minimum dimension of 300 mm or less (linear interpolation may be used to calculate β for cross sections with a minimum dimension between these limits); s_{rm} = average crack spacing; and ε_{fm} = average strain in FRP reinforcement.

The average crack spacing, s_{rm}, can be calculated as follows (mm):

$$s_{rm} = 50 + 0.25 k_b k_l \frac{d_b}{\rho_{f,eff}} \tag{6.5}$$

where k_b = 1.6 is a coefficient accounting for the bond properties of the FRP bars; k_l = 0.5 for flexure and 1.0 for pure tension; d_b is the equivalent diameter of the FRP bars in mm; and $\rho_{f,eff}$ is the effective reinforcement ratio, equal to $A_f / A_{c,eff}$, where $A_{c,eff}$ is the effective area in tension defined as the concrete area surrounding the tensile FRP reinforcement, having a depth equal to 2.5 times the distance between tension fiber and bar centroid.

In the case of bundled bars, the equivalent bar diameter d_b is taken as $d_b\sqrt{n}$ where n = the number of bars in the bundle (EC2-2004).

The average strain in the FRP reinforcement ε_{fm} shall be calculated as follows:

$$\varepsilon_{fm} = \frac{f_f}{E_f}\left[1 - \beta_1 \beta_2 \left(\frac{f_{fr}}{f_f}\right)^2\right] \tag{6.6}$$

where f_f is the stress in tension reinforcement at the serviceability limit state and f_{fr} is the stress in FRP reinforcement under conditions causing initial cracking, both calculated on the basis of a cracked section; $\beta_1 = 0.5$ and is a nondimensional coefficient accounting for the bond properties of FRP bars; and β_2 is a nondimensional coefficient accounting for the duration of loading (1.0 for short loads and 0.5 for long or cyclic loads).

6.7.1.5. Japan Society of Civil Engineers JSCE-97

The maximum crack width can be calculated according to JSCE-97 with the following equation:

$$w_{\max} = k_b \left(4c_c + 0.7\left(s - d_b\right)\right)\left(\frac{f_{fe}}{E_f} + \varepsilon'_{csd}\right) \tag{6.7}$$

in which c_c is the concrete cover (mm); $_s$ and d_b are the center-to-center distance and diameter of the FRP reinforcement (mm), respectively; k_b is a constant expressing the effects of bond characteristics and multiple placement of reinforcing materials (generally between1.0 and 1.3); f_{fe} is the stress increase in reinforcement; and ε'_{csd} is the compressive strain for assessing the increment of crack width due to concrete shrinkage and creep. According to JSCE-97, the allowable crack widths for esthetic considerations may generally be set to not more than 0.5 mm, depending on the ambient environment of the structure.

6.7.2. Service Stress Derivation in FRP-RC Members with Circular Section

In general, at service loads, the distribution of stresses in the compression zone of a cracked section is close to being linear. As shown in Fig. 6.10, the strain behavior of FRP reinforcement is elastic. As a result, an elastic consideration yields a good estimate of the concrete and FRP stresses at service loads (ACI 440.1R-15).

The calculations of the elastic analysis are based on the following assumptions:

- The strain variations are assumed to be the same in concrete and FRP.

- The stresses in FRP reinforcement and concrete are assumed to be proportional to the strains.
- The concrete tensile stresses are neglected.
- The FRP reinforcement in the compression zone should be disregarded in the elastic analysis.

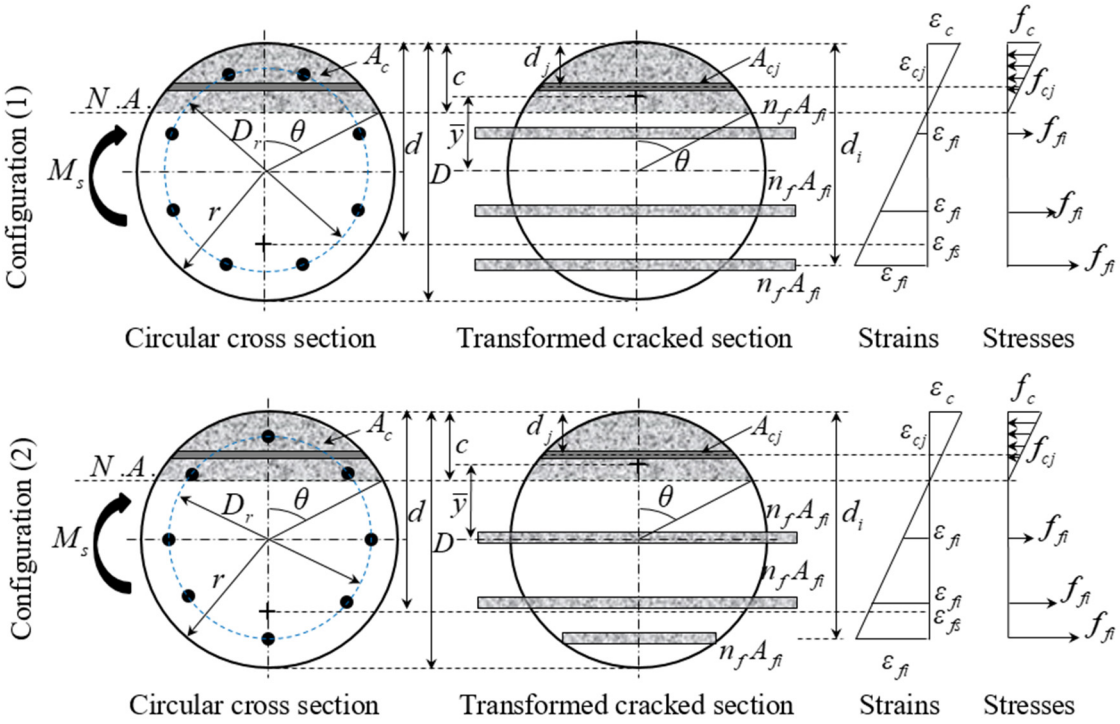

Figure 6.10 Transformed cracked section, strains, and stresses at service load condition.

The neutral axis is located at a distance, c, from the top compression fiber. The location of the neutral axis can be easily determined through a simple iteration of the neutral-axis depth c by taking the first moment of area about the location of the neutral axis using a cracked transformed section, as shown in Fig. 6.10 as follows:

$$A_c\left(c-r+\bar{y}\right)=\sum_{i=1}^{n} n_f A_{fi}\left(d_i-c\right) \tag{6.8}$$

$$A_c = r^2\left(\theta - sin\,\theta\, cos\,\theta\right) \tag{6.9}$$

$$\bar{y} = \frac{2r}{3}\left(\frac{sin^3\theta}{\theta - sin\theta\, cos\theta}\right) \tag{6.10}$$

$$cos\theta = 1 - \frac{c}{r} \tag{6.11}$$

where A_c is the area of the circular concrete segment; r is the radius of the circular cross section; A_{fi} is the area for the row of FRP bars at level i; d_i is the distance to the top compression fiber for each row of FRP bars at level i; c is the neutral-axis depth; and $\bar{y}$is the distance between the centroid of the circular concrete segment on the compression side to the centroid of the concrete cross section.

The service stress in the tensile FRP reinforcement f_{fs} can be computed with one of the following two approaches.

6.7.2.1. Approach (1): Calculation of Service Stress in the Extreme Tension Reinforcement

The service stress in the extreme tension FRP reinforcement f_{fs} can be computed using the service moment M_s as follows:

$$M_s = \sum_{j=1}^{m} A_{cj} f_{cj}\left(c - d_j\right) + \sum_{i=1}^{n} A_{fi} f_{fs} \frac{\left(d_i - c\right)}{\left(d_{i=1} - c\right)}\left(d_i - c\right) \tag{6.12.a}$$

$$\rightarrow M_s = \sum_{j=1}^{m} A_{cj} \frac{\left(c - d_j\right)}{c} f_c\left(c - d_j\right) + \sum_{i=1}^{n} A_{fi} f_{fs} \frac{\left(d_i - c\right)^2}{\left(d_{i=1} - c\right)} \tag{6.12.b}$$

$$\rightarrow M_s = \sum_{j=1}^{m} A_{cj} \frac{\left(c - d_j\right)^2}{c} \frac{c}{\left(d_{i=1} - c\right)} \frac{E_c}{E_f} f_{fs} + \sum_{i=1}^{n} A_{fi} f_{fs} \frac{\left(d_i - c\right)^2}{\left(d_{i=1} - c\right)} \tag{6.12.c}$$

$$\rightarrow M_s = \sum_{j=1}^{m} A_{cj} \frac{\left(c - d_j\right)^2}{\left(d_{i=1} - c\right)} \frac{1}{n_f} f_{fs} + \sum_{i=1}^{n} A_{fi} f_{fs} \frac{\left(d_i - c\right)^2}{\left(d_{i=1} - c\right)} \tag{6.12.d}$$

$$\rightarrow M_s = \frac{1}{n_f} f_{fs} \frac{1}{\left(d_{i=1} - c\right)} \sum_{j=1}^{m} A_{cj} \left(c - d_j\right)^2 + f_{fs} \frac{1}{\left(d_{i=1} - c\right)} \sum_{i=1}^{n} A_{fi} \left(d_i - c\right)^2 \tag{6.12.e}$$

$$\rightarrow M_s = f_{fs} \frac{1}{\left(d_{i=1} - c\right)} \left[\frac{1}{n_f} \sum_{j=1}^{m} A_{cj} \left(c - d_j\right)^2 + \sum_{i=1}^{n} A_{fi} \left(d_i - c\right)^2 \right] \tag{6.12.f}$$

$$f_{fs} = \frac{M_s \left(d_{i=1} - c\right)}{\left[\frac{1}{n_f} \sum_{j=1}^{m} A_{cj} \left(c - d_j\right)^2 + \sum_{i=1}^{n} A_{fi} \left(d_i - c\right)^2 \right]} \tag{6.13}$$

In the case of bending moment combined with axial compression force, Eq. (6.13) can be written as follows:

$$f_{fs} = \frac{\left(M_s - N_s \times \left(r - c\right)\right) \times \left(d_{i=1} - c\right)}{\left[\frac{1}{n_f} \sum_{j=1}^{m} A_{cj} \left(c - d_j\right)^2 + \sum_{i=1}^{n} A_{fi} \left(d_i - c\right)^2 \right]} - \frac{N_s}{A_{trans.}} \tag{6.14}$$

where n_f is the ratio of the modulus of elasticity of FRP bars to the modulus of elasticity of concrete; $d_{i=1}$ is the distance from the extreme tension FRP bars to the top compression fiber; A_{cj} is the area for the layer of concrete at level j; d_j is the distance to the top compression fiber for each layer of concrete at level j; N_s is the service axial compression force; and $A_{trans.} = A_c + \sum_{i=1}^{n} n_f A_{fi}$.

It should be noted that calculating service stress with Eq. (6.13) adjusted for circular FRP-reinforced sections provides values quite similar to those calculated with Eq. (6.15) in ACI 440.1R-15.

$$f_{fs} = M_s \frac{n_f \left(d_{i=1} - c\right)}{I_{cr}} \tag{6.15}$$

In the case of bending moment combined with axial compression force, Eq. (6.15) can be written as follows:

$$f_{fs} = \left(M_s - N_s \times (r-c)\right)\frac{n_f\left(d_{i=1}-c\right)}{I_{cr}} - \frac{N_s}{A_{trans.}} \tag{6.16}$$

where I_{cr} is the moment of inertia of the cracked circular section and can be calculated with Eq. 6.17.

$$I_{cr} = I_c + A_c\left(\left(c-r+\bar{y}\right)^2 - \bar{y}^2\right) + \sum_{i=1}^{n} n_f A_{fi}\left(d_i - c\right)^2 \tag{6.17}$$

$$I_c = \frac{r^4}{4}\left(\theta - \sin\theta\cos\theta + 2\sin^3\theta\cos\theta\right) \tag{6.18}$$

6.7.2.2. Approach (2): Calculation of Service Stress at Centroid of Tension Reinforcement

The service stress in the tension FRP reinforcement f_{fs} can be computed at a distance d from the top compression fiber by dividing the service moment M_s by the product of the reinforcement area and the internal moment arm (CSA S806-12; Nanni et al. 2014). In the case of bending moment combined with axial compression force, the service stress in the tension FRP reinforcement f_{fs} can be computed at a distance d from the top compression fiber by dividing the service moment $\left(M_s - N_s \times (r-c)\right)$ by the product of the reinforcement area and the internal moment arm, and then subtracting $N_s / A_{trans.}$ from the result.

The effective depth d is taken as the distance from the extreme compression fiber to the centroid of the tension reinforcement (see Fig. 6.11) and can be calculated using Eq. 6.19 given in AASHTO *LRFD Bridge Design Specifications* (2012) as proposed by Feltham (2004).

$$d = \frac{D}{2} + \frac{D_r}{\pi} \tag{6.19}$$

where D_r is the diameter of the circle passing through the centers of the longitudinal reinforcement; D is the diameter of the circular cross section; and the area of tension reinforcement A_f is the area of the FRP bars below the mid-depth of the section.

Feltham (2004) considered the effective flexural depth d to be taken as the depth to the centroid of the reinforcement below the centerline of the section (Fig. 6.11). The centroid's position depends on bar orientation. For six bars (the minimum number for a circular section), its distance below the centerline varies between $0.29D_r$ and $0.33D_r$. For larger numbers of bars, the distance tends to be D_r/π below the centerline. It was stated that, because, the orientation of the cages relative to the applied lateral force is usually unknown in the case of pier and pile applications, it seems reasonable to use this value for all sections, unless better information is known (Feltham 2004). The inaccuracy in d will always be less than 4%. It is worth mentioning that the linear-elastic behavior of FRP bars up to failure resulted in the centroid of area coinciding with the centroid of forces.

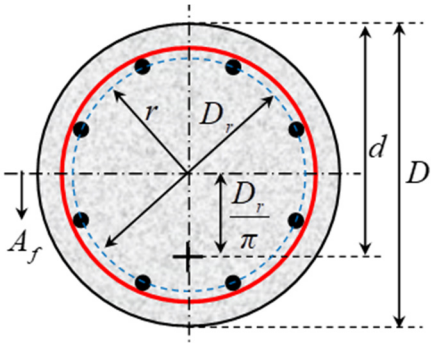

Figure 6.11 Definition of the effective depth, d .

6.7.3. Crack-Width Prediction for Circular FRP-RC Members

The applicability and accuracy of the current FRP codes and design guidelines for cracking control are assessed herein by comparing their predictions with the experimentally determined crack widths for the eight circular FRP-RC specimens. To help in assessing the accuracy of these crack-control equations and to account for the circular-section geometry, the different variables and parameters in the crack-control design equations are presented and explained below.

Figure 6.12 presents the redefinition of the parameters in the codes and design guidelines for checking cracking in members with circular cross sections with two different bar configurations. Figure 6.12(a) redefines the parameters in AASHTO-09, CSA S6-14, ACI 440.1R-15, and

JSCE-97 equations (Eqns. 6.1, 6.2, and 6.7) and Fig. 6.12 (b) redefines the parameters of the CNR-DT 203/2006 equation (Eq. 6.4), as follows:

- s = the center-to-center longitudinal-bar spacing, which can be calculated with Eq. (6.20):

$$s = \frac{\pi D_r}{N} \tag{6.20}$$

where N is the number of longitudinal bars.

- h_1 is taken as the distance from the extreme tension reinforcement to the neutral axis according to the calculation in Approach (1), h_{11}, and the distance from the centroid of the tension reinforcement to the neutral axis using Eq. 6.21 according to the calculation in Approach (2), h_{12} (in mm), as shown in Fig. 6.12:

$$h_1 = \left(\frac{D}{2} - c\right) + \frac{D_r}{\pi} \tag{6.21}$$

- h_2 is the distance from the extreme tension surface to the neutral axis (in mm):

- d_c is the concrete cover measured from the circle passing through the centers of the longitudinal reinforcement to the extreme surface of the circular section (in mm):

- $A_{c,eff}$ is the effective tension area of concrete surrounding the flexural tension reinforcement and having a depth equal to 2.5 times the distance between tension fiber and bar centroid, divided by the number of bars (in mm^2), and can be easily calculated for the circular section with Eq. (6.22):

$$A_{c,eff} = \frac{\pi\left(D^2 - \left(D - 5d_c\right)^2\right)/4}{N} \tag{6.22}$$

- $\rho_{f,eff}$ is the effective reinforcement ratio, which can be calculated for the circular section as follows:

$$\rho_{f,eff} = \rho_{ft} \frac{A_g}{A_{c,eff}} = \rho_{ft} \frac{D^2}{D^2 - (D - 5d_c)^2} \tag{6.23}$$

where A_g is the gross sectional area of the circular section and ρ_{ft} is the total reinforcement ratio.

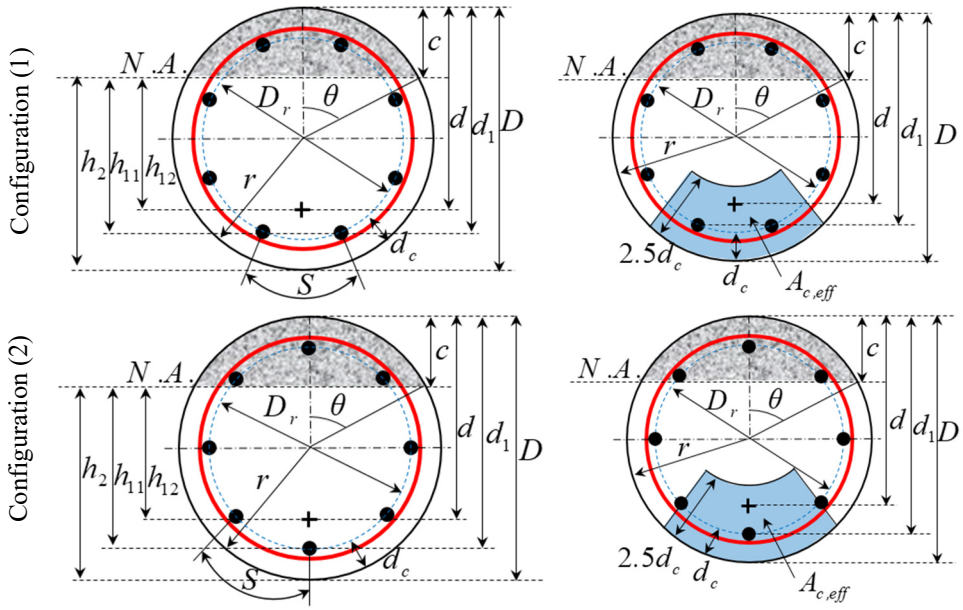

Figure 6.12 Notation of circular cross section according to (a) AASHTO-09, CSA S6-14, ACI440.1R-15, and JSCE-97; (b) CNR-DT 203/2006.

6.7.4. Crack-Width Comparison between the Experimental and Predicted Results

The accuracy of the crack-control equations in AASHTO-09, CSA S6-14, ACI 440.1R-15, CNR-DR 203/2006, and JSCE-97 are assessed herein by comparing their predictions with the experimentally determined crack widths. Tables 6.4 and 6.5 provide the mean values and the coefficients of variation (COV) for the ratios of the measured to predicted maximum crack widths $\left(w_{\exp.}/w_{pred.}\right)$ using the two approaches. Figures 6.13–6.17 show the comparison of the experimental and predicted results using AASHTO-09, CSA S6-14, ACI 440.1R-15, CNR-DT 203/2006, and JSCE-97.

Table 6.4 Experimental to predicted crack width $\left(w_{\exp.}/w_{pred.}\right)$ at service moment using Approach (1).

Specimen ID	Crack width w at (mm)		$w_{\exp.}/w_{pred.}$									
	2,000 με	0.30 M_n	AASHTO-09 k_b =1.4		CSA S6-14 k_b = 0.8		ACI440.1R-15 k_b =1.4 (ACI 440-H k_b =1.2)		CNR-DT 203/2006 k_b =1.6		JSCE-97 k_b =1.15	
			at 2,000 με	0.30 M_n	at 2,000 με	0.30 M_n	at 2,000 με	0.30 M_n	at 2,000 με	0.30 M_n	at 2,000 με	0.30 M_n
8G20	0.34	0.89	0.67	0.91	1.17	1.59	0.63 (0.73)	0.86 (1.00)	0.46	0.54	0.62	0.85
16G20	0.31	0.65	0.81	0.93	1.41	1.63	0.79 (0.93)	0.92 (1.07)	0.66	0.71	0.70	0.80
24G20	0.46	0.58	1.01	1.04	1.77	1.81	0.96 (1.12)	0.98 (1.15)	0.87	0.89	0.87	0.89
8C15	0.46	0.80	0.88	0.88	1.53	1.54	0.82 (0.96)	0.82 (0.96)	0.47	0.44	0.81	0.81
12C15	0.41	0.69	0.98	1.01	1.71	1.77	0.91 (1.06)	0.92 (1.07)	0.59	0.58	0.84	0.85
18C15	0.36	0.37	0.94	0.88	1.64	1.54	0.88 (1.02)	0.86 (1.00)	0.65	0.63	0.75	0.73
8B20	0.47	0.87	0.71	0.84	1.24	1.47	0.65 (0.76)	0.80 (0.93)	0.45	0.51	0.65	0.79
16B20	0.40	0.55	0.91	0.95	1.60	1.67	0.87 (1.01)	0.93 (1.09)	0.74	0.76	0.77	0.81
Average			0.86	0.93	1.51	1.63	0.81 (0.95)	0.89 (1.03)	0.61	0.63	0.75	0.82
Standard deviation			0.12	0.07	0.22	0.12	0.12 (0.14)	0.06 (0.07)	0.15	0.15	0.09	0.05
COV (%)			14	7	14	7	15 (15)	7 (7)	24	24	12	6

Table 6.5 Experimental to predicted crack width $\left(w_{\exp.}/w_{pred.}\right)$ at service moment using Approach (2).

Specimen ID	Crack width w at (mm)		$w_{\exp.}/w_{pred.}$									
	2,000 με	0.30 M_n	AASHTO-09 k_b =1.4		CSA S6-14 k_b = 0.8		ACI440.1R-15 k_b =1.4 (ACI 440-H k_b =1.2)		CNR-DT 203/2006 k_b =1.6		JSCE-97 k_b =1.15	
			at 2,000 με	0.30 M_n	at 2,000 με	0.30 M_n	at 2,000 με	0.30 M_n	at 2,000 με	0.30 M_n	at 2,000 με	0.30 M_n
8G20	0.34	0.89	0.49	0.66	0.85	1.16	0.57 (0.66)	0.77 (0.90)	0.41	0.49	0.57	0.77
16G20	0.31	0.65	0.63	0.73	1.11	1.27	0.78 (0.90)	0.89 (1.04)	0.63	0.69	0.69	0.78
24G20	0.46	0.58	0.82	0.85	1.44	1.49	1.00 (1.17)	1.04 (1.21)	0.92	0.94	0.92	0.95
8C15	0.46	0.80	0.71	0.70	1.24	1.23	0.82 (0.96)	0.82 (0.96)	0.47	0.45	0.81	0.82
12C15	0.41	0.69	0.81	0.82	1.41	1.44	0.95 (1.11)	0.96 (1.12)	0.62	0.60	0.87	0.88
18C15	0.36	0.37	0.71	0.70	1.24	1.23	0.88 (1.02)	0.86 (1.00)	0.65	0.64	0.75	0.74
8B20	0.47	0.87	0.67	0.69	1.18	1.21	0.80 (0.93)	0.81 (0.94)	0.58	0.51	0.78	0.80
16B20	0.40	0.55	0.69	0.73	1.21	1.28	0.85 (0.99)	0.90 (1.05)	0.73	0.74	0.75	0.80
Average			0.69	0.74	1.21	1.29	0.83 (0.97)	0.88 (1.03)	0.63	0.63	0.77	0.82
Standard deviation			0.11	0.07	0.18	0.11	0.13 (0.15)	0.09 (0.10)	0.16	0.16	0.11	0.07
COV (%)			15	9	15	9	16 (16)	10 (10)	25	25	14	8

As shown in Fig. 6.13, AASHTO-09 yielded good yet conservative predictions of the maximum crack width using Approach (1). The $w_{\exp.}/w_{pred.}$ ranged between 0.67 and 1.01 at 2,000 με with an average of 0.86±0.12 and a corresponding COV of 14%, and ranged between 0.84 and 1.04 at $0.30M_n$ with an average of 0.93±0.07 and a corresponding COV of 7%. While, AASHTO-09 exhibited conservative predictions of the maximum crack width using Approach (2) (see Fig. 6.13). The $w_{\exp.}/w_{pred.}$ ranged between 0.49 and 0.82 at 2,000 με with an average of 0.69±0.11 and a corresponding COV of 15%, and ranged between 0.66 and 0.85 at $0.30M_n$ with an average of 0.74±0.07 and a corresponding COV of 9%.

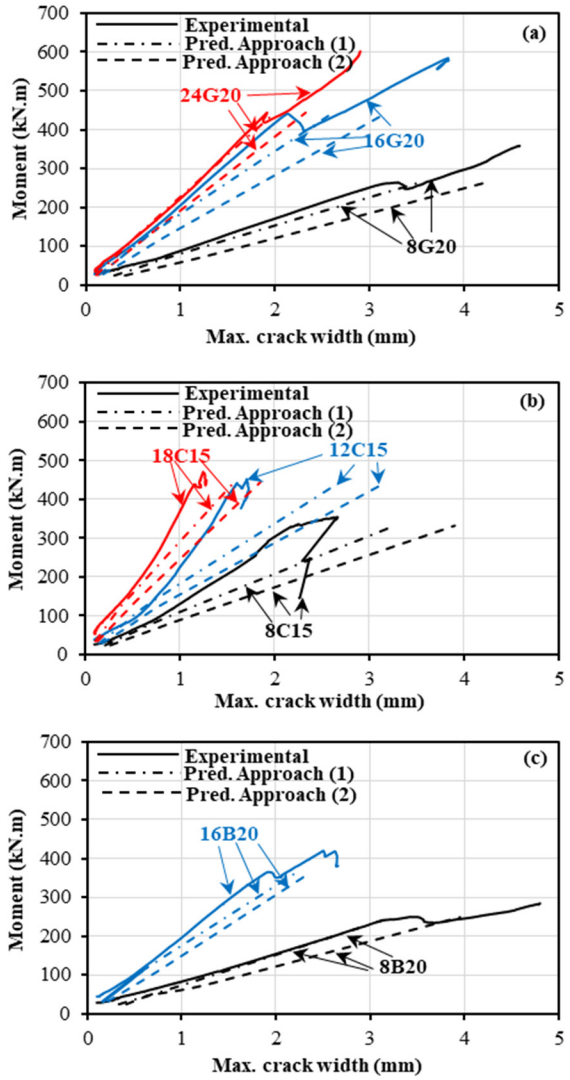

Figure 6.13 Comparisons of measured crack widths with AASHTO-09 predictions: (a) Group I, (b) Group II, (c) Group III.

The AASHTO equation accounts for the effect of varying reinforcement ratios by including the stress in the reinforcing bar f_{fs} and the spacing between the longitudinal bars. Therefore, the prediction equation reflects the effect of varying the reinforcement ratio and bar spacing on the maximum crack width. The conservative k_b value of 1.4, as recommended in AASHTO, resulted in conservative predictions of the crack widths.

The CSA S6-14 predictions underestimated the maximum crack width with Approach (1), as shown in Fig. 6.14. The $w_{\text{exp.}}/w_{pred.}$ ranged between 1.17 and 1.77 at 2,000 με with an average of 1.51±0.22 and a corresponding COV of 14%, and ranged between 1.47 and 1.81 at 0.30 M_n with an average of 1.63±0.12 and a corresponding COV of 7%. Similarly, CSA S6-14 yielded underestimated predictions of the maximum crack with Approach (2) (see Fig. 6.14). The $w_{\text{exp.}}/w_{pred.}$ ranged between 0.85 and 1.44 at 2,000 με with an average of 1.21±0.18 and a corresponding COV of 15%, and ranged between 1.16 and 1.49 at 0.30 M_n with an average of 1.29±0.11 and a corresponding COV of 9%. Similarly to the AAASHTO-09 equation, the CSA S6-14 equation accounts for the effect of varying reinforcement ratios by including the stress in reinforcing bar f_f the spacing between the longitudinal bars, and h_2/h_1 to account for the strain gradient. The recommended small value of k_b (0.8) in CSA S6-14 compared to those recommended in AASHTO (1.4) contributed to underestimating the crack widths.

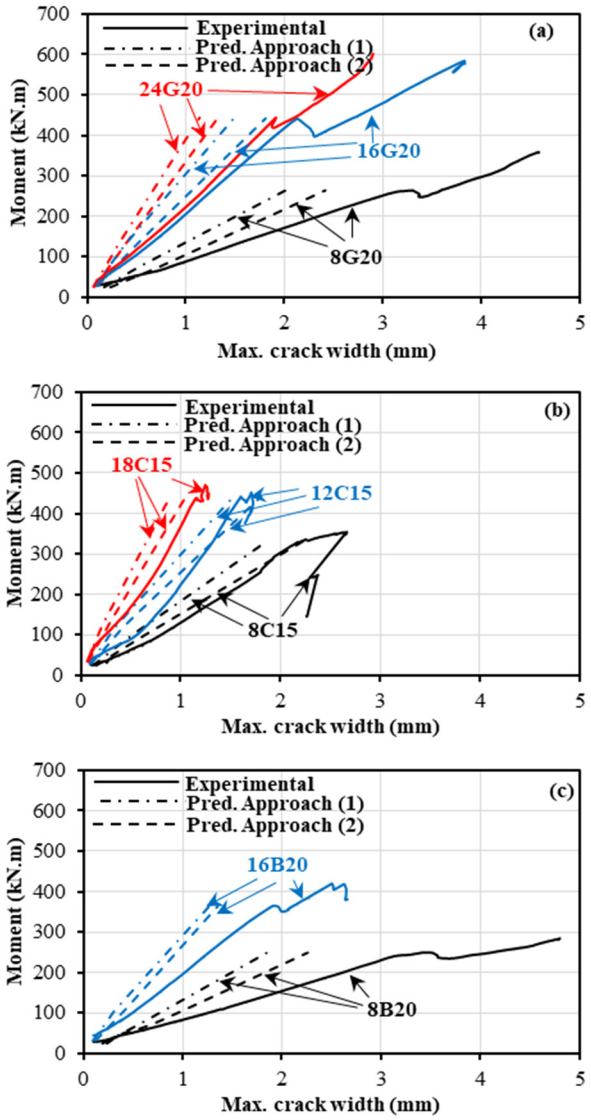

Figure 6.14 Comparisons of measured crack widths with CSA S6-14 predictions: (a) Group I, (b) Group II, (c) Group III.

As shown in Fig. 6.15, ACI 440.1R-15 yielded good yet conservative predictions of the maximum crack width using Approach (1). The $w_{\exp.}/w_{pred.}$ ranged between 0.63 and 0.96 at 2,000 με with an average of 0.81±0.12 and a corresponding COV of 15%, and ranged between 0.80 and 0.98 at $0.30M_n$ with an average of 0.89±0.06 and a corresponding COV of 7%. Similarly, ACI 440.1R-15 exhibited good yet conservative predictions of the maximum crack width using Approach (2) (see Fig. 6.15). The $w_{\exp.}/w_{pred.}$ ranged between 0.57 and 1.0 at 2,000 με with an average of 0.83±0.13 and a corresponding COV of 16%, and ranged between 0.77

and 1.04 at 0.30 M_n with an average of 0.88±0.09 and a corresponding COV of 10%. The ACI 440.1R-15 equation accounts for the effect of varying reinforcement ratios by including the stress in the reinforcing bar f_{fs} and the spacing between the longitudinal bars. Therefore, the prediction equation reflects the effect of varying the reinforcement ratio and bar spacing on the maximum crack width. The conservative k_b value of 1.4, as recommended in ACI 440.1R-15, resulted in conservative predictions of the crack widths.

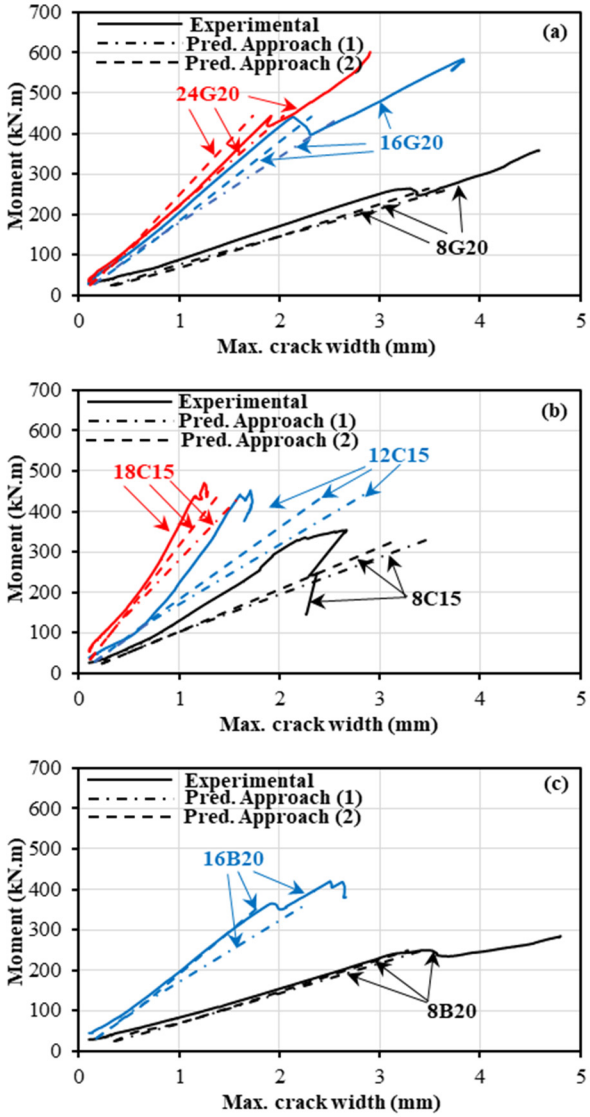

Figure 6.15 Comparisons of measured crack widths with ACI440.1R-15 predictions: (a) Group I, (b) Group II, (c) Group III.

Using a k_b value of 1.2, which is currently being considered for Subcommittee ACI 440-H (ACI 440, 2017), provided accurate predictions with Approach (1), on average, with a $w_{\text{exp.}}/w_{pred.}$ of 0.95 ± 0.14 with a COV of 15% and 1.03 ± 0.07 with a COV of 7% at 2,000 με and at $0.30M_n$, respectively. Similarly to Approach (1), Approach (2) yielded accurate predictions, on average, with a $w_{\text{exp.}}/w_{pred.}$ of 0.97 ± 0.15 with a COV of 16% and 1.03 ± 0.10 with a COV of 10% at 2,000 με and at $0.30M_n$, respectively.

The CNR-DT 203/2006 equation overestimated the maximum crack width with Approach (1) by a considerable margin, as shown in Fig. 6.16. The $w_{\text{exp.}}/w_{pred.}$ ranged between 0.45 and 0.87 at 2,000 με with an average of 0.61±0.15 and a corresponding COV of 24%, and ranged between 0.44 and 0.89 at $0.30M_n$ with an average of 0.63±0.15 and a corresponding COV of 24%. Similarly, the CNR-DT 203/2006 equation overestimated the maximum crack width with Approach (2), as shown in Fig. 6.16. The $w_{\text{exp.}}/w_{pred.}$ ranged between 0.41 and 0.92 at 2,000 με with an average of 0.63±0.16 and a corresponding COV of 25%, and ranged between 0.45 and 0.94 at $0.30M_n$ with an average of 0.63±0.16 and a corresponding COV of 25%. The CNR-DT 203/2006 equation accounts for the effect of varying reinforcement ratios by including the stress in the reinforcing bar, f_f, and the effective reinforcement ratio, $\rho_{f,eff}$. On the other hand, the recommended k_b value of 1.6 by CNR-DT 203/2006 attributed to overestimating the crack widths.

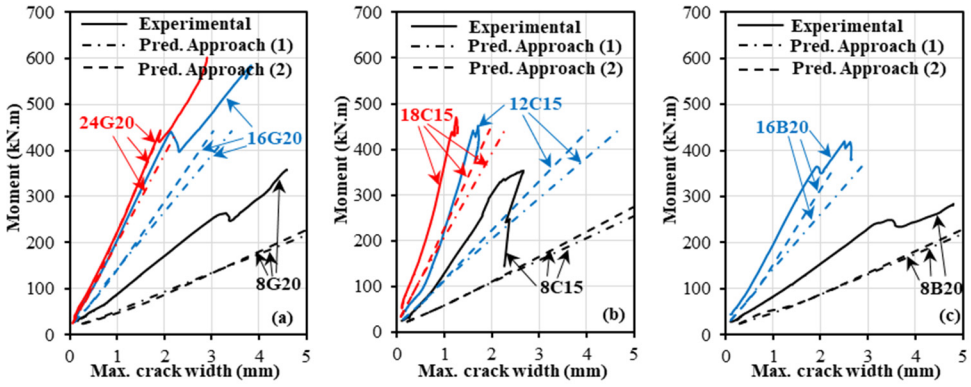

Figure 6.16 Comparisons of measured crack widths with CNR-DT 203/2006 predictions: (a) Group I, (b) Group II, (c) Group III.

Lastly, the JSCE-97 equation yielded conservative predictions of the maximum crack width with Approach (1) (see Fig. 6.17). The $w_{\exp.}/w_{pred.}$ ranged between 0.62 and 0.87 at 2,000 με with an average of 0.75±0.09 and a corresponding COV of 12%, and ranged between 0.73 and 0.89 at 0.30 M_n with an average of 0.82±0.05 and a corresponding COV of 6%. Similarly, the JSCE-97 equation exhibited conservative predictions of the maximum crack width with Approach (2) (see Fig. 6.17). The $w_{\exp.}/w_{pred.}$ ranged between 0.57 and 0.92 at 2,000 με with an average of 0.77±0.11 and a corresponding COV of 14%, and ranged between 0.74 and 0.95 at 0.30 M_n with an average of 0.82±0.07 and a corresponding COV of 8%. The k_b value of 1.15 taken in the calculation as the average of the range recommended in JSCE-97 resulted good yet conservative predictions. In conclusion, the crack-control formulae developed on rectangular members can be used for the cracking control of circular members when the parameters redefined herein are used.

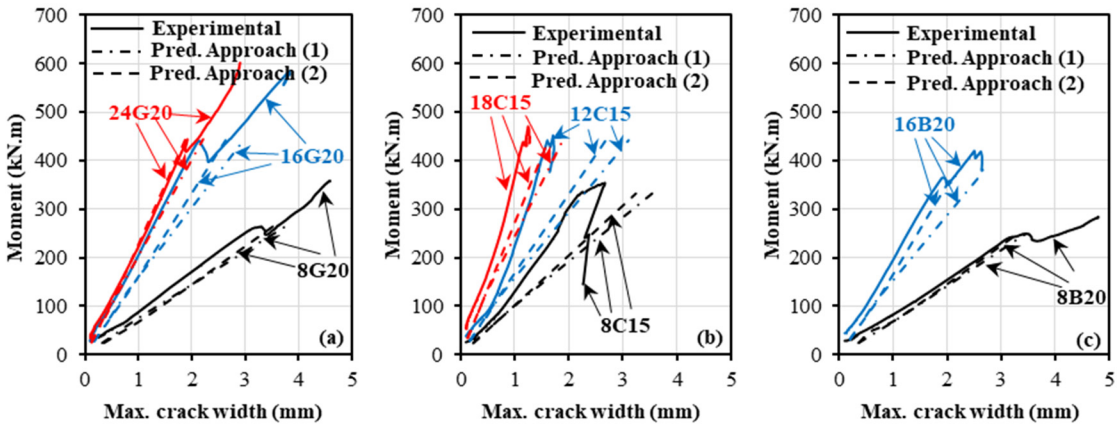

Figure 6.17 Comparisons of the measured crack widths with JSCE-97 predictions: (a) Group I, (b) Group II, (c) Group III.

6.7.5. Parametric Investigation

A parametric investigation was carried out to study the effect of axial compression load on the crack width of circular FRP-RC members. Specimen 16G20 was used in this investigation. The chosen axial compression-load level ranged from 0% to 30% of $0.3f'_cA_g$ in 5% increments, while a service load moment M_s of 0.30 M_n was kept constant. Figure 6.18 shows the relation

between the maximum crack width and the axial compression load level P_i/P_o, where P_i is the axial compression load level and $P_o = 0.3 f_c' A_g$. The crack widths reduced gradually by approximately 20% for each increment of 5% in the axial-load level considering the AASHTO-09 equation (see Fig. 6.18), and for both approaches 1 and 2. Similar proportions were obtained for CSA S6-14, ACI 440.1R-15, CNR-DT 203/2006, and JSCE-97. In conclusion, considering the axial compression load provided narrower crack widths at the same service load moment M_s, while ignoring its contribution, added to the level of conservativeness.

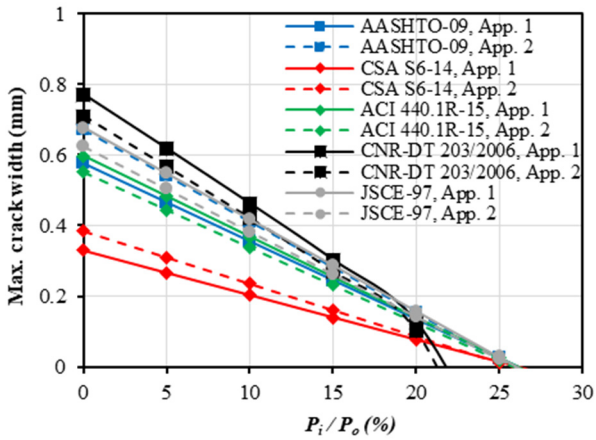

Figure 6.18 Crack width-axial load level relationship.

6.8. Conclusions

A total of nine full-scale circular RC specimens 0.5 m in diameter and 6 m in length were constructed and tested up to failure under four-point bending loading. The test specimens were divided into four groups according to the test parameters being investigated. The test parameters included the longitudinal reinforcement ratio; the longitudinal reinforcement type, including glass-FRP, carbon-FRP, basalt-FRP, and steel bars. Crack-control models developed for rectangular members in the current Bridge Design Codes (AASHTO-09 and CSA S6-14) and other available FRP codes and design guidelines were reexamined, extended, and applied to circular FRP-RC members. Crack width predictions were compared with the experimental results. Based on the results of this investigation, the following conclusions can be drawn:

1. Following cracking, the eight circular specimens reinforced with FRP bars (GFRP, CFRP, and BFRP) showed a linear crack response up to failure. On the other hand, the early yielding of the steel bars in 8S20 prior to concrete crushing resulted in wider and concentrated cracks in the constant moment zone.

2. As the reinforcement ratio increased in the circular GFRP-reinforced specimens, the average crack spacing and crack penetration depth decreased. Similar observations were made for the circular CFRP- and BFRP-reinforced specimens.

3. Based on the data presented in this study, the reference point at a tensile strain of 2,000 $\mu\varepsilon$ in the reinforcement might be more reasonable in defining the experimental service moment than $0.3\,M_n$.

4. As the axial stiffness of longitudinal reinforcement increased—regardless of the type of reinforcement—the measured crack width decreased at the same load level.

5. Decreasing the bar spacing in the specimens and increasing their axial stiffness decreased the crack width at the same load level. These results are in agreement with the AASHTO-09, CSA S6-14, ACI 440.1R-15, and JSCE-97 models for cracking, as the crack width is directly proportional to the maximum bar spacing.

6. Design equations for estimating the service stress in FRP reinforcement and the cracked moment of inertia were theoretically derived and presented for circular FRP-RC members.

7. The crack-control formulae developed on rectangular FRP-RC members are intended to allow for controlling the cracking of circular FRP-RC members using the redefined parameters developed and proposed in herein.

8. Comparing the crack widths predicted according to the various codes to the experimental results using the two approaches revealed that the AASHTO-09, ACI 440.1R-15, JSCE-97, and CNR-DT 203/2006 predictions were generally conservative with respect to the experimental crack width values. On the other hand, CAN/CSA S6-14 predictions were nonconservative compared to the experimental crack width values at high stress levels.

Further investigations on the bond coefficient k_b of 0.8 recommended by CAN/CSA S6-14 for sand-coated FRP bars are required.

9. Based on the parametric investigation on the effect of the axial load level, considering the axial compression load provided narrower crack widths, while ignoring its contribution, added to the level of conservativeness.

10. Design examples for estimating the crack widths of circular FRP-RC members were presented.

11. The experimental evidence from this investigation provides some experimental backbone for including crack design provisions in bridge-design specifications for the use of FRP bars in flexural members for bridge pier and pile applications. The present study on flexural behavior of circular concrete members reinforced with FRP bars and spirals (GFRP, CFRP, and BFRP) has answered significant number of questions in cracking and crack control issues.

CHAPTER 7. DEFLECTION PREDICTION METHODOLOGY FOR CIRCULAR RC MEMBERS REINFORCED WITH FRP BARS

Foreword

Authors and Affiliation:

- Salaheldin Mousa: Ph.D. candidate, Department of Civil Engineering, Université de Sherbrooke, Sherbrooke, Quebec, Canada, J1K 2R1.
- Hamdy M. Mohamed: Research Associate/Lecturer, Department of Civil Engineering, Université de Sherbrooke, Sherbrooke, Quebec, Canada, J1K 2R1.
- Brahim Benmokrane: Professor, Department of Civil Engineering, Université de Sherbrooke, Sherbrooke, Quebec, Canada, J1K 2R1.

Journal Title: *ACI Structural Journal*

Paper Status: Accepted on August 02, 2018

Contribution in thesis:

This chapter investigates serviceability performance in terms of deflection predictions of circular FRP-RC members experimentally and theoretically. The measured deflections and experimental values of the effective moment of inertia (I_e) were analyzed and compared with those predicted using available models in the literature, and in design guidelines and codes. Based on the analysis of the test results, a new equation was developed to accurately predict the deflection of the tested circular specimens. Moreover, an analytical model has been developed by using a layer-by-layer curvature analysis approach based on cross-sectional analysis satisfying strain compatibility and equilibrium conditions.

Abstract

The design of concrete members reinforced with fiber-reinforced polymer reinforcement (FRPRC members) is typically governed by serviceability-limit-state requirements rather than ultimate-limit-state requirements. ACI440.1R deflection design equations were introduced and assessed based on experimental work on FRPRC members with rectangular sections. These equations have not been assessed for circular sections for inclusion in an anticipated FRPRC design code currently being prepared by ACI 440 Committee.

This research program was designed to evaluate the deflection predictions of circular FRPRC members using the available design equations. A total of eight full-scale circular RC members measuring 500 mm (20 in.) in diameter and 6,000 mm (236.22 in.) in length were constructed and tested up to failure under four-point bending load. The test parameters included the type of FRP reinforcing bars and the reinforcement ratio. Three specimens were reinforced with glass-FRP (GFRP) bars, three were reinforced with carbon-FRP (CFRP) bars, and two were reinforced with basalt-FRP (BFRP) bars. The measured deflections and experimental values of the effective moment of inertia (I_e) were analyzed and compared with those predicted using models in the literature, as well as those in design guidelines and codes. Based on the analysis of the test results, a new equation was developed to accurately predict the deflection of the tested circular specimens. Moreover, an analytical model was developed using a layer-by-layer curvature-analysis approach based on cross-sectional analysis satisfying strain compatibility and equilibrium conditions. The load–deflection relationship for circular FRPRC members can be generated based on the calculation of curvature with an incremental-strain technique. The comparisons with the experimental results indicate the model's capability of reproducing the experimental load–deflection responses of the tested circular specimens.

Keywords: Circular concrete members, deflection, FRP, effective moment of inertia, serviceability.

7.1. Introduction

Deflection control is an important performance criterion that needs to be satisfied to ensure the serviceability of fiber-reinforced-polymer-reinforced concrete (FRPRC) structures. Under similar circumstances, in terms of concrete strength, applied loads, identical size, and reinforcement layout, FRP-reinforced concrete members are expected to develop larger deformations than steel-reinforced concrete members due to the variable stiffness, linear elastic behavior, and particular bond features of FRP reinforcement (ACI 440.1R-15). Deflections of flexural members are commonly computed using an elastic-deflection equation in conjunction with an effective moment of inertia I_e, a concept that empirically provides a transition between the upper and lower bounds of gross moment of inertia, I_g, and cracked moment of inertia, I_{cr}, as a function of the ratio of cracking to applied moment, M_{cr}/M_a.

Both ACI 318-14 and CSA A23.3-14 design codes provide an expression introduced by Branson (1965) for establishing the effective moment of inertia used in the deflection analysis of steel-RC members. The cubic form of Branson's equation is intended to model the transition from gross (uncracked) section stiffness $\left(E_c I_g\right)$ to full cracked section stiffness $\left(E_c I_{cr}\right)$. This transition is nonlinear as a result of the tension-stiffening effects of the concrete between adjacent cracks. FRPRC members typically have I_g/I_{cr} between 5 and 25, and deflection is underpredicted because the tension-stiffening component using Branson's equation is grossly overestimated for members with I_g/I_{cr} greater than about 4 (Bischoff 2007). In addition, Branson's equation is based on an incorrect mechanical model that represents the rigidities of the cracked and uncracked regions as springs in parallel, when, in fact, they are in series (Bischoff and Scanlon 2007).

Several authors have proposed coefficients to modify Branson's equation to simulate the real behavior of FRPRC rectangular members (Benmokrane et al. (1996); Theriault and Benmokrane (1998); Alsayed et al. (2000); Toutanji and Saafi (2000); Yost et al. (2003); Mousavi and Esfahani (2012); Adam et al. (2015)). Others have proposed deflection-calculation models derived from integration of curvatures (Razaqpur et al. (2000); Bischoff (2005, 2007); Bishcoff and Gross (2011a, b)). Based on these different approaches, equations for calculating the

deflection of FRPRC members have been included in design guidelines and codes (ACI 440.1R-15; CSA S806-12; CNR-DT 203/2006). These models and code provisions were developed mainly based on experimental work on rectangular FRPRC members. Despite the valuable applications of circular RC members—such as bridge piers and piles, contiguous pile walls, and fender piles in marine structures—no research seems to have investigated RC members of circular cross section reinforced with FRP bars. Moreover, there are practically no code provisions or guidelines for the flexural design and serviceability of circular concrete members, with FRP reinforcement. ACI 440.1R-15, however, points out that there is no evidence that the flexural theory—developed for rectangular sections—applies equally well to non-rectangular sections; the behavior of such members has yet to be confirmed experimentally.

In general, the deflection control of rectangular members can be easily evaluated. A regular section of the concrete compression part and tension reinforcement arranged, in most cases, in a single layer provide for simple calculation of the transformed cracked section through elastic analysis. In contrast to the reinforcement in rectangular RC members, the bars in circular RC members are usually distributed in a circle at discrete points, somewhat complicating calculation of the elastic analysis of the transformed cracked section. In addition, the stresses, which are variable over the section depth, are also distributed over an area of variable width. This fact leads to a very small part of the circular section exhibiting maximum compression strain. In contrast, the extreme tension reinforcement might reach the ultimate strain, while the other layers of reinforcement experience lower strains, possibly as low as zero along the neutral axis. This produces a larger concrete compression zone and a smaller internal lever arm compared to rectangular sections with equivalent dimensions. Consequently, a smaller effective moment of inertia and larger deflections might be obtained in members with circular sections compared to those with rectangular sections.

The work reported herein is a part of an ongoing comprehensive research program in which full-scale FRPRC members with circular sections are tested under different loading conditions—pure compression (Afifi et al. 2014a), axial combined bending (Hadhood et al. 2017a), shear (Ali et al. 2017a), and flexure (current study)—to investigate different variables and design parameters. In this study, the experimental data and theoretical analysis on deflection predictions provide the evidence required to include design provisions in the forthcoming ACI

440 and AASHTO LFRD codes for the design of FRPRC members with circular sections. The objectives of our research can be summarized as follows: (1) To experimentally investigate the effect of test parameters on the load–deflection behavior of circular concrete members reinforced with FRP bars (GFRP, CFRP, and BFRP); (2) To review and verify the accuracy of using deflection equations in code provisions and those available in the literature; (3) To propose a new equation to predict the effective moment of inertia of circular FRPRC members; and (4) To analytically predict the load–deflection relationship of circular FRPRC members by using the nonlinear curvature analysis layered approach.

7.2. Research Significance

Considerable research work has investigated the effective moment of inertia and deflection of rectangular concrete members reinforced with FRP bars. No research, however, seems to have done on circular concrete members reinforced with FRP reinforcement. This paper reports on eight full-scale circular concrete members reinforced with different types of FRP bars (GFRP, CFRP, and BFRP) that were tested up to failure under four-point bending load. The paper examines the accuracy of using the deflection equations in code provisions and those available in the literature for circular FRPRC members. A new equation was proposed to predict the effective moment of inertia of such members. In addition, the load–deflection relationships of the tested circular specimens were predicted analytically using the nonlinear curvature analysis layered approach.

7.3. Experimental Work

7.3.1. Test Parameters and Procedure

Eight full-scale circular members reinforced with different types of FRP bars (GFRP, CFRP, and BFRP) were tested up to failure under four-point bending load. All of the specimens measured 500 mm (20 in.) in diameter and 6,000 mm (236.22 in.) in length. The test parameters included the longitudinal-reinforcement ratio and the longitudinal-reinforcement type. The effect of reinforcement ratio on the load–deflection behavior was investigated by testing three specimens reinforced longitudinally with 8, 16, and 24 (2 x 12 bundled) #6 GFRP bars with a reinforcement ratio of 1.2%, 2.3%, and 3.5%; three specimens reinforced longitudinally with 8,

12, and 18 #5 CFRP bars with a reinforcement ratio of 0.8%, 1.2%, and 1.8%; and two specimens reinforced longitudinally with 8 and 16 #6 BFRP bars with a reinforcement ratio of 1.2% and 2.3%. Each specimen is identified with a tripartite code. The first number refers to the number of longitudinal bars. The letters G, C, and B identify specimens as being reinforced longitudinally with GFRP, CFRP, and BFRP bars, respectively. The second number indicates the nominal diameter of the longitudinal bars. Table 7.1 provides the test matrix; Fig. 7.1 gives the cross-sectional details of the specimens.

Table 7.1 Test matrix, details of tested specimens, and summary of test results.

Specimen ID	Longitudinal reinforcement		Transversal reinforcement	f'_c [b] (MPa)	f_t [b] (MPa)	EA(kN)	Load (kN)			Deflection (mm)	
	ρ_{fl}(%) [a]	Number of bars					P_{cr}	P_s	$P_{failure}$	δ_s	$\delta_{failure}$
8G20	1.2	GFRP bars (8 #20 mm)	GFRP spiral # 4 @125	41.4	3.8	145,700	23.0	75	251	22.4	104
16G20	2.3	GFRP bars (16 #20 mm)	GFRP spiral # 4 @125			291,400	26.6	126	420	24.1	101
24G20	3.5	GFRP bars (24 #20 mm)	GFRP spiral # 4 @125			437,100	24.4	127	423	19.1	76
8C15	0.8	CFRP bars (8 #15 mm)	GFRP spiral # 4 @125	45.8	4.3	224,500	22.7	95	316	25.7	99
12C15	1.2	CFRP bars (12 #15 mm)	GFRP spiral # 4 @125			336,700	27.3	126	421	23.8	91
18C15	1.8	CFRP bars (18 #15 mm)	GFRP spiral # 4 @125			505,100	32.7	127	423	15.9	64
8B20	1.2	BFRP bars (8 #20 mm)	BFRP spiral # 4 @125	41.4	3.5	145,200	23.2	71	237	22.9	99
16B20	2.3	BFRP bars (16 #20 mm)	BFRP spiral # 4 @125			290,500	30.2	104	348	19.5	85

[a] Total reinforcement ratio (longitudinal reinforcement area divided by the gross area of the circular specimen).
[b] Average of at least 3 cylinders (100 x 200 mm) at time of testing.
Note: 1 kN = 0.225 kip, 1 mm = 0.0394 in., 1 MPa = 0.145 ksi

The test setup was designed and fabricated at the University of Sherbrooke's Canadian Foundation for Innovation (CFI) structural laboratory. Two concentrated loads were applied to the specimens using an MTS 1000 kN (224.8 kip), servo-controlled, hydraulic actuator and spreader beam, as shown in Fig. 7.2. The load was applied at a displacement-controlled rate of 0.5 mm/min. (0.02 in./min). A clear span of 4950 mm (194.88 in.) and a constant bending moment zone of 750 mm (29.5 in.) were kept constant for all the tested specimens. At the

loading and support points, steel saddles were designed to accommodate the circular geometry of the specimens. Strains in the longitudinal reinforcing bars and spirals were measured using electrical resistance strain gauges with a gauge length of 10 mm (0.39 in.) (see Fig. 7.1). In addition, nine strain gauges with a gauge length of 60 mm (2.36 in.) were mounted on the concrete surface at four different levels (D, D/8, D/4, and D/3) at mid-span and at quarter span to measure concrete compressive strains. Specimen deflection was measured with three linear potentiometers (LPOTs) placed at the mid-span and at the quarter-span to monitor the deflection profile along the span. An automatic data-acquisition system monitored by a computer was used to record the readings of the load cell, strain gauges, and LPOTs.

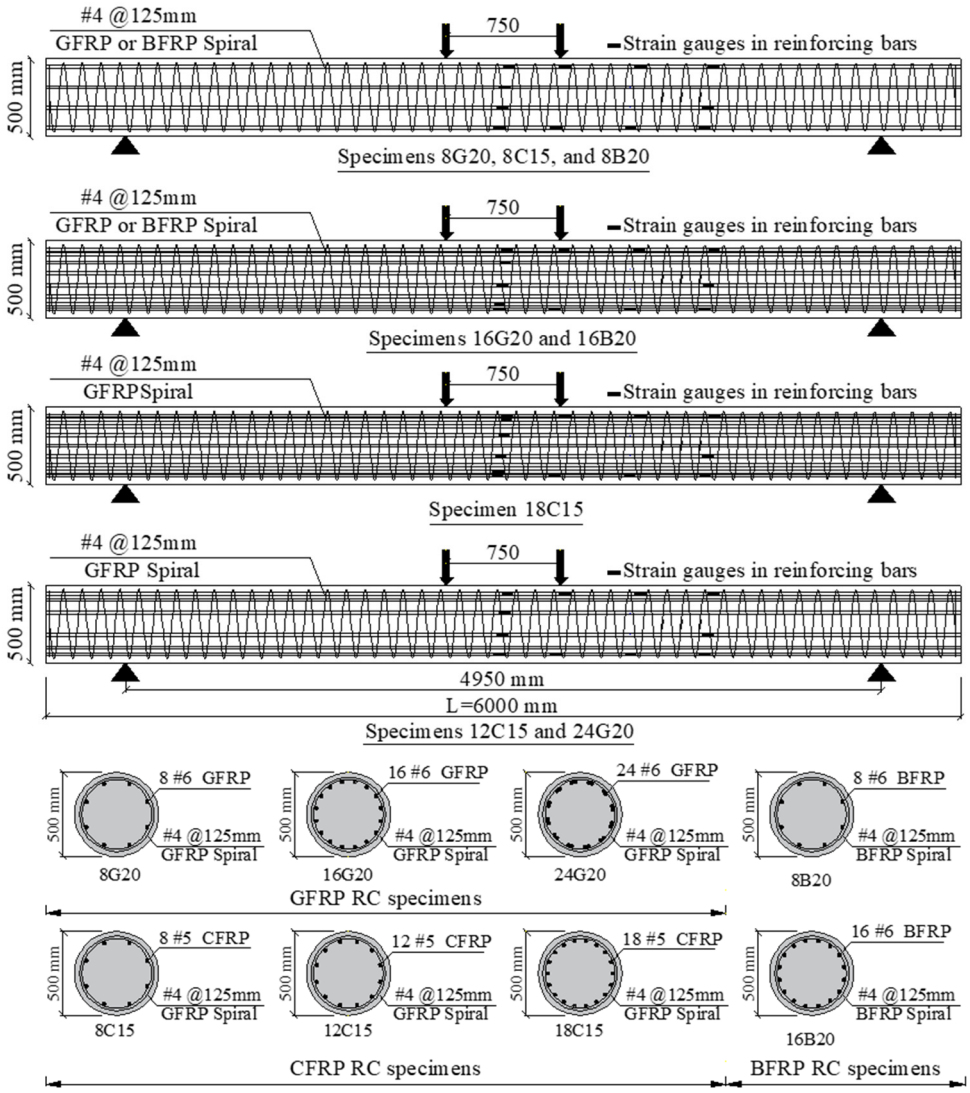

Figure 7.1 Geometry and reinforcement details of the tested circular specimens (dimensions are in mm).

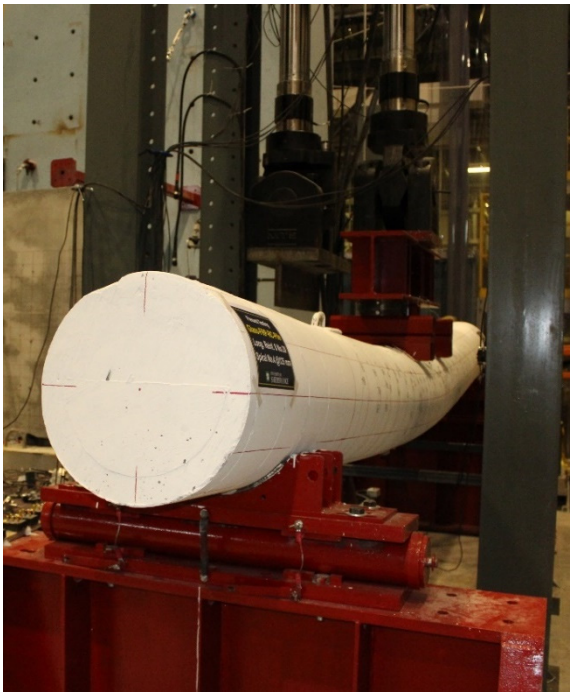

Figure 7.2 Test setup.

7.3.2. Material Characteristics

The GFRP, CFRP, and BFRP reinforcement was manufactured with the same technique by pultruding continuous glass, carbon, and basalt fibers, respectively, impregnated with a thermosetting vinyl-ester resin (Pultrall, 2015). The GFRP, CFRP, and BFRP bars and spirals had the same sand-coated surface texture to enhance bond and force transfer between the bars and concrete, as shown in Fig. 7.3. The fiber contents in percentage by weight were 82%, 80%, and 81% for the GFRP, CFRP, and BFRP bars, respectively. The ultimate tensile strength, f_{fu}, and modulus of elasticity, E_f, of the longitudinal GFRP, CFRP, and BFRP bars and the straight portion of the bent GFRP and BFRP spirals were determined according to ASTM D7205. Table 7.2 provides the guaranteed properties of these bars, as reported by the manufacturer. The tensile strength and elastic modulus were calculated using a nominal cross-sectional area. The test specimens were constructed using normal-weight, ready-mixed concrete in three batches with a specified concrete strength of 40 MPa (5.8 ksi) at 28 days. Table 7.1 provides the actual compressive and tensile strengths of the concrete.

Table 7.2 Mechanical properties of the GFRP, CFRP, and BFRP reinforcement.

RFT Type	Material Type	d_b (mm)	A_f [a] (mm²)	A_{im} [c] (mm²)	E_f (GPa)	f_{fu} (MPa)	ε_{fu} (%)
Longitudinal bars	GFRP	20	285	339±0	63.9±0.4	1591±13	2.5±0.2
	CFRP	15	199	222±1	141±3.0	1680 ±22	1.2±0.1
	BFRP	20	285	346±2	63.7±0.8	1646±40	2.5±0.1
Spirals	GFRP	13	129	148±1	52.1±1.2	1126 [b] ±20	2.2±0.0
	BFRP	13	129	139±1	51.4±0.2	1414 [b] ±11	2.7±0.2

[a] Nominal cross-sectional area.
[b] Tensile strength of the straight bars.
[c] Immersed cross-sectional area (measured).
Note: Properties calculated based on the nominal cross-sectional area, (1 mm = 0.0394 in.; 1 mm^2 = 0.00155 in.^{2}; 1 MPa = 0.145 ksi).

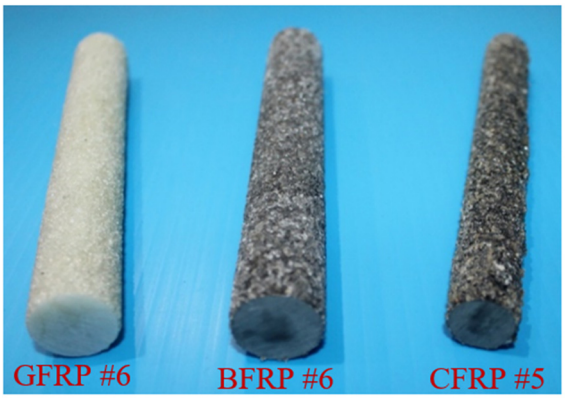

Figure 7.3 FRP bar types and surface characteristics.

7.4. Experimental Results

Table 7.1 gives a summary of the test results. This table lists the applied load at flexural cracking (P_{cr}), service load (P_s), and failure load $(P_{failure})$, in addition to the mid-span deflection at service (δ_s), and failure $(\delta_{failure})$ loads. Each specimen was symmetrically loaded with two concentrated loads and, consequently, the applied load is their sum. The following section provides the test results in terms of load–deflection relationships and the effect of test parameters on the behavior of the specimens.

7.4.1. Load-Deflection Behavior

The applied load versus deflection relationships of the GFRP-, CFRP-, and BFRP-RC specimens at mid-span and quarter span up to concrete-cover spalling, are presented in Figs.

7.4(a), 7.4(b), and 7.4(c), respectively. The typical load–deflection curves can be defined in two distinct stages (pre-cracking and post-cracking). At the pre-cracking stage, an identical linear load–deflection behavior was observed in all the test specimens, regardless of their reinforcement ratio and type, representing the uncracked condition governed by the properties of the circular concrete section. At the post-cracking stage, however, the flexural stiffness was reduced and dependent on the axial stiffness of the reinforcing bars, which is a function of the area A_f and modulus of elasticity E_f. This change in stiffness represents the transition from gross- to effective-section properties. At this stage, the specimens behaved nearly linearly with reduced stiffness up to failure. This is attributed to the linear–elastic characteristics of the FRP reinforcement. The failure of the eight test specimens was initiated by concrete-cover spalling on the compression side (compression failure mode). The maximum recorded compressive strains at mid-span ranged between –3600 με and –5100 με. The recorded compressive concrete strains were higher than the specified design limit in ACI440.1R-15 (–3000 με) and CSA S806-12 (–3500 με).

The maximum recorded tensile strains in the GFRP bars at concrete crushing were 12,800, 11,900, and 8,400 με, representing 50%, 46%, and 33% of the ultimate tensile GFRP bar strain for 8G20, 16G20, and 24G20, respectively. The maximum recorded strains in the CFRP bars at concrete crushing were 8,400, 10,300, and 7,100 με (71%, 87.5%, and 60% of the ultimate tensile CFRP bar strain) for 8C15, 12C15, and 18C15, respectively. The strain gauges were damaged before 8C15 failed, which accounts for the strain value less than that of 12C15 at concrete crushing. Lastly, the maximum recorded tensile strains in the BFRP bars at concrete crushing were 13,200 and 9,670 με (64% and 51% of the ultimate tensile BFRP bar strain) for 8B20 and 16B20, respectively. Figure 7.5(a) presents the failure mode and the deflected shape of the test specimens.

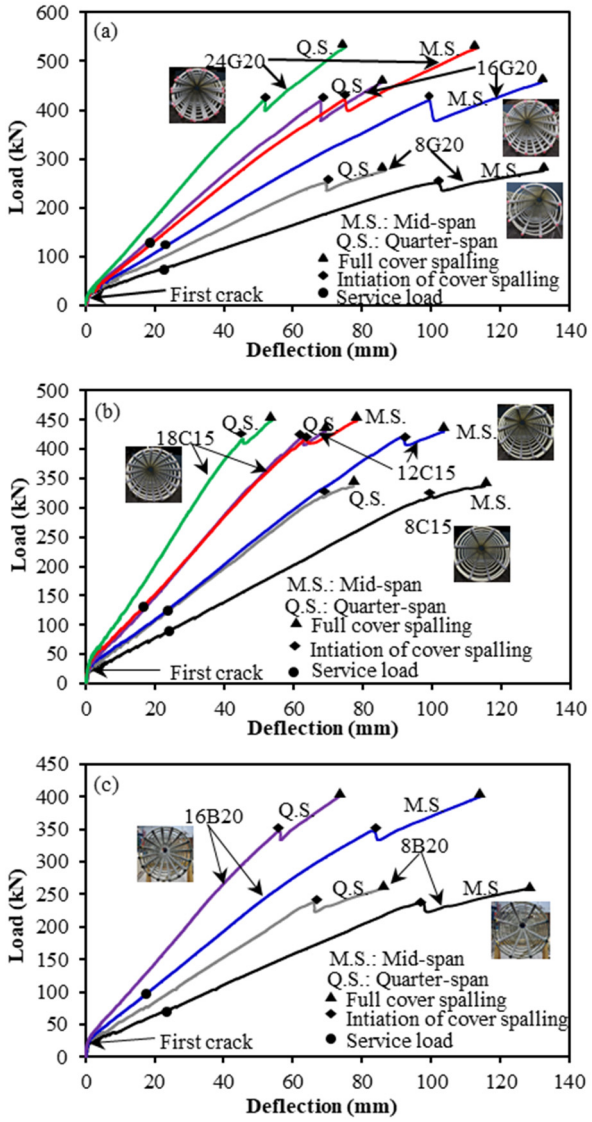

Figure 7.4 Load–deflection relationships: (a) GFRP specimens; (b) CFRP specimens; (c) BFRP specimens. (Note: 1 mm = 0.0394 in.; 1 kN = 0.225 kip)

(a)

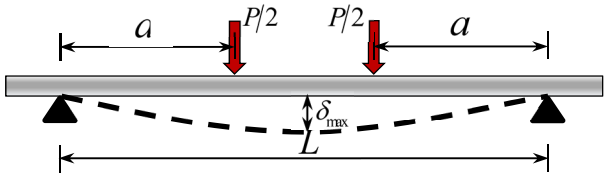

(b)

Figure 7.5 (a) Overview of deflected shape and failure modes of the tested specimens, (b) Deflected shape of a simply supported concrete member subjected to two equal concentrated loads.

Increasing the amount of longitudinal reinforcement enhanced the performance of the tested specimens—regardless of the type of FRP reinforcement—when compared at the same load level. Figures 7.4(a), 7.4(b), and 7.4(c) show an increase in flexural capacity and reduction in deflection for an increase in the amount of longitudinal reinforcement. In addition, the flexural stiffness significantly increased when the reinforcement ratio increased. Increasing the reinforcement ratio in the GFRP specimens from 1.2% (8G20) to 2.3% (16G20) and 3.5% (24G20) resulted in an increase in flexural capacity of 67% and 68% with a reduction in mid-span deflection of 92% and 150%, respectively, when compared at the same load level. The flexural stiffness of 16G20 and 24G20 (ρ_{fl} = 2.3% and 3.5%) after initial cracking increased,

in comparison to 8G20 (ρ_{ft} = 1.2%) by 100% and 168%, respectively. In contrast, CFRP specimens 12C15 and 18C15 had lower deflection and higher flexural capacity than 8C15 by 33.1% and 33.6%, respectively. 18C15 did not gain as much strength as 12C15 when the reinforcement ratio was increased from 1.20% to 1.80%. This could be attributed to the fact that 18C15 reached its full flexural capacity, as it was governed by concrete and CFRP-bar crushing. In contrast, test results indicate that increasing the CFRP-reinforcement ratio significantly affected the post-cracking flexural stiffness of the test specimens. The post-cracking flexural stiffness of 12C15 (ρ_{ft} =1.2%) was 46% higher than that of 8C15 (ρ_{ft} = 0.8%). Similarly, the post-cracking flexural stiffness of 18C15 (ρ_{ft} = 1.8%) was 120% higher than that of 8C15 (ρ_{ft} = 0.8%) and 51% higher than that of 12C15 (ρ_{ft} = 1.2%). In the BFRP specimens, however, increasing the reinforcement ratio from 1.2% (8B20) to 2.3% (16B20), resulted in a flexural-capacity increase of 46% with a reduction in mid-span deflection of 95% when compared at the same load level. The flexural stiffness of 16B20 (ρ_{ft} = 2.3%) increased by 80% after initial cracking when compared to 8B20 (ρ_{ft} = 1.2%).

7.5. Overview of Deflection Prediction Equations for FRPRC Members

The maximum mid-span flexural deflection, $\delta_{\max}$, for a simply supported circular member with a span of Lsubjected to two equal concentrated loads of $P/2$ magnitude symmetrically placed at a distance a from the support (see Fig. 7.5(b)) is given as follows:

$$\delta_{\max} = \frac{Pa}{48E_c I_e}\left(3L^2 - 4a^2\right) \tag{7.1}$$

where E_c = modulus of elasticity of the concrete, taken as $E_c = 4700\sqrt{f_c'}$ (MPa) (ACI 318-14); and I_e = effective moment of inertia of the circular cross section. At the pre-cracking stage $\left(M_a \le M_{cr}\right)$, the applied moment M_a is less than the cracking moment M_{cr}. Accordingly, the uncracked section has a moment of inertia equal to the gross moment of inertia, I_g. At post-cracking stage $\left(M_a \ge M_{cr}\right)$, the contribution of concrete to the tensile stiffness between the

cracks of a reinforced-concrete member is influenced by the tension stiffening phenomenon. This phenomenon affects the stiffness and deflection of flexural members. The effective moment of inertia, I_e, was developed to provide a transition between the upper and lower bounds of gross moment of inertia, I_g, and cracked moment of inertia, I_{cr}, as a function of the ratio M_{cr}/M_a.

The ACI 318-14 building code and the CSA A23.3-14 design codes provide an expression introduced by Branson (1965) for establishing the effective moment of inertia used in the deflection analysis of steel-reinforced concrete members as follows:

$$I_e = \left(M_{cr}/M_a\right)^3 I_g + \left[1-\left(M_{cr}/M_a\right)^3\right] I_{cr} \le I_g \tag{7.2}$$

in which $M_{cr} = f_r I_g / y_t$, where f_r = the modulus of rupture and can be calculated as $0.62\sqrt{f_c'}$ (MPa) (ACI 318-14) or $0.6\sqrt{f_c'}$ (MPa) (CSA A23.3-14); y_t = the distance from the centroidal axis of the cross section to the extreme fiber in tension; and f_c' = unconfined concrete strength, obtained from the cylinder tests.

Several authors have proposed effective moment of inertia expressions for rectangular FRPRC members. Benmokrane et al. (1996) first incorporated empirical correction factors (α and β) in Branson's equation, through a comprehensive experimental program on GFRP-reinforced beams, that was needed to reduce tension stiffening and gave reasonable estimates of computed deflection, as follows:

$$I_e = \left(M_{cr}/M_a\right)^3 \frac{I_g}{\beta} + \left[1-\left(M_{cr}/M_a\right)^3\right] \alpha I_{cr} \le I_g \tag{7.3}$$

where α and β = 0.84 and 7, respectively.

Thériault and Benmokrane (1998) continued to experimentally investigate the deflection behavior of GFRP-reinforced beams, and then introduced a new modification of Branson's equation, as follows:

$$I_e = \left(M_{cr}/M_a\right)^3 \beta_d I_g + \left[1-\left(M_{cr}/M_a\right)^3\right] I_{cr} \le I_g \tag{7.4}$$

where β_d = reduction coefficient equal to 0.6. This factor was later modified by Gao et al. (1998) [Eq. (7.5)] and adopted in ACI 440.1R-03.

$$\beta_d = \alpha_b \left(\frac{E_f}{E_s}+1\right) \tag{7.5}$$

in which α_b = bond-dependent coefficient, assumed to be 0.5 until more data became available; E_f and E_s = modulus of elasticity of the FRP and steel reinforcement, respectively.

Yost et al. (2003) proposed an equation for α_b to account for the effect of the reinforcement ratio ρ_f with reference to a balanced reinforcement ratio ρ_{fb}, as follows:

$$\alpha_b = 0.064\frac{\rho_f}{\rho_{fb}} + 0.13 \tag{7.6}$$

Based on an assessment of the experimental results from several studies, ACI 440.1R-06 proposed the following simple relationship for β_d:

$$\beta_d = \frac{1}{5}\left(\frac{\rho_f}{\rho_{fb}}\right) \le 1.0 \tag{7.7}$$

Alsayed et al. (2000) proposed two models to determine I_e for beams reinforced with GFRP bars based on experimental results. In the first model (model A), the equation suggests replacing the power of 3 by 5.5 in Branson's equation. The second model (model B) was suggested by regression analysis of the experimental results for their tested beams reinforced with GFRP bars. Toutanji and Saafi (2000), however, showed that the order of Branson's equation depends on both the modulus of elasticity of the FRP and the reinforcement ratio. Mousavi and Esfahani (2012) proposed two equations that account for the most effective parameters such as modulus of elasticity of FRP bars, relative reinforcement ratio, and levels of loading for calculating deflection. Adam et al. (2015) proposed an equation for calculating I_e using the same parameters considered by Mousavi and Esfahani (2012).

On the basis of a study conducted by Mota et al. (2006), ISIS Canada No. 3 (2007) proposed an equation to calculate the effective moment of inertia I_e as follows:

$$I_e = \frac{I_t I_{cr}}{I_{cr} + \left(1 - 0.5\left(M_{cr}/M_a\right)^2\right)\left(I_t - I_{cr}\right)} \tag{7.8}$$

in which I_t and I_{cr} are the moment of inertia of a non-cracked section transformed to concrete and cracked moment of inertia, respectively.

Bischoff (2005, 2007) proposed a new expression for the effective moment of inertia, I_e, based on the fundamental concepts of tension stiffening, as follows:

$$I_e = \frac{I_{cr}}{1 - \left(1 - \left(I_{cr}/I_g\right)\right)\left(M_{cr}/M_a\right)^2} \tag{7.9}$$

Bischoff and Gross (2011a and b) proposed an equation to calculate I_e [Eq. (7.10)], which includes an additional factor, γ, to account for the change in stiffness along the length of beams and dependent on the boundary conditions and loading type.

$$I_e = \frac{I_{cr}}{1 - \gamma\left(1 - \left(I_{cr}/I_g\right)\right)\left(M_{cr}/M_a\right)^2} \tag{7.10}$$

For a four-point bending load, which is the load arrangement used in our study, Bischoff and Gross (2011a) suggested the following expression based on the integration of curvature along the span to calculate γ.

$$\gamma = \frac{3\left(a/L\right) - 4\left[4\left(M_{cr}/M_a\right) - 3\right]\left(a/L\right)^3}{3\left(a/L\right) - 4\left(a/L\right)^3} \tag{7.11}$$

ACI 440.1R-15 recommends calculating I_e based on the equation proposed by Bischoff and Gross (2011a) [Eq. (7.10)].

Ovitigala et al. (2017), in response to Peter H. Bischoff's discussion, assessed the ACI 440.1R-15 equation for calculating I_e [Eq. (7.10)] based on the experimental results from eight rectangular BFRPRC beams. This assessment revealed that the model was less conservative than the rest of the investigated models and overestimated the value of I_e with respect to the experimental I_e. Ovitigala et al. (2017) proposed new equation that fits well the experimental I_e of their tested beams, as follows:

$$I_e = \frac{I_{cr}\left(M_{cr}/M_a\right)^5}{\left(M_{cr}/M_a\right)^5 - C_1\left(M_{cr}/M_a\right) + C_2} \le I_g \tag{7.12}$$

where $C_1 = \frac{3(a/L)+12(a/L)^3}{3(a/L)-4(a/L)^3}\left(1-\left(I_{cr}/I_g\right)\right)$ and $C_2 = \frac{16(a/L)^3}{3(a/L)-4(a/L)^3}\left(1-\left(I_{cr}/I_g\right)\right)$.

CSA-S806 (2012), based on Razaqpur et al. (2000), has recommended the integration of curvature along the span to determine deflections. The CSA S806-12 (2012) approach is based on an assumption that the moment–curvature relationship of a cracked FRPRC member remains linear under increasing load, which ignores the tension stiffening effect. A simple equation derived by Razaqpur et al. (2000) for calculating the deflection of simply supported four-point bending of FRPRC members was provided as follows:

$$\delta_{\max} = \frac{PL^3}{48E_cI_{cr}}\left[3\left(\frac{a}{L}\right) - 4\left(\frac{a}{L}\right)^3 - 8\left(1-\frac{I_{cr}}{I_g}\right)\left(\frac{L_g}{L}\right)^3\right] \tag{7.13}$$

where L_g is the distance from support to point where $M_a = M_{cr}$.

CNR-DT 203/2006 (Italian national research council) calculated the deflection, $\delta_{\max}$, for FRP concrete members using Eq. (7.14) based on Eurocode (EC2-2004). After cracking occurs, the deflection $\delta_{\max}$ is obtained by deflection δ_1, considering the inertia of the uncracked section, and deflection δ_2, considering the inertia of the cracked section with the following expression:

$$\delta_{\max} = \beta_1\beta_2\left(M_{cr}/M_a\right)^2\delta_1 + \left[1-\beta_1\beta_2\left(M_{cr}/M_a\right)^2\right]\delta_2 \tag{7.14}$$

where $\beta_1 = 0.5$ is a nondimensional coefficient accounting for the bond properties of FRP bars and $\beta_2 =$ is a nondimensional coefficient accounting for loading duration (1.0 for short-time loads; 0.5 for long-time or cyclic loads).

7.6. Calculation of the Cracked Moment of Inertia of Circular FRPRC Members

This section provides the calculation of the moment of inertia of the cracked section, I_{cr}, for circular FRPRC members using an elastic analysis of the transformed section (see Fig. 7.6). In general, at service load, the distribution of stresses in the compression zone of a cracked section is close to being linear, so the strain behavior of FRP reinforcement is elastic. As a result, an elastic consideration yields a good estimate of the concrete and FRP stresses at service load (ACI 440.1R-15).

The elastic-analysis calculations are based on the following assumptions:

- The strain variations are assumed to be the same in the concrete and FRP.

- The stresses in the FRP reinforcement and concrete are assumed to be proportional to the strains.

- The concrete tensile stresses are neglected.

- The FRP reinforcement in the compression zone should be disregarded in the elastic analysis.

The neutral axis is located at a distance, $_c$, from the top compression fiber. The location of the neutral axis can be easily determined through a simple iteration of the neutral-axis depth $_c$ by taking the first moment of area about the location of neutral axis using a cracked transformed section, as shown in Fig. 7.6, as follows:

$$A_c\left(c - r + \bar{y}\right) = \sum_{i=1}^{n} n_f A_{fi}\left(d_i - c\right) \tag{7.15}$$

$$A_c = r^2\left(\theta - sin\,\theta\, cos\,\theta\right) \tag{7.16}$$

$$\bar{y} = \frac{2r}{3}\left(\frac{sin^3\theta}{\theta - sin\theta\, cos\theta}\right) \tag{7.17}$$

$$cos\theta = 1 - \frac{c}{r} \tag{7.18}$$

where A_c is the area of the circular concrete segment; r is the radius of the circular cross section; A_{fi} is the area for the row of the FRP bars at level i; d_i is the distance for each row of FRP bars at level i to the top compression fiber; c is the neutral-axis depth; n_f is the ratio of modulus of elasticity of the FRP bars to the modulus of elasticity of the concrete; and $\bar{y}$ is distance between the centroid of the circular concrete segment on the compression side to the centroid of the concrete cross section.

The moment of inertia of the cracked circular section, I_{cr}, can be calculated using Eq. 7.19.

$$I_{cr} = I_c + A_c\left(\left(c - r + \bar{y}\right)^2 - \bar{y}^2\right) + \sum_{i=1}^{n} n_f A_{fi}\left(d_i - c\right)^2 \tag{7.19}$$

$$I_c = \frac{r^4}{4}\left(\theta - \sin\theta\cos\theta + 2\sin^3\theta\cos\theta\right) \tag{7.20}$$

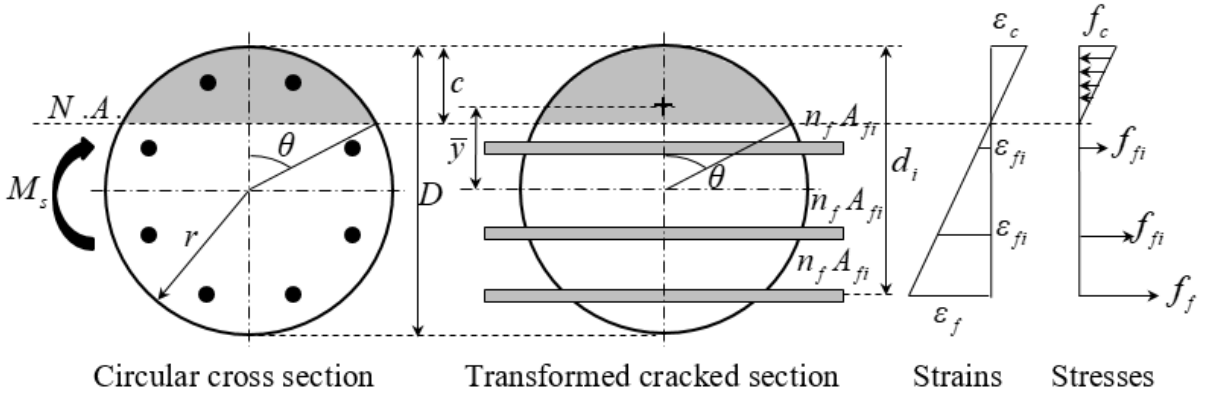

Figure 7.6 Transformed cracked section, strains, and stresses at service load.

7.7. Evaluation of the Effective Moment of Inertia of Circular FRPRC Specimens

The values of the experimental moment of inertia I_{exp} for the tested circular specimens were determined with the following equation:

$$I_{\exp} = \frac{\left(P_{\exp} + P_{eq.}\right)a}{48E_c\delta_{\exp}}\left(3L^2 - 4a^2\right) \tag{7.21}$$

where P_{exp} = the laboratory-measured applied load; $P_{eq.}$ = the equivalent load due to self-weight of the test specimens (the magnitude of the equivalent load was determined such that the mid-span moments for the equivalent point loads and the specimen self-weight as a uniformly distributed force pattern are the same); and δ_{exp} = the experimentally measured mid-span deflection.

The effective-to-gross moment of inertia I_e/I_g was plotted for each circular specimen versus the applied-to-cracking moment ratio M_a/M_{cr}, as shown in Fig. 7.7. The analysis was carried out to investigate the effectiveness of the analytical models in predicting the I_e. I_e models according to Benmokrane et al. (1996), Bischoff (2005, 2007), ACI 440.1R-15, ISIS Canada (2007) and Ovitigala et al. (2017) were plotted and compared to the experimental results. The experimental and models results in this study were assessed at service load. For this purpose, service load is defined as the load corresponding to 30% of the applied load at failure, $P_{failure}$, as suggested by Bischoff et al. (2009). As shown in Fig. 7.7, the ACI 440.1R-15 model overestimates the I_e and thus underestimates the service deflections with less conservative values for both low and high reinforcement ratios, regardless of FRP-reinforcement type. The Bishcoff (2005, 2007) model yielded better predictions of I_e than the ACI 440.1R-15 model. The Benmokrane et al. (1996), ISIS Canada (2007), and Ovitigala et al. (2017) models, in contrast, provided conservative predictions at service load for all of the test specimens. At high load levels, (M_a/M_{cr} greater than 3), all the investigated models' predictions were higher than the experimental I_e, except for the Benmokrane et al. (1996) model.

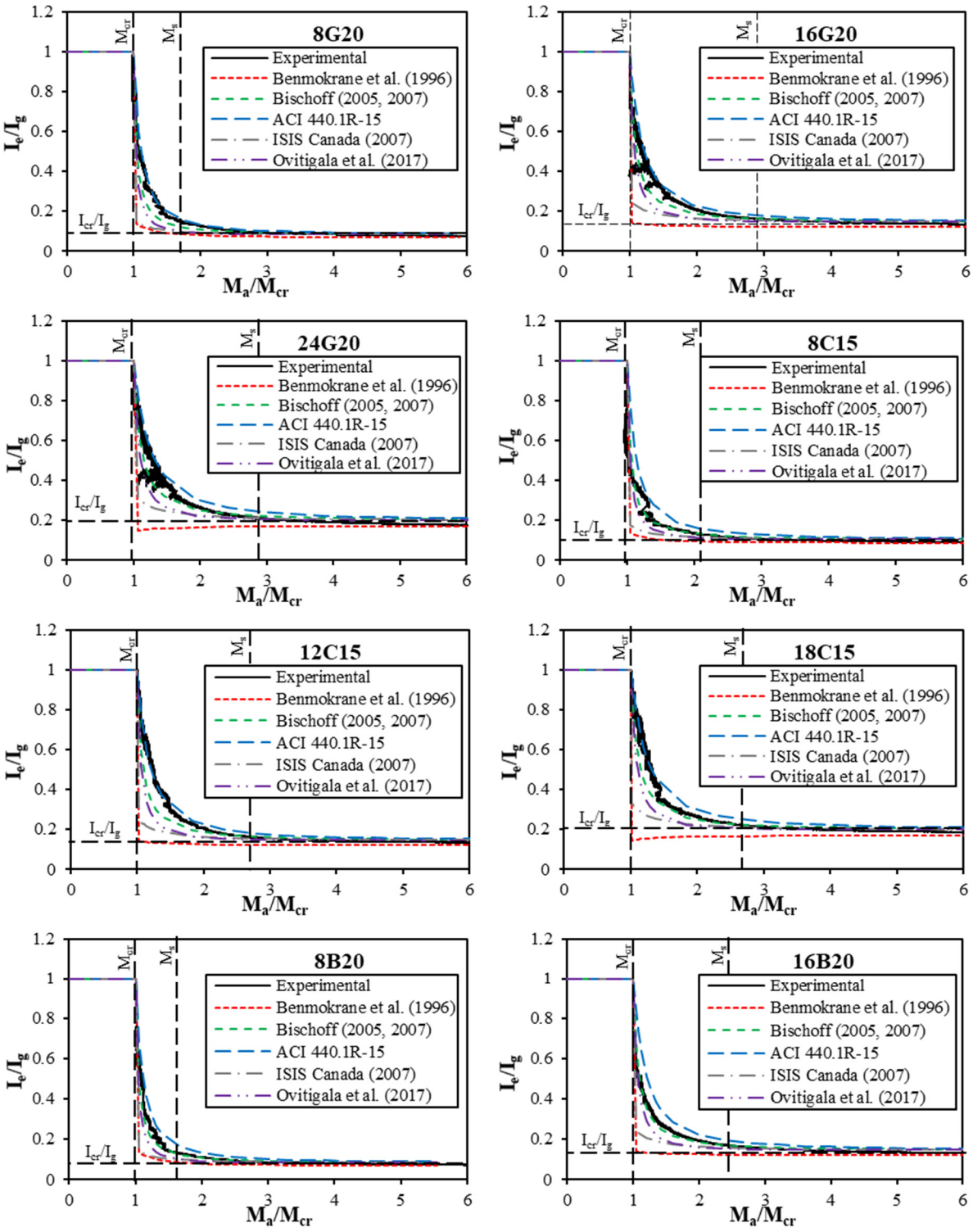

Figure 7.7 Effective-to-gross moment of inertia I_e/I_g versus M_a/M_{cr}.

In conclusion, based on the experimental results, the current ACI 440.1R-15 approach overestimated the experimental I_e of the tested circular specimens and needs modification to account for the actual response of the tested circular specimens. In the following section, the ACI 440.1R-15 model—based on Bishcoff and Gross (2011a)—is addressed and modified to calculate the actual service deflection of the test specimens considering circular-section geometry.

7.8. Modified Bishcoff Equation for Circular FRPRC Specimens

Deflection models have been developed and assessed based on experimental work on FRPRC members with rectangular cross sections. In contrast to rectangular RC members, circular RC members usually have their reinforcement bars distributed in a circle at discrete points. In addition, the stresses, which are variable over the section depth, are also distributed over an area of variable width. This fact leads to a very small part of the circular section exhibiting maximum compression strain. In contrast, the extreme tension reinforcement might reach the ultimate strain, while the other layers of reinforcement experience lower strains, possibly as low as zero along the neutral axis. This produces a larger concrete compression zone and a smaller internal lever arm compared to rectangular sections with equivalent dimensions. Consequently, a smaller effective moment of inertia and larger deflections might be obtained in members with circular sections compared to those with rectangular sections.

Bishcoff's model is theoretically considered to be the most reliable model, as I_e is predicted based on integration of curvature. An assessment of Bishcoff's model reveals that it overestimated the value of I_e with respect to the experimental $I_{\exp}$.

Similar to Bischoff's equation [Eq. (7.10)], the effective moment of inertia can be calculated using Eq. (7.22) as follows:

$$I_{\exp} = \frac{I_{cr}}{1-\gamma\left(1-\left(I_{cr}/I_g\right)\right)\left(M_{cr}/M_a\right)^m} \Rightarrow \frac{I_{\exp}-I_{cr}}{\gamma\left(1-\left(I_{cr}/I_g\right)\right)I_{\exp}} = \left(M_{cr}/M_a\right)^m \qquad (7.22)$$

Increasing the power m in Eq. (7.22) will result in a steeper slope and will tend to reduce the gap between the predicted and experimental results. The power m can be obtained using I_{exp} and M_{cr}/M_a values as follows:

$$m = \frac{\log\left(\dfrac{I_{exp} - I_{cr}}{\gamma\left(1-\left(I_{cr}/I_g\right)\right)I_{exp}}\right)}{\log\left(M_{cr}/M_a\right)} \tag{7.23}$$

The regression analysis was performed on the results for the service-load range. The results suggest that the average value of the power m for circular FRPRC specimens can be taken as approximately 3.5, rather than 2 suggested by Bishcoff (2005, 2007). Thus, the suggested model can be considered as a modified Bischoff's equation to determine the effective moment of inertia for circular FRPRC specimens and can be written as follows:

$$I_e = \frac{I_{cr}}{1-\gamma\left(1-\left(I_{cr}/I_g\right)\right)\left(M_{cr}/M_a\right)^{3.5}} \tag{7.24}$$

in which γ can be calculated with Eq. (7.11), as suggested by Bischoff and Gross (2011a).

7.9. Comparative Deflection Analysis of Experimental and Code Models and the Modified Bishcoff Equation

Figure 7.8 shows the comparison of the experimental and predicted results using the ACI 440.1R-15, CSA S806-12, CNR-DT 203/2006, and modified Bischoff equations. Table 7.3 provides the mean values and the coefficients of variation (COV) for the ratios of the measured-to-predicted deflections $\left(\delta_{exp.}/\delta_{pred.}\right)$. The deflections were predicted at the service-load level. As can be seen, ACI 440.1R-15 underestimated the predictions, on average, with $\delta_{exp.}/\delta_{pred.}$ of 1.23 ± 0.12 with a COV of 9.5%. In contrast, CSA S806-12 and CNR-DT 203/2006 provided conservative predictions, on average, with $\delta_{exp.}/\delta_{pred.}$ of 0.96 ± 0.06 with a COV of 6.6% and 0.97 ± 0.06 with a COV of 6.2%, respectively. The modified equation [Eq. (7.24)] yielded better

predictions than ACI 440.1R-15, on average, with $\delta_{exp.}/\delta_{pred.}$ of 0.99 ± 0.05 with a COV of 5.6%.

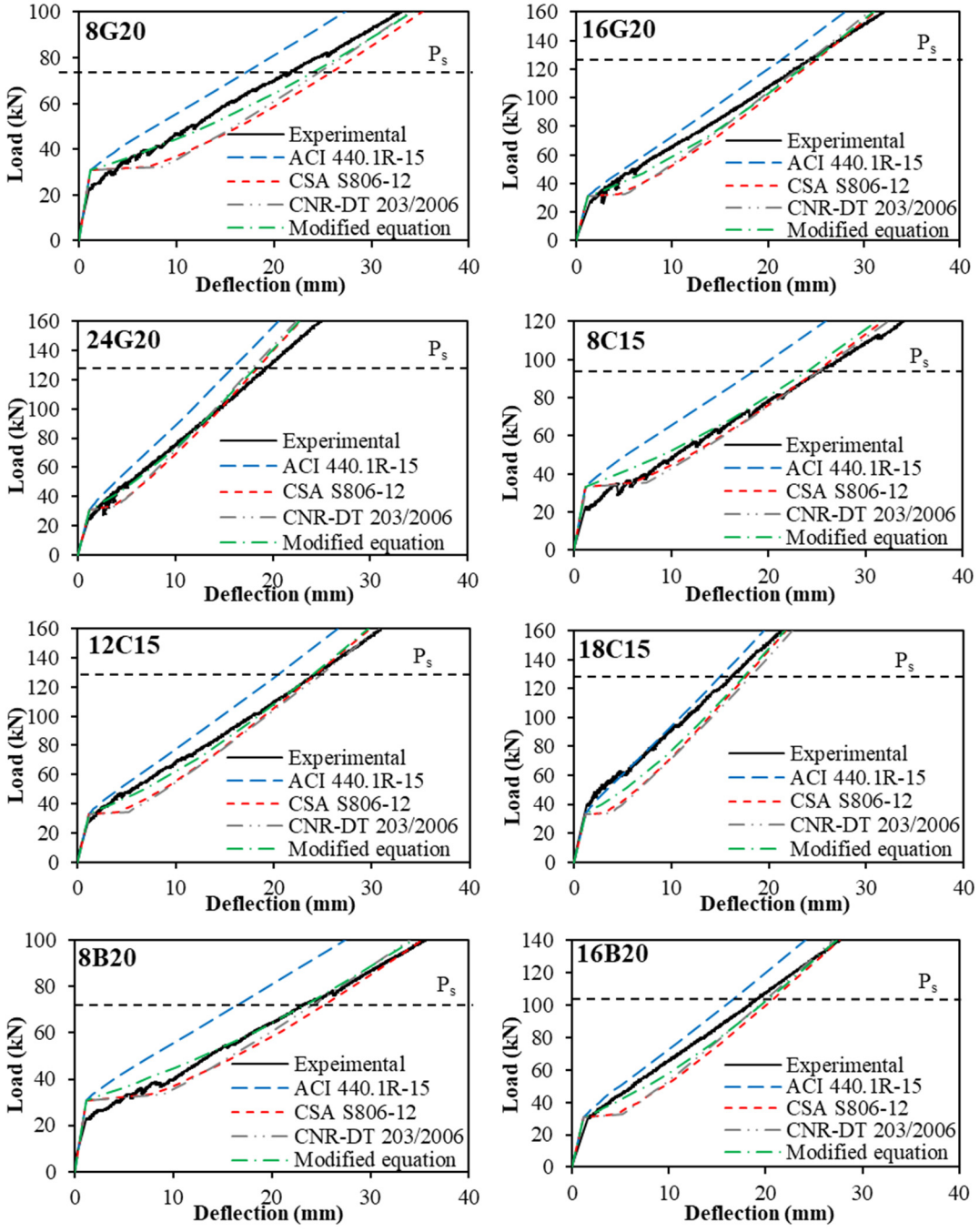

Figure 7.8 Load–deflection relationships measurements and predictions. (Note: 1 mm = 0.0394 in.; 1 kN = 0.225 kip)

Table 7.3 Experimental-to-predicted deflection $\left(\delta_{\text{exp.}}/\delta_{pred.}\right)$ at the service-load level.

Specimen ID	Experimental	ACI440.1R-15		CSA S806-12		CNR-DT 203/2006		Modified equation	
	δ_s (mm)	$\delta_{pred.}$ (mm)	$\delta_{\text{exp.}}/\delta_{pred.}$	$\delta_{pred.}$ (mm)	$\delta_{\text{exp.}}/\delta_{pred.}$	$\delta_{pred.}$ (mm)	$\delta_{\text{exp.}}/\delta_{pred.}$	$\delta_{pred.}$ (mm)	$\delta_{\text{exp.}}/\delta_{pred.}$
8G20	22.4	17.6	1.27	26.2	0.85	25.1	0.89	24.6	0.91
16G20	24.1	21.2	1.14	24.9	0.97	24.2	1.00	24.6	0.98
24G20	19.1	15.8	1.21	18.3	1.04	17.8	1.07	18.1	1.06
8C15	25.7	18.8	1.37	25.2	1.02	25.4	1.01	24.3	1.06
12C15	23.8	19.9	1.20	23.8	1.00	24.3	0.98	23.4	1.02
18C15	15.9	14.8	1.07	17.4	0.91	17.9	0.89	17.2	0.92
8B20	22.9	16.1	1.42	24.9	0.92	23.7	0.97	23.0	1.00
16B20	19.5	16.7	1.17	20.8	0.94	20.1	0.97	20.3	0.96
Average		----	1.23	----	0.96	----	0.97	----	0.99
Standard deviation		----	0.12	----	0.06	----	0.06	----	0.05
C.O.V. (%)		----	9.5	----	6.6	----	6.2	----	5.6

Note: 1 mm = 0.0394 in.

7.10. Analytical Model for Load-Deflection Relationship

The simplified code procedures are mainly developed for predicting deflections under service-load conditions. At higher loads, significant nonlinearity is expected to occur, and nonlinear analysis is required to accurately estimate deflection. In the following sections, a layer-by-layer iterative procedure is used to obtain the load–deflection relationship of the circular concrete members reinforced with FRP bars by idealizing the cross section as a series of layers to assess the sectional forces corresponding to a given strain distribution.

7.10.1. Development of the Model

Based on the principles of force equilibrium and strain compatibility, an analytical model was developed to predict the load–deflection relationship of circular FRPRC members using a layer-by-layer approach to integrate the stresses over the cross-sectional areas of the concrete and longitudinal bars. The main assumptions considered in the model are:

1. Strain in the concrete and FRP reinforcement is proportional to the distance from the neutral axis (a plane section remains plane after deformation up to failure).
2. The maximum usable compressive strain in the concrete is assumed to be 0.0035.

3. The tensile behavior of the FRP reinforcement is linearly elastic up to failure.
4. The strain in FRP reinforcement, whether in tension or compression, is the same as that in the surrounding concrete (i.e., perfect bond exists between FRP reinforcement and concrete).

7.10.2. Materials Behavior

The unconfined concrete stress–strain model proposed by Popovics (1973) was used in this study. As shown in Fig. 7.9(a), the compressive stress f_c corresponding to strain ε_c in the Popovics model, is given by:

$$f_c = \frac{f_c'(\varepsilon_c/\varepsilon'_c)\mu}{\mu - 1 + (\varepsilon_c/\varepsilon'_c)^{\mu}} \tag{7.25}$$

where f_c' = unconfined concrete strength, obtained from the cylinder tests; ε'_c = corresponding strain; and $\mu = E_{\tan}/(E_{\tan} - E_{\sec})$. The tangent and secant moduli, $E_{\tan}$ and $E_{\sec}$, are determined as $E_{\tan} = 4700\sqrt{f_c'}$ (MPa), as recommended in ACI 318-14 and $E_{\sec} = f_c'/\varepsilon'_c$, respectively.

For concrete in tension, the Vecchio and Collins (Collins and Mitchell 1997) model was adopted, as illustrated in Fig. 7.9(a). The tensile stress in the concrete f_c corresponding to strain ε_c is given as $f_c = E_{tan}\varepsilon_c$ when the strain $\varepsilon_c < \varepsilon_{cr}$. For $\varepsilon_c > \varepsilon_{cr}$, the following equation is used:

$$f_c = \frac{f_{cr}}{1 + \sqrt{500(\varepsilon_c - \varepsilon_{cr})}} \tag{7.26}$$

where f_{cr} = cracking strength of concrete, taken as $f_{cr} = 0.62\sqrt{f_c'}$ (MPa) (ACI 318-14) and is related to the cracking strain ε_{cr} as $f_{cr} = E_{\tan}\varepsilon_{cr}$.

The FRP longitudinal bars were modeled as linear elastic up to failure, as shown in Fig. 7.9(b). The compressive modulus of elasticity of the GFRP and CFRP was taken as 80% and 85% of the tensile modulus of elasticity, respectively (ACI 440.1R-15). The modulus of elasticity of the BFRP in compression was taken as 80% of its tensile modulus of elasticity, similar to the GFRP.

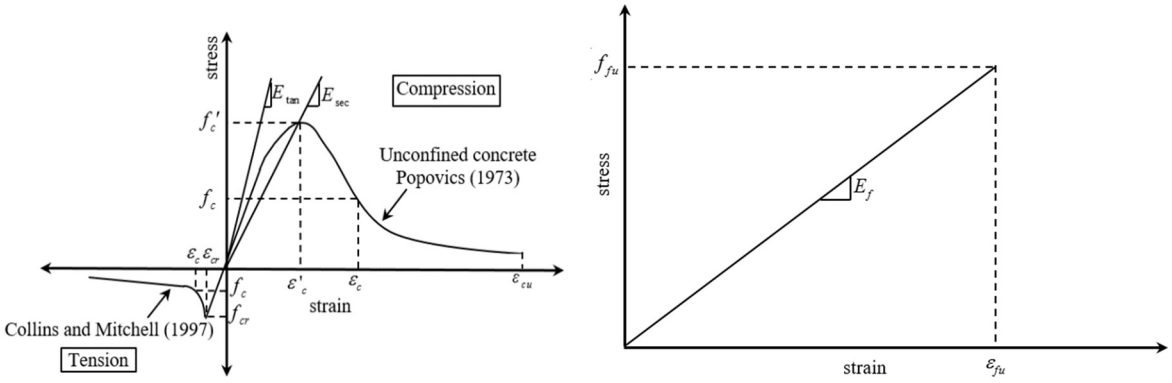

(a) Concrete (b) FRP bars

Figure 7.9 Stress-strain curves of the materials used in the analytical model.

7.10.3. Prediction of Load–Deflection Relationships

Figure 7.10 shows the actual cross section and idealized geometry of the circular FRPRC members. The depth of the section, D, is divided into n number of layers of equal thickness, t_i. The centroid of each layer is located at its mid thickness, and the depth to its center from the top level is h_i. Strains are linearly distributed along the depth of the section. The stresses in the concrete and FRP bars are based on the material relationships shown in Figs. 7.9(a) and 7.9(b). The stresses at the centroid of a strip are assumed constant throughout its thickness. Figure 7.10 also shows the linear strain distribution across the depth, where the top and bottom strains are ε_{Top} and ε_{Bottom}, respectively. The depth of the compression zone from the top of the section is the neutral-axis depth, c.

To obtain the load–deflection relationship of circular FRPRC members, the procedure can be summarized in the following steps, in relation to Fig. 7.10:

1. Specify the circular-section diameter, material properties, locations and areas of FRP bars, and number of layers, n.
2. Assume a value for the compressive strain ε_c in the extreme top fiber.
3. Assume a reasonable value for the neutral-axis depth, c.
4. For each layer i, from 1 to n, calculate h_i and the area of concrete, A_{ci}.

5. For each layer i, calculate the strain ε_i according to strain compatibility and compute the corresponding compressive or tensile stresses, f_{ci}.
6. Calculate the strain ε_j in the FRP bars at each level j according to strain compatibility, then calculate the corresponding stress, f_{bj}.
7. Calculate the compressive and tensile forces of concrete C_{ci} and T_{ci} as the summation of the all forces in all layers.
8. Calculate the compressive and tensile forces C_{bj} and T_{bj} in the FRP bars at each level, j.
9. Check for equilibrium by satisfying the condition that the absolute value of the sum of the total compressive and tensile forces is less than a certain allowable tolerance.
10. If equilibrium is not achieved, go to step 3, assume another value of c, and repeat the process until equilibrium is achieved.
11. Once equilibrium is achieved, the internal moments are calculated for individual layers and summed. The total moment corresponds to the strain level entered in step 2 and the corresponding curvature ψ is the slope of the strain profile, i.e., $\psi = \varepsilon_c / c$.
12. Go to step 2, increase ε_c, and repeat the procedure until the full moment–curvature response is established.
13. Calculate the deflection using the virtual work method as expressed by Eq. (7.27)

$$\delta_{\max} = \int_0^L \frac{m_{(x)} M_{(x)}}{E_c I_{(x)}} dx = \int_0^L m_{(x)} \psi_{(x)} dx \tag{7.27}$$

where L= the clear span of simply supported member; $M_{(x)}$= the applied moment; $I_{(x)}$ = the moment of inertia of the cross section; $m_{(x)}$ = the moment caused by a unit load applied at the point where deflection is being calculated; and $\psi_{(x)}$ = the curvature.

The analytical model is implemented with a computer program to facilitate the calculation procedures.

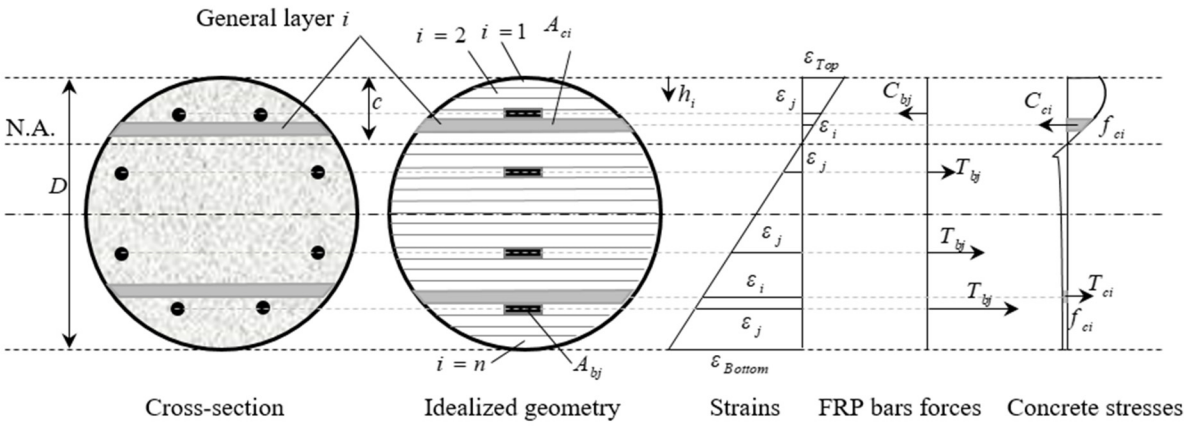

Figure 7.10 Idealized cross-section and stress and strain distributions in the analytical model.

7.10.4. Verification of the Analytical Model with Experimental Results

Analytical-model predictions were compared to the experimental load–deflection responses for the eight circular FRPRC specimens tested in this study, as shown in Fig. 7.11. The comparisons in the figure indicate the model's capability of reproducing the experimental load–deflection responses of the tested circular specimens. The results, in general, are in good agreement with the experimental results. In contrast, the model provides conservative predictions in terms of the predicted flexural capacity. The predicted results were less than the experimental results within a reasonable percentage. The average experimental flexural capacity over the predicted value was 1.14 with a coefficient of variation of 9.6%.

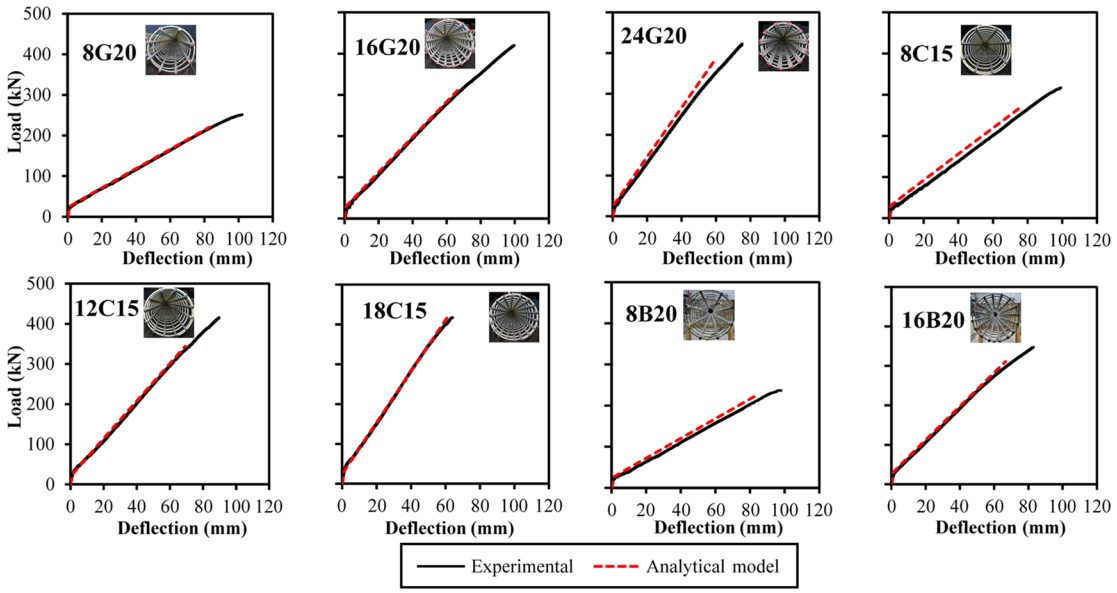

Figure 7.11 Experimental vs. analytical model load–deflection relationships of FRP-RC specimens. (Note: 1 mm = 0.0394 in.; 1 kN = 0.225 kip)

7.11. Conclusions

A total of eight full-scale circular RC specimens measuring 500 mm (20 in.) in diameter and 6,000 mm (236.22 in.) in length were constructed and tested up to failure under four-point bending load. The test parameters were the longitudinal-reinforcement ratio and the longitudinal-reinforcement type, including glass FRP, carbon FRP, and basalt FRP. The measured deflections and experimental values of the I_e were analyzed and compared with those predicted by available models. Based on the principles of force equilibrium and strain compatibility, an analytical model was developed to predict the load–deflection relationship of circular FRPRC members by using curvature analysis. The experimental data and theoretical analysis on deflection predictions provided the evidence required to include design provisions in the forthcoming ACI 440 and AASHTO codes for the design of FRPRC members with circular sections. Based on the results of this investigation, the following conclusions can be drawn:

1. All the specimens showed similar linear pre-cracking responses, regardless of the reinforcement type. Following cracking, all eight specimens evidenced a reduced-slope linear response up to failure.

2. The I_e prediction model recommended in ACI 440.1R-15 overestimated the experimental I_e and thus underestimated the service-load deflections with less conservative values, regardless of FRP reinforcement type, and at both low and high reinforcement ratios. The experimental-to-predicted deflection ratio $\left(\delta_{\exp}/\delta_{pred}\right)$ was 1.23 ± 0.12 with a COV of 9.5%.
3. The Bishcoff (2005, 2007) model yielded better predictions of I_e than the ACI 440.1R-15 model. The Benmokrane et al. (1996), ISIS Canada (2007), and Ovitigala et al. (2017) models, in contrast, provided conservative predictions at service load for all of the test specimens.
4. CSA S806-12 and CNR-DT 203/2006 provided conservative predictions of service-load deflections, on average, with a ratio $\left(\delta_{\exp}/\delta_{pred}\right)$ of 0.96 ± 0.06 with a COV of 6.6% and 0.97 ± 0.06 with a COV of 6.2%, respectively.
5. Based on the experimental results, a modified ACI 440.1R-15 equation (Bishcoff's equation) was suggested to predict the actual service-load deflection of the tested circular specimens. The modified equation yielded better predictions of service-load deflection than ACI 440.1R-15, on average, with $\delta_{\exp.}/\delta_{pred.}$ of 0.99 ± 0.05 with a COV of 5.6%.
6. An analytical model was developed to predict the load–deflection relationship of circular FRPRC members by using a layer-by-layer approach to integrate the stresses over the cross-sectional areas of concrete and longitudinal bars to account for concrete nonlinearity at high load levels. The comparisons with the experimental results indicate the model's capability of reproducing the experimental load–deflection responses of the tested circular specimens.

CHAPTER 8. SUMMARY, CONCLUSIONS, AND RECOMMENDATIONS

8.1. Summary

In this research study, an experimental program was designed to investigate the flexural behavior and serviceability of concrete members with circular section and reinforced with FRP bars and spirals. A total of nine large-scale specimens with a total length of 6,000 mm and 500 mm in diameter were constructed and tested under four-point bending. The test parameters included the longitudinal-reinforcement ratio and the longitudinal-reinforcement type, including GFRP, CFRP, BFRP, and steel bars. The experimental results are reported in terms of moment–deflection behavior, flexural capacity, mode of failure, crack patterns, crack spacing, and crack widths. An analytical strain-compatibility model capable of predicting the flexural strength of circular FRP-RC members, including the sequential progressive failure, was developed and verified with the experimental results. Moreover, a simplified method, including design equations and design chart, was presented using non-iterative analysis. In addition, a finite element model was developed to simulate the response of tested specimens and was used to extend the range of investigated parameters. Crack-control models in the current FRP codes and design guidelines were reexamined, extended, and applied to circular FRP-RC members. Finally, the measured deflections and experimental values of the effective moment of inertia (I_e) were analyzed and compared with those predicted using available models. Moreover, an analytical model has been developed by using a layer-by-layer approach to predict the load-deflection relationship of circular FRP-RC members.

8.2. Conclusions

Based on the experimental and analytical results obtained in this research considering the previous parameters associated with this research program, the following general conclusions are drawn:

8.2.1. General Behavior and Failure Mode

1. The failure of circular GFRP-RC specimens occurred by gradual concrete crushing. Interestingly, the GFRP-RC specimens did not lose their load-carrying capacity after concrete crushing. Instead, they continued to sustain additional loads. This behavior can be attributed to the confinement effect provided by the GFRP bars and spirals that enhanced specimen deformability and strength. In contrast, specimen 8S20 failed as the result of steel yielding, followed by concrete crushing.

2. The failure of the circular hybrid CFRP/GFRP-RC specimens occurred by concrete crushing, followed by rupture of tension bars in 8C15 and compressive failure of compression bars in 12C15 and 18C15.

3. In the circular BFRP-RC specimens, crushing of concrete in compression side of the constant moment zone took place; then the specimens continued to resist more loads until compressive failure of compression BFRP bars.

4. All the specimens showed similar linear pre-cracking responses regardless of reinforcement type. Following cracking, the eight circular specimens reinforced with FRP bars (GFRP, CFRP, and BFRP) showed a reduced slope linear response up to failure. On the other hand, a typical steel-yielding plateau was obtained in the specimen reinforced with steel.

5. The flexural strength at concrete crushing of FRP-RC specimens was 1.9 to 3.3 times greater than that of the counterpart steel-RC specimen with a similar reinforcement ratio.

6. The reinforcement ratio significantly affected the behavior of the circular FRP-RC specimens. As the reinforcement ratio increased, both the flexural stiffness and capacity increased. The flexural capacity at concrete crushing, however, was limited by concrete compressive strength and strain.

7. Based on the test results and parametric investigation, the failure of FRP-RC specimens under flexural load is not triggered by bar rupture on the tension side, provided that the minimum reinforcement ratio is not less than 0.8% for normal-strength concrete ($30 \leq f_c' \leq 60$ MPa).

8. The recorded concrete strains for all specimens were higher than the specified design limit in ACI440.1R-15 (–3,000 με) and CSA S806-12 (–3,500 με).

9. The compression strain of the GFRP reinforcing bars in the test specimens did not show compression failure. In addition, the GFRP bars developed up to 11,000 με of compressive strain, confirming that the GFRP bars were effective in resisting compression until after crushing of the concrete.

10. The experimental evidence of this study indicates that using GFRP and BFRP spirals as transverse reinforcement effectively prevented the buckling of the FRP bars and confined the concrete core in the post-peak stages up to a high strain level.

11. The neutral-axis depth before cracking was located at approximately the mid-height of the circular cross section and shifted towards the compression side just after cracking. Subsequently, its value remained constant and increased slightly at high load levels just before concrete crushing occurred.

8.2.2. Ductility and Deformability

12. Although all the circular FRP-RC specimens failed due to compression failure, a high degree of deformability was attained before failure. In all cases, the calculated deformability factor was higher than that required in CSA S6.

13. A deformability J-factor exceeding 6 is proposed and recommended to be used for FRP-RC members with circular sections similar to that required in CSA S6 for nonrectangular section (T-section).

8.2.3. Sectional Analysis

14. A strain compatibility model was developed to predict the flexural capacity of circular FRP-RC members using the strain compatibility and force equilibrium (setting the strength factors to unity). This model was capable of conservatively predicting the flexural capacity of the test specimens. Considering the compression contribution of the FRP bars (GFRP, CFRP, and BFRP) in the strain-compatibility and force-equilibrium

analyses provided accurate predictions of the flexural-moment capacities, while neglecting this contribution added to the level of conservativeness.

15. The computer program proposed in this study is capable of predicting the flexural capacity of circular FRP-RC members. The accuracy of the computer program's results was in good agreement with the measured values.

16. A simplified method including design equations, design chart, and step-by-step design procedures were presented using non-iterative analysis. This method can be considered a simple and more straightforward for practicing engineers.

8.2.4. Finite Element Analysis

17. The developed finite element model using ANSYS program was able to simulate the BFRP circular specimens and predict the failure moment as well as the moment-deflection relationship, showing a good prediction when compared to experimental results. The verified model was used to extend the range of investigated parameters.

8.2.5. Cracking and Crack Control

18. The specimens with lower reinforcement ratios—regardless of the type of FRP reinforcement—experienced fewer flexural cracks. Increasing the reinforcement ratio helped in the formation of several well-distributed flexural cracks. On the other hand, the early yielding of the steel bars in 8S20 prior to concrete crushing resulted in wider and concentrated cracks in the constant moment zone.

19. As the reinforcement ratio increased in the circular GFRP-reinforced specimens, the average crack spacing and crack-penetration depth decreased. Similar observations were made for the circular CFRP- and BFRP-reinforced specimens.

20. The crack width was directly proportional to the strain in the FRP reinforcement (GFRP, CFRP, and BFRP) up to failure. This was due to the elastic–linear behavior of the FRP bars, and, in case of RC specimen with steel reinforcement up to the yielding of the steel.

21. The crack width varied linearly with the applied moment up to failure in GFRP-reinforced specimens. Similar moment–crack-width relationships were obtained in the CFRP- and BFRP-reinforced specimens. This is attributed to the elastic–linear behavior of the FRP reinforcement. The control specimen, however, varied linearly until the steel reinforcement yielded.

22. As the axial stiffness of longitudinal reinforcement increased—regardless of the type of reinforcement—the measured crack width decreased at the same load level.

23. Decreasing the bar spacing in the specimens and increasing their axial stiffness decreased the crack width at the same load level. These results are in agreement with the AASHTO-09, CSA S6-14, ACI 440.1R-15, and JSCE-97 models for cracking, as the crack width is directly proportional to the maximum bar spacing.

24. The design equations for estimating the service stress in FRP reinforcement and the cracked moment of inertia were theoretically derived and presented for circular FRP-RC members.

25. The crack-control formulae developed on rectangular FRP-RC members are intended to allow for controlling the cracking of circular FRP-RC members using the redefined parameters developed and proposed in herein.

26. Comparing the crack widths predicted according to the various codes to the experimental results revealed that the AASHTO-09, ACI 440.1R-15, JSCE-97, and CNR-DT 203/2006 predictions were generally conservative with respect to the experimental crack-width values. On the other hand, CAN/CSA S6-14 predictions were nonconservative compared to the experimental crack-width values at high stress levels.

27. The experimental evidence from this investigation provides some experimental backbone for including crack design provisions in bridge-design specifications for the use of FRP bars in flexural members for bridge pier and pile applications. The present study on flexural behavior of circular concrete members reinforced with FRP bars and spirals (GFRP, CFRP, and BFRP) has answered significant number of questions in cracking and crack control issues.

8.2.6. Deflection and Effective Moment of Inertia

28. The I_e prediction model recommended in ACI 440.1R-15 overestimated the experimental I_e and thus underestimated the service-load deflections with less conservative values, regardless of FRP reinforcement type, and at both low and high reinforcement ratios. The experimental-to-predicted deflection ratio $\left(\delta_{\exp}/\delta_{pred}\right)$ was 1.23 ± 0.12 with a COV of 9.5%.
29. The Bishcoff (2005, 2007) model yielded better predictions of I_e than the ACI 440.1R-15 model. The Benmokrane et al. (1996), ISIS Canada (2007), and Ovitigala et al. (2017) models, in contrast, provided conservative predictions at service load for all of the test specimens.
30. CSA S806-12 and CNR-DT 203/2006 provided conservative predictions of service-load deflections, on average, with a ratio $\left(\delta_{\exp}/\delta_{pred}\right)$ of 0.96 ± 0.06 with a COV of 6.6% and 0.97 ± 0.06 with a COV of 6.2%, respectively.
31. Based on the experimental results, a modified ACI 440.1R-15 equation (Bishcoff's equation) was suggested to predict the actual service-load deflection of the tested circular specimens. The modified equation yielded better predictions of service-load deflection than ACI 440.1R-15, on average, with $\delta_{\exp.}/\delta_{pred.}$ of 0.99 ± 0.05 with a COV of 5.6%.
32. An analytical model was developed to predict the load–deflection relationship of circular FRPRC members by using a layer-by-layer approach to integrate the stresses over the cross-sectional areas of concrete and longitudinal bars to account for concrete nonlinearity at high load levels. The comparisons with the experimental results indicate the model's capability of reproducing the experimental load–deflection responses of the tested circular specimens.

8.3. Recommendations for Future Work

Results of this study present a promising step toward the use of the FRP bars as main flexural reinforcement in circular concrete members. This study has mainly focused on studying the flexural behavior of circular members, such as soft-eyes in tunnels and fender piles in marine structures that are usually subjected to pure bending moment without axial load. In addition, the current study addressed the worst (critical) case when the flexural demand prevails over the axial load in columns, piles and piers. Additional research is recommended based on the findings of the current study to cover the following points:

1. Experimental works are needed to consider the effect of axial load on the flexural strength and serviceability of circular FRP-RC members.

2. Serviceability (deflection and cracking) study should be extended to include the Circular FRP prestressed concrete members.

3. Different concrete types may also be investigated such as high strength concrete, self-consolidated concrete, and high-performance concrete.

4. Performance of circular FRP reinforced members subjected to fatigue and cyclic loads at service conditions might be investigated.

French version of this section is presented below:

8.4. Résumé

Dans cette étude, un programme expérimental a été conçu pour étudier le comportement en flexion, à l'ultime et en service, des éléments en béton à section circulaire et renforcés avec des barres et des spirales en PRF. Au total, neuf spécimens à grande échelle d'une longueur totale de 6 000 mm et d'un diamètre de 500 mm ont été construits et testés à la flexion en quatre points. Les paramètres d'essai comprenaient le rapport de renforcement longitudinal et le type de barres utilisées, soit le PRFV, le PRFC, le PRFB et les barres d'acier. Les résultats expérimentaux comprennent le comportement moment-déformation, la résistance en flexion, le mode de rupture, le patron de fissuration, l'espacement des fissures et la largeur des fissures. Un modèle analytique basé sur la compatibilité des déformations, capable de prédire la résistance en flexion des éléments circulaires en BA-PRF et incluant le mode de rupture progressif, a été développé

et validé avec les résultats expérimentaux. De plus, une méthode simplifiée, non itérative, comprenant des équations et un graphique, est présentée. En outre, un modèle d'éléments finis a été développé pour simuler la réponse des échantillons testés et a été utilisé pour étendre la gamme des paramètres étudiés. Les modèles de contrôle de fissure dans les normes couvrant les PRF et les directives de conception actuelle sont réexaminés, étendus et appliqués aux éléments circulaires en BA-PRF. Lors de l'analyse, les déflexions mesurées et les valeurs expérimentales du moment d'inertie effectif ont été analysées et comparées à celles prédites en utilisant les modèles disponibles. Finalement, un modèle analytique a été développé en utilisant une approche couche par couche pour prédire la relation charge-déformation des éléments circulaires en BA-PRF.

8.5. Conclusions

Sur la base des résultats expérimentaux et analytiques obtenus dans cette recherche, compte tenu des paramètres précédents associés à ce programme de recherche, les conclusions générales suivantes sont tirées:

8.5.1. Comportement général et mode de rupture

1. La défaillance des échantillons circulaires en BA-PRFV s'est produite par un écrasement graduel du béton. Fait intéressant, les spécimens en BA-PRFV n'ont pas perdu leur capacité de charge après l'écrasement du béton. Au lieu de cela, ils ont continué à supporter des charges supplémentaires. Ce comportement peut être attribué à l'effet de confinement fourni par les barres et les spirales en PRFV qui ont amélioré capacité de déformation et la résistance de l'élément. D'autre part, l'échantillon 8S20 a atteint la charge de rupture suite à la plastification de l'acier directement suivie par l'écrasement du béton.
2. La rupture des éléments circulaires hybrides BA-PRFC/PRFV s'est produite par écrasement du béton, suivie de la rupture des barres de tension en 8C15 et de la rupture en compression des barres de compression en 12C15 et 18C15.
3. Dans les échantillons circulaires en BA-PRFB, il y a eu écrasement du béton sur le côté en compression de la zone de moment constant; ensuite, les éléments ont continué à résister à des charges supplémentaires jusqu'à la rupture en compression des barres en PRFB.

4. Tous les échantillons ont présenté des réponses linéaires de pré fissuration similaires, quel que soit le type de renforcement. Après la fissuration, les huit spécimens circulaires renforcées avec des barres en PRF (PRFV, PRFC et PRFB) ont montré une réponse linéaire à pente réduite jusqu'à la rupture. D'autre part, un plateau typique lors de la plastification des barres a été obtenu pour l'élément renforcé avec des barres en acier.
5. La résistance en flexion lors de l'écrasement du béton des spécimens en BA-PRF était de 1,9 à 3,3 fois supérieure à la résistance de ceux en BA-acier avec un rapport de renforcement similaire.
6. Le rapport de renforcement a affecté significativement le comportement des échantillons circulaires en BA-PRF. À mesure que le rapport de renforcement augmentait, la rigidité en flexion et la capacité augmentaient. La capacité en flexion lorsque la rupture est initiée par l'écrasement du béton était cependant limitée par la résistance à la compression du béton ainsi que sa déformation.
7. Sur la base des résultats des essais et des analyses paramétriques, la rupture des spécimens en BA-PRF sous charge de flexion n'est pas déclenchée par la rupture des barres, à condition que le taux de renforcement minimal ne soit pas inférieur à 0,8% pour un béton de résistance normale ($30 \leq f_c' \leq 60$ MPa).
8. Les déformations de béton enregistrées pour tous les spécimens étaient supérieures à la limite de conception spécifiée dans l'ACI440.1R-15 (–3,000 με) et dans la CSA S806-12 (–3,500 με).
9. La déformation en compression des barres d'armature en PRFV dans les spécimens n'a pas causé la rupture des barres. En outre, les barres en PRFV se sont déformées jusqu'à 11 000 με en compression, confirmant que les barres en PRFV étaient efficaces pour résister à la compression jusqu'à l'écrasement du béton.
10. Les résultats expérimentaux de cette étude indiquent que l'utilisation de spirales en PRFV et en PRFB comme renforcement transversal a efficacement empêché le flambage des barres de PRF et a confiné le noyau de béton dans les phases post-pic jusqu'à un niveau de déformation élevé.
11. La profondeur de l'axe neutre avant la fissuration était située approximativement à la mi-hauteur de la section transversale circulaire et décalée vers le côté en compression juste

après la fissuration. Par la suite, sa valeur est restée constante et a légèrement augmenté à des niveaux de charge élevés juste avant l'écrasement du béton.

8.5.2. Ductilité et déformabilité

13. Bien que tous les spécimens circulaires en BA-PRF aient atteint la rupture par épuisement de la résistance en compression, un haut degré de déformabilité a été atteint avant la rupture. Dans tous les cas, le facteur de déformabilité calculé était supérieur à celui requis dans la norme CSA S6.
14. Un facteur J de déformabilité supérieur à 6 est proposé et recommandé pour les éléments en BA-PRF avec des sections circulaires semblables à celles requises dans la norme CSA S6 pour une section non rectangulaire (section en T).

8.2.3. Analyse sectionnelle

15. Un modèle basé sur la compatibilité des déformations a été développé pour prédire la capacité en flexion des spécimens circulaires en BA-PRF en utilisant les équations de compatibilité des déformations et l'équilibre des forces (en prenant les coefficients de pondération de résistance égaux à l'unité). Ce modèle était capable de prédire de manière conservatrice la capacité de flexion des spécimens. Considérant la contribution en compression des barres en PRF (PRFV, PRFC et PRFB) dans les analyses par compatibilité des déformations et d'équilibre des forces, on obtient des prédictions précises de la résistance en flexion. Négliger cette dernière contribution élève le niveau de conservatisme.
16. Le programme informatique proposé dans cette étude est capable de prédire la capacité de flexion des éléments circulaires en BA-PRF. Les résultats donnés par le programme informatique étaient en bon accord avec les valeurs mesurées expérimentalement.
17. Une méthode simplifiée non itérative comprenant des équations, un diagramme et des procédures étape par étape pour la conception a été présentée. Cette méthode peut être considérée comme suffisamment simple pour les ingénieurs de la pratique.

8.2.4 Analyse par éléments finis

18. Le modèle par éléments finis développé utilisant le programme ANSYS a été capable de simuler le comportement des spécimens circulaires en PRFB et de prédire le moment de rupture ainsi que la relation moment-déplacement, montrant une bonne prédiction par rapport aux résultats expérimentaux. Le modèle vérifié a été utilisé pour étendre la gamme de paramètres étudiés.

8.2.5 Fissuration et contrôle de la fissuration

19 Les spécimens avec des ratios de renforcement inférieurs - quel que soit le type de renforcement en PRF - ont subi moins de fissuration en flexion. L'augmentation du taux de renforcement a contribué à la formation de plusieurs fissures de flexion bien réparties. D'un autre côté, la plastification des barres d'acier pour le spécimen 8S20, avant l'écrasement du béton, a entraîné la formation de fissures plus larges et plus concentrées dans la zone des moments constants.

20 À mesure que le ratio de renforcement augmentait dans les spécimens circulaires renforcés par des barres en PRFV, l'espacement moyen des fissures et la profondeur de pénétration des fissures diminuaient. Des observations similaires ont été faites pour les échantillons circulaires renforcés par des barres en PRFC et en PRFB.

21 La largeur de la fissure était directement proportionnelle à la déformation dans les armatures de PRF (PRFV, PRFC et PRFB) jusqu'à la rupture. Cela était dû au comportement élastique linéaire des barres en PRF et, dans le cas de spécimens en BA avec armature en acier, jusqu'à la plastification de l'acier.

22 La largeur de la fissure varie linéairement avec le moment appliqué jusqu'à la rupture dans les spécimens renforcées par le PRFV. Des relations moment-largeur de fissure similaires ont été obtenues pour les spécimens renforcés par PRFC et avec du PRFB. Ceci est dû au comportement élastique linéaire du renforcement en PRF. Le spécimen de contrôle, cependant, a varié linéairement jusqu'à ce que l'armature en acier cède.

23 Au fur et à mesure que la rigidité axiale des armatures longitudinales augmentait, quel que soit le type de renforcement, la largeur de la fissure mesurée diminuait pour un même niveau de charge.

24 La réduction de l'espacement des barres dans les spécimen et l'augmentation de leur rigidité axiale ont diminué la largeur de fissures pour un même niveau de charge. Ces résultats sont en accord avec les modèles AASHTO-09, CSA S6-14, ACI 440.1R-15 et JSCE-97 pour la fissuration, car la largeur de la fissure est directement proportionnelle à l'espacement maximal des barres.

25 Les équations pour l'estimation de la contrainte de service dans le renforcement en PRF et le moment d'inertie fissuré ont été dérivées théoriquement et présentées pour les éléments circulaires en BA-PRF.

26 Les formules de contrôle des fissures développées pour les éléments rectangulaires en BA-PRF sont destinées à permettre le contrôle de la fissuration des éléments circulaires en BA-PRF en utilisant les paramètres redéfinis développés et proposés ici.

27 La comparaison de la largeur des fissures prédites selon les divers codes aux résultats expérimentaux a révélé que les prédictions selon l'AASHTO-09, l'ACI 440.1R-15, le JSCE-97 et le CNR-DT 203/2006 étaient généralement prudentes par rapport à la largeur de fissure mesurée expérimentalement. D'un autre côté, les prédictions de la norme CSA S6-14 étaient non conservatrices par rapport aux valeurs expérimentales de largeur de fissure à des niveaux de contrainte élevés.

28 Les données recueillies lors de cette étude fournissent une base expérimentale permettant d'inclure des règles de conception par rapport au contrôle de la fissuration dans les codes de conception de ponts concernant l'utilisation de barres en PRF dans des éléments en flexion pour des applications telles que pour des piliers et des pieux. La présente étude sur le comportement en flexion des éléments en béton circulaires renforcés par des barres et des spirales en PRF (PRFV, PRFC et PRFB) a permis de répondre à un nombre important de questions sur les problèmes de fissuration et de contrôle des fissures.

8.2.6 Flèche et moment d'inertie effectif

29 Le modèle de prédiction pour I_e recommandé par l'ACI 440.1R-15 surestime la valeur expérimentale de I_e et sous-estime donc les flèches sous charge de service,

indépendamment du type de renforcement en PRF, et pour des rapports de ferraillage faible et élevé.

30 Le modèle de Bishcoff (2005, 2007) permet de mieux prédire la valeur de I_e que le modèle de l'ACI 440.1R-15. D'autre part, les modèles de Benmokrane et al. (1996), ISIS Canada (2007) et Ovitigala et al. (2017) fournissent des prévisions sécuritaires au niveau de la charge de service pour tous les spécimens testés.

31 La norme CSA S6-14 et la norme CNR-DT 203/2006 permettent une évaluation sécuritaire de la flèche sous charges de service.

32 Sur la base des résultats expérimentaux, une équation ACI 440.1R-15 modifiée (équation de Bishcoff) a été suggérée pour prédire la déviation réelle de la charge de service des spécimens circulaires testées.

33 Un modèle analytique a été développé pour prédire la relation charge-déformation des éléments circulaires en BA-PRF, en utilisant une approche couche par couche pour intégrer les contraintes sur les sections transversales du béton et des barres longitudinales pour tenir compte de la non-linéarité du béton à des niveaux de charge élevés. Les comparaisons avec les résultats expérimentaux montrent la capacité du modèle à reproduire les réponses expérimentales charge-déplacement des spécimens circulaires testés.

8.3 Recommandations pour des travaux futurs

Sur la base des résultats et des conclusions de cette étude, les suggestions suivantes seront faites concernant les travaux futurs:

1. Des études supplémentaires sont nécessaires pour vérifier l'effet de la charge axiale sur la résistance à la flexion et sur les critères sous charges de services pour les éléments circulaires en BA-PRF.

2. L'étude des critères en service (flèche et fissuration) devrait être étendue pour inclure les éléments circulaires en béton, précontraint à l'aide de PRF.

3. Différents types de béton peuvent également être étudiés, tels que le béton à haute résistance, le béton autoplaçant et le béton à haute performance.

4. Les performances des éléments circulaires renforcés de PRF soumis à la fatigue et aux charges cycliques dans des conditions de service pourraient être étudiées.

REFERENCES

Adam M. A., Said, M., Mahmoud, A. A., and Shanour, A. S. (2015). "Analytical and experimental flexural behavior of concrete beams reinforced with glass fiber reinforced polymers bars." *Constr. Build. Mater.*, 84, 354–366.

Afifi, M. Z., Mohamed, H. M., and Benmokrane, B. (2014a). "Axial capacity of circular concrete columns reinforced with GFRP bars and spirals." *J. Compos. Constr.*, 18(1), 04013017.

Afifi, M. Z., Mohamed, H. M., and Benmokrane, B. (2014b). "Strength and Axial Behavior of Circular Concrete Columns Reinforced with CFRP Bars and Spirals." *J. Compos. Constr.*, 18(2), 04013035.

Afifi, M. Z., Mohamed, H. M., and Benmokrane, B. (2015). "Theoretical stress-strain model for circular concrete columns confined by GFRP spirals and hoops." *Eng. Struct.*, 102, 202–213.

Ali, A. H., Mohamed, H. M., and Benmokrane, B. (2016). "Shear Behavior of Circular Concrete Members Reinforced with GFRP Bars and Spirals at Shear Span-to-Depth Ratios between 1.5 and 3.0." *J. Compos. Constr.*, 20(6), 04016055.

Ali, A. H., Mohamed, H. M., and Benmokrane, B. (2017a). "Shear Strength of Circular Concrete Beams Reinforced with Glass Fiber-Reinforced Polymer Bars and Spirals." *ACI Struct. J.*, 114(1), 39-49.

Ali, A. H., Mohamed, H. M., and Benmokrane, B. (2017b). "Strength and Behavior of Circular FRP-Reinforced Concrete Sections without Web Reinforcement in Shear." *J. Struct. Eng.*, 143(3), 04016196.

Ali, M. A., and El-Salakawy E. (2016) "Seismic Performance of GFRP-Reinforced Concrete Rectangular Columns," *J. Compos. Constr.*, 20(3), 04015074.

Alsayed, S. H., Al-Salloum, Y. A., and Almusallam, T. H. (2000). "Performance of fiber reinforced plastic bars as a reinforcing material for concrete structures." *Compos. Part B*., 31, 555–567.

ANSYS Verification Manual (2009) "Release 12.0". ANSYS, Inc., United States.

American Association of State Highway and Transportation Officials (AASHTO). (2009). *AASHTO LRFD bridge design guide specifications for GFRP–reinforced concrete bridge decks and traffic railings*, Washington, D.C.

American Association of State Highway and Transportation Officials (AASHTO). (2012). *AASHTO LRFD bridge design guide specifications*, 6th Ed., Washington, D.C.

American Concrete Institute (ACI) Committee 318. (2014). "Building code requirements for structural concrete and commentary." *ACI 318R-14*, Farmington Hills, MI.

American Concrete Institute (ACI) Committee 440. (2001). "Guide for the design and construction of concrete reinforced with FRP bars." *ACI 440.1R-01*, Farmington Hills, MI.

American Concrete Institute (ACI) Committee 440. (2003). "Guide for the design and construction of concrete reinforced with FRP bars." *ACI 440.1R-03*, Farmington Hills, MI.

American Concrete Institute (ACI) Committee 440. (2006). "Guide for the design and construction of concrete reinforced with FRP bars." *ACI 440.1R-06*, Farmington Hills, MI.

American Concrete Institute (ACI) Committee 440. (2015). "Guide for the design and construction of concrete reinforced with FRP bars." *ACI 440.1R-15*, Farmington Hills, MI.

American Concrete Institute (ACI) Committee 440. (2017). Subcommittee ACI 440-H FRP Reinforced Concrete – "Design Standard for Concrete Structures Reinforced with GFRP Bars (under preparation)" *ACI 440.XXX Code*, Farmington Hills, MI.

American Concrete Institute (ACI) Committee 440. (2012). "Guide Test Methods for Fiber-Reinforced Polymers (FRPs) for Reinforcing or Strengthening Concrete Structures." *ACI 440.3R-12*, Farmington Hills, MI.

ASTM. (2011). "Standard test method for tensile properties of fiber reinforced polymer matrix composite bars." *ASTM D7205-11*, West Conshohocken, PA.

ASTM. (2017). "Standard specification for solid round glass fiber reinforced polymer bars for concrete reinforcement." *ASTM D7957-17*, West Conshohocken, PA.

Bakis, C., Ospina, C., Bradberry, T., Benmokrane, B., Gross, S., Newhook, J., and Thiagarajan, G., (2006). "Evaluation of Crack Widths in Concrete Flexural Members Reinforced with FRP Bars." *Proceedings of the 3rd International Conference on FRP Composites in Civil Engineering (CICE 2006)*, Florida International University, Miami, FL, 307-310.

Barris, C., Torres, Ll., Turon, A., Baena, M., and Catalan, A. (2009). "An experimental study of the flexural behaviour of GFRP-RC beams and comparison with prediction models." *Compos. Struct.*, 91, 286–295.

Barris, C., Torres, L., Vilanova, I., Miàs, C., Llorens, M. (2017). “Experimental study on crack width and crack spacing for Glass-FRP reinforced concrete beams.” *Eng. Struct.*, 131, 231–242.

Bergfelder, J. and Dittfach, J. (1992). “Limitation of the crack width for in-situ concrete piles.” *Beton- and stahlbetonbau*, 87(1), 4–8 and 46–49 (In German).

Bencardino, F., Condello, A., and Ombres, L. (2016). “Numerical and analytical modeling of concrete beams with steel, FRP and hybrid FRP-steel reinforcements.” Compos. Struct., 140, 53–65.

Benmokrane, B., Chaallal, O. and Masmoudi, R. (1996). “Flexural response of concrete beams reinforced with FRP reinforcing bars.” *ACI Struct. J.*, 93(1), 46-55.

Benmokrane, B., Elgabbas, F., Ahmed, E., and Cousin, P. (2015) “Characterization and comparative durability study of glass/vinylester, basalt/vinylester, and basalt/epoxy FRP bars.” *J. Compos. Constr.*,19(6), 04015008.

Bischoff, P. H. (2005). “Reevaluation of deflection prediction for concrete beams reinforced with steel and fiber reinforced polymer bars.” *J. Struct. Eng.*, 131(5), 752–767.

Bischoff, P. H. (2007). “Deflection calculation of FRP reinforced concrete beams based on modifications to the existing Branson equation.” *J. Compos. Constr.*, 11(1), 4–14.

Bischoff, P. H., and Gross, S. P. (2011a). “Design approach for calculating deflection of FRP reinforced concrete.” *J. Compos. Constr.*, 15(4), 490–499.

Bischoff, P. H., and Gross, S. P. (2011b). “Equivalent moment of inertia based on integration of curvature.” *J. Compos. Constr.*, 15(3), 263–273.

Bischoff P. H., Gross S., Ospina C. E. (2009). “The story behind the proposed changes to the ACI 440 deflection requirements for FRP-reinforced concrete.” *ACI Special Publication*, 264, 53-76.

Bischoff, P. H., and Scanlon, A. (2007). “Effective moment of inertia for calculating deflections of concrete members containing steel reinforcement and FRP reinforcement.” *ACI Struct. J.*, 104(1), 68–75.

Branson, D. E. (1965). “Instantaneous and time-dependent deflections of simple and continuous reinforced beams.” *HPR Rep. No. 7, Part 1*, Alabama Highway Department, Bureau of Public Roads, Montgomery, AL.

Canadian Standards Association (CSA). (2002). "Design and construction of building components with fiber reinforced polymers." *CAN/CSA S806-02*, Mississauga, Ontario, Canada.

Canadian Standards Association (CSA). (2012). "Design and construction of building components with fiber reinforced polymers." *CAN/CSAS806-12*, Mississauga, Ontario, Canada.

Canadian Standards Association (CSA). (2006). "Canadian highway bridge design code." *CAN/CSA S6-06*, Mississauga, Ontario, Canada.

Canadian Standards Association (CSA). (2014). "Canadian highway bridge design code." *CAN/CSA-S6-14*, Mississauga, Ontario, Canada.

Canadian Standards Association (CSA). (2010). "Specification for fibre reinforced polymers." *CAN/CSA S807-10*, Mississauga, Ontario, Canada.

Carbonell-Márquez, J. F., Gil-Martín, L. M., Fernández-Ruíz, M. A., and Hernández-Montes, E. (2014). "Effective area in tension stiffening of reinforced concrete piles subjected to flexure according to Eurocode 2." *Eng. Struct.*, 76, 62–74.

CEN (European Committee for Standardization). (2004). "Design of concrete structures—Part 1-1: General rules and rules for buildings." *Eurocode 2*, Brussels, Belgium.

CNR (National Research Council). (2007). "Guide for the design and construction of concrete structures reinforced with fiber-reinforced polymer bars." *CNR DT-203/2006*, Italian Research Council, Rome.

Collins, M. P., and Mitchell, D. (1997). Prestressed concrete structures, Response Publications, Canada.

De Domenico, D., Pisano, A. A., and Fuschi, P. (2014). "A FE-based limit analysis approach for concrete elements reinforced with FRP bars." Compos. Struct., 107, 594–603.

De Luca, A., Matta, F., and Nanni, A. (2010). "Behavior of full-scale glass fiber-reinforced polymer reinforced concrete columns under axial load." *ACI Struct. J.*, 107 (5), 589-596.

Elgabbas, F., Ahmed, E., and Benmokrane, B. (2015) "Physical and mechanical characteristics of new basalt-FRP rods for reinforcing concrete structures." *J. Construct. Build. Mater.*, 95, 623-635.

Elgabbas, F., Ahmed, E., and Benmokrane, B. (2016a). "Experimental Testing of Concrete Bridge-Deck Slabs Reinforced with Basalt-FRP Reinforcing Bars under Concentrated Loads." *J. Bridge Eng.*, 21(7), 04016029.

Elgabbas, F., Ahmed, E., and Benmokrane, B. (2017). "Flexural Behavior of Concrete Beams Reinforced with Ribbed Basalt-FRP Bars under Static Loads." *J. Compos. Constr.*, 21(3), 04016098.

Elgabbas, F., Vincent, P., Ahmed, E., and Benmokrane, B. (2016b). "Experimental testing of basalt-fiber-reinforced polymer bars in concrete beams." *Compos. Part B.*, 91, 205–216.

El-Gamal, S., El-Salakawy, E., and Benmokrane, B. (2005). "Behavior of concrete bridge deck slabs reinforced with fiber-reinforced polymer bars under concentrated loads." *ACI Struct. J.*, 102(5), 727–735.

El-Nemr, A., Ahmed, E. A., Barris, C., and Benmokrane, B. (2016). "Bond-dependent coefficient of glass- and carbon-FRP bars in normal- and high-strength concretes." *J. Constr. Build. Mater.*, 113, 77-89.

El-Nemr, A., Ahmed, E. A., and Benmokrane, B. (2013). "Flexural behavior and serviceability of normal- and high-strength concrete beams reinforced with glass fiber-reinforced polymer bars." *ACI Struct. J.*, 110 (6), 1077-1088.

El-Salakawy, E., Kassem, C. and Benmokrane, B., (2002). "Flexural behaviour of concrete beams reinforced with carbon FRP composite bars." *4th Structural Specialty Conference of the Canadian Society for Civil Engineering*, Montréal, Quebec, Canada, June 5-8, 2002.

El-Salakawy, E. and Benmokrane, B. (2004). "Serviceability of Concrete Bridge Deck Slabs Reinforced with Fiber-Reinforced Polymer Composite Bars." *ACI Struct. J.*, 101 (5), 727-736.

El-Sayed, A. K., El-Salakawy, E. F., and Benmokrane, B. (2006). "Shear Strength of FRP-Reinforced Concrete Beams without Transverse Reinforcement." *ACI Struct. J.*, 103 (2), 235-243.

Elshamandy, M. G., Farghaly, A. S., and Benmokrane, B. (2018) "Experimental Behavior of Glass Fiber-Reinforced Polymer- Reinforced Concrete Columns under Lateral Cyclic Load," *ACI Struct. J.*, 115(2), 337-349.

Faza, S. S. and GangaRao, H. V. S. (1993). "Theoretical and Experimental Correlation of Behavior of Concrete Beams Reinforced with Fiber Reinforced Plastic Rebars." *ACI Special Publication*, 138, 599-614.

Feltham, I. (2004). “Shear in Reinforced Concrete Piles and Circular.” *Struct. Eng.*, 82(11), 27-31.

Fib (International Federation for Structural Concrete). (2007). “FRP reinforcement in RC structures.” Bulletin 40, Technical Rep., Lausanne, Switzerland.

Frosch, R. J. (1999). “Another look at cracking and crack control in reinforced concrete.” *ACI Struct. J.*, 96(3), 437–442.

Gao, D., Masmoudi, R., and Benmokrane, B. (1998). “A calculating method of flexural properties of FRP-reinforced concrete beam: Part 1: crack-width and deflection.” *Technical Repor*t, Department of Civil engineering, University of Sherbrooke, Sherbrooke, Quebec, Canada, 24p.

Gergely, P., and Lutz, L. A. (1968). “Maximum crack width in RC flexural members, causes, mechanism and control of cracking in concrete.” SP-20, *American Concrete Institute*, Farmington Hills, MI, 87–117.

Gribniak, V., Arnautov, A. K., Kaklauskas, G., Tamulenas, V., Timinskas, E., and Sokolov, A. (2015). “Investigation on application of basalt materials as reinforcement for flexural elements of concrete bridges.” *Baltic J. Road Bridge Eng.*, 10(3), 201–206.

Guérin, M., Mohamed, H. M., Benmokrane, B., Nanni, A., and Shield, C. K. (2018) “Eccentric Behavior of Full-Scale Reinforced Concrete Columns with Glass Fiber-Reinforced Polymer Bars and Ties.” *ACI Struct. J.*, 115(2), 489-499.

Hadhood, A., Mohamed, H. M. and Benmokrane, B. (2017a). “Axial load–moment interaction diagram of circular concrete columns reinforced with CFRP bars and spirals: experimental and theoretical investigations.” *J. Compos. Constr.*, 21(2), 04016092.

Hadhood, A., Mohamed, H. M., Ghrib, F. and Benmokrane, B. (2017b). “Efficiency of glass-fiber reinforced-polymer (GFRP) discrete hoops and bars in concrete columns under combined axial and flexural loads.” *Compos. Part B.*, 114, 223–236.

Hadi, M. N. S., Karim, H., and Sheikh, M. N. (2016). “Experimental Investigations on Circular Concrete Columns Reinforced with GFRP Bars and Helices under Different Loading Conditions.” *J. Compos. Constr.*, 20(4), 04016009.

ISIS Canada Research Network (2001). “Reinforced Concrete Structures with Fibre Reinforced Polymers” *ISIS Manual No.3*, University of Manitoba, Winnipeg, MB, Canada.

ISIS Canada Research Network (2007). "Reinforced Concrete Structures with Fibre Reinforced Polymers" *ISIS Manual No.3*, University of Manitoba, Winnipeg, MB, Canada.

Jaeger, L. G., Mufti, A. A., and Tadros, G. (1997). "The concept of the overall performance factor in rectangular-section reinforced concrete members." Proc., 3rd Int. Symp. *on Non-Metallic (FRP) Reinforcement for Concrete Structures*, FRPRCS-3, V. 2, Japan Concrete Institute, Tokyo, 551–559.

JSCE (Japan Society of Civil Engineers). (1997). "Recommendation for design and construction of concrete structures using continuous fiber reinforcing materials." *JSCE-97*, Tokyo.

Jua, M., Park, Y., and Park, C. (2017). "Cracking control comparison in the specifications of serviceability in cracking for FRP reinforced concrete beams." *Compos. Struct.*, 182, 674–684.

Kani G. N. J. (1964). "The riddle of shear failure and its solution." *ACI journal*, 61(4), 441-467.

Kara, I. F. and Ashour, A. F. (2012). "Flexural performance of FRP reinforced concrete beams." *Compos. Struct.*, 94, 1616–1625.

Kara, I. F., Ashour, A. F., and Köroglu, M. A. (2015). "Flexural behavior of hybrid FRP/steel reinforced concrete beams." *Compos. Struct.*, 129, 111–121.

Kara, I. F., Köroglu, M. A., and Ashour, A. F. (2017). "Tests of continuous concrete slabs reinforced with basalt fiber-reinforced plastic bars." *ACI Struct. J.*, 114(5), 1201-1213.

Karim, H., Sheikh, M. N., and Hadi, M. N. S. (2017). "Load and Moment Interaction Diagram for Circular Concrete Columns Reinforced with GFRP Bars and GFRP Helices." *J. Compos. Constr.*, 21(1), 04016076.

Kassem, C., Farghaly, A. S., and Benmokrane, B. (2011). "Evaluation of flexural behaviour and serviceability performance of concrete beams reinforced with FRP bars." *J. Compos. Constr.*, 15(5), 682-695.

Khan, Q. S., Sheikh, M. N., and Hadi, M. N. S. (2018). "Concrete Filled Carbon FRP Tube (CFRP-CFFT) columns with and without CFRP reinforcing bars: Axial-flexural interactions." *Compos. Part B.*, 133, 42–52.

Mahroug, M. E. M., Ashour, A. F., and Lam, D. (2014). "Experimental response and code modelling of continuous concrete slabs reinforced with BFRP bars." *Compos. Struct.*, 107, 664–674.

Maranan, G. B., Manaloa, A. C., Benmokrane, B., Karunasenaa, W., Mendisc, P., and Nguyen, T. Q. (2018). “Shear behaviour of geopolymer-concrete beams transversely reinforced with continuous rectangular GFRP composite spirals.” *Compos. Struct.*, 187, 454–465.

Masmoudi, R., Benmokrane, B., and Chaallal, O. (1996), “Cracking behaviour of concrete beams reinforced with fiber reinforced plastic rebars.” *Can. J. Civ. Eng.*, 23, 1172-1179.

Masmoudi, R., Theriault, M. and Benmokrane, B. (1998), “Flexural Behavior of Concrete Beams Reinforced with Deformed Fiber Reinforced Plastic Reinforcing Rods.” *ACI Struct. J.*, 95(6), 665-676.

Matos, B., Correia, J. R., Castro, L. M. S., and França, P. (2012). “Structural response of hyperstatic concrete beams reinforced with GFRP bars: Effect of increasing concrete confinement.” *Compos. Struct.*, 94, 1200–1210.

Miàs, C., Torres, Ll., Turon, A., Baena, M., and Barris, C. (2010). “A simplified method to obtain time-dependent curvatures and deflections of concrete members reinforced with FRP bars.” *Compos. Struct.*, 92, 1833–1838.

Miàs, C., Torres, L., Turon, A., and Barris, C. (2013). “Experimental study of immediate and time-dependent deflections of GFRP reinforced concrete beams.” *Compos. Struct.*, 96, 279–285.

Mohamed, H. M., Afifi, M. Z., and Benmokrane, B. (2014). “Performance evaluation of concrete columns reinforced longitudinally with FRP bars and confined with FRP hoops and spirals under axial load.” *J. Bridge Eng.*, 19(7), 04014020.

Mohamed, H. M., Ali, A. H., and Benmokrane, B. (2017). “Behavior of Circular Concrete Members Reinforced with Carbon-FRP Bars and Spirals under Shear.” *J. Compos. Constr.*, 21(2), 04016090.

Mohamed, H. M. and Benmokrane, B. (2014). “Design and performance of reinforced concrete water chlorination tank totally reinforced with GFRP bars: case study.” *J. Compos. Constr.*, 18(1), 05013001.

Mohamed, H. M., and Masmoudi, R. (2010). “Flexural strength and behavior of steel and FRP-reinforced concrete-filled FRP tube beams.” *Eng. Strut.*, 32, 3789-3800.

Mota, C., Alminar, S., and Svecova, D. (2006). “Critical review of deflection formulas for FRP-RC members.” *J. Compos. Constr.*, 10(3), 183–194.

Mousavi, S. R. and Esfahani, M. R. (2012). "Effective Moment of Inertia Prediction of FRP-Reinforced Concrete Beams Based on Experimental Results." *J. Compos. Constr.*, 16(5), 490-498.

Naaman, A. E., and Jeong, S. M. (1995). "Structural ductility of concrete beams prestressed with FRP tendons." Proc., 2nd Int. RILEM Symp. *on Non-Metallic (FRP) Reinforcement for Concrete Structures*, RILEM, Bagneux, France, 379–386.

Nanni, A. (1993). "Flexural behaviour and design of RC members using FRP reinforcement." *J. Struct. Eng.*, 119(11), 3344-3359.

Nanni, A., De Luca, A., and Zadeh, H. J. (2014). "Reinforced concrete with FRP bars: mechanics and design." *CRC Press*.

Newmark N. M. (1943). "Numerical procedure for computing deflections, moments, and buckling loads". *ASCE Trans.*, 108(1),1161–1188.

Noël, M. and Soudki. K. (2014). "Estimation of the crack width and deformation of FRP-reinforced concrete flexural members with and without transverse shear reinforcement." *Eng. Struct.*, 59, 393–398.

Ospina, C. E., and Bakis, C. E. (2007). "Indirect Flexural Crack Control of Concrete Beams and One-Way Slabs Rein-forced with FRP Bars," *Proceedings of the 8th International Symposium on Fiber Reinforced Polymer Reinforcement for Concrete Structures* (FRP-RCS-8), University of Patras, Patras, Greece, July 16-18.

Ovitigala, T., Ibrahim, M. A., and Issa, M. A. (2016). "Serviceability and ultimate load behavior of concrete beams reinforced with basalt fiber-reinforced polymer bars." *ACI Struct. J.*, 113(4), 757-768.

Ovitigala, T., Ibrahim, M. A., and Issa, M. A. (2017). "Serviceability and ultimate load behavior of concrete beams reinforced with basalt fiber-reinforced polymer bars." *ACI Struct. J.*, 113(4), 757-768, Discussion by Peter H. Bischoff, *ACI Struct. J.*, 114(4), 1067-1071.

Popovics, S. (1973). "A numerical approach to the complete stress-strain curve of concrete." *Cem. Concr. Res.*, 3(5), 583–599.

Pultrall (2015). Data Sheet – Fiberglass and Carbon Reinforcements. www.pultrall.com

Rafi, M. M., Nadjai, A., Ali, F. and Talamona, D. (2008). "Aspects of behaviour of CFRP reinforced concrete beams in bending." *J. Constr. Build. Mater.*, 22(3), 277-285.

Razaqpur, A. G., Svecova, D., and Cheung, M. S. (2000). "Rational method for calculating deflection of fiber-reinforced polymer reinforced beams." *ACI Struct. J.*, 97(1), 175–185.

Shalaby, A. M., Fouad, F. H., and Albanese, R. (2011). "Strength and deflection behavior of spun concrete poles with CFRP reinforcement." *PCI Journal*, 56(2), 55-77.

Sharbatdar, M. K., Saatcioglu, M., and Benmokrane, B. (2011). "Seismic flexural behavior of concrete connections reinforced with CFRP bars and grids." *Compos. Struct.*, 93, 2439–2449.

Tavassoli, A., Liu, J., and Sheikh, S. (2015) "Glass Fiber-Reinforced Polymer-Reinforced Circular Columns under Simulated Seismic Loads," *ACI Struct. J.*, 112(1), 103-114.

Tegos, I. A., Giannakas, N. C. and Chrysanidis, T. A. (2011). "Serviceability cracking check of circular section piers." *Bridge Structures*, 7, 43–52.

Theriault, M. and Benmokrane, B. (1998). "Effects of FRP reinforcement ratio and concrete strength on flexure behavior of concrete beams." *J. Compos. Constr.*, 2(1), 7-16.

Tobbi, H., Farghaly, A. S., and Benmokrane, B. (2012) "Concrete Columns Reinforced Longitudinally and Transversally with Glass Fiber-Reinforced Polymer Bars." *ACI Struct. J.*, 109(4), 1-8.

Tomlinson, D., and Fam, A. (2015). "Performance of concrete beams reinforced with basalt FRP for flexure and shear." *J. Compos. Constr.*, 19(2), 04014036.

Toutanji H. and Deng Y. (2003). "Deflection and crack-width prediction of concrete beams reinforced with glass FRP rods." *J. Constr. Build. Mater.*,17, 69-74.

Toutanji H. A. and Saafi M. (2000). "Flexural behavior of concrete beams reinforced with glass fiber-reinforced polymer (GFRP) bars." *ACI Struct. J.*, 97(5), 712-719.

Urbański, M., Lapko, A., and Garbacz, A. (2013). "Investigation on concrete beams reinforced with basalt rebars as an effective alternative of conventional R/C structures*." J. Procedia Eng.*, 57, 1183–1191.

Vijay, P. V. and GangaRao, H. V. (2001). "Bending Behaviour and Deformability of Glass Fiber-Reinforced Polymer Reinforced Concrete Members." *ACI Struct. J.*, 98(6), 834-842.

Wolanski, A.J. (2004). Flexural behavior of reinforced and prestressed concrete beams using finite element analysis. *M.Sc. Thesis*, Marquette University, Milwaukee, Wisconsin.

Wiese, H., Curbach, M., Speck, K., Weiland, S., Eckfeld, L. and Hampel, T. (2004). "Verification of crack limitation for circular cross section." *Beton- and stahlbetonbau*, 99(4), 253–261 (In German).

Yost, J. R. and Gross, S. P. (2002). “Flexural design methodology for concrete beams reinforced with fiber-reinforced polymers.” *ACI Struct. J.*, 99(3), 308-316.

Yost, J. R., Gross, S. P., and Dinehart, D. W. (2003). “Effective moment of inertia for glass fiber-reinforced polymer-reinforced concrete beams.” *ACI Struct. J.*, 100(6), 732–739.

Zadeh, H. J., and Nanni, A. (2013). “Design of RC Columns Using Glass FRP Reinforcement.” *J. Compos. Constr.*, 17(3), 294-304.

Zhang, H., Yao, Y., Zhu, D., Mobasher, B., and Huang, L. (2015). “Tensile mechanical properties of basalt fiber reinforced polymer composite under varying strain rates and temperatures.” *Polymer Testing*, 51, 29–39.

APPENDIX A. DESIGN EXAMPLE: FLEXURAL CAPACITY OF A CIRCULAR GFRP-RC MEMBER

Design a circular concrete member of diameter D = 500 mm with adequate flexural strength. It must resist service-load moments M_D = 76 kN.m and M_L = 47 kN.m. Assume interior exposure conditions.

f_c' = 28 MPa, f_{fu}*= 550 MPa, and E_f = 45,000 MPa (*This example is similar to Example 3M in the ACI440.1R-15 for rectangular sections*)

Calculations

Design material properties:

C_E = 0.8 [440.1R, Table 6.2]

$f_{fu} = C_E f_{fu}$ *= (0.8) (550) = 440 MPa [440.1R, Eq. (6.2a)]

Method 1 – Using the Proposed Simplified Method

1. Assume a reinforcement ratio.

Assume $\rho_f > 1.4\rho_{fb}$

Assume No. 13 spirals and No. 25 bar diameter: d_b = 25.4 mm

For interior exposure, the clear cover is 38 mm:

$$D_r = 500 - \left(2\left(38 + 12.7 + \frac{25.4}{2}\right)\right) = 373.2\,\text{mm}$$

$$d = \frac{D}{2} + \frac{D_r}{\pi} = \frac{500}{2} + \frac{373.2}{\pi} = 368.79\,\text{mm}$$ [Eq. (3. 20)]

Distance from extreme tension bar to top compression fiber = $500 - \left(38 + 12.7 + \frac{25.4}{2}\right) = 436.6$ mm

Calculate the balanced reinforcement ratio:

$$\rho_{fb} = 0.85\frac{f_c'}{f_{fb}}\frac{r^2\left(\theta_b - \sin\theta_b \cos\theta_b\right)}{Dd}$$ [Eq. (3.22)]

$$C_b = \frac{0.003}{0.003 + \left(\frac{440}{45,000}\right)}(436.6) = 102.5 \text{ mm}$$

$$\theta_b = cos^{-1}\left(1 - \frac{\beta_1 c_b}{r}\right) = cos^{-1}\left(1 - \frac{(0.85)(102.5)}{250}\right) = 0.861 rad. = \frac{0.861(180)}{\pi} = 49.35° \text{ [Eq. (3.23)]}$$

$$f_{fb} = \frac{(368.79 - 102.5)}{(436.6 - 102.5)}(440) = 350.4 \text{ MPa}$$

$$\rho_{fb} = 0.85\frac{28}{350.4}\frac{250^2\left(0.861 - sin\,(49.35)cos\,(49.35)\right)}{(500)(368.79)} = 0.0084$$

$$\rho_f > 1.4(0.0084) = 0.0118$$

The section is compression-controlled since $\rho_f \geq 1.4\rho_{fb}$, $\phi = 0.65$

2. Determine the required reinforcement and select bars.

$$A_f > 0.0118(500)(368.79) = 2176 \text{ mm}^2$$

Select 12 No. 25 bars ($A_f = 3060$ mm^2 and $A_{ft} = 6120$ mm^2).

3. Determine the capacity of the cross section.

$$\theta = 2.14\rho_{ft}^{0.18}\left(1.03 - 0.69\left(\frac{f_c'}{E_f}\right)^{0.17}\right) = 2.14\left(\frac{6120(100)}{\frac{\pi(500)^2}{4}}\right)^{0.18}\left(1.03 - 0.69\left(\frac{28}{45}\right)^{0.17}\right) = 1.03 rad.$$

[Eq. (3.27)]

$$\theta = \frac{1.03(180)}{\pi} = 59.2°$$

$$f_f = 0.85\frac{f_c'}{A_f}r^2(\theta - sin\theta cos\theta) = 0.85\frac{28}{3060}(250)^2\left(1.03 - sin\,(59.2)cos\,(59.2)\right) = 286.89 \text{ MPa}$$

[Eq. (3.26)]

$$\bar{y} = \frac{2r}{3}\left(\frac{sin^3\theta}{\theta - sin\,\theta\,cos\,\theta}\right) = \frac{2(250)}{3}\left(\frac{sin^3(59.2)}{1.03 - sin\,(59.2)cos\,(59.2)}\right) = 178.97 \text{ mm [Eq. (3.7)]}$$

Calculate the moment capacity as follows:

$$M_n = A_f f_f \left(\bar{y} + \frac{D_r}{\pi} \right) = 3060(286.89)\left(178.97 + \frac{373.2}{\pi} \right) \Big/ 10^6 = 261.4 \text{ kN.m} \qquad \text{[Eq. (3.25)]}$$

$$\phi M_n = 0.65(261.4) = 169.91 \text{kN.m}$$

$$M_u = 1.2M_D + 1.6M_L = 1.2(76) + 1.6(47) = 166.4 \text{kN.m} < \phi M_n = 169.91 \text{kN.m} \quad \text{OK}$$

Method 2- Using the Strain-Compatibility Iterative Method

1. **Assume a reinforcement ratio.**

After iteration, 12 No. 25 bars are selected as in Method 1 for comparison.

2. **Determine the location of the neutral axis** (*neglecting the effect of compression reinforcement*).

Assume the failure is compression failure, then, $\varepsilon_{cu} = 0.003$ and $\varepsilon_{f1} < \varepsilon_{fu}$

Iteration yields $c = 135.61 \text{mm}$.

Check the strain in the extreme tension bars.

$$\varepsilon_{f1} = \frac{\varepsilon_{cu}}{c} d_1 = \frac{0.003}{135.61}(311.4) = 0.00689 < \varepsilon_{fu} = \frac{440}{45{,}000} = 0.0098 \text{ OK (compression failure).}$$

3. Calculation of forces to check equilibrium.

a. Concrete compression force

$$\theta = cos^{-1}\left(1 - \frac{\beta_1 c}{r}\right) = cos^{-1}\left(1 - \frac{0.85(135.61)}{250}\right) = 57.39° = \frac{\pi\,(57.39)}{180} = 1 rad.$$

[Eq. (8)]

$$A_c = r^2\left(\theta - sin\,\theta\, cos\,\theta\right) = 250^2\left(1 - sin\,(57.39) cos\,(57.39)\right) = 34127.38 \text{ mm}^2$$

[Eq. (6)]

$$F_c = \alpha_1 f_c' A_c = 0.85(28)(34127.38)/10^3 = 812.23 \text{ kN} \qquad \text{[Eq. (3.5)]}$$

b. GFRP tension-bar forces

$$\varepsilon_{f1} = 0.00689$$

$$\varepsilon_{f2} = \frac{\varepsilon_{cu}}{c} d_2 = \frac{0.003}{135.61}(259.4) = 0.00574$$

$$\varepsilon_{f3} = \frac{\varepsilon_{cu}}{c} d_3 = \frac{0.003}{135.61}(170.4) = 0.00376$$

$$\varepsilon_{f4} = \frac{\varepsilon_{cu}}{c} d_4 = \frac{0.003}{135.61}(66.4) = 0.00146$$

$$F_{tb}=\sum_{i=1}^{n_t}\varepsilon_{fi}E_fA_{fi}=(45,000)(2)\left(\pi(25.4)^2/4\right)(0.00689+0.00574+0.00376+0.00146)\Big/10^3$$

=814 kN [Eq. (3.9)]

$F_{tb}\simeq F_c$ then, equilibrium is achieved.

4. Determine the capacity of the cross section.

$$M_n=F_c\bar{y}+\sum_{i=1}^{n_t}\varepsilon_{fi}E_fA_{fi}y_{ti}$$

$$\bar{y}=\frac{2r}{3}\left(\frac{sin^3\theta}{\theta-sin\theta\,cos\theta}\right)=\frac{2(250)}{3}\left(\frac{sin^3(57.39)}{1-sin(57.39)cos(57.39)}\right)=182.44\text{ mm}$$

$$M_n=F_c\bar{y}+\sum_{i=1}^{n_t}\varepsilon_{fi}E_fA_{fi}y_{ti}=\left(\left(812.23x10^3\right)(182.44)\right)$$
$$+(45,000)(2)\left(\pi(25.4)^2/4\right)\left((0.00689x197+0.00574x145+0.00376x56+0.00146x48)\right)\Big/10^6$$

[Eq. (11)]

=260.84 kN.m

$$\phi M_n=0.65(260.84)=169.55\,\text{kN.m}$$

$$M_u=1.2M_D+1.6M_L=1.2(76)+1.6(47)=166.4\,\text{kN.m}<\phi M_n=169.55\,\text{kN.m}\quad\text{OK}$$

The section with diameter D=500 mm with 12 No. 25 bars uniformly distributed has adequate flexural strength to resist the applied loads in both methods.

APPENDIX B. DESIGN EXAMPLE: CRACKING CONTROL OF A CIRCULAR GFRP-RC MEMBER

A circular bridge pier is being designed for a factored moment M_u = 250 kN.m and a factored compression force N_u = 500 kN. The pier diameter has been sized as 500 mm, and the required area of GFRP reinforcement has been chosen as 16 #6 GFRP bars. Check the pier for cracking control. The unfactored service-load moment is M_s=75 kN.m and the factored service-load compression force is N_s=150 kN. Assume exterior exposure conditions.

Solution:

f_c' = 41.4 MPa, E_c = 30.24 MPa, E_f = 63.9 MPa, $s = \frac{\pi D_r}{N} = \frac{\pi \times (500 - 2 \times 61)}{16}$ = 74 mm

$d_c = 38 + 13 + \frac{20}{2} = 61$ mm, $n_f = \frac{E_f}{E_c} = \frac{63.9}{30.24} = 2.11$, $d = \frac{D}{2} + \frac{D_r}{\pi} = \frac{500}{2} + \frac{(500 - 2x61)}{\pi} = 370.3$ mm

ACI 440.1R-15

1. Check the limitations on the value of d_c :

$$d_c \le \frac{E_f w}{2 f_{fs} \beta k_b}$$

Assume a maximum allowable crack width w of 0.7 mm.

Take k_b=1.4.

The parameters β and f_{fs} can be determined from cracked section analysis under service load by taking the first moment of area about the location of the neutral axis using a cracked transformed section. With reference to Fig. 10, the location of the neutral axis using a simple iteration of Eq. (8) was found to be c = 113.19 mm and $\theta = 56.82°$.

Case 1: ignoring the axial compression force

Approach (1)

The service stress f_{fs} can be calculated by dividing the compression-concrete circular segment to 10 layers of equal thickness with Eq. (13) as follows:

$$f_{fs} = \frac{M_s\left(d_{i=1} - c\right)}{\left[\frac{1}{n_f}\sum_{j=1}^{m} A_{cj}\left(c - d_j\right)^2 + \sum_{i=1}^{n} A_{fi}\left(d_i - c\right)^2\right]}$$

$$= \frac{75\times10^6\left(439 - 113.19\right)}{\left[\frac{1}{2.11}\sum_{j=1}^{10} A_{cj}\left(113.19 - d_j\right)^2 + \sum_{i=1}^{6} 2\times\frac{\pi\left(20\right)^2}{4}\left(d_i - 113.19\right)^2\right]}$$

= 105.78 MPa

$$\beta = \frac{h_2}{h_1} = \frac{D-c}{d_{i=1}-c} = \frac{500-113.19}{439-113.19} = 1.19$$

$$d_c \le \frac{E_f w}{2 f_{fs}\beta k_b}$$

$$61 \le \frac{63.9\times10^3\times0.5}{2\times105.78\times1.19\times1.4}$$

$61 < 90.6$ Ok

2. Check bar spacing against maximum spacing:

$$s_{\max} = 1.15\frac{E_f w}{f_{fs} k_b} - 2.5c_c \le 0.92\frac{E_f w}{f_{fs} k_b}$$

$$s_{\max} = 1.15\frac{\left(63.9\times10^3\right)\left(0.50\right)}{\left(105.78\right)\left(1.4\right)} - 2.5\left(51\right) \le 0.92\frac{\left(63.9\times10^3\right)\left(0.50\right)}{\left(105.78\right)\left(1.4\right)}$$

$s_{\max} = 120.6 \le 198.5$, so $s_{\max} = 120.6$ mm

$s = 74 < s_{\max} = 120.6$ Ok

Approach (2)

$$f_{fs} = \frac{M_s}{A_f\left(\bar{y} + \frac{D_r}{\pi}\right)} = \frac{75x10^6}{8x285\left(183.1 + \frac{378}{\pi}\right)} = 108.4 \text{ MPa}$$

$$\beta = \frac{h_2}{h_1} = \frac{D-c}{d-c} = \frac{500-113.19}{370.3-113.19} = 1.5$$

$$d_c \le \frac{E_f w}{2 f_{fs} \beta k_b}$$

$$61 \le \frac{63.9 \times 10^3 \times 0.5}{2 \times 108.4 \times 1.5 \times 1.4}$$

$61 < 70.2$ Ok

2. Check bar spacing against maximum spacing:

$$s_{\max} = 1.15 \frac{E_f w}{f_{fs} k_b} - 2.5 c_c \le 0.92 \frac{E_f w}{f_{fs} k_b}$$

$$s_{\max} = 1.15 \frac{\left(63.9 \times 10^3\right)\left(0.50\right)}{\left(108.4\right)\left(1.4\right)} - 2.5\left(51\right) \le 0.92 \frac{\left(63.9 \times 10^3\right)\left(0.50\right)}{\left(108.4\right)\left(1.4\right)}$$

$s_{\max} = 114.6 \le 193.7$, so $s_{\max} = 114.6$ mm

$s = 74 < s_{\max} = 114.6$ Ok

Case 2: considering the axial compression force

Approach (1)

The service stress f_{fs} can be calculated by dividing the compression-concrete circular segment to 10 layers of equal thickness with Eq. (14) as follows:

$$f_{fs} = \frac{\left(M_s - N_s \times \left(r - c\right)\right) \times \left(d_{i=1} - c\right)}{\left[\frac{1}{n_f} \sum_{j=1}^{m} A_{cj} \left(c - d_j\right)^2 + \sum_{i=1}^{n} A_{fi} \left(d_i - c\right)^2\right]} - \frac{N_s}{A_{trans.}}$$

$$\frac{\left(75 \times 10^6 - 150 \times 10^3 \times \left(250 - 113.19\right)\right) \times \left(439 - 113.19\right)}{\left[\frac{1}{2.11} \sum_{j=1}^{10} A_{cj} \left(113.19 - d_j\right)^2 + \sum_{i=1}^{6} 2 \times \frac{\pi \left(20\right)^2}{4} \left(d_i - 113.19\right)^2\right]} - \frac{150 \times 10^3}{36773}$$

= 72.75 MPa

$$\beta = \frac{h_2}{h_1} = \frac{D - c}{d_{i=1} - c} = \frac{500 - 113.19}{439 - 113.19} = 1.19$$

$$d_c \le \frac{E_f w}{2 f_{fs} \beta k_b}$$

$$61 \le \frac{63.9 \times 10^3 \times 0.5}{2 \times 72.75 \times 1.19 \times 1.4}$$

$61 < 131.8$ Ok

2. Check bar spacing against maximum spacing:

$$s_{\max} = 1.15\frac{E_f w}{f_{fs} k_b} - 2.5c_c \le 0.92\frac{E_f w}{f_{fs} k_b}$$

$$s_{\max} = 1.15\frac{(63.9\times10^3)(0.50)}{(72.75)(1.4)} - 2.5(51) \le 0.92\frac{(63.9\times10^3)(0.50)}{(72.75)(1.4)}$$

$s_{\max} = 233.25 \le 288.6$, so $s_{\max} = 233.25$ mm

$s = 74 < s_{\max} = 233.25$ Ok

Approach (2)

$$f_{fs} = \frac{M_s - N_s\times(r-c)}{A_f\left(\bar{y} + \frac{D_r}{\pi}\right)} - \frac{N_s}{A_{trans.}} = \frac{\left(75\times10^6 - 150\times10^3\times(250-113.19)\right)}{8\times285\left(183.1 + \frac{378}{\pi}\right)} - \frac{150\times10^3}{36773} = 74.7 \text{ MPa}$$

$$\beta = \frac{h_2}{h_1} = \frac{D-c}{d-c} = \frac{500-113.19}{370.3-113.19} = 1.5$$

$$d_c \le \frac{E_f w}{2 f_{fs} \beta k_b}$$

$$61 \le \frac{63.9\times10^3\times0.5}{2\times74.7\times1.5\times1.4}$$

$61 < 101.8$ Ok

2. Check bar spacing against maximum spacing:

$$s_{\max} = 1.15\frac{E_f w}{f_{fs} k_b} - 2.5c_c \le 0.92\frac{E_f w}{f_{fs} k_b}$$

$$s_{\max} = 1.15\frac{(63.9\times10^3)(0.50)}{(74.7)(1.4)} - 2.5(51) \le 0.92\frac{(63.9\times10^3)(0.50)}{(74.7)(1.4)}$$

$s_{\max} = 223.83 \le 281.1$, so $s_{\max} = 223.83$ mm

$s = 74 < s_{\max} = 223.83$ Ok

AASHTO-09

Case 1: ignoring the axial compression force

$$w = 2\frac{f_f}{E_f}\frac{h_2}{h_1}k_b\sqrt{{d_c}^2+\left(\frac{s}{2}\right)^2}$$

Approach (1)

$$w=(2)\frac{(105.78)}{(63.9x10^3)}\frac{(500-113.19)}{(439-113.19)}(1.4)\sqrt{(61)^2+\left(\frac{74}{2}\right)^2}=0.39\ \text{mm}<0.5\,\text{mm}$$

Approach (2)

$$w=(2)\frac{(108.4)}{(63.9x10^3)}\frac{(500-113.19)}{(370.3-113.19)}(1.4)\sqrt{(61)^2+\left(\frac{74}{2}\right)^2}=0.49\ \text{mm}\le 0.5\,\text{mm}$$

Case 2: considering the axial compression force

Approach (1)

$$w=(2)\frac{(72.75)}{(63.9x10^3)}\frac{(500-113.19)}{(439-113.19)}(1.4)\sqrt{(61)^2+\left(\frac{74}{2}\right)^2}=0.27\ \text{mm}<0.5\,\text{mm}$$

Approach (2)

$$w=(2)\frac{(74.7)}{(63.9x10^3)}\frac{(500-113.19)}{(370.3-113.19)}(1.4)\sqrt{(61)^2+\left(\frac{74}{2}\right)^2}=0.34\ \text{mm}\le 0.5\,\text{mm}$$

<u>CSA S6-14</u>

Case 1: ignoring the axial compression force

$$w = 2\frac{f_f}{E_f}\frac{h_2}{h_1}k_b\sqrt{{d_c}^2+\left(\frac{s}{2}\right)^2}$$

Approach (1)

$$w=(2)\frac{(105.78)}{(63.9x10^3)}\frac{(500-113.19)}{(439-113.19)}(0.8)\sqrt{(61)^2+\left(\frac{74}{2}\right)^2}=0.22\ \text{mm}<0.5\,\text{mm}$$

Approach (2)

$$w=(2)\frac{(108.4)}{(63.9x10^3)}\frac{(500-113.19)}{(370.3-113.19)}(0.8)\sqrt{(61)^2+\left(\frac{74}{2}\right)^2}=0.28\ \text{mm}<0.5\,\text{mm}$$

Case 2: considering the axial compression force

Approach (1)

$$w=(2)\frac{(72.75)}{(63.9x10^3)}\frac{(500-113.19)}{(439-113.19)}(0.8)\sqrt{(61)^2+\left(\frac{74}{2}\right)^2}=0.15\ \text{mm}<0.5\,\text{mm}$$

Approach (2)

$$w=(2)\frac{(74.7)}{(63.9x10^3)}\frac{(500-113.19)}{(370.3-113.19)}(0.8)\sqrt{(61)^2+\left(\frac{74}{2}\right)^2}=0.20\ \text{mm}<0.5\,\text{mm}$$

CNR-DT 203/2006

$$w_{\max}=\beta s_{rm}\varepsilon_{fm}$$

$$\rho_{f,eff}=\rho_{ft}\frac{D^2}{D^2-(D-5d_c)^2}=(0.024)\frac{(500)^2}{(500)^2-(500-5(61))^2}=0.0283$$

$$s_{rm}=50+0.25k_bk_l\frac{d_b}{\rho_{f,eff}}=50+0.25(1.6)(0.5)\frac{20}{0.0283}=191.3\,\text{mm}$$

Case 1: ignoring the axial compression force

Approach (1)

$$\varepsilon_{fm}=\frac{f_f}{E_f}\left[1-\beta_1\beta_2\left(\frac{f_{fr}}{f_f}\right)^2\right]=\frac{(105.78)}{(63.9x10^3)}\left[1-(0.5)(1.0)\left(\frac{39.5}{105.78}\right)^2\right]=0.00154$$

$$w_{\max}=1.7(191.3)(0.00154)=0.5\,\text{mm}$$

Approach (2)

$$\varepsilon_{fm}=\frac{f_f}{E_f}\left[1-\beta_1\beta_2\left(\frac{f_{fr}}{f_f}\right)^2\right]=\frac{(108.4)}{(63.9x10^3)}\left[1-(0.5)(1.0)\left(\frac{40.5}{108.4}\right)^2\right]=0.00158$$

$$w_{\max}=1.7(191.3)(0.00158)=0.51\,\text{mm}$$

Case 2: considering the axial compression force

Approach (1)

$$\varepsilon_{fm}=\frac{f_f}{E_f}\left[1-\beta_1\beta_2\left(\frac{f_{fr}}{f_f}\right)^2\right]=\frac{(72.75)}{(63.9x10^3)}\left[1-(0.5)(1.0)\left(\frac{39.5}{72.75}\right)^2\right]=0.00097$$

$$w_{\max}=1.7(191.3)(0.00097)=0.32\,\text{mm}$$

Approach (2)

$$\varepsilon_{fm}=\frac{f_f}{E_f}\left[1-\beta_1\beta_2\left(\frac{f_{fr}}{f_f}\right)^2\right]=\frac{(74.7)}{\left(63.9x10^3\right)}\left[1-(0.5)(1.0)\left(\frac{40.5}{74.7}\right)^2\right]=0.000997$$

$$w_{\max}=1.7(191.3)(0.000997)=0.32\,\text{mm}$$

JSCE-97

$$w=k_b\left(4c_c+0.7(s-d_b)\right)\left(\frac{f_{fe}}{E_f}+\varepsilon'_{csd}\right)$$

Case 1: ignoring the axial compression force

Approach (1)

$$w=1.15\left(4(51)+0.7(74-20)\right)\left(\frac{105.78}{63.9\times10^3}+0\right)=0.46\ \text{mm}<0.5\,\text{mm}$$

Approach (2)

$$w=1.15\left(4(51)+0.7(74-20)\right)\left(\frac{108.4}{63.9\times10^3}+0\right)=0.47\ \text{mm}<0.5\,\text{mm}$$

Case 2: considering the axial compression force

Approach (1)

$$w=1.15\left(4(51)+0.7(74-20)\right)\left(\frac{72.75}{63.9\times10^3}+0\right)=0.32\ \text{mm}<0.5\,\text{mm}$$

Approach (2)

$$w=1.15\left(4(51)+0.7(74-20)\right)\left(\frac{74.7}{63.9\times10^3}+0\right)=0.33\ \text{mm}<0.5\,\text{mm}$$